Multiphase Equilibria and Miscibility of Reservoir Fluids in Tight/Shale Reservoirs

by

Hao Sun

A thesis submitted in partial fulfillment of the requirements for the degree of

Doctor of Philosophy

in

Petroleum Engineering

Department of Civil and Environmental Engineering
University of Alberta

ABSTRACT

The phase behavior of reservoir fluids in tight/shale reservoirs can be dramatically altered from the bulk phase behavior due to the strong capillarity and confinement effects introduced by the confined nanopores found in the unconventional reservoirs. Therefore, an accurate description of the phase behavior of reservoir fluids in unconventional reservoirs cannot be obtained from the conventional multiphase equilibrium calculation algorithm when a high capillary pressure is present in nanopores. Moreover, due to the shift of reservoir fluids' phase behavior in nanopores, the miscibility between the reservoir fluids and the injection gas becomes different from that in the bulk conditions. Consequently, the compositional reservoir simulation that uses the conventional phase behavior calculation model will result in unreliable outputs when it is used to simulate tight/shale reservoirs. Therefore, calculation algorithms that can capture the effects of capillarity and confinement on the multiphase equilibrium and oil-gas minimum miscibility pressure (MMP) in nanopores are needed.

This thesis aims to minimize the difference between the multiphase equilibrium calculation results and the results obtained from experiments. The thesis first employs a modified Young-Laplace equation proposed by Tan and Piri (2015) and couples it with the Peng-Robinson equation of state (PR-EOS) model (Peng and Robinson, 1976). Then, the experimental data of phase transitions in confined nanopores are collected from literature to develop the λ correlations in the modified Young-Laplace equation for pure hydrocarbons and mixtures. The phase behavior results calculated using the proposed algorithm are validated by the experimental data.

Efforts are also made to develop a robust and comprehensive three-phase equilibrium calculation algorithm package that can reliably predict the three-phase equilibria of reservoir fluids in

nanopores with two capillary pressures. The two capillary pressures refer to the capillary pressure between the gas phase and the oleic phase as well as the capillary pressure between the oleic phase and the aqueous phase. The new three-phase equilibrium calculation algorithm is capable of predicting the aqueous-oleic-vapor three-phase boundary for a given mixture in nanopores. The results show that the aqueous-oleic-vapor three-phase envelope in confined nanopores appears to be different from the one in bulk conditions. This is the first modeling study investigating how two capillary pressures affect the aqueous-oleic-vapor three-phase equilibria in nanopores.

Another task of this thesis is to improve the prediction of MMP of crude oil being displaced by carbon dioxide (CO_2) in nanopores by coupling the capillarity and confinement effect into the modified Multiple-Mixing-Cell (MMC) method (Ahmadi and Johns, 2011). A state-of-art volume translation model is used in the PR-EOS model for a better prediction of phase densities. This work also proposes a simple MMP calculation strategy that considers the pore size distribution of tight/shale cores. Using the developed MMC code, we investigate how nanopore size, pore size distribution, and temperature influence the MMP between CO_2 and crude oil.

The last work of this thesis is to develop a modified cell-to-cell method that can be used to simultaneously calculate MMP and oil recovery factors during the gas flooding process in a confined space. In this work, the original cell-to-cell method proposed by Metcalf *et al.* (1973) is coupled with the capillary-pressure model and the critical point shift model (Tan *et al.*, 2019). The advantage of this cell-to-cell simulation model (Metcalfe *et al.*, 1973) over the MMC method developed by Ahmadi and Johns (2011) is that the cell-to-cell model mimics the physical 1-D gas displacement process. MMP as well as the final oil recovery factor can be obtained through the modified cell-to-cell calculation algorithm.

PREFACE

A version of **Chapter 2** has been published as Sun, H. and Li, H. 2020. Phase Behavior Modeling of Hydrocarbon Fluids in Nanopores Using PR-EOS Coupled with a Modified Young-Laplace Equation. ACS Omega, 5, 15177-15191. Sun, H. is responsible for the theoretical development, simulation results, analysis, and manuscript composition. Li, H. is the supervisory author and gets involved in the concept formation, theoretical development, analysis, and manuscript composition.

A version of **Chapter 3** has been published as Sun, H. and Li, H. 2019. A New Three-Phase Flash Algorithm Considering Capillary Pressure in a Confined Space. Chemical Engineering Science, 193, 346-363. Sun, H. is responsible for the theoretical development, simulation results, analysis, and manuscript composition. Li, H. is the supervisory author and gets involved in the concept formation, theoretical development, analysis, and manuscript composition.

A version of **Chapter 4** has been accepted for publication as Sun, H. and Li, H. 2021. Minimum Miscibility Pressure Determination in Confined Nanopores Considering Pore Size Distribution of Tight/Shale Formations. Fuel, 286. Sun, H. is responsible for the theoretical development, simulation results, analysis, and manuscript composition. Li, H. is the supervisory author and gets involved in the concept formation, theoretical development, analysis, and manuscript composition.

A version of **Chapter 5** was submitted to *Oil & Gas Science and Technology* for possible publication on March 14, 2021. Sun, H. is responsible for the theoretical development, simulation results, analysis, and manuscript composition. Li, H. is the supervisory author and gets involved in the concept formation, theoretical development, analysis, and manuscript composition.

Chapter 1 summarizes the research background, problem statement, research objectives, and thesis structure. **Chapter 6** summarizes the conclusions reached in this thesis as well as the

recommendations for future research. **Chapters 1** and **6** are originally written by Hao Sun and have never been published elsewhere.

DEDICATION

This dissertation is dedicated to my dearest parents: Mrs. Junling Yao and Mr. Xudong Sun and my lovely wife Mrs. Wenran Zhao.

ACKNOWLEDGMENTS

I would like to express my appreciation to my supervisor Dr. Huazhou Li for his guidance towards my Ph.D. research and his assistance in preparing this thesis. I am also grateful to Dr. Ergun Kuru, Dr. Hongbo Zeng, Dr. Nobuo Maeda, Dr. Sohrab Zendehboudi, and Dr. Zhehui Jin for serving as my examination committee members as well as providing constructive comments/suggestions.

I would also like to thank the following individuals or organizations for their support during my Ph.D. program:

- The past and present group members in Dr. Li's research group.
- Natural Sciences and Engineering Research Council (NSERC) for one Discovery Grant to Dr. Li.
- All my friends in Edmonton for their friendship.

TABLE OF CONTENTS

LIST OF TABLES

LIST OF FIGURES

CHAPTER 1 INTRODUCTION

1.1. Research Background

Tight/shale reservoirs have been contributing more oil/gas productions in the last several decades. A common feature is shared in such reservoirs: abundance in confined nanopores. It is found that the nanopores in shale reservoirs have diameters ranging from 5 to 1000 nm (Wang *et al*., 2009; Loucks *et al*., 2009). The capillary pressure, which is generally neglected in conventional reservoir modeling, could be large enough in nanopores to pose a noticeable impact on the phase behavior (Brusllovsky, 1992; Al-Rub and Datta, 1999; Nojabaei *et al*., 2013), the adsorption behavior (Ping *et al*., 1996; Jin and Firoozabadi, 2016), and the flow dynamics of reservoirs fluids (van Dijke *et al*., 2001; Hustad and Browning, 2010; Moortgat and Firoozabadi, 2013; Wang *et al*., 2013; Dong, 2014).

Many researchers have studied the effect of the capillary pressure on multi-phase equilibrium calculations and found that the vapor-liquid equilibria are greatly altered due to the capillarity effect (Brusllovsky, 1992; Al-Rub and Datta, 1999; Hamada *et al.*, 2007; Qi *et al.,* 2007; Firincioglu *et al.*, 2012; Pang *et al.*, 2012; Wang *et al.*, 2013; Sandoval *et al.*, 2015). Specifically, the bubble point pressure is decreased while the dew point pressure is increased in confined nanopores at a fixed temperature (Brusllovsky, 1992). More recently, Nojabaei *et al.* (2013) investigated the effect of capillary pressure on the shifting of the entire two-phase envelope for hydrocarbon mixture. They have come to the conclusion that, due to the strong capillarity effect, the dew point pressure is decreased when the bulk pressure is lower than the cricondentherm point, while it is increased when the bulk pressure is higher than the cricondentherm point.

While most of the studies so far focus on the two-phase equilibrium calculations in nanopores, three-phase equilibrium in nanopores are also commonly encountered due to water presence (Wong *et al.*, 2000; Li *et al.*, 2008; Iwere *et al.*, 2012; Li *et al.*, 2015). Numerical simulation studies on three-phase equilibrium calculations in tight/shale reservoirs have been conducted with the effect of capillary pressure (van Dijke *et al.,* 2001; Hustad and Browning, 2010; Moortgat and Firoozabadi, 2013; Dong, 2014). A common finding in their research is that the large capillary pressures between the vapor, aqueous, and oleic phases reduce the final oil recovery in an oil-wet formation. However, these studies focus on the fluid dynamics in the reservoir instead of static three-phase equilibrium in nanopores. Later, several studies touched on the three-phase equilibrium calculations in nanopores (Siripatrachai *et al.*, 2017; Neshat *et al.*, 2018). Siripatrachai *et al.* (2017) modified the negative flash algorithm and coupled it with capillary pressure. They found that the oil recovery is increased in a water-wet formation. Neshat *et al*. (2018) calculated the capillary pressure between the vapor and oleic phases using an equation of connate water saturation. Then the equation is implemented in the two-phase equilibrium calculations to include the effect of water and capillary pressure on two-phase equilibria in nanopores. They also observed reductions of the bubble point and dew point pressure at a fixed temperature (Neshat *et al*., 2018). Nevertheless, this study is performed on a basis of two-phase equilibrium calculations, neglecting that the presence of the aqueous phase might affect the fugacity-equality condition during the calculations.

With more attention paid to the gas-injection enhanced oil recovery (EOR) methods in tight/shale reservoirs, it is necessary to describe the oil-gas minimum miscibility pressure (MMP) accurately in nanopores. The conventional ways of determining the oil-gas MMP include experimental studies (Rathmell *et al*., 1971; Yellig, 1982; Christiansen and Haines, 1987; Randall and Bennion,

1988; Rao, 1997; Nguyen *et al*., 2015), empirical correlations (Holm and Josendal, 1974; Lee, 1979; Mungan, 1981; Orr and Jensen, 1984; Shokir, 2007; ZareNezhad, 2016; Li *et al*., 2012; Ahmadi *et al*., 2017), and computational simulations (Johns and Orr, 1996; Wang and Orr, 1997; Ahmadi and Johns, 2011). Many of these methods have been modified recently to reflect the effect of nanopores on the oil-gas MMP in tight/shale reservoirs. Gamadi *et al*. (2013) used real tight/shale core samples in coreflood tests to measure the oil-CO_2 MMP in tight/shale reservoirs. They observed that the oil recovery increases significantly with increasing injection pressure up to the oil-CO_2 MMP. Several other studies applied this modification on the coreflood test and reached similar results (Zhang and Gu, 2015; Li *et al*., 2017; Li *et al*., 2018).

Computational MMP calculation methods are less expensive and much faster in determining the oil-gas MMPs in nanopores compared to experimental methods. Teklu *et al*. (2014) coupled capillary pressure and a critical point shift model (Zarragoicoechea and Kuz, 2004) in the multiple-mixing-cell model (Ahmadi and Johns, 2011) and found that the oil-gas MMPs are reduced in nanopores compared to the bulk MMPs. Zhang *et al*. (2017a) coupled the effect of nanopores in Peng-Robinson equation of state (PR-EOS) (Peng and Robinson, 1976) and calculated the confined oil-gas MMP using the vanishing interfacial tension (IFT) model. It is found that the oil-gas MMP in nanopores is reduced compared to the bulk one. Zhang *et al*. (2017b) applied a similar method and observed an increasing confined oil-gas MMP with an increasing temperature.

1.2.Problem Statement

The following technical problems are required to be addressed in this thesis:

- When conducting the multiphase equilibrium calculations that consider the capillarity effect, the assumptions made during calculations and the algorithm's inability of

considering adsorption often weakens the accuracy of the results. It is proposed to implement a tuning parameter λ to address this issue. However, due to the severe lack of experimental data, the tuning parameter λ for hydrocarbon mixtures cannot be readily obtained.

- It is common to encounter a three-phase fluid system (aqueous-oleic-vapor) in nanopores of tight/shale reservoirs. The large capillary pressure induced by nanopores may alter the three-phase equilibria of the reservoir fluids in a significant manner. However, the conventional three-phase flash calculation does not consider the effect of two capillary pressures on the three-phase equilibria.
- The MMC method (Ahmadi and Johns, 2011) used to calculate oil-CO_2 MMP becomes invalid when it is used to predict MMP in tight/shale reservoirs due to strong capillarity and confinement effects. Currently, there is no comprehensive model that considers the effects of capillarity, confinement, and pore size distribution on oil-CO_2 MMP calculations.
- The original MMC method (Metcalf *et al.*, 1973) can predict the variation trend of oil recovery factor versus pressure and MMP during a gas flooding process. However, it is not appropriate for MMP calculations for tight/shale reservoirs as it does not consider the confinement effect in nanopores.

1.3.Research Objectives

The objective of this research is to develop robust and efficient algorithms for multiphase equilibrium and miscibility calculations in nanopores. The effects of capillarity and confinement are considered in this research. In order to accomplish this task, the short-term and long-term objectives are provided as follows:

Short-term objectives:

- Improve the accuracy of two-phase flash calculation coupled with capillary pressure on predicting two-phase equilibrium in confined space by implementing a modified Young-Laplace equation (Tan and Piri, 2015) in the PR-EOS model.
- Develop a three-phase equilibrium calculation algorithm that considers the capillarity effect in nanopores.
- Develop a robust oil-CO_2 MMP calculation algorithm that couples the effect of capillarity, confinement, and pore size distribution.
- Develop a modified MMC method that can be used to simultaneously calculate MMP and oil recovery factors during the gas flooding process in a confined space.

Long-term objective:

- Implement the proposed algorithms into compositional reservoir simulation tools to study the effect of capillarity and confinement on oil recovery in tight/shale reservoirs.

1.4.Thesis Structure

This thesis is a paper-based thesis and a total of six chapters are presented and organized as follows:

Chapter 1 introduces the basic research background, as well as the problem statement and the major research objectives. In **Chapter 2**, the PR-EOS model (Peng and Robinson, 1976) is coupled with a modified Young-Laplace equation (Tan and Piri, 2015) to improve the accuracy of the vapor-liquid equilibrium calculation of hydrocarbons in confined nanopores. Correlations of the tuning parameter λ for six pure hydrocarbon substances and two binary hydrocarbon mixtures are also developed. In **Chapter 3**, a new three-phase pressure-temperature (P-T) flash calculation algorithm is proposed. The effect of capillarity is coupled in the proposed algorithm in order to reflect the effect of confined nanopores on the three-phase equilibrium calculations in tight/shale

reservoirs. In **Chapter 4**, a new MMP calculation algorithm is developed to predict the oil-gas MMP in confined nanopores. The MMC method (Ahmadi and Johns, 2011) is coupled with the effects of capillarity and confinement. A mixing rule is proposed to calculate the confined oil-gas MMP if the pore size distribution is considered for a real tight/shale formation. In **Chapter 5**, a confined MMP calculation algorithm based on the original cell-to-cell simulation model (Metcalfe *et al.*, 1973) is developed to estimate the oil-gas MMP in tight/shale reservoirs. The effects of temperature, pore radius, and injection gas impurity are studied in detail. Finally, **Chapter 7** summarizes the conclusions highlighted from the present research and the recommendations for future work.

References

Abu Al-Rub, F. and Datta, R. 1999. Theoretical Study of Vapor-Liquid Equilibrium Inside Capillary Porous Plates. *Fluid Phase Equilibria*, 162(1-2), 83-96.

Ahmadi, K. and Johns, R. 2011. Multiple-Mixing-Cell Method for MMP Calculations. *SPE Journal*, 16(04), 733-742.

Ahmadi, M., Zendehboudi, S., and James, L. 2017. A Reliable Strategy to Calculate Minimum Miscibility Pressure of CO_2-Oil System in Miscible Gas Flooding Processes. *Fuel*, 208, 117-126.

Brusilovsky, A. 1992. Mathematical Simulation of Phase Behavior of Natural Multicomponent Systems at High Pressures with an Equation of State. *SPE Reservoir Engineering*, 7(01), 117-122.

Christiansen, R.L. and Haines, H.K. 1987. Rapid Measurement of Minimum Miscibility Pressure with the Rising-Bubble Apparatus. *SPE Reservoir Engineering*, 2(4), 443–449.

Dong, J. 2014. A High Order Method for Three Phase Flow in Homogeneous Porous Media. *SIAM Undergraduate Research Online*, 7, 74-88.

Firincioglu, T., Ozkan, E., and Ozgen, C. 2012. Thermodynamics of Multiphase Flow in Unconventional Liquids-Rich Reservoirs. In: SPE Annual Technical Conference and Exhibition. San Antonio: Society of Petroleum Engineers.

Gamadi, T.D., Sheng, J.J., and Soliman, M.Y. 2013. An Experimental Study of Cyclic Gas Injection to Improve Shale Oil Recovery. In: SPE Annual Technical Conference and Exhibition. New Orleans: Society of Petroleum Engineers.

Hamada, Y., Koga, K., and Tanaka, H. 2007. Phase Equilibria and Interfacial Tension of Fluids Confined in Narrow Pores. *The Journal of Chemical Physics*, 127(8), 084908.

Holm, L. and Josendal, V. 1974. Mechanisms of Oil Displacement by Carbon Dioxide. *Journal of Petroleum Technology*, 26(12), 1427-1438.

Hustad, O. and Browning, D. 2010. A Fully Coupled Three-Phase Model for Capillary Pressure and Relative Permeability for Implicit Compositional Reservoir Simulation. *SPE Journal*, 15(04), 1003-1019.

Iwere, F. O., Heim, R. N., and Cherian, B. V. 2012. Numerical Simulation of Enhanced Oil Recovery in the Middle Bakken and Upper Three Forks Tight Oil Reservoirs of the Williston Basin. In: The Americas Unconventional Resources Conference. Pittsburgh: Society of Petroleum Engineers.

Jin, Z. and Firoozabadi, A. 2016. Thermodynamic Modeling of Phase Behavior in Shale Media. *SPE Journal*, 21(01), 190-207.

Lee, J.I. 1979. Effectiveness of Carbon Dioxide Displacement under Miscible and Immiscible Conditions. Report RR-40. Petroleum Recovery Institute, Calgary.

Li, H., Qin, J., and Yang, D. 2012. An Improved CO_2–Oil Minimum Miscibility Pressure Correlation for Live and Dead Crude Oils. *Industrial & Engineering Chemistry Research*, 51(8), 3516-3523.

Li, L., Sheng, J., Su, Y., and Zhan, S. 2018. Further Investigation of Effects of Injection Pressure and Imbibition Water on CO_2 Huff-n-Puff Performance in Liquid-Rich Shale Reservoirs. *Energy & Fuels*, 32(5), 5789-5798.

Li, L., Zhang, Y., and Sheng, J. 2017. Effect of the Injection Pressure on Enhancing Oil Recovery in Shale Cores during the CO_2 Huff-n-Puff Process When it is above and below the Minimum Miscibility Pressure. *Energy & Fuels*, 31(4), 3856-3867.

Li, X., Wei, H., Chen, B., Liu, X., Wang, W., and Zhao, X. 2008. Multi-Stage Fracturing Stimulations Improve Well Performance in Tight Oil Reservoirs of the Changqing Oilfield. In: The International Petroleum Technology Conference. Kuala Lumpur: International Petroleum Technology Conference.

Li, Z., Qu, X., Liu, W., Lei, Q., Sun, H., and He, Y. 2015. Development Modes of Triassic Yanchang Formation Chang 7 Member tight oil in Ordos Basin, NW China. *Petroleum Exploration and Development*, 42(2), 241-246.

Metcalfe, R.S., Fussell, D.D., and Shelton, J.L. 1973. A Multicell Equilibrium Separation Model for the Study of Multiple Contact Miscibility in Rich-Gas Drives. *SPE Journal*, 13(3), 147-155.

Moortgat, J. and Firoozabadi, A. 2013. Three-Phase Compositional Modeling with Capillarity in Heterogeneous and Fractured Media. *SPE Journal*, 18(06), 1150-1168.

Mungan, N. 1981. Carbon Dioxide Flooding-Fundamentals. *Journal of Canadian Petroleum Technology*, 20(01), 87-92.

Neshat, S. S., Okuno, R., and Pope, G. A. 2018. A Rigorous Solution to the Problem of Phase Behavior in Unconventional Formations with High Capillary Pressure. *SPE Journal*, 23(04), 1438-1451.

Nguyen, P., Mohaddes, D., Riordon, J., Fadaei, H., Lele, P., and Sinton, D. 2015. Fast Fluorescence-Based Microfluidic Method for Measuring Minimum Miscibility Pressure of CO_2 in Crude Oils. *Analytical Chemistry*, 87(6), 3160-3164.

Nojabaei, B., Johns, R., and Chu, L. 2013. Effect of Capillary Pressure on Phase Behavior in Tight Rocks and Shales. *SPE Reservoir Evaluation & Engineering*, 16(03), 281-289.

Orr, F. and Jensen, C. 1984. Interpretation of Pressure-Composition Phase Diagrams for CO_2/Crude-Oil Systems. *SPE Journal*, 24(05), 485-497.

Pang, J., Zuo, J., Zhang, D., and Du, L. 2012. Impact of Porous Media on Saturation Pressures of Gas and Oil in Tight Reservoirs. In: SPE Canadian Unconventional Resources Conference. Calgary: Society of Petroleum Engineers.

Peng, D. and Robinson, D. 1976. A New Two-Constant Equation of State. *Industrial & Engineering Chemistry Fundamentals*, 15(1), 59-64.

Ping, G., Liangtian, S., Li, S., and Sun, L., 1996. A Theoretical Study of the Effect of Porous Media on the Dew Point Pressure of a Gas Condensate. In: SPE Gas Technology Symposium. Calgary: Society of Petroleum Engineers.

Qi, Z., Liang, B., Deng, R., Du, Z., Wang, S., and Zhao, W. 2007. Phase Behavior Study in the Deep Gas-Condensate Reservoir with Low Permeability. In: SPE Europec/EAGE Annual Conference and Exhibition. London: Society of Petroleum Engineers.

Randall, T. and Bennion, D. 1988. Recent Developments in Slim Tube Testing for Hydrocarbon-Miscible Flood (HCMF) Solvent Design. *Journal of Canadian Petroleum Technology*, 27(06), 33-44.

Rao, D. 1997. A New Technique of Vanishing Interfacial Tension for Miscibility Determination. *Fluid Phase Equilibria*, 139(1-2), 311-324.

Sandoval, D., Yan, W., Michelsen, M., and Stenby, E. 2015. Phase Envelope Calculations for Reservoir Fluids in the Presence of Capillary Pressure. In: SPE Annual Technical Conference and Exhibition. Houston: Society of Petroleum Engineers.

Shokir, E. 2007. CO_2-Oil Minimum Miscibility Pressure Model for Impure and Pure CO_2 Streams. *Journal of Petroleum Science and Engineering*, 58(1-2), 173-185.

Siripatrachai, N., Ertekin, T., and Johns, R. 2017. Compositional Simulation of Hydraulically Fractured Tight Formation Considering the Effect of Capillary Pressure on Phase Behavior. *SPE Journal*, 22(04), 1046-1063.

Tan, S. and Piri, M. 2015. Equation-of-State Modeling of Confined-Fluid Phase Equilibria in Nanopores. *Fluid Phase Equilibria*, 393, 48-63.

Tan, S., Qiu, X., Dejam, M., and Adidharma, H. 2019. Critical Point of Fluid Confined in Nanopores: Experimental Detection and Measurement. *The Journal of Physical Chemistry C*, 123(15), 9824-9830.

Teklu, T., Alharthy, N., Kazemi, H., Yin, X., Graves, R., and AlSumaiti, A. 2014. Phase Behavior and Minimum Miscibility Pressure in Nanopores. *SPE Reservoir Evaluation & Engineering*, 17(03), 396-403.

van Dijke, M., McDougall, S., and Sorbie, K. 2001. Three-Phase Capillary Pressure and Relative Permeability Relationships in Mixed-Wet System. *Transport in Porous Media*, 44(1), 1-32.

Wang, Y., Yan, B., and Killough, J. 2013. Compositional Modeling of Tight Oil Using Dynamic Nanopore Properties. In: SPE Annual Technical Conference and Exhibition. New Orleans: Society of Petroleum Engineers.

Wong, S. W., O'Dell, P. M., de Pater, C. J., and Shaoul, J. 2000. Fresh Water Injection Stimulation in a Deep Tight Oil Reservoir. In: the 2000 SPE/AAPG Western Regional Meeting. Long Beach: Society of Petroleum Engineers.

Yellig, W. 1982. Carbon Dioxide Displacement of a West Texas Reservoir Oil. *SPE Journal*, 22(06), 805-815.

ZareNezhad, B. 2016. A New Correlation for Predicting the Minimum Miscibility Pressure Regarding the Enhanced Oil Recovery Processes in the Petroleum Industry. *Petroleum Science and Technology*, 34(1), 56-62.

Zarragoicoechea, G. and Kuz, V. 2004. Critical Shift of a Confined Fluid in a Nanopore. *Fluid Phase Equilibria*, 220(1), 7-9.

Zhang, K. and Gu, Y. 2015. Two Different Technical Criteria for Determining the Minimum Miscibility Pressures (MMPs) from the Slim-Tube and Coreflood Tests. *Fuel*, 161, 146-156.

Zhang, K., Jia, N., Zeng, F., and Luo, P. 2017a. A New Diminishing Interface Method for Determining the Minimum Miscibility Pressures of Light Oil–CO_2 Systems in Bulk Phase and Nanopores. *Energy & Fuels*, 31(11), 12021-12034.

Zhang, K., Jia, N., and Li, S. 2017b. Exploring the Effects of Four Important Factors on Oil–CO_2 Interfacial Properties and Miscibility in Nanopores. *RSC Advances*, 7(85), 54164-54177.

CHAPTER 2 PHASE-BEHAVIOR MODELING OF HYDROCARBON FLUIDS IN NANOPORES USING PR-EOS COUPLED WITH A MODIFIED YOUNG–LAPLACE EQUATION

A version of this chapter has been published in *ACS Omega*.

Abstract

The effect of capillary pressure on the vapor-liquid two-phase equilibrium calculation has been extensively studied for the past two decades. However, the calculation accuracy is often weakened by the false assumptions and inherent flaws present in the modeling process. In this work, a modified Young-Laplace equation proposed by Tan and Piri is coupled with volume-translated Peng-Robinson equation of state (PR-EOS) to study the effect of capillary pressure on the two-phase equilibrium calculation in confined nanopores. In order to successfully apply the modified Young-Laplace equation during the vapor-liquid equilibrium calculation process, this study models the tuning parameter λ in the modified Young-Laplace equation (as proposed by Tan and Piri for perturbed-chain statistical associating fluid theory equation of state (PC-SAFT EOS)) for several pure hydrocarbons and their mixtures by matching experimental data collected from the literature. The tuning parameter λ can be expressed as a unique function for each pure substance or mixture. It is found that the tuning parameter λ shows a quadratic polynomial relationship with temperature, and the value of λ is always less than one. The λ can become negative under certain circumstances, which adjusts the capillary pressure to a lower value. It increases with an increasing pore radius; this is different from the results obtained by Tan and Piri which showed that the tuning parameter λ decreases with an increasing pore radius. The above rules apply to the tuning parameter λ obtained for both pure substances and mixtures. Using the two-phase equilibrium calculation coupled with the modified Young-Laplace equation, the calculated vapor pressures for pure substances and two-phase boundaries for mixtures match very well with the experimental data. Implementation of the modified Young-Laplace equation greatly improves the accuracy of the two-phase equilibrium calculation considering the capillarity effect. Such a modeling strategy

could be integrated into a reservoir simulator to conduct more accurate flow simulations for tight/shale reservoirs.

Keywords: Phase behavior, Thermodynamic modeling, Two-phase flash, Capillary pressure, Unconventional reservoir

2.1. Introduction

Tight/shale reservoirs are featured with nano-scale pores. It is well established that the confined space in those nanopores introduces large capillary pressure which can pose a significant impact on the phase behavior and flow dynamics of reservoir fluids.[1-5] Experimental works and theoretical approaches to describe the vapor-liquid two-phase equilibrium in a confined space are thereby developed to grasp an understanding of the reservoir-fluid phase behavior inside nanopores.[6-10]

Saturation pressure curves of pure hydrocarbon components in confined nanopores are studied experimentally in many research studies.[11-18] The saturation pressure curves can be determined by measuring the adsorption volume of hydrocarbons at different temperatures in a nanomaterial such as SBA-15 or MCM-41. It was found that the saturation pressures of hydrocarbons at given temperatures are reduced significantly inside a nanomaterial. [11-14] Saturation pressures of hydrocarbon mixtures inside confined space have also been studied experimentally.[8,9] Qiu *et al*.[8] used a novel high-pressure differential scanning calorimeter (DCS)[19] to measure the dew point pressures at different temperatures for the C_1-C_2 mixture in the nanomaterial SBA-15. This apparatus is then later used to measure saturation pressures of C_2 in confined nanopores.[17] It was found that saturation pressures of C_2 and the C_1-C_2 mixture significantly decreased because of the strong capillarity effect in a confined space.[8,17] Zhong *et al*.[9] fabricated multiple nanochannels on a microfluidic device and measured the dew point pressures for the C_1-C_3 mixture at different temperatures inside the nanochannels. In the experiments, they all observed a dramatic reduction of the dew point pressures for hydrocarbon mixtures because of the capillarity effect. Critical points of some reservoir fluids are recently measured in nanopores to reveal the effect of confinement on critical-property-shifts.[19,20] In their works[19,20], a micro DSC apparatus[18] was used to measure the critical points of two pure components (CO_2 and C_2H_6) and one C_1-C_2 mixture in

the nanomaterial SBA-15. They found that the critical pressures of the investigated fluids in nanopores are greatly reduced from their bulk critical pressures. On the basis of the measured data, they also developed a set of equations to calculate critical pressure/temperature shifts in the confined space. The critical-property-shift model they developed[19,20] has a similar format as the model proposed by Zarragoicoechea and Kuz[21].

Experiments are costly and time-consuming. Theoretical works are thereby drawing more attention over the years. One of the earliest works that theoretically studied the capillarity effect on the vapor-liquid equilibrium in a porous medium was conducted by Brusilovsky[1]. The author proposed a new equation of state (EOS) to couple the effect of the capillary pressure into the two-phase equilibrium calculation for hydrocarbon mixtures. The modeling results show that the bubble point becomes lower than the bulk one, and the dew point pressure becomes higher than the bulk one when capillary pressure is considered in EOS calculations.[1] In the following years, many research studies have also suggested that the vapor-liquid equilibria are greatly affected by the capillary pressure in nanopores.[4,22-26] The deviation of the entire two-phase envelope from the bulk condition due to capillary pressure in nanopores was studied by Nojabaei *et al.,*[6] they found that the dew point pressure increases in the upper dew point branch (at pressures above the cricondentherm point), but decreases in the lower dew point branch (at pressures below the cricondentherm point). Moreover, the vapor-liquid equilibrium is not affected by confined nanopores at the critical point because the capillary pressure reaches zero at the critical point.[6] The above findings concur with a later work by Sandoval *et al.*[27] Rezaveisi *et al*.[28] performed multiple two-phase flash calculations coupled with capillary pressure and concluded that there exists a maximum capillary pressure at each temperature above which, the two-phase equilibrium is not possible.

Apart from simply coupling the capillary pressure into the vapor-liquid equilibrium calculation, other methods have also been developed to improve the accuracy of the two-phase equilibrium description in confined nanopores. Zarragoicoechea and Kuz[21] developed an analytical model to calculate the critical property shift because of the confinement effect in nanopores. This model assumes a neutral wall. The effect of adsorption on the critical property shift is thereby not reflected in this model. They compared their modeling results against the experimental data of critical point shift in nanopores for several pure substances. It was observed that this model offers a better fitting to the experimental data when the pore radius is relatively large. When the pore radius is relatively small, the multilayer adsorption may affect the shift of the critical properties significantly in experiments, while it was not considered in the proposed model.[21] This results in a poor agreement between the modeling results and the experiment data when the pore radius is small. Nevertheless, this method is coupled in several research to study the combined effect of capillarity and confinement on the multiphase equilibrium in nanopores.[29-31] In 2010, Travalloni *et al*.[32] modified the van der Waals EOS by adding an additional term and they predicted a shift in the two-phase critical point because of the capillarity effect. The additional term is a function of pore radius, potential width, and potential energy between the pore wall and fluid molecules. The most significant advantage of this method is that the phase equilibrium predicted by this model in nanopores can be reduced to the bulk one when the pore radius approaches infinity. This is not featured in the model proposed by Zarragoicoechea and Kuz[21]. Furthermore, the model proposed by Travalloni *et al*.[32] can also be implemented in the most widely used Peng-Robinson EOS (PR EOS)[33]. Pang *et al.*[34] took the effect of porous media into account during the vapor-liquid equilibrium calculation in nanopores. They employed the Blake-Kozeny model to calculate the tortuosity factor of porous media and then calculated the pore radius using the tortuosity factor,

permeability, and porosity. It was concluded that the effect of porous media on the two-phase equilibrium calculation is significant and cannot be neglected when the pore radius is less than 1000 nm. Jin and Firoozabadi[5] coupled both capillary pressure and surface adsorption into the vapor-liquid equilibrium calculation. A deviation of the two-phase boundaries from its bulk condition due to capillary pressure and surface adsorption was observed in their study. They further concluded that the effect of surface adsorption on the vapor-liquid equilibrium in nanopores is insignificant, compared to the effect of the capillary pressure, when the pore radius is larger than 10 nm. More recently, another modified PR-EOS[33] is proposed to account for the interaction between pore walls and fluid molecules in nanopores.[35] In this model, the molar volume term in PR EOS[33] is modified to be a function of the effective molecule volume coefficient and the ratio of the fluid molecule radius to the confined nanopore radius. This model takes into account the fluid adsorption and effective molar volume of the confined nanopore. The critical-property-shifts for pure substances calculated by this model match the experimental data fairly well. It was seen in this study that the degree of the critical temperature shift due to the confined nanopore increases linearly with a decreasing pore radius, while the degree of the critical pressure shift due to the confined nanopore increases quadratically with a decreasing pore radius.[35] Nevertheless, this method is computationally expensive.

Recently, by introducing an empirical parameter tuning parameter, λ, Tan and Piri[36] modified the Young-Laplace equation for more accurate modeling of confined phase behavior. They developed correlations of the tuning parameter λ for several pure substances including nitrogen, carbon dioxide, argon, oxygen, krypton, pentane, and hexane. In their paper, they coupled the modified Young-Laplace equation with the perturbed-chain statistical associating fluid theory equation of state (PC-SAFT EOS)[37] to study the phase behavior of certain fluids in confined nanopores. They

also suggested a simple linear mixing rule to calculate λ for mixtures using the λ correlations obtained for pure substances. However, their innovative work still bears some issues. The λ correlations for pure substances in their work[36] were developed specifically to couple with the PC-SAFT EOS[37], which is more computationally demanding compared to other EOSs such as PR-EOS[33]. However, the λ correlations for pure substances developed in their work were only applicable to subcritical temperatures. This can be sometimes troublesome when one applies the linear mixing rule to calculate λ for mixtures because the critical temperature of mixtures often exceeds the critical temperature of some individual components. Taking the binary mixture methane-ethane (14.98 mol% methane and 85.02 mol% ethane) as an example, the critical temperature of this binary mixture is 295.9 K, while the critical temperature of pure methane is merely 190.6 K. In order to successfully utilizing the linear mixing rule to calculate λ for mixtures such as methane-ethane, the λ correlation of pure methane under supercritical temperatures must be developed. The λ correlation under supercritical conditions exists as merely a parameter to adjust the vapor-liquid capillary pressure of mixtures; it does not necessarily have any physical meaning other than being a tuning constant.

This work aims to address the issue that the current CEOS-based modeling method cannot well reproduce the measured phase behavior in confined nanopores reported recently in the literature. This issue can be visualized in **Fig. 2-1**.

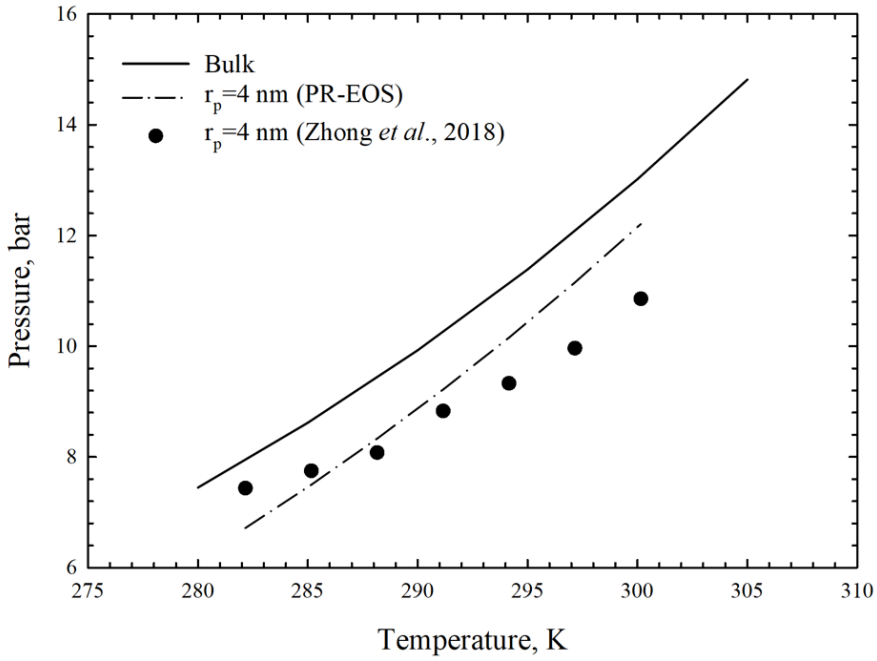

Fig. 2-1. Dew point pressures of the binary mixture C_1-C_3 measured using a nanofluidic device with nanochannels[9] and calculated from PR-EOS[33] coupled with capillary pressure (with the assumption of zero contact angle). The experimental data are retrieved from the study by Zhong *et al*. (2018).[9]

Fig. 2-1 gives an example of the dew-point-pressure curve for the binary mixture C_1-C_3 calculated by the volume translated PR-EOS and measured in experiments[9]. The black dots represent the dew point pressures measured at different temperatures[9]. The solid line and the dashed line represent the dew point pressure curve calculated in bulk conditions and in the confined space, respectively. PR-EOS[33] coupled with capillary pressure tends to overpredict dew point pressures at higher temperatures and underestimate dew point pressures at lower temperatures. This work is thus devoted to improving the accuracy of the vapor-liquid equilibrium calculation in confined nanopores by developing a new two-phase flash calculation algorithm employing the commonly used PR-EOS[33] and a modified Young-Laplace equation.[36] This paper extends and improves the work of Tan and Piri[36] by developing the λ correlations for pure substances and mixtures that can

be coupled with a more efficient EOS, namely, PR-EOS[33]. This study also calculates a correlation of the tuning parameter λ for pure methane under supercritical conditions. As mentioned previously, the implementation of the modified Young-Laplace equation relies on the modeling of the tuning parameter λ. To derive the λ correlation for various hydrocarbons, experimental data are collected from the literature, including capillary condensation data for pure hydrocarbons and dew point pressure data for hydrocarbon mixtures. We first present the vapor-liquid equilibrium calculation algorithm that is coupled with the modified Young-Laplace equation. Then the tuning parameter λ for six pure substances and two mixtures is computed based on the collected experimental data. Finally, the measured vapor pressures for pure substances and phase boundaries for mixtures are compared against the calculated ones using the generalized tuning parameter λ. The novelty of this work is that this study employs PR-EOS[33] in confined two-phase equilibrium calculations instead of PC-SAFT[37] used in the work of Tan and Piri[36]. The motivation for doing so is that PR-EOS[33] is simpler and more straightforward than PC-SAFT[37], making it still the most commonly used EOS in numerical simulations. Moreover, this work develops λ correlations for two hydrocarbon mixtures to examine the application of the modified Young-Laplace equation[36] to hydrocarbon mixtures. This is not featured in the work of Tan and Piri[36].

The rest of this paper is divided into four main sections. First, the methodology is presented. All the main equations governing the two-phase equilibrium calculation and capillary pressure calculation are presented. Then, the numerical algorithm of the flash calculation is presented in detail. The next section presents all the two-phase equilibrium calculation results for pure substances and mixtures. Finally, all the major findings are summarized in the Conclusions section.

2.2.Methodology

A two-phase equilibrium can be determined by satisfying the chemical potential equality relation at a given pressure, temperature, and feed composition.[45] In a conventional two-phase equilibrium, the liquid phase has the same pressure as the vapor phase. In confined nanopores, because of the existence of capillary pressure, the pressure of the non-wetting phase (vapor phase) is larger than the pressure of the wetting phase (liquid phase). The chemical potential equality condition can thereby be modified as:[45]

$$\mu_{ix}(P_l, T, x = \{x_i\}) = \mu_{iy}(P_v, T, y = \{y_i\}) \qquad i = 1, \dots, N_c \tag{2-1}$$

where μ_{ix} is the chemical potential of the *i*th component in the liquid phase, μ_{iy} is the chemical potential of the *i*th component in the vapor phase, P_l is the pressure in the liquid phase, P_v is the pressure in the vapor phase, T is the system temperature, x is the liquid-phase composition, y is the vapor-phase composition, and N_c is the number of components. The chemical potential equality condition can then be readily translated into fugacity equality condition:[45]

$$f_{ix}(P_l, T, x = \{x_i\}) = f_{iy}(P_v, T, y = \{y_i\}) \qquad i = 1, \dots, N_c \tag{2-2}$$

where f_{ix} is the fugacity of the *i*th component in the liquid phase, and f_{iy} is the fugacity of the *i*th component in the vapor phase. In this work, PR-EOS[33] is employed to calculate the fugacity of each component in each phase:[33]

$$ln\frac{f_i}{y_i P} = ln\,\phi_i = \frac{B_i}{B}(Z-1) - ln(Z-B) + \frac{A}{2\sqrt{2}B}\left(\frac{B_i}{B} - \frac{2}{A}\sum_{i=1}^{N_c} y_i A_{ij}\right) ln\left(\frac{Z+(1+\sqrt{2}B)}{Z-(1-\sqrt{2}B)}\right), i = 1, \dots, N_c \tag{2-3}$$

where y_i is the mole fraction of the *i*th component in any phase, P is the phase pressure, ϕ_i is the fugacity coefficient of the *i*th component in any phase, Z is the phase compressibility factor, and

A and *B* are EOS constants. Provided that the pressures of the liquid phase and the vapor phase are different in confined nanopores, the relation between P_l and P_v is given as:

$$P_c = P_v - P_l = \frac{2\sigma}{r_p} \tag{2-4}$$

where P_c is the capillary pressure across the equilibrating phases, σ is IFT and r_p is the pore radius. Capillary pressure is calculated using the Young-Laplace equation[39] with assumptions of equal principle curvature radii and zero contact angle. The IFT between the liquid phase and the vapor phase is calculated using the following Weinaug-Katz model:[46]

$$\sigma = \sum_{i=1}^{N_c} P_{chi}\left(x_i \frac{\rho_l}{M_l} - y_i \frac{\rho_g}{M_g}\right)\Big]^4_{lg} \qquad i = 1, \dots, N_c \tag{2-5}$$

where σ is the IFT between the liquid phase and the vapor phase, P_{chi} is the Parachor constant of the *i*th component, and ρ_l and ρ_g are the density of the liquid phase and the vapor phase, respectively. Here the phase densities are calculated by volume translated PR-EOS[33] which adopts the volume translation method proposed by Abudour *et al*.[47] and Abudou *et al*.[48] M_l and M_g are the molecular weights of the liquid phase and the vapor phase, respectively; x_i and y_i are the mole fractions of the *i*th component in the liquid phase and the vapor phase, respectively. In order to achieve better accuracy in IFT predictions, an approach proposed by Hugill and van Welsenes[49] is applied to calculate mixture Parachor constant. This approach can be expressed in Eq. (2-6).

$$\begin{cases} P_{chl} = \sum_{i=1}^{N_c} \sum_{j=1}^{N_c} x_i x_j P_{chij} \\ P_{chv} = \sum_{i=1}^{N_c} \sum_{j=1}^{N_c} y_i y_j P_{chij} \\ P_{chij} = \varphi_{ij}(P_{chi} + P_{chj})/2 \end{cases} \tag{2-6}$$

where P_{chl} and P_{chv} are the Parachor of the liquid phase and the vapor phase, respectively, ϕ_{ij} is the interactive parameter that needs to be calculated using the experimental IFT data. It was shown in the work of Hugill and van Welsenes[49] that the interactive parameter ϕ_{ij} tends to have a linear relationship with temperature. The vapor-liquid IFT can be calculated using Eq. (2-7).

$$\sigma_{lg} = [P_{chl}\left(\sum_{i=1}^{N_c} x_i \frac{\rho_l}{M_l}\right) - P_{chv}\left(\sum_{i=1}^{N_c} y_i \frac{\rho_g}{M_g}\right)]^4 \tag{2-7}$$

The accuracy of predicting vapor-liquid IFT using Eqs. (2-6)-(2-7) is validated below. The IFT data for mixtures C_1-C_3 and C_1-C_2 are collected from Weinaug and Katz[46] and Baidakov *et al*.[50] Then we calculate interactive parameters at different temperatures using the collected experimental data. If there are more than one data point for each temperature, the average values of the interactive parameter at each temperature are used to develop ϕ_{ij} correlations. Finally, vapor-liquid IFTs are calculated using the volume translated PR-EOS and Eqs. (2-6)-(2-7); the calculation results are compared with the measured data. The ϕ_{ij} correlation developed for C_1-C_3 and C_1-C_2 systems is given in Eq. (2-8).

$$\begin{cases} \varphi_{ij}\,(C_1 - C_3) = -0.0110T + 3.9728 \\ \varphi_{ij}(C_1 - C_2) = 0.0046T + 0.3694 \end{cases} \tag{2-8}$$

Fig. 2-2 shows parity charts of the calculated and experimental IFT for C_1-C_3 and C_1-C_2. It is seen from **Fig. 2-2** that the volume-translated PR-EOS and Eqs. (2-6)-(2-8) offer acceptable accuracy in reproducing the vapor-liquid IFT for the hydrocarbon mixtures.

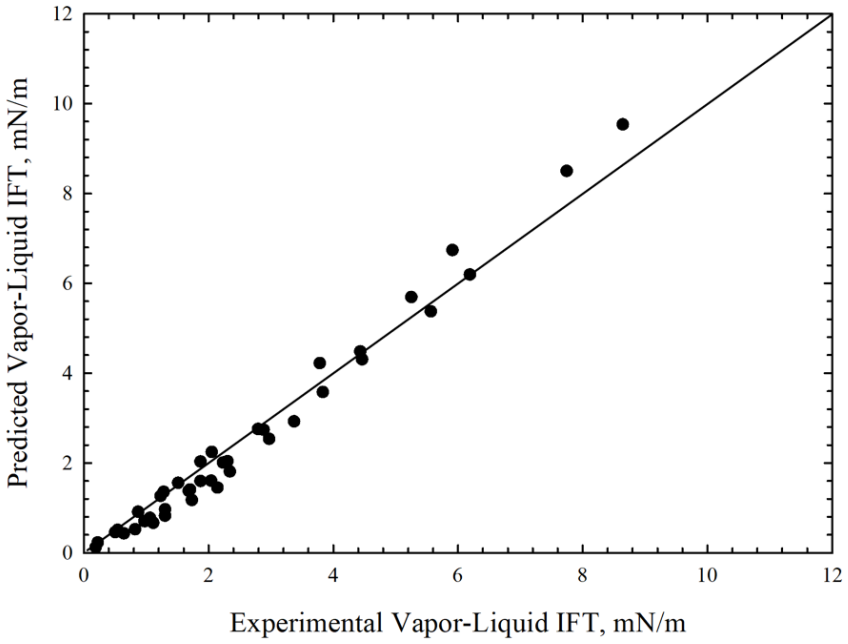

(a)

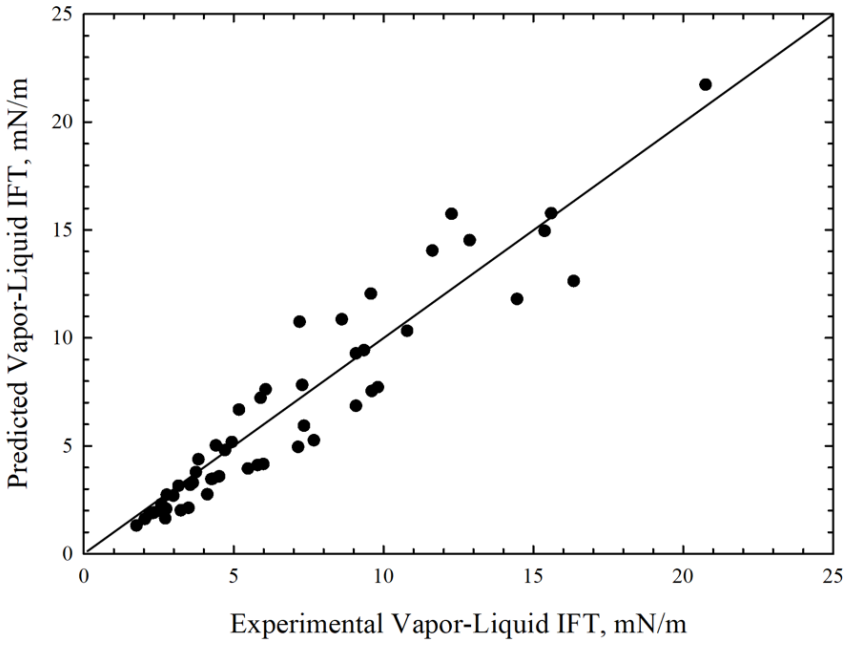

(b)

Fig. 2-2. Comparison between the calculated vapor-liquid IFTs and the experimental data[46,50] for (a) C_1-C_3 and (b) C_1-C_2 mixtures.

A combination of the Young-Laplace equation[39] and Weinaug-Katz model[46] with proper prediction of the Parachor constant provides a simple and quick estimation of the capillary pressure present. However, the capillary pressure calculated using this method does not necessarily represent the true situation in confined nanopores. The assumption of zero contact angle greatly weakens the correctness of the calculation results due to the fact that it is difficult for any reservoir to reach a complete liquid-wet condition. This assumption could make the calculation results less reliable. Moreover, when this method is applied to study the two-phase equilibrium in confined nanopores that have a pore radius less than 10 nm, the adsorption effect can become significant, leading to the creation of an adsorption layer and hence a reduction in pore radius.[3] Pore-radius reduction is not considered in the original Young-Laplace equation[39] during the calculation of capillary pressure.

In order to improve the accuracy of two-phase equilibrium calculations in confined nanopores and to mitigate the deviation of modeling results from experimental results, this work employs a modified Young-Laplace equation proposed by Tan and Piri[36]. The modified Young-Laplace equation is given below:[36]

$$P_c = \frac{2\sigma}{r_p(1-\lambda)} \tag{2-9}$$

This new Young-Laplace equation[36] modifies the original one by adding another term, i.e., the tuning parameter λ. This tuning parameter could take into account both contact angle and the reduction in the pore radius because of the adsorption effect. The correlation of the tuning parameter λ can be empirically developed by fitting the experimental capillary condensation results. In this work, we first set the value of the tuning parameter λ to be zero and calculate the saturation pressure of a given fluid at a given temperature and pore radius. Then, we gradually change the

value of the tuning parameter λ until the calculated saturation pressure matches precisely with the measured one. After we obtain the λ values for all the experimental data points, curve fitting is employed to generate a λ correlation. It was previously suggested that the tuning parameter λ tends to be a function of temperature and radius.[36] The developed λ correlation can then be embedded into the modified Young-Laplace equation[1] to improve the capillary pressure prediction in nanopores.

2.3. Numerical Algorithm

The two-phase equilibrium calculation algorithm coupled with a modified Young-Laplace equation[36] is constructed with an outer loop and an inner loop. The outer loop solves for the fugacity equality relation and updates the phase equilibrium ratio (k_i), while the inner loop solves the Rachford-Rice equation[51] which can be derived from the material balance equation. The Rachford-Rice equation is given as:[51]

$$\sum_{i=1}^{N_c}(y_i - x_i) = \sum_{i=1}^{N_c}\left(\frac{z_i(k_i - 1)}{1 + \beta_y(k_i - 1)}\right) = 0 \qquad i = 1, \ldots, N_c \tag{2-10}$$

where β_y is the vapor phase mole fraction, and z_i is the mixture feed composition.

To start the calculation procedure, the phase equilibrium ratio must be initialized using the Wilson equation:[52]

$$k_i = \frac{P_{ci}}{P} exp[\,5.37(1 + \omega_i)(1 - \frac{T_{ci}}{T})] \qquad i = 1, \ldots, N_c \tag{2-11}$$

where P_{ci} is the critical pressure of the ith component, ω_i is the acentric factor of the ith component, T_{ci} is the critical temperature of the ith component, and T is the system temperature.

The phase equilibrium ratio is then fed into the inner loop to solve the Rachford-Rice equation[51] using the successive substitution method. By solving the Rachford-Rice equation[51], the phase compositions and phase mole fractions can be obtained. The obtained results are then used to calculate the capillary pressure using the modified Young-Laplace equation[36] and the developed λ correlations. Then the component fugacities (f_{ix}, f_{iy}) are calculated to check for the fugacity-equality condition. If the fugacity-equality condition is satisfied, then the calculation is stopped, and the phase compositions and mole fractions are obtained. If the fugacity equality condition is not satisfied, the phase equilibrium ratio is then updated using the calculated component fugacities with the following equation:[45]

$$k_{iy}^{n+1} = k_{iy}^{n} \frac{f_{iy}^{n}}{f_{ix}^{n}} \qquad i = 1, \dots, N_c \tag{2-12}$$

where n represents the current iteration and $n+1$ represents the next iteration. The updated phase equilibrium ratio is then used to solve the Rachford-Rice equation[51] and the entire calculation procedure is repeated until the fugacity equality condition is satisfied. A flowchart is provided in **Fig. 2-3** to depict the calculation procedure of the two-phase equilibrium calculation coupled with the modified Young-Laplace equation[36].

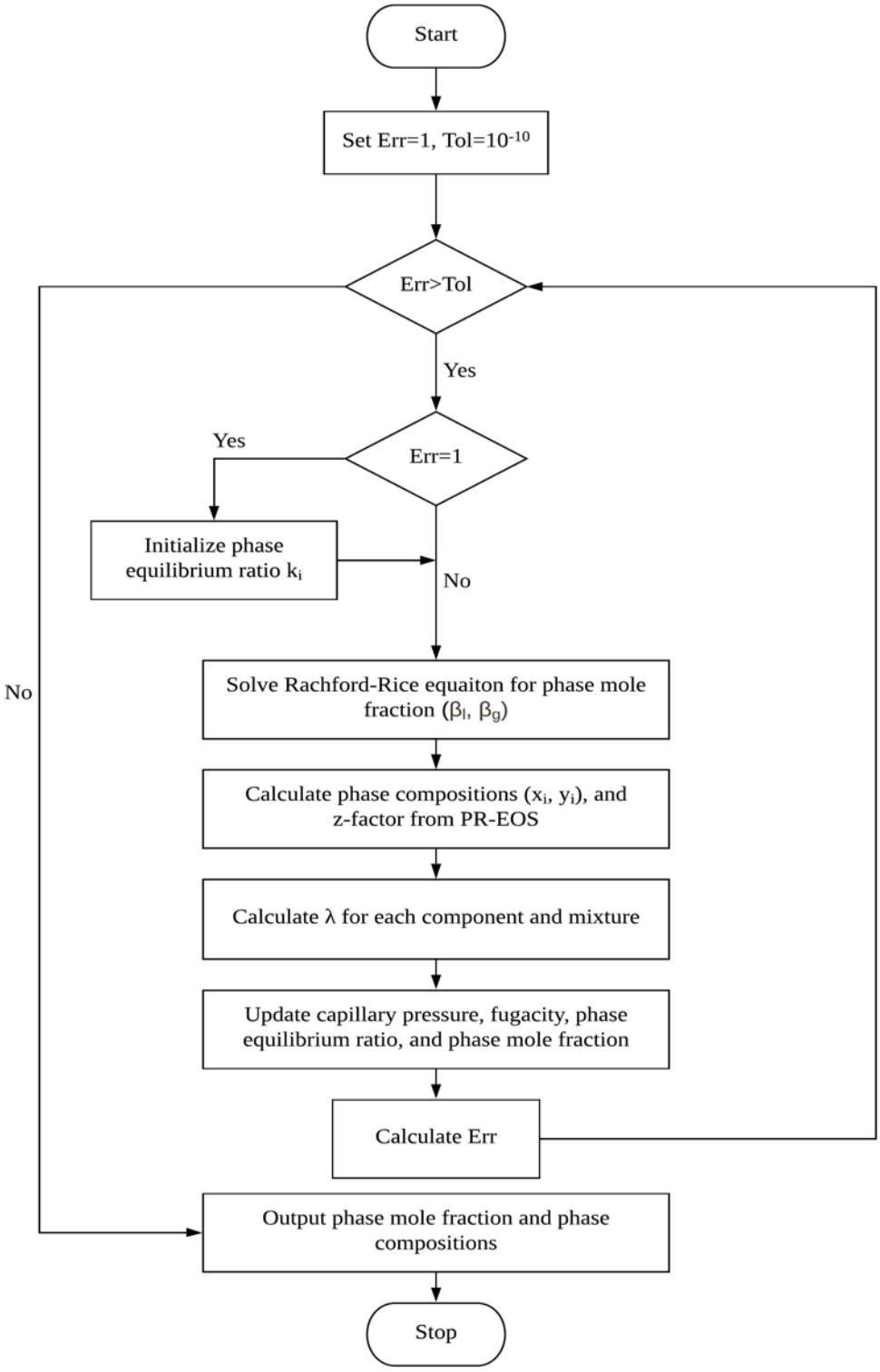

Fig. 2-3. Calculation procedure of vapor-liquid equilibrium calculation coupled with the modified Young-Laplace equation[36].

2.4. Results and Discussion

This work employs a modified Young-Laplace equation[36] in a two-phase flash calculation algorithm to study the vapor-liquid equilibrium in confined nanopores. The proposed algorithm is applied to calculate the vapor-liquid equilibrium in confined nanopores for seven examples of hydrocarbon fluids to examine the robustness of the proposed algorithm. The examples presented in this section include six pure substances and two binary mixtures. For each example, we first collected experimental saturation pressure data for hydrocarbons in confined nanopores from the literature. The collected experimental data are summarized in **Table 2-1**. **Table 2-2** lists the properties of all hydrocarbon components that are involved in the example studies.

Table 2-1. Summary of Experimental Works Used to Develop Correlations of the Tuning Parameter Lambda for Different Fluids.

Fluid	Material	Pore Radii, nm	Temperature, K	References
C_2	SBA-15	1.704-3.281	262.15-300.15	Qiu *et al*., 2019[19] Qiu *et al*., 2020[17]
C_3	MCM-41	1.291-3.030	279.55-323.95	Barsotti *et al.,* 2018[11]
n-C_4	MCM-41	1.291-3.030	279.55-323.65	Barsotti *et al.,* 2018[11]
n-C_5	MCM-41, SBA-15	2.285, 3.935	258-298	Russo *et al.,* 2012[12]
n-C_6	MCM-41	1.203-2.122	303-323	Qiao *et al.,* 2004[13]
n-C_7	SBA-15	2.3-3.9	299.15-309.15	Vinh-Thang *et al.,* 2005[14]
C_1-C_2	SBA-15	1.704-3.281	242-273	Qiu *et al.,* 2018[8]
C_1-C_3	A nanofluidic device with nanochannels	4, 40	282.15-301.15	Zhong *et al*., 2018[9]

Table 2-2. Physical Properties of Methane, Ethane, Propane, *n*-Butane, *n*-Pentane, *n*-Hexane, and *n*-Heptane used in the PR-EOS Model.[38]

Substance	T_c, K	P_c, bar	ω	MW, g/mol	P_{chi}
C_1	190.6	46	0.008	16.04	77.33
C_2	305.4	48.84	0.098	30.07	108
C_3	369.8	42.46	0.152	44.10	157.31
n-C_4	425.2	38	0.192	58.12	189.9
n-C_5	469.6	33.94	0.251	72.15	231.5
n-C_6	507.4	29.69	0.296	86.17	271
n-C_7	540.2	27.36	0.351	100.20	312.5

2.4.1 Examples of Pure Substances

The vapor-liquid equilibrium of six pure hydrocarbon substances in confined nanopores are studied in this work, including pure ethane (C_2), pure propane (C_3), pure *n*-butane (*n*-C_4), pure *n*-pentane (*n*-C_5), pure *n*-hexane (*n*-C_6), and pure *n*-heptane (*n*-C_7). The saturation pressures of these hydrocarbon fluids are calculated using the aforementioned methodology and compared with the experimental data. As for C_2 C_3, *n*-C_4, *n*-C_5, and *n*-C_6, the saturation pressures calculated using PR-EOS[2] and the original Young-Laplace equation[39] are larger than the saturation pressures measured in experiments at all temperatures. As for *n*-C_7, however, the saturation pressures calculated by PR-EOS[33] and the original Young-Laplace equation[39] can become lower than the measured saturation pressure; this implies that negative values of the tuning parameter λ are required to match the measured results.

In order to adjust the calculated capillary pressure to match the real capillary pressure present in experiments, the tuning parameter λ is first computed using the aforementioned procedure for each pore radius. The computed tuning parameter λ for C_2 C_3, *n*-C_4, *n*-C_5, *n*-C_6, and *n*-C_7 at different temperatures and pore radii is given in **Figs. 2-4 – 2-9**.

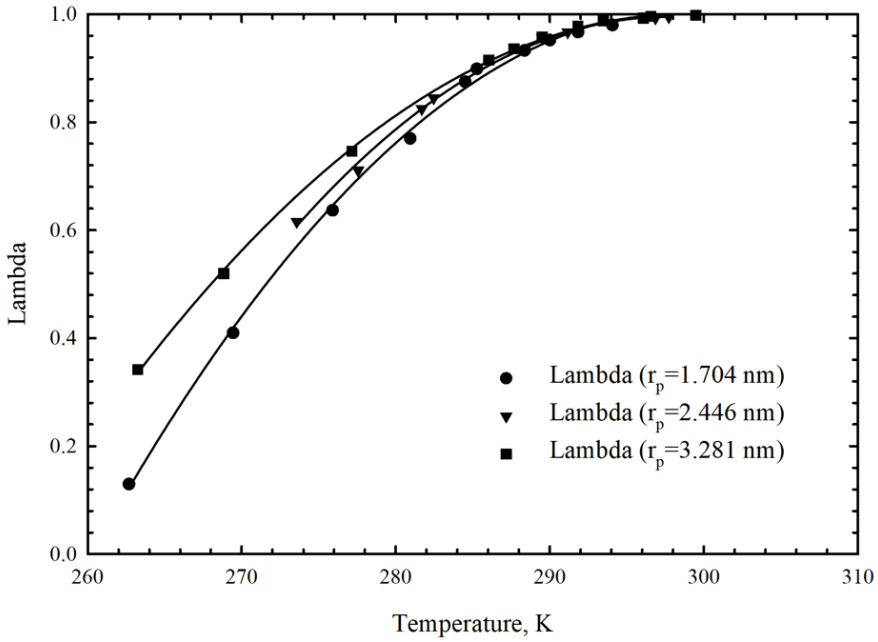

Fig. 2-4. Computed tuning parameter λ of C_2 based on the experimental data[17,19]. The solid lines are trend lines which are drawn for visual guide purpose.

Based on the calculated λ shown in **Fig. 2-4**, the following empirical correlation for λ can be developed for C_2 (R^2=0.9902).

$$\lambda = -63.8 + 0.43230T + 0.45240r_p - 0.00072T^2 - 0.00153Tr_p \quad (2\text{-}13)$$

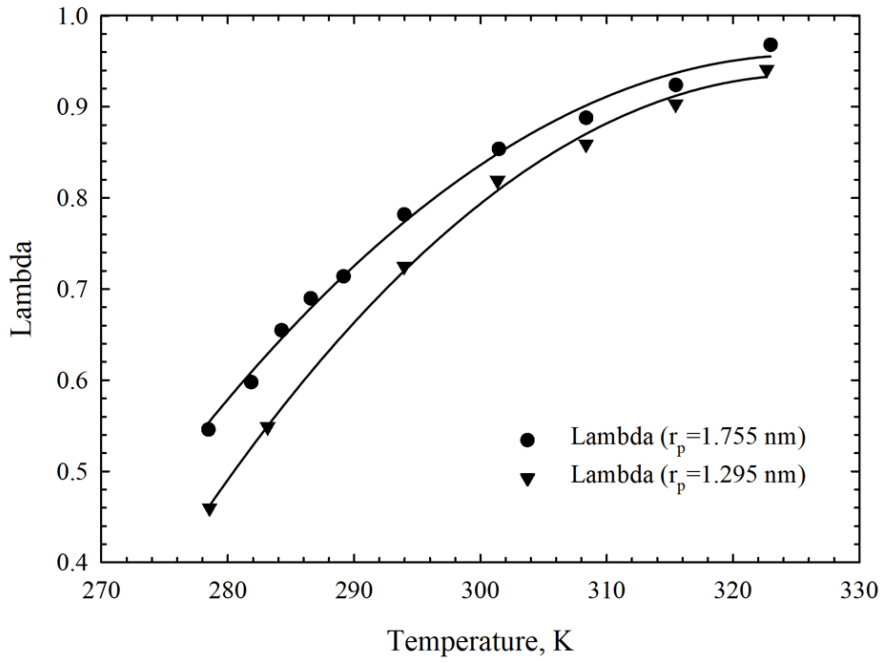

Fig. 2-5. Computed tuning parameter λ of C_3 based on the experimental data11. The solid lines are trend lines which are drawn for visual guide purpose.

Based on the results shown in **Fig. 2-5**, the following empirical correlation for λ can be developed for C_3 (R^2=0.9984).

$$\lambda = -22.15 + 0.13530T + 1.3140r_p - 0.00020T^2 - 0.00396Tr_p \quad (2\text{-}14)$$

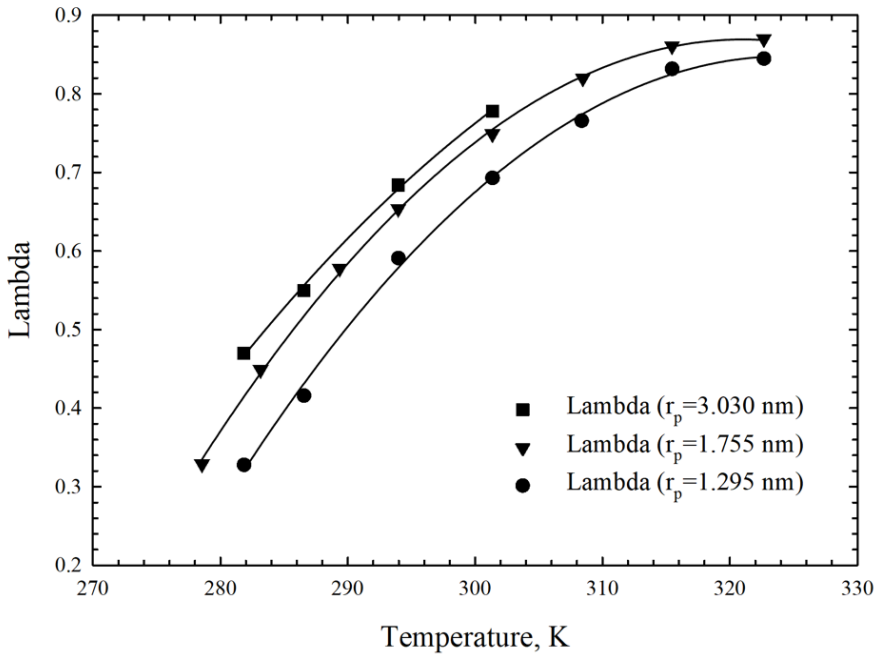

Fig. 2-6. Computed tuning parameter λ of pure n-C_4 based on the experimental data11. The solid lines are trend lines which are drawn for visual guide purpose.

Based on the regression of the experimental data shown in **Fig. 2-6**, we can obtain the following λ correlation for *n*-C_4 (R^2=0.9474).

$$\lambda = -27.75 + 0.17490T + 0.26790r_p - 0.00027T^2 - 0.00073Tr_p \qquad (2\text{-}15)$$

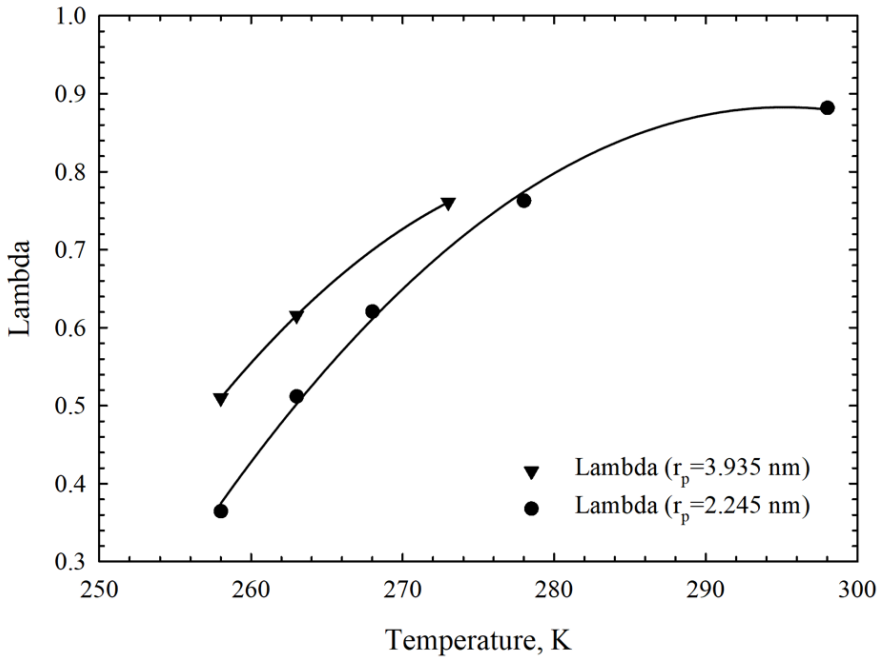

Fig. 2-7. Computed tuning parameter λ of pure *n*-C_5 based on the experimental data12. The solid lines are trend lines which are drawn for visual guide purpose.

By using the curve fitting tool, we can obtain the following λ correlation for *n*-C_5 (R^2=0.9973) based on the results shown in **Fig. 2-7**.

$$\lambda = -33.19 + 0.22460T + 0.86970r_p - 0.00037T^2 - 0.00306Tr_p \quad (2\text{-}16)$$

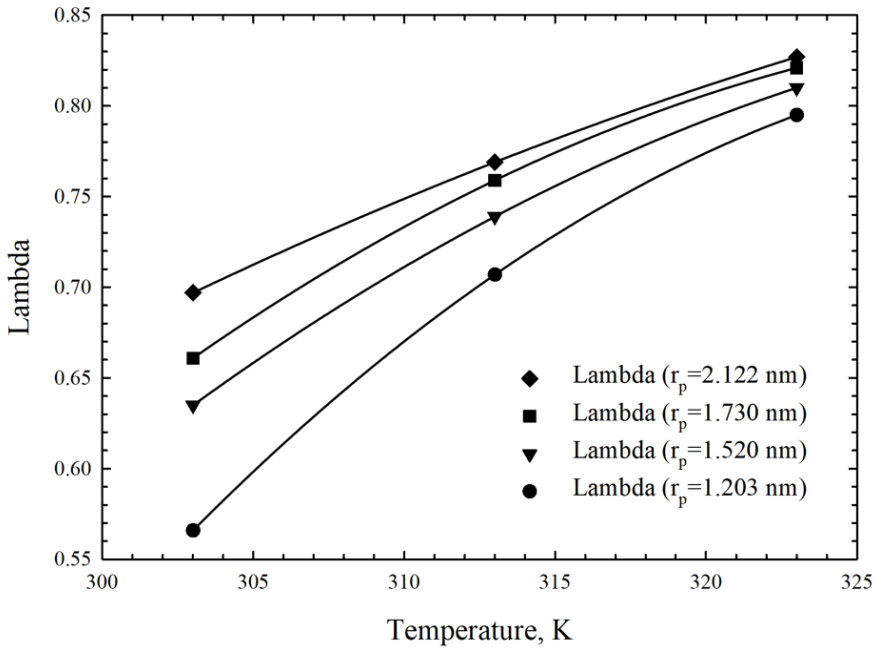

Fig. 2-8. Computed tuning parameter λ of pure *n*-C_6 based on the experimental data13. The solid lines are trend lines which are drawn for visual guide purpose.

Based on the regression of the experimental data shown in **Fig. 2-7**, we can readily develop the following λ correlation for *n*-C_6 (R^2=0.9981).

$$\lambda = -21.06 + 0.12160T + 1.6470r_p - 0.00017T^2 - 0.00501Tr_p \quad (2\text{-}17)$$

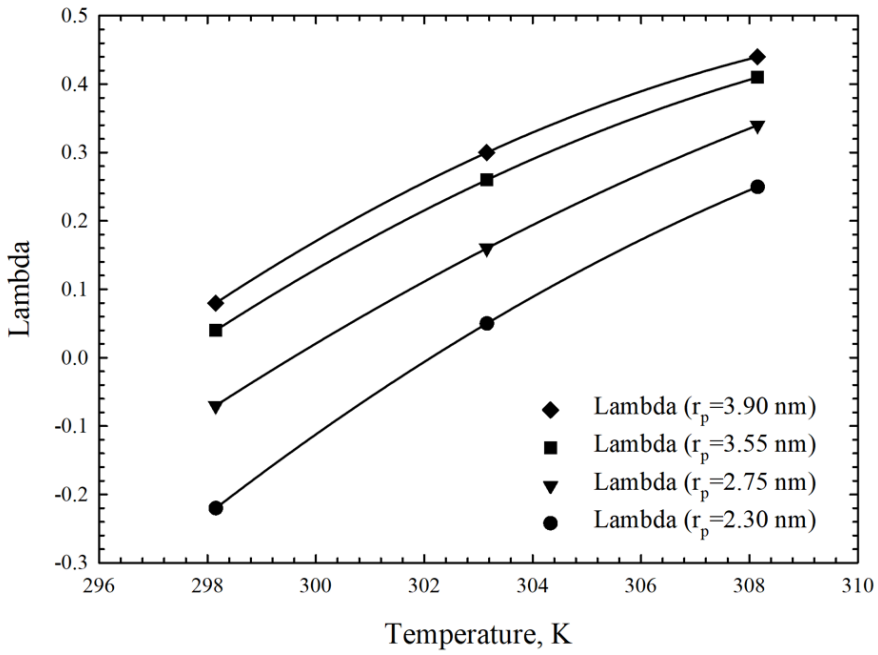

Fig. 2-9. Computed tuning parameter λ of pure *n*-C_7 based on the experimental data[14]. The solid lines are trend lines which are drawn for visual guide purpose.

At a temperature of 298.15 K, the tuning parameter λ of pure n-heptane becomes negative for pore radii of 2.30 nm and 2.75 nm. This negative value of the tuning parameter λ effectively reduces the calculated capillary pressure. Based on the results shown in **Fig. 2-9**, we can develop the following λ correlation for *n*-C_7 (R^2=0.9916).

$$\lambda = -32.51 + 0.15330T + 2.01010r_p - 0.00016T^2 - 0.00615Tr_p \quad (2\text{-}18)$$

To compare the tuning parameter λ of different hydrocarbons, we calculate λ of C_2 to *n*-C_7 over 295-310 K at a pore radius of 1 nm. Results are shown in **Fig. 2-10**. Despite the fact that experimental saturation pressure data for C_2 to *n*-C_7 are collected from different research groups, it is interesting to observe from **Fig. 2-10** that, at a fixed temperature and pore radius, λ shows a monotonic decreasing trend for hydrocarbons with an increasing carbon number.

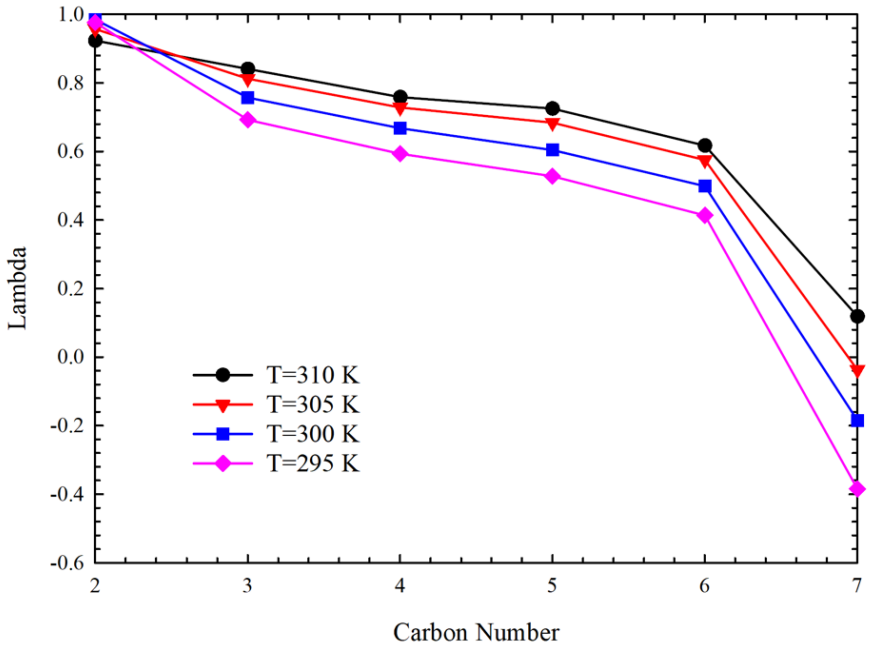

Fig. 2-10. Lambda of C_2 to *n*-C_7 in nanopores with a pore radius of 1 nm at different temperatures. Equations (2-13)-(2-18) are used for these calculations.

In this work, when the modified Young-Laplace equation[36] is coupled with PR-EOS, the calculated λ for C_2, C_3, *n*-C_4, *n*-C_5, *n*-C_6, and *n*-C_7 suggests a quadratic polynomial relationship between λ and temperature. Moreover, λ increases with increasing pore radii for all temperatures; this is different from the results obtained by Tan and Piri[36] which showed that the tuning parameter λ decreases with an increasing pore radius. The tuning parameter λ for C_2 C_3, *n*-C_4, *n*-C_5, *n*-C_6, and *n*-C_7 can be empirically determined by using Eqs. (2-13)-(2-18), respectively, at a given temperature and a given pore radius. The calculated λ can then be fed into the modified Young-Laplace equation to adjust the calculated capillary pressure. **Figs. 2-11 – 2-16** present the saturation pressure curves of C_2, C_3, *n*-C_4, *n*-C_5, *n*-C_6, and *n*-C_7 measured from experiments and calculated from two-phase equilibrium calculations coupled with capillary pressure calculated by using the original Young-Laplace equation[39] and the modified Young-Laplace equation[36].

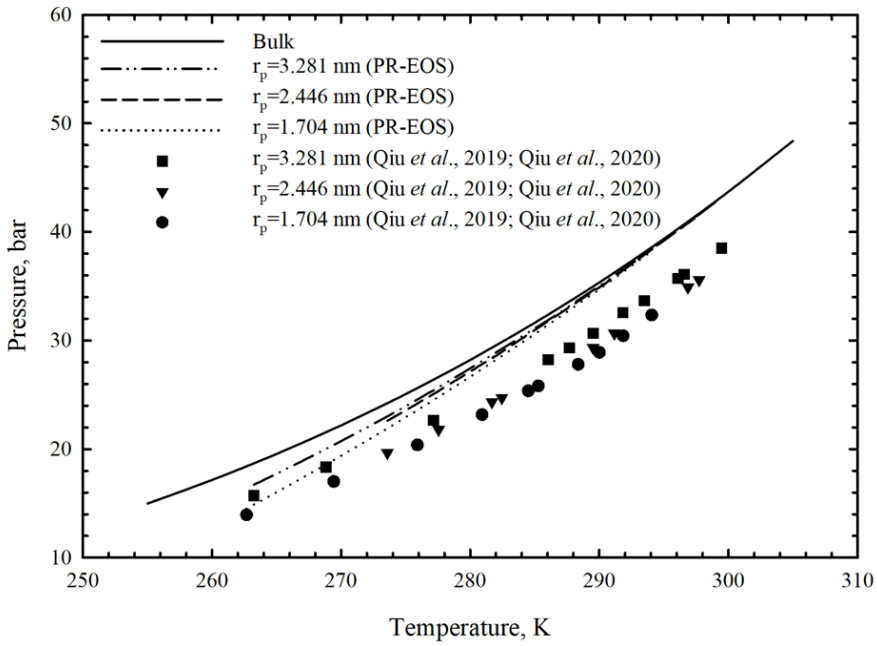

(a)

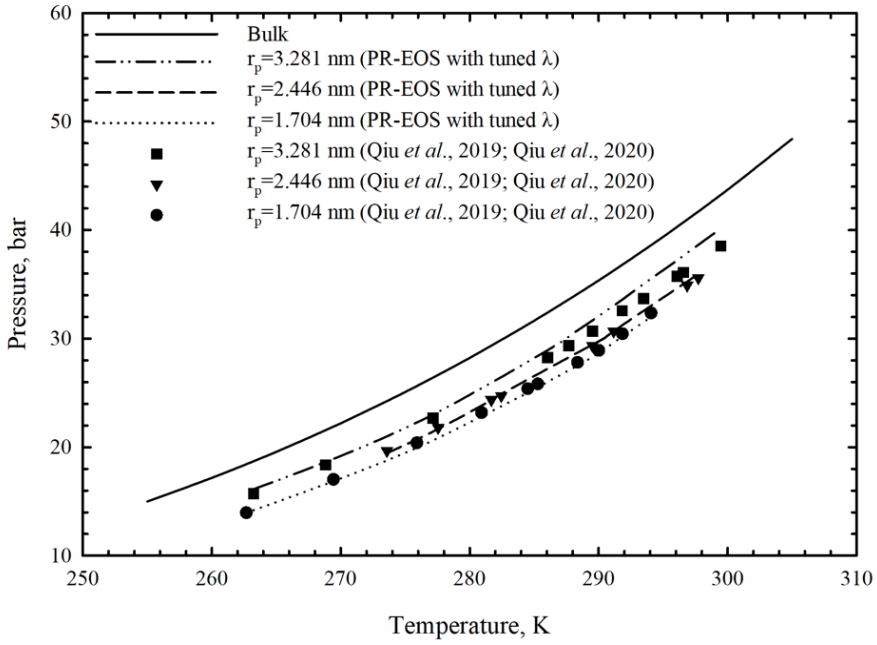

(b)

Fig. 2-11. Saturation pressures of C_2 measured in SBA-15[17,19] and calculated from vapor-liquid equilibrium calculations coupled with the (a) original Young-Laplace equation[39] and the (b) modified Young-Laplace equation[36]. The experimental data are retrieved from the study by Qiu *et al*. (2019) and Qiu *et al*., (2020).[17,19]

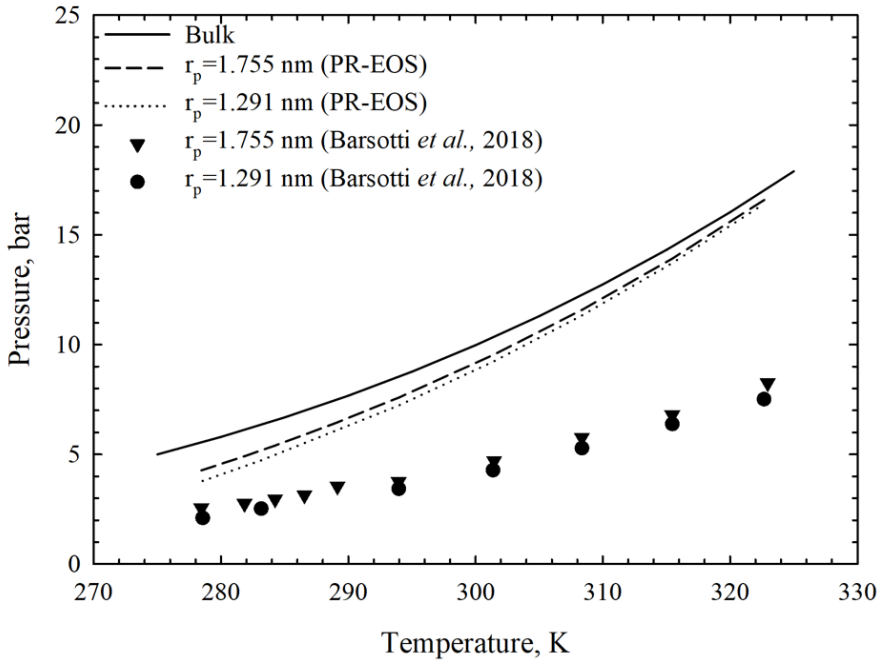

(a)

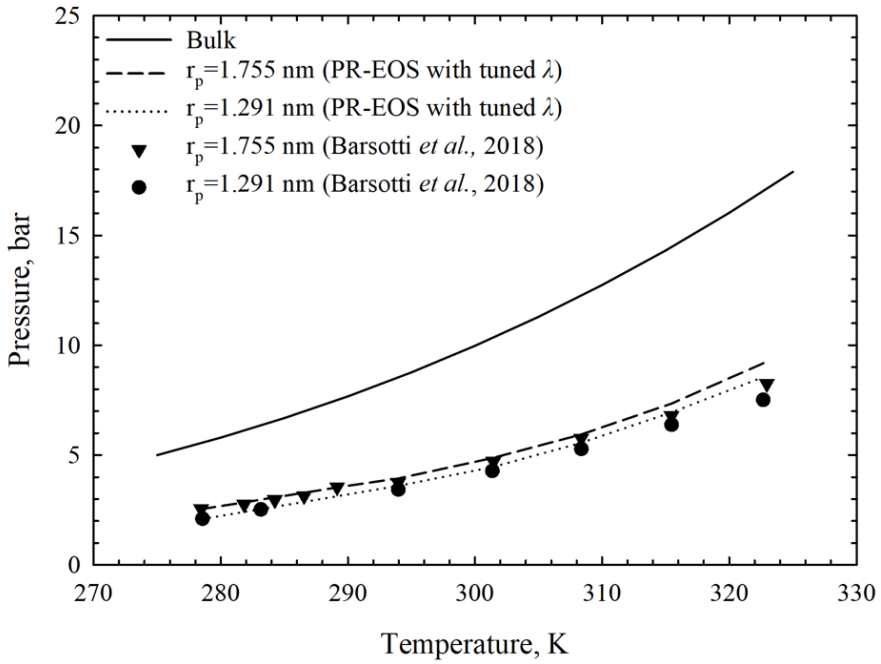

(b)

Fig. 2-12. Saturation pressures of C_3 measured in MCM-41[11] and calculated from vapor-liquid equilibrium calculations coupled with the (a) original Young-Laplace equation[39] and the (b) modified Young-Laplace equation[36]. The experimental data are retrieved from the study by Barsotti *et al*. (2018).[11]

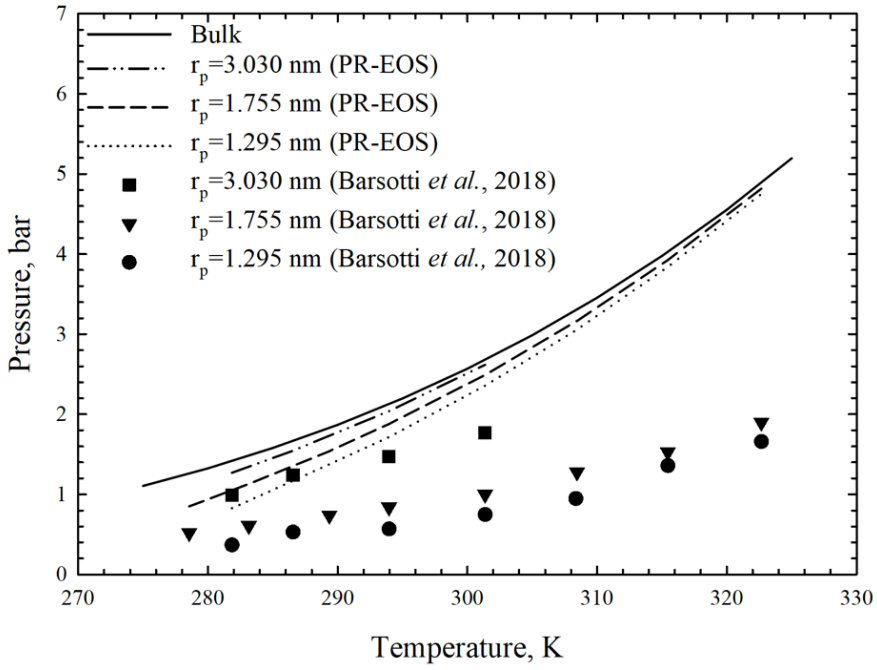

(a)

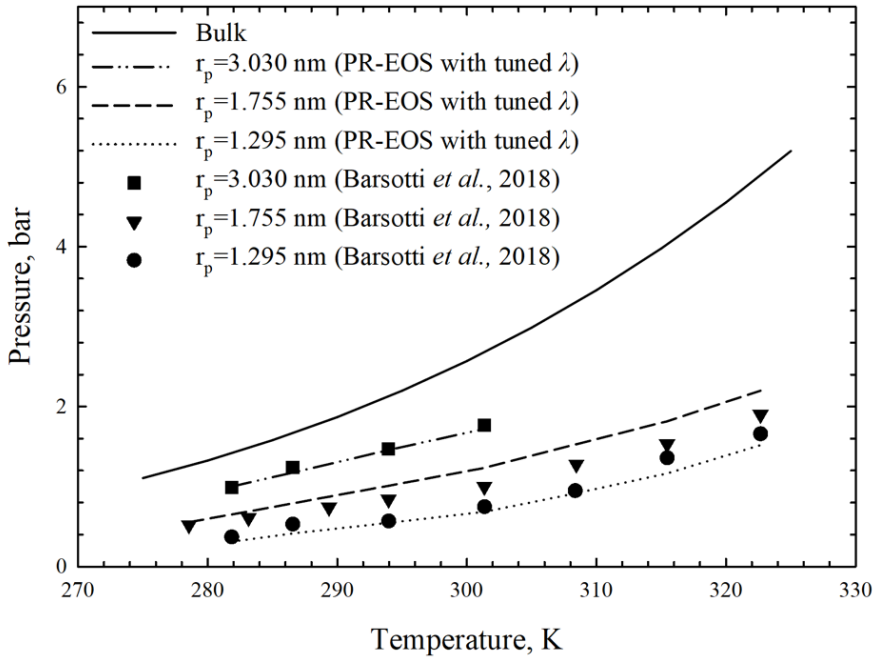

(b)

Fig. 2-13. Saturation pressures of pure *n*-C_4 measured in MCM-41[11] and calculated from vapor-liquid equilibrium calculations coupled with the (a) original Young-Laplace equation[39] and the (b) modified Young-Laplace equation[36]. The experimental data are retrieved from the study by Barsotti *et al*. (2018).[11]

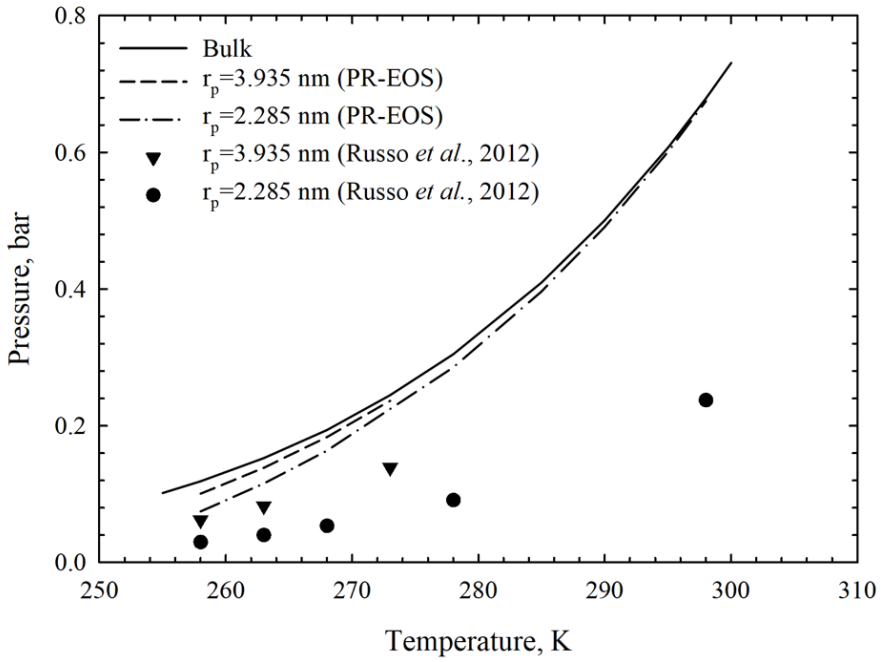

(a)

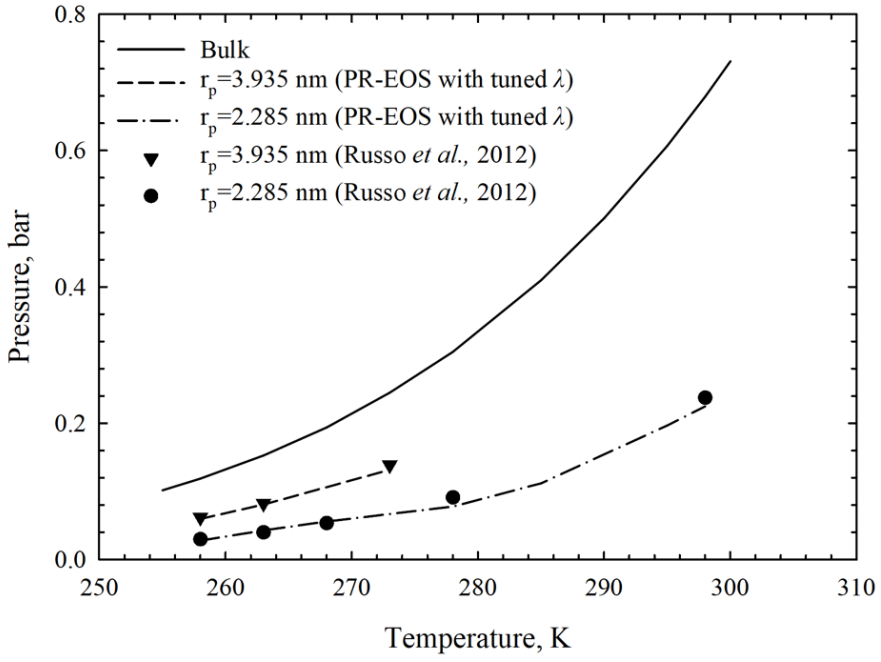

(b)

Fig. 2-14. Saturation pressures of pure *n*-C_5 measured in MCM-41 and SBA-15[12] and calculated from vapor-liquid equilibrium calculations coupled with the (a) original Young-Laplace equation[39] and the (b) modified Young-Laplace equation[36]. The experimental data are retrieved from the study by Russo *et al*. (2012).[12]

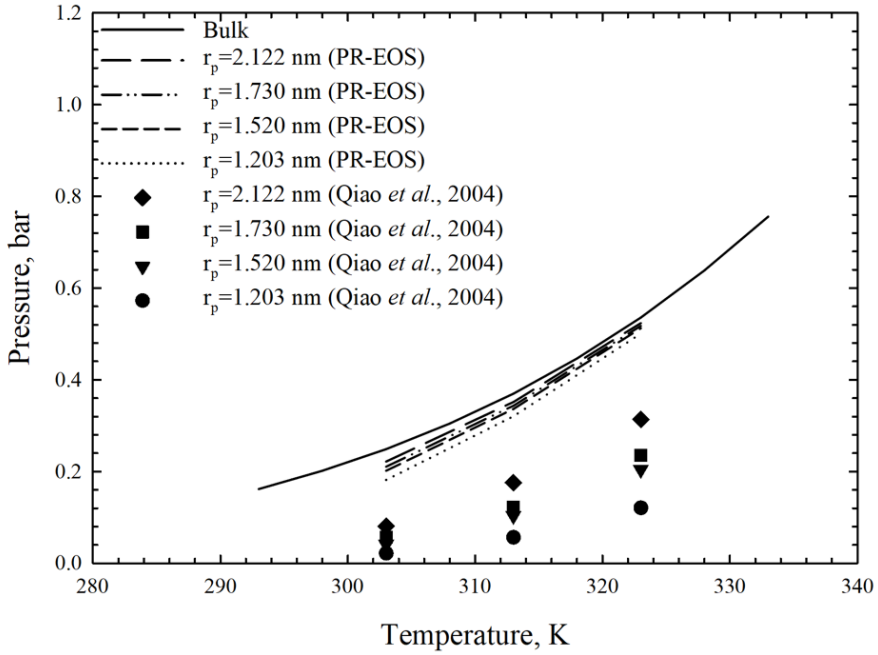

(a)

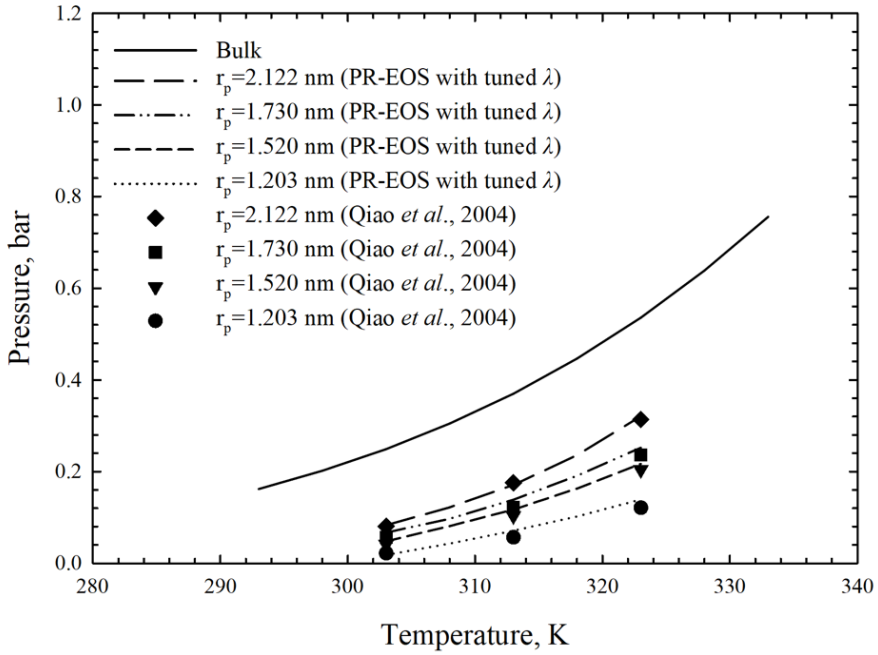

(b)

Fig. 2-15. Saturation pressures of *n*-C_6 measured in MCM-41[13] and calculated from vapor-liquid equilibrium calculations coupled with the (a) original Young-Laplace equation[39] and the (b) modified Young-Laplace equation[36]. The experimental data are retrieved from the study by Qiao *et al*. (2004).[13]

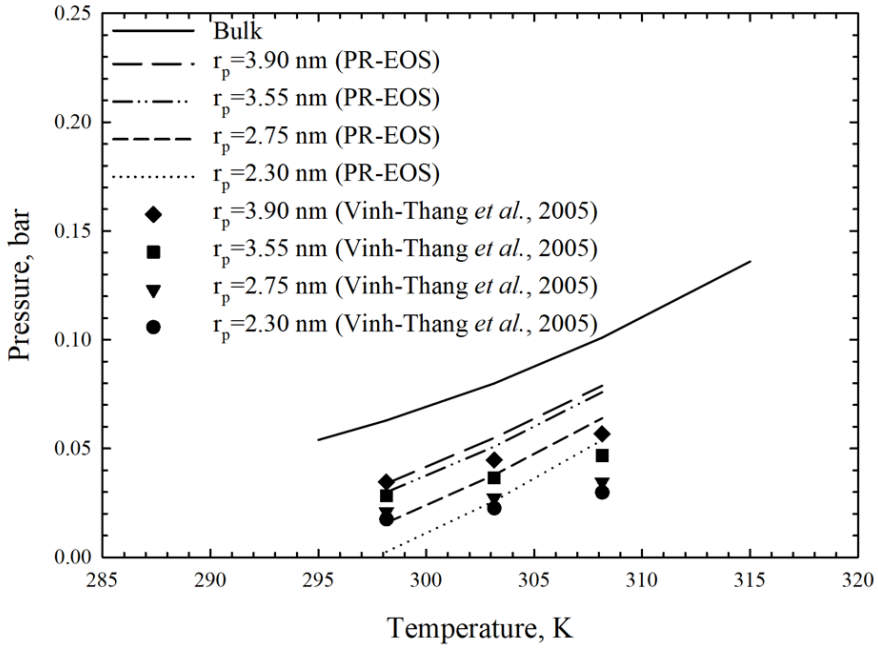

(a)

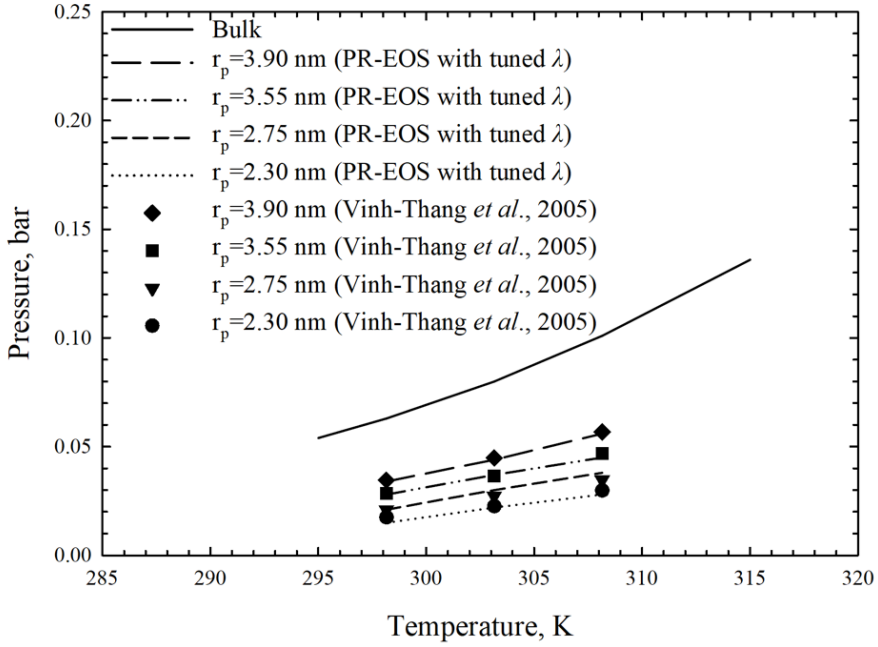

(b)

Fig. 2-16. Saturation pressures of *n*-C_7 SBA-15[14] and calculated from vapor-liquid equilibrium calculations coupled with the (a) original Young-Laplace equation[39] and the (b) modified Young-Laplace equation[36]. The experimental data are retrieved from the study by Vinh-Thang *et al.* (2005).[14]

In **Figs. 2-11 – 2-16**, the solid curves represent the vapor-liquid equilibria of pure hydrocarbon fluids under bulk conditions. The black symbols represent experimental saturation pressure data, and the different dashed curves represent saturation pressure curves calculated by vapor-liquid equilibrium calculations coupled with the original Young-Laplace equation[39] and the modified Young-Laplace equation[36]. It is shown in **Figs. 2-11 – 2-16 (a)** that the saturation pressures of C_2 C_3, *n*-C_4, *n*-C_5, *n*-C_6, and *n*-C_7 in confined nanopores measured from experiments and calculated from vapor-liquid equilibrium calculations are all reduced compared to the bulk one. As for C_3, *n*-C_4, *n*-C_5, and *n*-C_6, the saturation pressures predicted from vapor-liquid equilibrium calculations coupled with the original Young-Laplace equation[39] are larger than the saturation pressures obtained from experiments at all pore radii. Furthermore, as the temperature rises, the deviation between the measured and calculated saturation pressures becomes larger. This suggests that the actual capillary pressure existing in confined nanopores in the experiments is larger than the calculated capillary pressure. One of the major reasons that may cause this is that the surface adsorption reduces pore radius, which, in turn, increases capillary pressure dramatically.

As for *n*-C_7, the calculated saturation pressures of *n*-C_7 in confined nanopores are in better agreement with the experimental data. The calculated saturation pressures of *n*-C_7 are mostly larger than the experimental data. At a temperature of 298.15 K, for pore radii of 2.75 nm and 2.30 nm, the calculated saturation pressures become lower than the experimental data.

After the modified Young-Laplace equation and the λ correlations are applied, the calculated saturation pressures of C_2 C_3, *n*-C_4, *n*-C_5, *n*-C_6, and *n*-C_7 in confined nanopores match the experimental data with decent accuracy. The application of the modified Young-Laplace equation with the λ correlations is effective in increasing the capillary pressure for C_2 C_3, *n*-C_4, *n*-C_5, and *n*-C_6 resulting in a good agreement with the measured saturation pressure data. The λ correlation for

n-C_7 reduces the capillary pressures at lower temperatures but increases the capillary pressures at higher temperatures. Overall, the implementation of the modified Young-Laplace equation[36] with proper modeling of the tuning parameter λ greatly improves the accuracy of the vapor-liquid equilibrium calculations for C_2 C_3, *n*-C_4, *n*-C_5, *n*-C_6, and *n*-C_7 in confined nanopores.

2.4.2 Examples of Binary Mixtures

In the work of Tan and Piri[36], pure substances were studied to develop the correlations of the tuning parameter λ. A linear mixing rule is proposed in their work to calculate the mixture λ based on the pure-substance λ. This practice was then applied in subsequent studies.[40,41] In their studies, λ for mixtures of acetone/ethanol,[40] ethanol/water,[40] and CO_2/*n*-C_5[41] are calculated using the mixing rule and λ for the constituting components. Results showed that the application of the linear mixing rule offers a satisfactory accuracy in calculating the mixture λ. To examine the dependence of λ for hydrocarbon mixtures on temperature and pore radius, vapor-liquid equilibria of the binary mixture C_1-C_2 and the binary mixture C_1-C_3 in confined nanopores are studied in this section. The feed composition of the mixture C_1-C_2 is 14.98 mol% C_1 and 85.02 mol% C_2, while the feed composition of the mixture C_1-C_3 is 20 mol% C_1 and 80 mol% C_3. The experimental dew point pressures of the mixture C_1-C_2 in confined nanopores are collected from Qiu *et al.,*[8] while the experimental dew point pressures of the mixture C_1-C_3 are collected from Zhong *et al.*[9] The capillary pressure is coupled in a two-phase equilibrium calculation to compute the dew point pressures of the two tested mixtures in confined nanopores. The binary interaction parameters (BIP) for the mixture C_1-C_2 and the mixture C_1-C_3 used in the PR-EOS model are given in **Table 2-3** and **Table 2-4**, respectively.

Table 2-3. BIP for the Mixture C_1-C_2 Used in the PR-EOS Model.[42]

BIP	C_1	C_2
C_1	0	0.0027
C_2	0.0027	0

Table 2-4. BIP for the Mixture C_1-C_3 Used in the PR-EOS Model.[42]

BIP	C_1	C_3
C_1	0	0.006
C_3	0.006	0

The computed tuning parameter λ for the mixture C_1-C_2 and C_1-C_3 are shown in **Fig. 2-17** and **Fig. 2-18**, respectively.

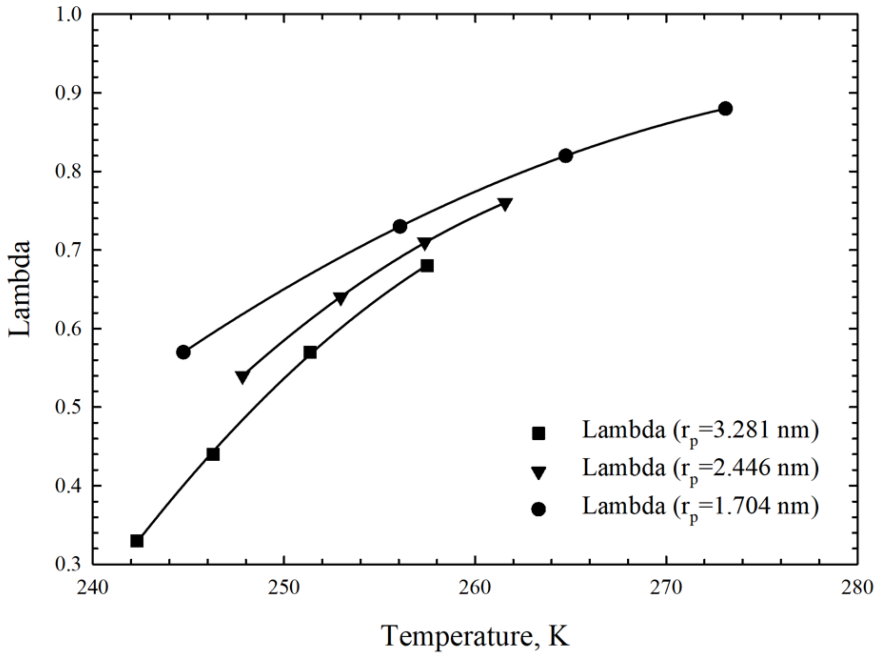

Fig. 2-17. Computed tuning parameter λ for the binary mixture C_1-C_2 based on the experimental data[8]. The solid lines are trend lines which are drawn for visual guide purpose.

Based on the regression of the experimental data shown in **Fig. 2-17**, the following λ correlation for the binary mixture methane-ethane can be obtained (R^2=0.9726).

$$\lambda = -56.18 + 0.42430T + 0.42810r_p - 0.00079T^2 - 0.00137Tr_p \quad (2\text{-}19)$$

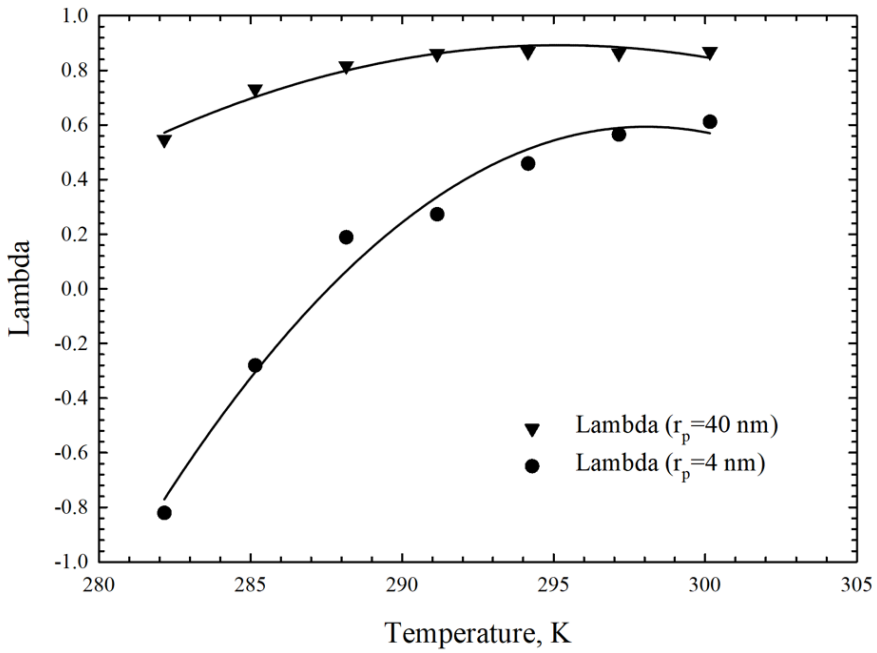

Fig. 2-18. Computed tuning parameter λ of the binary mixture C_1-C_3 based on the experimental data[9]. The solid lines are trend lines which are drawn for visual guide purpose.

Based on the results shown in **Fig. 2-18**, we develop the following λ correlation for the binary mixture C_1-C_3 (R^2=0.9313).

$$\lambda = -58.12 + 0.31950T + 0.49150r_p - 0.00041T^2 - 0.00163Tr_p \quad (2\text{-}20)$$

The above correlations can then be applied in the modified Young-Laplace equation[36] to adjust the calculated capillary pressure to improve the accuracy of the two-phase equilibrium calculation in confined nanopores. **Fig. 2-19** and **Fig. 2-20** show the dew point pressure curves of the mixture C_1-C_2 and the mixture C_1-C_3, respectively, obtained from the experiment and from two-phase equilibrium calculations coupled with the original Young-Laplace equation[39] and the modified Young-Laplace equation[36].

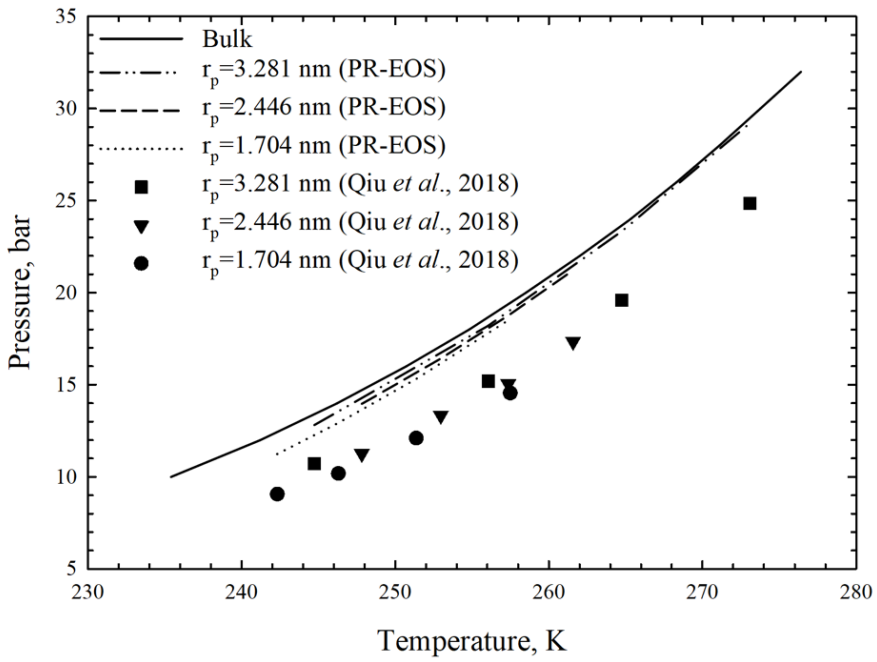

(a)

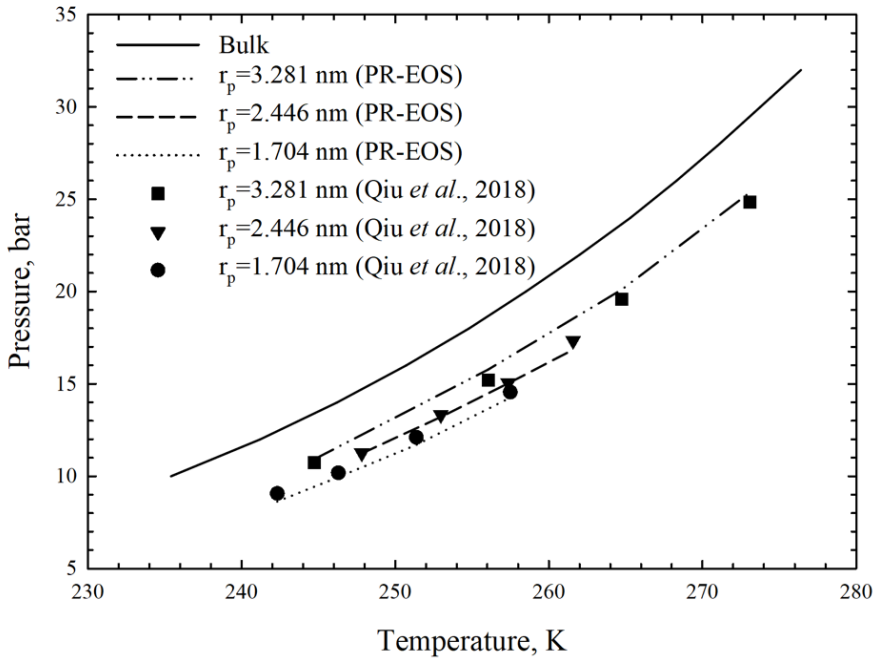

(b)

Fig. 2-19. Dew point pressures of the binary mixture C_1-C_2 measured in SBA-15[8] and calculated from vapor-liquid equilibrium calculations coupled with the (a) original Young-Laplace equation[39] and the (b) modified Young-Laplace equation[36]. The experimental data are retrieved from the study by Qiu *et al*. (2018).[8]

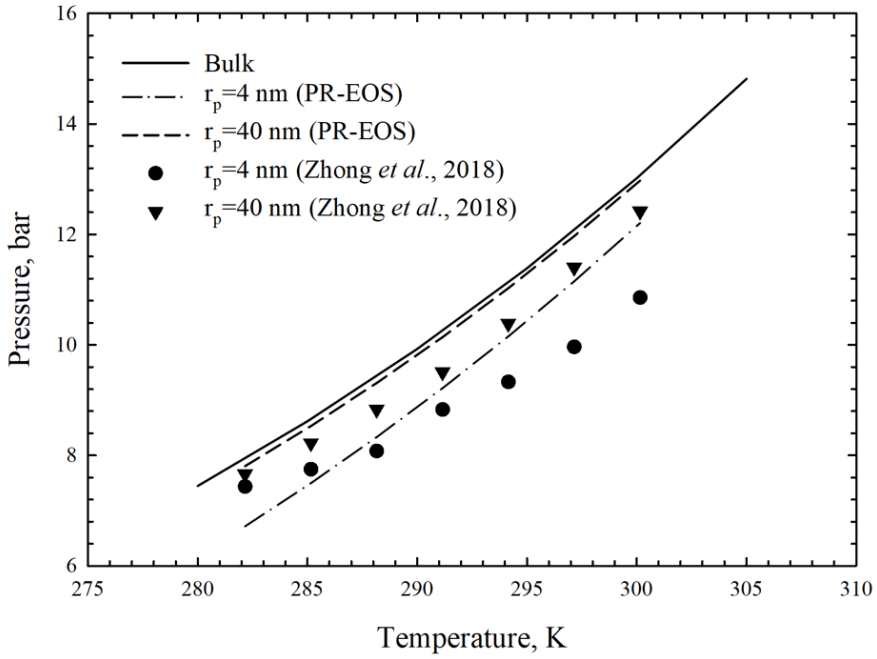

(a)

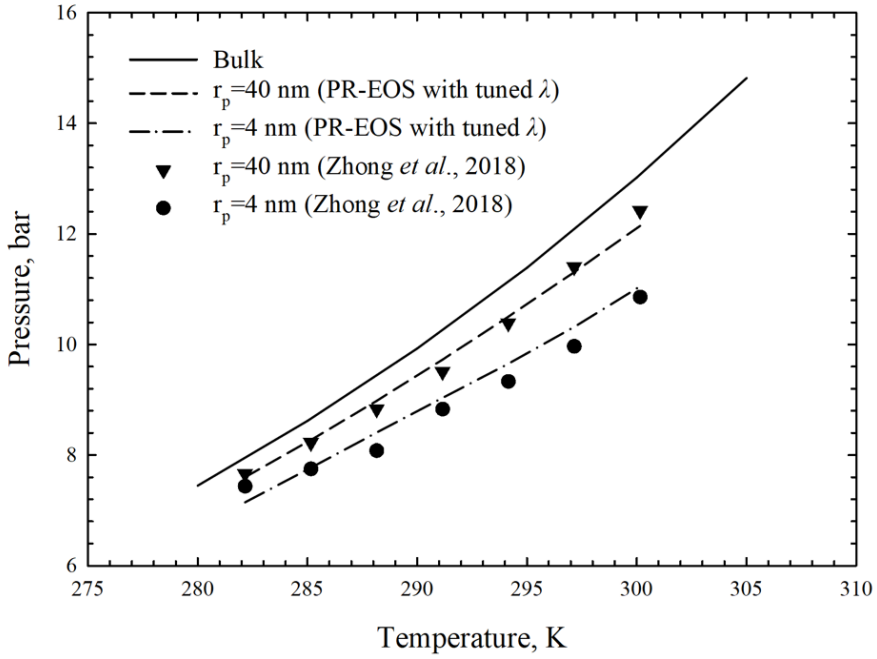

(b)

Fig. 2-20. Dew point pressures of the binary mixture C_1-C_3 measured using a nanofluidic device with nanochannels[9] and calculated from vapor-liquid equilibrium calculations coupled with the (a) original Young-Laplace equation[39] and the (b) modified Young-Laplace equation[36]. The experimental data are retrieved from the study by Zhong *et al*. (2018).[9]

It can be found in **Figs. 2-19** and **2-20** that the calculated dew point pressures of the two mixtures C_1-C_2 and C_1-C_3 in confined nanopores greatly deviate from the experimental data. For the mixture C_1-C_2, the calculated dew point pressures are larger than the measured ones. This suggests that the capillary pressure calculated by using the original Young-Laplace equation[39] is not capable of accurately representing the actual capillary pressure. For the mixture C_1-C_3, at most of the tested temperatures, the calculated dew point pressures are larger than the experimental data. At temperatures of 282.15 K and 285.15 K, however, the calculated dew point pressures are lower than the experimental data measured at a pore radius of 4 nm. This implies that negative values of λ are needed in this case. Based on the measured dew point pressure data, the tuning parameter λ for the binary mixtures C_1-C_2 and C_1-C_3 can be determined at different temperatures and different pore radii.

After the modified Young-Laplace equation[36] is coupled with PR-EOS[33], the dew point pressures of the binary mixture C_1-C_2 and C_1-C_3 in confined nanopores calculated using the proposed algorithm match the experimental data with good accuracy. The λ correlations obtained for the two tested mixtures are proved to be effective in adjusting the calculated capillary pressure to the true capillary pressure in experiments.

Ideally, λ for mixtures can be determined based on the λ of individual components using a certain type of mixing rule. Tan and Piri[36] suggested using a simple linear mixing rule to calculate the mixture λ based on the pure substance λ:

$$\lambda_m = \sum_{i=1}^{N_c} x_i \lambda_i \tag{2-21}$$

where λ_m is the mixture λ, N_c is the number of components in the mixture, x_i is the mole fraction of the ith component in liquid phase, and λ_i is the λ of the ith component. It can be seen in previous

examples that, under certain circumstances, the temperature interval of the C_1-C_2 mixture's two-phase region is above the critical temperature of C_1 in the mixture. Therefore, the λ correlation for C_1 under supercritical condition needs to be determined before calculating the mixture λ with the mixing rule (i.e., Eq (2-21)). In this following exercise, we first validate the application of the mixing rule on calculating the mixture λ using λ of pure substances. Then, we use the λ correlations of the mixture C_1-C_2 and pure C_2 to back calculate the λ correlation of C_1 under supercritical conditions. It is worth noting that the experimental saturation pressure data for the mixture C_1-C_2 and pure C_2 is collected from experiments conducted by the same research groups. They used exactly the same material when measuring the saturation pressures of the mixture C_1-C_2 and C_2 in confined nanopores. The purpose of this example calculation is to demonstrate that there exists a λ correlation of C_1 under supercritical conditions.

To examine if the mixing rule is feasible for calculating the mixture λ, we calculate bubble points of the binary hydrocarbon mixture *n*-C_5-*n*-C_7 (50 mol%-50 mol%) at different temperatures and pore radii. The λ of this mixture is calculated using the mixing rule (Eq. (2-21)) and the fitted λ for pure *n*-C_5 and *n*-C_7. The calculated results are then compared with the measured bubble point data reported by Alfi *et al*.[43]. The BIP used for calculation is given in **Table 2-5**.

Table 2-5: BIP for the Mixture *n*-C_5-*n*-C_7 used in the PR-EOS Model.[42]

BIP	*n*-C_5	*n*-C_7
n-C_5	0	0.0021
n-C_7	0.0021	0

Experimental vapor-liquid interfacial tension (IFT) data for the *n*-C_5-*n*-C_7 system are collected from Mohsen-Nia *et al*.[44] to develop the ϕ_{ij} correlation. The ϕ_{ij} correlation developed for *n*-C_5-*n*-C_7 system is given in Eq. (2-22).

$$\varphi_{ij} = 0.0060T - 1.0088 \tag{2-22}$$

Fig. 2-21 shows the comparison between the calculation results and measured ones. It is interesting to observe from **Fig. 2-21** that the bubble points yielded by PR-EOS[33] and the λ correlations match fairly well with the measured ones at small pore radii. The match is surprisingly satisfactory because the experimental data used for developing the λ correlations are conducted on nanodevices that are different from the ones used to measure the bubble points of *n*-C_5-*n*-C_7 mixtures.

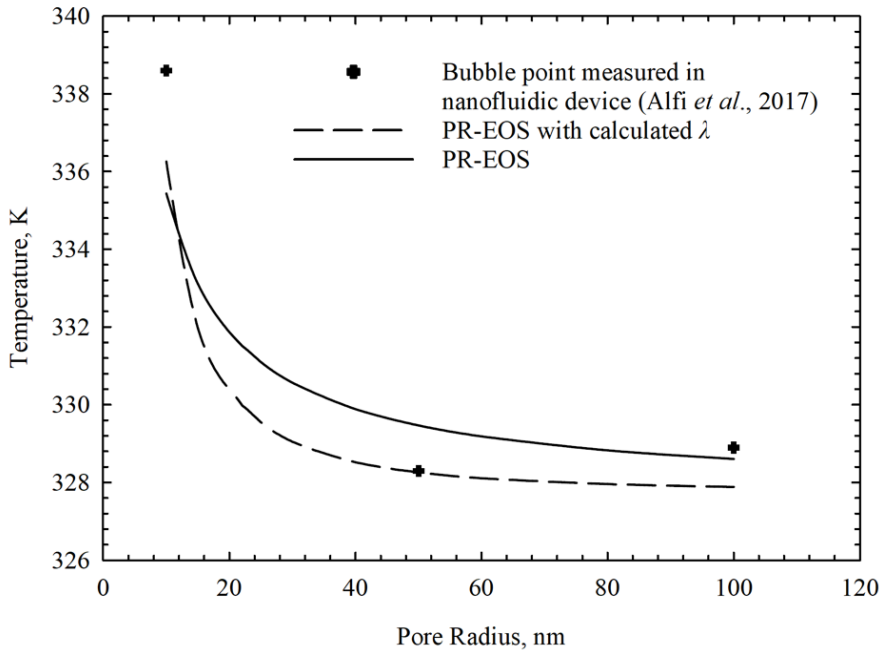

Fig. 2-21. Bubble points of the binary mixtures *n*-C_5-*n*-C_7 measured using a nanofluidic device[43] and calculated from vapor-liquid equilibrium calculations coupled with the modified Young-Laplace equation[36]. The experimental data are retrieved from the study by Alfi *et al*. (2017).[43]

The back calculated λ correlation of C_1 under supercritical conditions is given in Eq. (2-23).

$$\lambda = -12.93 + 0.37890T + 0.29020r_p - 0.00938T^2 - 0.01779Tr_p \tag{2-23}$$

The calculation result suggests that there exist correlations of λ for C_1 under supercritical condition and the correlations are still quadratic polynomial functions with temperature. Moreover, the tuning parameter λ becomes larger with an increasing pore radius. Such an example calculation confirms the feasibility of utilizing a simple mixing rule in calculating the mixture λ using λ of pure components. In the practice of calculating the mixture λ using λ correlations of constituting substances, certain precautions should be applied. The best way of validating the λ correlations developed for the constituting substances and the mixing rule is to conduct systematic phase behavior experiments for pure substances and their mixtures using the same nanofluidic device or DSC setup. However, such a comprehensive experimental dataset is lacking. Future experimental works are needed to fill this gap.

2.5. Summary and Conclusions

The vapor-liquid equilibria of pure substances and mixtures in confined nanopores are studied in this research. This work aims to improve the accuracy of vapor-liquid equilibrium calculation of hydrocarbons in confined nanopores by coupling a modified Young-Laplace equation[36] in the PR-EOS model. We developed correlations of the tuning parameter λ for six pure hydrocarbon substances and two binary hydrocarbon mixtures and applied the modified Young-Laplace equation in vapor-liquid equilibrium calculations. The following conclusions can be drawn from this study:

- For both pure substance and mixture, the correlation of the tuning parameter λ can be expressed as a quadratic polynomial function with temperature when the modified Young-Laplace equation[36] is coupled with the PR-EOS model[33].

- The tuning parameter λ becomes larger with an increased pore radius. This trend is valid for pure hydrocarbons and their mixtures.
- λ generally becomes smaller for pure hydrocarbon substances with smaller carbon numbers.
- The value of λ is always less than one. The λ can become negative under certain circumstances, which adjusts the capillary pressure to a lower value.
- The λ for C_1 under supercritical conditions can be expressed as polynomial functions with temperature. We also demonstrated that the λ under supercritical conditions can be back-calculated using the mixing rule.
- The accuracy of the vapor-liquid equilibrium calculations in confined nanopores can be significantly improved by applying the modified Young-Laplace equation[36] with the experimentally derived λ correlations.
- One advantage of using PR-EOS[33] in the modeling strategy is that this enables the proposed approach to be readily integrated into the existing reservoir simulators. However, it must be noted that the development of λ correlations highly hinges on the availability of phase transition experiments in nanopores. But these experimental data are hardly available because of the technical challenges associated with such nano-scale experiments.

Acknowledgments

The authors acknowledge a Discovery Grant from the Natural Sciences and Engineering Research Council of Canada (NSERC) (Grant No.: NSERC RGPIN-2020-04571) and a Young Scientists Fund of the National Natural Science Foundation of China (Grant No.: 51704234) to H. Li.

Nomenclature

A = equation of state constant

B = equation of state constant

EOS = equation of state

f_{ix} = fugacity of component i in liquid phase, bar

f_{iy} = fugacity of component i in vapor phase, bar

IFT = interfacial tension, mN/m

k_i = phase equilibrium ratio of component i

M_l = molecular weight of liquid phase, g/mol

M_g = molecular weight of vapor phase, g/mol

N_c = total number of components

P = bulk pressure, bar

P_{chi} = Parachor of component i

P_{ci} = critical pressure of component i

P_g = vapor phase pressure, bar

P_l = liquid phase pressure, bar

P_c = vapor-liquid capillary pressure, bar

r_p = pore radius, nm

R = universal gas constant, 83.14459848 $cm^3 \cdot bar \cdot K^{-1} \cdot mol^{-1}$

T = bulk temperature, K

T_c= critical temperature, K

T_{ci} = critical temperature of component i

x_i = mole fraction of component i in liquid phase

y_i = mole fraction of component i in vapor phase

Z = compressibility factor

z_i = feed composition

β_y = vapor phase mole fraction

σ = vapor-liquid interfacial tension, mN/m

ρ_g = vapor phase density, g/cm^3

ρ_l = liquid phase density, g/cm^3

ϕ_{ix} = fugacity coefficient of component i in liquid phase

ϕ_{iy} = fugacity coefficient of component i in vapor phase

μ_{ix} = chemical potential of component i in liquid phase

μ_{iy} = chemical potential of component i in vapor phase

λ = tuning parameter in the modified Yong-Laplace equation

λ_i = tuning parameter λ of component i

λ_m = tuning parameter λ of mixture

References

(1) Brusilovsky, A. Mathematical Simulation of Phase Behavior of Natural Multicomponent Systems at High Pressures with an Equation of State. *SPE Res. Eng*. 1992, *7*, 117-122.

(2) Hustad, O.; Browning, D. A Fully Coupled Three-Phase Model for Capillary Pressure and Relative Permeability for Implicit Compositional Reservoir Simulation. *SPE J*. 2010, *15*, 1003-1019.

(3) Moortgat, J.; Firoozabadi, A. Three-Phase Compositional Modeling with Capillarity in Heterogeneous and Fractured Media. *SPE J*. 2013, *18*, 1150-1168.

(4) Wang, Y.; Yan, B.; Killough, J. Compositional Modeling of Tight Oil Using Dynamic Nanopore Properties. *SPE Annual Technical Conference and Exhibition, New Orleans, Louisiana,* Society of Petroleum Engineers: September 30-October 2, 2013.

(5) Jin, Z.; Firoozabadi, A. Thermodynamic Modeling of Phase Behavior in Shale Media. *SPE J*. 2016, *21*, 190-207.

(6) Nojabaei, B.; Johns, R.; Chu, L. Effect of Capillary Pressure on Phase Behavior in Tight Rocks and Shales. *SPE Res. Eval. & Eng*. 2013, *16*, 281-289.

(7) Dong, J. A High Order Method for Three Phase Flow in Homogeneous Porous Media. *SIAM Underg. Res. Online.* 2013, *7*, 74-88.

(8) Qiu, X.; Tan, S.; Dejam, M.; Adidharma, H. Simple and Accurate Isochoric Differential Scanning Calorimetry Measurements: Phase Transitions for Pure Fluids and Mixtures in Nanopores. *Phy. Chem. Chem. Phy*. 2018, *21*, 224-231.

(9) Zhong, J.; Zhao, Y.; Lu, C.; Xu, Y.; Jin, Z.; Mostowfi, F.; Sinton, D. Nanoscale Phase Measurement for the Shale Challenge: Multicomponent Fluids in Multiscale Volumes. *Langmuir* 2018, *34*, 9927-9935.

(10) Nikpoor, M.; Dejam, M.; Chen, Z.; Clarke, M. Chemical–Gravity–Thermal Diffusion Equilibrium in Two-Phase Non-isothermal Petroleum Reservoirs. *Energy & Fuels* 2016, *30*, 2021-2034.

(11) Barsotti, E.; Tan, S.; Piri, M.; Chen, J. Phenomenological Study of Confined Criticality: Insights from the Capillary Condensation of Propane, n-Butane, and n-Pentane in Nanopores. *Langmuir* 2018, *34*, 4473-4483.

(12) Russo, P.; Ribeiro Carrott, M.; Carrott, P. Trends in the Condensation/Evaporation and Adsorption Enthalpies of Volatile Organic Compounds on Mesoporous Silica Materials. *Microp. Mesop. Mat*. 2012, *151*, 223-230.

(13) Qiao, S.; Bhatia, S.; Nicholson, D. Study of Hexane Adsorption in Nanoporous MCM-41 Silica. *Langmuir* 2004, *20*, 389-395.

(14) Vinh-Thang, H.; Huang, Q.; Eić, M.; Trong-On, D.; Kaliaguine, S. Adsorption of C_7 Hydrocarbons on Biporous SBA-15 Mesoporous Silica. *Langmuir* 2005, *21*, 5094-5101.

(15) Sheng, L.; Lutkenhaus, J. L.; Nasrabadi, H. Experimental Study of Confinement Effect on Hydrocarbon Phase Behavior in Nano-Scale Porous media Using Differential Scanning Calorimetry. *SPE Annual Technical Conference and Exhibition, Houston*, Society of Petroleum Engineers: September 28-30, 2015.

(16) Xu, Y.; Riordon, J.; Cheng, X.; Bao, B.; Sinton, D. The Full Pressure-Temperature Phase Envelope of a Mixture in 1000 Microfluidic Chambers. *Angew. Chem. Int.* 2017, *129*, 13963-13967.

(17) Qiu, X.; Tan, S.; Dejam, M.; Adidharma, H. Isochoric Measurement of the Evaporation Point of Pure Fluids in Bulk and Nanoporous Media Using Differential Scanning Calorimetry. *Phy. Chem. Chem. Phy*. 2020, *22*, 7048-7057.

(18) Adidharma, H.; Dejam, M.; Qiu, X. Methods and Systems for Isochoric Measurements Using Differential Scanning Calorimetry. *U.S. Patent Application* 16/548,898. 2020.

(19) Qiu, X.; Tan, S.; Dejam, M.; Adidharma, H. Experimental Study on the Criticality of a Methane/Ethane Mixture Confined in Nanoporous Media. *Langmuir* 2019, *35*, 11635-11642.

(20) Tan, S.; Qiu, X.; Dejam, M.; Adidharma, H. Critical Point of Fluid Confined in Nanopores: Experimental Detection and Measurement. *J. Phy. Chem.* 2019, *123*, 9824-9830.

(21) Zarragoicoechea, G.; Kuz, V. Critical Shift of a Confined Fluid in a Nanopore. *Fluid Phase Equilibr*. 2004, *220*, 7-9.

(22) Abu Al-Rub, F.; Datta, R. Theoretical Study of Vapor–Liquid Equilibrium inside Capillary Porous Plates. *Fluid Phase Equilibr.* 1999, *162*, 83-96.

(23) Hamada, Y.; Koga, K.; Tanaka, H. Phase Equilibria and Interfacial Tension of Fluids Confined in Narrow Pores. *J. Chem. Phy*. 2007, *127*, 084908.

(24) Qi, Z.; Liang, B.; Deng, R.; Du, Z.; Wang, S.; Zhao, W. Phase Behavior Study in the Deep Gas-Condensate Reservoir with Low Permeability. *SPE Europec/EAGE Annual Conference and Exhibition, London*, Society of Petroleum Engineers: June 11-14, 2007.

(25) Firincioglu, T.; Ozkan, E.; Ozgen, C. Thermodynamics of Multiphase Flow in Unconventional Liquids-Rich Reservoirs. *SPE Annual Technical Conference and Exhibition, San Antonio, Texas,* Society of Petroleum Engineers: October 8-10, 2012.

(26) Tan, S.; Piri, M. Retrograde Behavior Revisited: Implications for Confined Fluid Phase Equilibria in Nanopores. *Phy. Chem. Chem. Phy*. 2017, *19*, 18890-18901.

(27) Sandoval, D.; Yan, W.; Michelsen, M.; Stenby, E. Phase Envelope Calculations for Reservoir Fluids in the Presence of Capillary Pressure. *SPE Annual Technical Conference and Exhibition. Houston, Texas*, Society of Petroleum Engineers: September 28-30, 2015.

(28) Rezaveisi, M.; Sepehrnoori, K.; Pope, G.; Johns, R. Thermodynamic Analysis of Phase Behavior at High Capillary Pressure. *SPE J*. 2018, *23*, 1977-1990.

(29) Teklu, T.; Alharthy, N.; Kazemi, H.; Yin, X.; Graves, R.; AlSumaiti, A. Phase Behavior and Minimum Miscibility Pressure in Nanopores. *SPE Res. Eval. & Eng*. 2014, *17*, 396-403.

(30) Dong, X.; Liu, H.; Hou, J.; Wu, K.; Chen, Z. Phase Equilibria of Confined Fluids in Nanopores of Tight and Shale Rocks Considering the Effect of Capillary Pressure and Adsorption Film. *Ind. & Eng. Chem. Res*. 2016, *55*, 798-811.

(31) Zuo, J.; Guo, X.; Liu, Y.; Pan, S.; Canas, J.; Mullins, O. Impact of Capillary Pressure and Nanopore Confinement on Phase Behaviors of Shale Gas and Oil. *Energy & Fuels* 2018, *32*, 4705-4714.

(32) Travalloni, L.; Castier, M.; Tavares, F.; Sandler, S. Thermodynamic Modeling of Confined Fluids Using an Extension of the Generalized van der Waals Theory. *Chem. Eng. Sci*. 2010, *65*, 3088-3099.

(33) Peng, D.; Robinson, D. A New Two-Constant Equation of State. *Ind. Eng. Chem. Fund*. 1976, *15*, 59-64.

(34) Pang, J.; Zuo, J.; Zhang, D.; Du, L. Impact of Porous Media on Saturation Pressures of Gas and Oil in Tight Reservoirs. *SPE Canadian Unconventional Resources Conference, Calgary, Alberta*, Society of Petroleum Engineers: October 30-November 1, 2012.

(35) Cui, X.; Yang, E.; Song, K.; Huang, J.; Killough, J.; Dong, C. Phase Equilibrium of Hydrocarbons Confined in Nanopores from a Modified Peng-Robinson Equation of State.

SPE Annual Technical Conference and Exhibition, Dallas, Texas, Society of Petroleum Engineers: September 24-26, 2018.

(36) Tan, S.; Piri, M. Equation-of-State Modeling of Confined-Fluid Phase Equilibria in Nanopores. *Fluid Phase Equilibr.* 2015, *393*, 48-63.

(37) Gross, J.; Sadowski, G. Perturbed-Chain SAFT: An Equation of State Based on a Perturbation Theory for Chain Molecules. *Ind. & Eng. Chem. Res.* 2001, *40*, 1244-1260.

(38) Firoozabadi, A.; Katz, D.; Soroosh, H.; Sajjadian, V. Surface Tension of Reservoir Crude Oil/Gas Systems Recognizing the Asphalt in the Heavy Fraction. *SPE Res. Eng*. 1988, *3*, 265-272.

(39) Young, T. An Essay on the Cohesion of Fluids. *Philos. Trans. R. Soc. B.*, 1805, *95*, 65-87.

(40) Tan, S.; Piri, M. Equation-of-State Modeling of Associating-Fluids Phase Equilibria in Nanopores. *Fluid Phase Equilibr.* 2015, *405*, 157-166.

(41) Tan, S.; Piri, M. Application of Material Balance for the Phase Transition of Fluid Mixtures Confined in Nanopores. *Fluid Phase Equilibr.* 2019, *496*, 31-41.

(42) Oellrich, L.; Plocker, U.; Prausnitz, J.; Knapp, H. Equation-of-State Methods for Computing Phase Equilibria and Enthalpies. *Int. Chem. Eng*. 1981, *21*, 1-15.

(43) Alfi, M.; Nasrabadi, H.; Banerjee, D. Effect of Confinement on Bubble Point Temperature Shift of Hydrocarbon Mixtures: Experimental Investigation Using Nanofluidic Devices. *SPE Annual Technical Conference and Exhibition, San Antonio, Texas*, Society of Petroleum Engineers: October 9-11, 2017.

(44) Mohsen-Nia, M.; Rasa, H.; Naghibi, S.F. Experimental and Theoretical Study of Surface Tension of *n*-Pentane, *n*-Heptane, and Some of Their Mixtures at Different Temperatures. *J. Chem. Thermod*. 2009, *42*, 110-113.

(45) Whitson, C.; Brulé, M. Phase Behavior; 2000, Richardson, Texas: Society of Petroleum Engineers: ISBM: 978-1-55563-087-4.

(46) Weinaug, C.; Katz, D. Surface Tensions of Methane-Propane Mixtures. *Ind. & Eng. Chem*. 1943, *35*, 239-246.

(47) Abudour, A.M.; Mohammad, S.A.; Robinson Jr., R.L.; Gasem, K.A.M. Volume-Translated Peng-Robinson Equation of State for Saturated and Single-Phase Liquid Densities. *Fluid Phase Equilibr*. 2012, *335*, 74-87.

(48) Abudour, A.M.; Mohammad, S.A.; Robinson Jr., R.L.; Gasem, K.A.M. Volume-translated Peng-Robinson Equation of State for Liquid Densities of Diverse Binary Mixtures. *Fluid Phase Equilibr*. 2013, *349*, 37-55.

(49) Hugill, J.A.; van Welsenes, A.J. Surface Tension: A Simple Correlation for Natural Gas + Condensate System. *Fluid Phase Equilibr*. 1986, *29*, 383-390.

(50) Baidakov, V.G.; Kaverin, A.M.; Khotienkova, M.N. Surface Tension of Ethane-Methane Solutions: 1. Experiment and Thermodynamic Analysis of the Results. *Fluid Phase Equilibr*. 2013, *356*, 90-95.

(51) Rachford, H.; Rice, J. Procedure for Use of Electronic Digital Computers in Calculating Flash Vaporization Hydrocarbon Equilibrium. *J. Pet. Tech*. 1952, *4*, 19-3.

(52) Wilson, G. M. A Modified Redlich-Kwong Equation of State, Application to General Physical Data Calculations. *65th National AIChE Meeting*. *Cleveland*: 1969, Paper No. 15C.

CHAPTER 3 A NEW THREE-PHASE FLASH ALGORITHM CONSIDERING CAPILLARY PRESSURE IN A CONFINED SPACE

A version of this chapter has been published in *Chemical Engineering Science*.

Abstract

Tight/shale reservoirs are extensively containing nanopores, and the confined space in nanopores can greatly alter the phase behavior of reservoir fluids due to the strong capillarity effect. Many researches have been recently conducted to investigate the effect of capillary pressure in nanopores on altering the oleic-vapor two-phase equilibria. Few attempts have been made to describe the effect of capillarity on the aqueous-oleic-vapor three-phase equilibria. This work proposes a new algorithm for performing three-phase pressure-temperature (*P-T)* flash coupled with capillary effect. This algorithm considers two capillary pressures that exist across the two interfaces dividing the three phases in a nanopore. When describing the three-phase equilibria, two types of reservoir wettability are considered: water-wet formation and oil-wet formation. In each case, the distribution of the three phases in a nanopore is determined based on the spreading coefficient which refers to the spreading ability of an oleic phase over the spreading ability of an aqueous phase. Example calculations are conducted to show the robustness of the new algorithm as well as to study the effect of capillarity on the three-phase equilibria. Computation results show that the three-phase *P-T* envelope for a given hydrocarbons/water mixture in a nanopore can be significantly altered by capillary pressure, but how the envelope moves will depend on the wettability of the nanopore and the spreading coefficient. The general trend is that both the upper branch (i.e., the oleic-aqueous/vapor-oleic-aqueous boundary) and the lower branch (i.e., the liquid-vapor/liquid-liquid-vapor boundary) of the three-phase envelope tend to move downward. Compared to the water-wet case, the oil-wet nanopore will shift the three-phase boundaries to a much larger degree. In addition to the alteration of the three-phase envelope, the presence of capillarity will also lead to the alteration of the phase fractions and phase compositions in the nanopore.

Keywords: Three-phase flash, *P-T* flash, Capillary pressure, Unconventional reservoir, Phase behavior

3.1. Introduction

Tight/shale reservoirs start to contribute more oil/gas productions in the last several decades. Such reservoirs share a common feature: abundance in nano-scale pores. For example, the nanopores in shale reservoirs have diameters ranging between 5 to 1000 nm (Wang *et al*., 2009; Loucks *et al.*, 2009). The capillary pressure, which is generally neglected in conventional reservoir modeling, could be large enough in the nano-scale pores to pose a noticeable impact on the adsorption behavior (Ping *et al*., 1996; Jin and Firoozabadi, 2016), phase behavior (Brusllovsky, 1992; Al-Rub and Datta, 1999; Nojabaei *et al.*, 2013; Wu *et al*., 2016) and flow dynamics of reservoirs fluids (van Dijke *et al.*, 2001; Hustad and Browning, 2010; Moortgat and Firoozabadi, 2013; Wang *et al.*, 2013; Dong, 2014).

Two-phase flash coupled with capillary-pressure effect has been studied extensively in the past years. One of the early contributions is from Brusllovsky (1992); a new equation of state (EOS) was developed in this paper to predict thermodynamic properties of pure substances and mixtures under the impact of capillary pressure. The author also mathematically proved that, under a large capillary pressure, the bubble point pressure will decrease but the dew point pressure will increase. Al-Rub and Datta (1999) proposed a semi-analytical model to study the effect of surface tension of a binary mixture on its phase behavior and confirmed that the vapor-liquid equilibria are altered due to the capillarity effect. Some recent works also echo this finding (Hamada *et al.,* 2007; Qi *et al.,* 2007; Pang *et al.,* 2012; Wang *et al.,* 2013; Sandoval *et al.*, 2015). In addition, Firincioglu *et al.* (2012) studied the effect of both capillary pressure and surface force on the fluid phase behavior. The surface force here refers to the van der Waals attractive force between a solid surface and the fluid molecules. They concluded that the surface force has an insignificant effect on the two-phase equilibria, while capillary pressure can pose a significant effect. Note that other forces, in addition

to the van der Waals force, might also pose effects on the phase equilibria in confined space; but, to our knowledge, no study has explicitly touched on this subject. They also analyzed how a gas bubble appears in a liquid phase confined in a pore and summarized that the diameter of the pore must be larger than 38 nm to reach a vapor-liquid equilibrium if a gas bubble with a size of 1 nm is formed in the liquid phase (Firincioglu *et al.*, 2012). Nojabaei *et al.* (2013) studied the effect of capillary pressure on the possible shifting of the entire two-phase envelope. They showed that the dew point pressure decreases when bulk pressure is lower than the cricondentherm point, while the dew point pressure is increased when bulk pressure is higher than the cricondentherm point due to the capillary pressure. The critical point is not shifted since the IFT at the critical point is zero. Jin and Firoozabadi (2016) included the effect of the surface adsorption into their study of hydrocarbon phase behavior in the shale reservoirs. They observed a shift of the two-phase boundaries due to the capillarity effect and the surface adsorption. They also concluded that the effect of the surface adsorption on hydrocarbon phase behavior can be neglected when the pore radius is larger than 10 nm. Zhang *et al.* (2016) examined the effect of pore radius on the two-phase flash results and concluded that for pores larger than 50 nm, the capillary effect is insignificant.

So far, most of the previous researches mainly focus on the capillary effect on two-phase equilibrium. However, water production is prevalent in many tight/shale reservoirs (Wong *et al.,* 2000; Li *et al.,* 2008; Iwere *et al.,* 2012; Li *et al.,* 2015). This implies that vapor-aqueous-oleic three-phase equilibria can readily occur under reservoir conditions. Several numerical simulation studies examined the effect of three-phase capillary pressure on actual oil production from tight/shale reservoirs (van Dijke *et al.,* 2001; Hustad and Browning, 2010; Moortgat and Firoozabadi, 2013; Dong, 2014). Their results show that, in general, the large capillary pressures

between vapor, aqueous and oleic phases reduce the oil recovery in oil-wet reservoirs. Yet, the above researches only incorporated the three-phase capillary pressure into the solving of the transport equations, and did not consider it during the process of calculating three-phase equilibria. In tight/shale reservoirs, three-phase equilibria in nano-scale pores could be significantly affected by the large capillary pressures existing among the three phases. This will alter the fugacity equality conditions governing the multiphase equilibria, hence rendering the three-phase equilibria different from the conventional ones without the capillarity effect. Thus, the shifting of three-phase equilibria themselves due to capillary pressure should also be considered when conducting reservoir simulation study for tight/shale reservoirs.

Recently, several studies touched on the effect of capillary pressure on three-phase equilibria in nano pores. Siripatrachai *et al.* (2017) modified negative flash algorithm to calculate vapor-oleic phase equilibria with the presence of an aqueous phase. Although the effect of aqueous phase on vapor-oleic capillary pressure is addressed, only vapor-oleic capillary pressure is considered when they were conducting the fugacity equality calculation. Their simulation results showed that the oil production is increased due to capillary pressure (Siripatrachai *et al.,* 2017); this is expected since the reservoir studied in this publication is water-wet. Later, to study the vapor-oleic equilibria in presence of connate water in tight/shale reservoirs, Neshat *et al.* (2018) considered the connate water saturation in the equation used for calculating the capillary pressure between vapor and oleic phases. The presence of connate water tends to reduce the vapor-oleic capillary pressure. The dew point and bubble point pressure are thereby affected to a lesser extent by capillary pressure (Neshat *et al.,* 2018). However, when performing phase equilibria calculations for water/hydrocarbon mixtures under actual reservoir conditions, the aqueous phase should be considered in conjunction with the vapor phase and liquid phase, as water may possess a sufficiently high fugacity to affect

the actual phase equilibria, in particular, at higher temperature conditions. Neglecting this may result in inaccurate prediction of the actual vapor-aqueous-oleic three-phase equilibria in the pore space (Li and Li, 2018; Pang and Li, 2017).

When a three-phase equilibrium is reached in a nanopore, capillary pressure exists between every two contacting phases. Three capillary pressures should be considered but the possible fluid distribution in a nanopore shows that only two of them could coexist at the same time (Øren *et al.,* 1992; Øren and Pinczewski, 1994; Kantzas *et al.,* 1998). Without considering the effect of the two capillary pressures, the three-phase split calculation will yield inaccurate estimation of the phase fractions and phase composition in the confined space. With the presence of capillary pressures, the phase pressure is no longer equal to each other. The fugacity equality conditions should be modified to simultaneously consider the two capillary pressures during three-phase equilibria calculations. Neshat et al. (2018) studied three-phase equilibrium calculation in tight reservoirs with two coexisting capillary pressure and they concluded that without considering the capillary pressure, the predicted cumulated gas production could present an error of 10%. Although the model they used in calculating capillary pressure is applicable in any wettability situation, only one possible fluid distribution is considered. Failing to consider all possible fluid distribution could weaken the universality of the findings because the pressure of each phase under the effect of capillary pressure directly depends on fluid distribution. It is thereby of great importance to develop a new three-phase flash algorithm that takes into account the effect of two coexisting capillary pressure on the three-phase vapor-oleic-aqueous equilibria in a confined pore space.

In this work, we propose a new three-phase flash algorithm to couple the capillarity effect with conventional three-phase flash algorithm. For practical purposes, the effects of the surface force (van der Waals force, electrostatic force, and hydrogen bonding force), molecule-wall interaction,

and adsorption effect are not included in the present study. The novelty of the new algorithm lies in that two capillary pressures are considered simultaneously based on fluid distribution in the conventional three-phase equilibria calculations. We first present the fundamental equations used in the new algorithm and then provide the procedure of conducting three-phase equilibria calculations under the influence of the two capillary pressures. The new algorithm is tested on four fluid mixtures to evaluate its performance and robustness. The effect of two coexisting capillary pressures on the three-phase equilibria is studied in detail.

3.2. Theoretical Approaches

Pore surface wettability is a crucial parameter to be considered while studying the phase behavior of reservoir fluids and their flow behavior in a nanopore. Wu *et al*. (2017) proposed a model to calculate water flow in a confined space. This model considered both pore surface wettability and pore dimensions. They found that the water flow capacity in a confined space is decreased in a hydrophilic pore and is increased in a hydrophobic pore. Wu *et al*. (2018) came to a similar conclusion by studying water flow in a confined space with different surface wettability under various temperatures. This work focuses on the phase behavior of a three-phase fluid in a nanopore which corresponds to three-phase equilibria in a confined space. Three-phase equilibria in a confined space have a more complicated fluid distribution compared to two-phase equilibria. The distribution of different phases, which mainly depends on pore surface wettability, determines the pressure of each phase. When capillarity effect is sufficiently strong, the pressure of non-wetting phase is always larger than the pressure of wetting phase and the difference between these two pressures is corresponding to the capillary pressure.

Two capillary pressures simultaneously exist in a three-phase equilibrium in a confined space, and wettability-dependent phase distribution should be considered in determining the actual three-phase equilibrium. In a tight/shale reservoir, although pores that contain the organic matters are mostly oil-wet, there are also some water-wet pores which are made of water-wet minerals (such as clays) (Passey *et al*., 2010). Therefore, it is necessary to model both water-wet and oil-wet scenarios in this work. Moreover, each wetting condition can be further classified to be spreading case and non-spreading case according to the spreading coefficient (Kantzas *et al*., 1998). When a vapor phase, a wetting liquid phase, and a non-wetting liquid phase coexist, there exist two possible types of phase distributions (See **Fig. 3-1**). In **Fig. 3-1 (a)**, a wetting liquid phase and a vapor phase are separated by a non-wetting liquid phase, while a wetting liquid phase occupies the corner. The other possible phase distribution is shown in **Fig. 3-1 (b)**, where a non-wetting liquid phase and a vapor phase stay separate, but inside a wetting liquid phase.

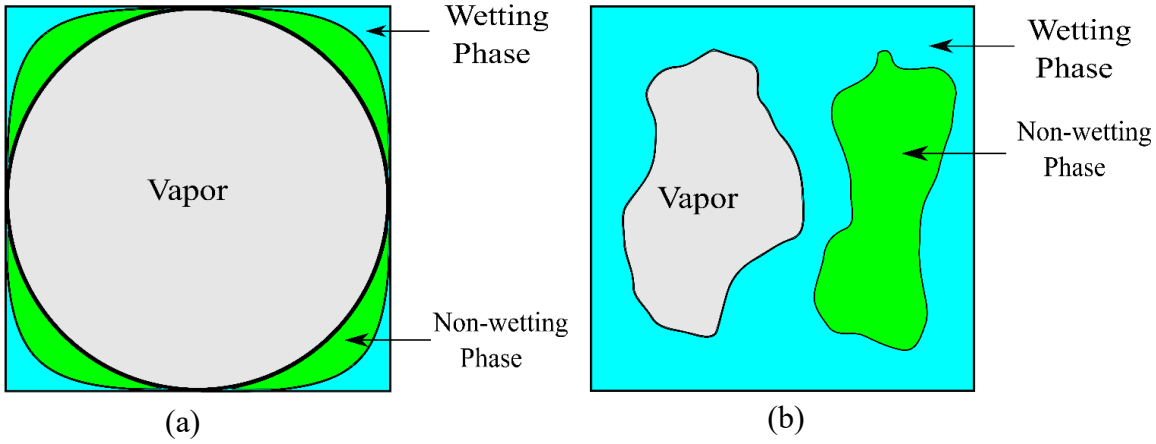

Fig. 3-1. Three-phase fluid distributions in a pore space when spreading coefficient is (a) positive and (b) negative (Adapted from Kantzas *et al*., 1998).

Spreading coefficient can be used to determine which type of phase distribution exists at certain pressure and temperature. In a water-wet formation, aqueous phase is the wetting liquid phase,

while oleic phase is the non-wetting liquid phase. Spreading coefficient in the water-wet formation is defined as the spreading ability of the oleic phase over the spreading ability of the aqueous phase. The equation used to calculate the spreading coefficient is given as (Kantzas *et al*., 1998),

$$S = \sigma_{wg} - (\sigma_{og} + \sigma_{wo}) \tag{3-1}$$

where S is the spreading coefficient, σ_{wg} is the aqueous-vapor IFT, σ_{og} is the oleic-vapor IFT, and σ_{wo} is the aqueous-oleic IFT. When the spreading coefficient is positive, the oleic phase spreads more extensively than the aqueous phase; this corresponds to the phase distribution as shown in Fig. 1(a). When the spreading coefficient is negative, the oleic phase spreads less extensively than the aqueous phase; this corresponds to the phase distribution as shown in Fig. 1(b) (Øren *et al*., 1992, Kantzas *et al*., 1998).

In a capillary tube, a given combination of wettability and spreading coefficient may generate a given type of three-phase fluid distribution. **Fig. 3-2** summarizes six types of possible fluid distributions in a 1D capillary tube: (a) A positive spreading coefficient in a water-wet formation; (b) A negative spreading coefficient in a water-wet formation; (c) A positive spreading coefficient in an oil-wet formation; (d) A negative spreading coefficient in an oil-wet formation; (e) Vapor-phase trapping in a water-wet formation; (f) Vapor-phase trapping in an oil-wet formation. In **Fig. 3-2**, the vapor phase is always assumed to be a non-wetting phase with zero contact angle.

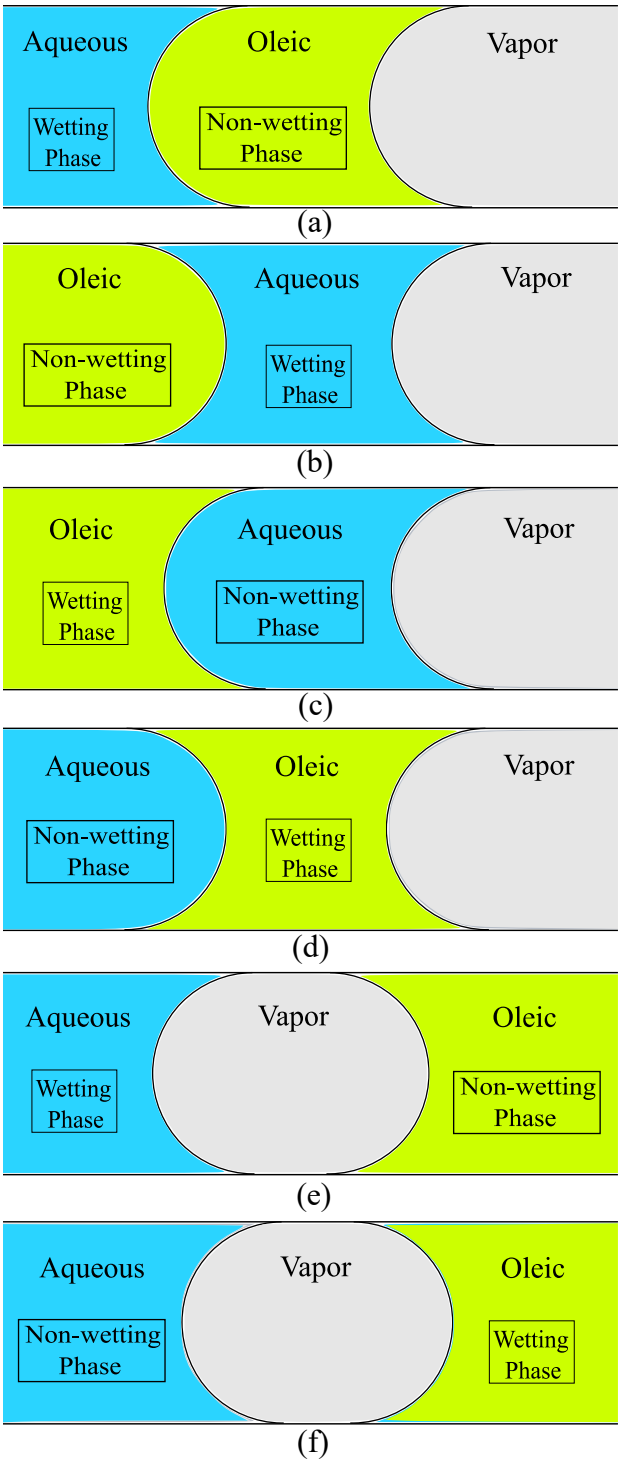

Fig. 3-2. Possible fluid distribution in a confined pore considering capillary pressure: (a) A positive spreading coefficient in a water-wet formation; (b) A negative spreading coefficient in a water wet formation; (c) A positive spreading coefficient in an oil-wet formation; (d) A negative spreading coefficient in an oil-wet formation; (e) Vapor-phase trapping in a water-wet formation; (f) Vapor-phase trapping in an oil-wet formation.

As for the scenario shown in **Fig. 3-2(a)**, the pressures of different phases can be calculated as per,

$$\begin{cases} P_g - P_o = P_{cog} \\ P_o - P_w = P_{cwo} \end{cases} \tag{3-3}$$

where P_g is the vapor-phase pressure, P_w is the aqueous-phase pressure, P_o is the oleic-phase pressure, P_{cwg} is the capillary pressure between the aqueous phase and the vapor phase, P_{cog} is the capillary pressure between the oleic phase and the vapor phase, and P_{cwo} is the capillary pressure between the aqueous phase and the oleic phase.

As for the scenario shown in **Fig. 3-2(b)**, the pressures of different phases can be calculated as per,

$$\begin{cases} P_g - P_w = P_{cwg} \\ P_o - P_w = P_{cwo} \end{cases} \tag{3-4}$$

As for the scenario shown in **Fig. 3-2(c)**, the pressures of different phases can be calculated as per,

$$\begin{cases} P_g - P_w = P_{cwg} \\ P_w - P_o = P_{cwo} \end{cases} \tag{3-5}$$

As for the scenario shown in **Fig. 3-2(d)**, the pressures of different phases can be calculated as per,

$$\begin{cases} P_g - P_o = P_{cog} \\ P_w - P_o = P_{cwo} \end{cases} \tag{3-6}$$

As for the scenarios shown in **Fig. 3-2(e)**, the pressures of different phases can be calculated as per,

$$\begin{cases} P_g - P_w = P_{cwg} \\ P_g - P_o = P_{cog} \end{cases} \tag{3-7}$$

As for the scenario shown in **Fig. 3-2(f)**, the pressures of different phases can be calculated as per,

$$\begin{cases} P_g - P_o = P_{cog} \\ P_g - P_w = P_{cwg} \end{cases} \tag{3-8}$$

Fig. 3-2(e) and **Fig. 3-2(f)** represent vapor-phase trapping scenarios in a water-wet formation and an oil-wet formation, respectively. In the scenario of a water-wet formation shown in **Fig. 3-2(e)**, the vapor phase cannot flow through the aqueous phase and is thereby trapped in the middle (Green and Willhite, 1998). This can happen when the oleic-vapor capillary pressure is greater than the aqueous-vapor capillary pressure according to Eq. (3-7) (Green and Willhite, 1998). With the assumptions of equal principle curvature radii and zero contact angle when using the Young-Laplace equation (Young, 1805) to calculate capillary pressure, we can readily decide if vapor-phase trapping is possible in a water-wet formation by calculating the oleic-vapor IFT and the aqueous-vapor IFT: when the oleic-vapor IFT is greater than the aqueous-vapor IFT, the vapor-phase trapping can happen in a water-wet formation. In the case of an oil-wet formation shown in **Fig. 3-2(f)**, when the oleic-phase pressure is greater than the aqueous-phase pressure, the vapor phase could be trapped between the aqueous phase and the oleic phase. By examining Eq. (7) and the Young-Laplace equation (Young, 1805), it can be concluded that the vapor-phase trapping can happen in an oil-wet formation only when the aqueous-vapor IFT is greater than the oleic-vapor IFT (Green and Willhite, 1998).

3.3. Mathematical Formulations

To capture the three-phase equilibria as shown in **Fig. 3-2**, the two capillary pressures need to be considered in conjunction with the fugacity-equality conditions. Young-Laplace equation is used to calculate the capillary pressure between each two phases with the assumptions of equal principle curvature radii and zero contact angle (Young, 1805):

$$P_c = \frac{2\sigma}{r} \tag{3-9}$$

where P_c is capillary pressure, σ is IFT, and r is pore radius.

The IFT between each two phases is calculated with two different models. Weinaug-Katz model is used to calculate either the oleic-vapor IFT or the aqueous-vapor IFT (Weinaug and Katz 1943),

$$\sigma_{\mathrm{lg}} = [\sum_{i=1}^{N_c} P_{chi}(x_i \frac{\rho_l}{M_l} - y_i \frac{\rho_g}{M_g})]^4 \qquad i = 1, \ldots, N_c \tag{3-10}$$

where σ_{lg} is the liquid-vapor IFT, P_{chi} is the Parachor constant of each component, ρ_l and ρ_g are the density of liquid and vapor phases, M_l and M_g are the molecular weight of liquid and vapor phases, x_i and y_i are the mole fraction of each component in the liquid phase and the vapor phase, respectively.

The Weinaug-Katz model tends to be less accurate when used to calculate the aqueous-oleic IFT. Firoozabadi and Ramey (1988) analyzed a suite of measured aqueous-oleic IFT data and found the aqueous-oleic IFT should be a function of water density, oleic phase density, temperature, and oleic phase critical temperature, i.e.,

$$f(\sigma_{hw}) = (\frac{\sigma_{hw}^{0.25}}{\rho_w - \rho_h})(\frac{T}{T_{ch}})^{0.3125} \tag{3-11}$$

where σ_{hw} is the aqueous-oleic IFT, ρ_w and ρ_h are the density of water and liquid hydrocarbon, respectively, and T_{ch} is the critical temperature of the oleic phase. Based on the above relation,

Danesh (2007) developed the following aqueous-oleic IFT correlation that is applicable to hydrocarbons with carbon numbers less than or equal to 20,

$$\sigma_{hw} = 111(\rho_w - \rho_h)^{1.024}\left(\frac{T}{T_{ch}}\right)^{-1.25} \tag{3-12}$$

Eq. (3-12) is used in this work to calculate the IFT between aqueous phase and oleic phase. For mixtures, the following mixing rule is applied to calculate the critical temperature in a given phase,

$$T_{ch} = \sum_{i=1}^{N_c} x_i T_{ci} \qquad i = 1, \ldots, N_c \tag{3-13}$$

where T_{ci} is the critical temperature of the *i*th component in the oleic phase.

3.4. Numerical Implementation of Three-Phase P-T Flash Calculation Considering Capillary Pressures

The three-phase equilibrium is reached when the chemical potentials of each component in vapor, aqueous and oleic phase are equal to each other. Such chemical-potential-equality conditions can then be readily converted to fugacity-equality conditions. Typical three-phase flash algorithm contains an outer loop and an inner loop; the outer loop satisfies the fugacity-equality conditions, while the inner loop satisfies the Rachford-Rice relations (Rachford and Rice, 1952). The two capillary pressures existing in a three-phase equilibrium can be considered in the outer loop of the flash algorithm. Considering a mixture with N_c components, the three-phase equilibrium is reached at a given pressure P and a given temperature T when the chemical potentials of each component are equal across the aqueous, vapor, and oleic phases. The chemical-potential-equality condition is given as (Whitson and Brulé, 2000),

$$\mu_{ix} = \mu_{iy} = \mu_{iw} \qquad i = 1, \ldots, N_c \tag{3-14}$$

where μ_{ix} is the chemical potential of the *i*th component in oleic phase, μ_{iy} is the chemical potential of the *i*th component in vapor phase, and μ_{iw} is the chemical potential of the *i*th component in aqueous phase. Chemical-potential-equality condition is equivalent to the fugacity-equality condition as given below (Whitson and Brulé, 2000),

$$f_{ix} = f_{iy} = f_{iw} \qquad i = 1, \ldots, N_c \tag{3-15}$$

where f_{ix} is the fugacity of the *i*th component in oleic phase, f_{iy} is the fugacity of the *i*th component in vapor phase, and f_{iw} is the fugacity of the *i*th component in aqueous phase.

Peng-Robinson EOS is employed to calculate the fugacity of each component in each phase (Peng and Robinson 1976a),

$$ln\frac{f_i}{y_i P} = ln\,\phi_i = \frac{B_i}{B}(Z-1) - ln(Z-B) + \frac{A}{2\sqrt{2}B}\left(\frac{B_i}{B} - \frac{2}{A}\sum_{i=1}^{N_c} y_i A_{ij}\right) ln\left[\frac{Z+(1+\sqrt{2}B)}{Z-(1-\sqrt{2}B)}\right], i = 1, \ldots, N_c \tag{3-16}$$

where y_i represents the mole fraction of the *i*th component in any phase, P is the phase pressure, ϕ_i is the fugacity coefficient of the *i*th component, *Z* is the compressibility factor, *A* and *B* are EOS constants which can be calculated by (Peng and Robinson 1976a),

$$A = \sum_{i=1}^{N_c}\sum_{j=1}^{N_c} y_i y_j A_{ij} \qquad i = 1, \ldots, N_c \tag{3-17}$$

$$B = \sum_{i=1}^{N_c} y_i B_i \qquad i = 1, \ldots, N_c \tag{3-18}$$

where $A_{ij} = (1-k_{ij})\sqrt{A_i A_j}$ and k_{ij} is the binary interaction parameter (BIP). Eq. (3-19) is used to calculate the EOS constants of each component A_i and B_i (Peng and Robinson, 1976a).

$$\begin{cases} A_i = 0.45724R^2 \frac{T_{ci}^2}{P_{ci}}[1 + m_i(1 - \sqrt{\frac{T}{T_{ci}}})]^2 \\ B_i = 0.0778R \frac{T_{ci}^2}{P_{ci}} \end{cases} \qquad i = 1, \dots, N_c \qquad (3\text{-}19)$$

where R is the universal gas constant, T_{ci} is the critical temperature of the *i*th component, P_{ci} is the critical pressure of the *i*th component, and $m_i = 0.37464 + 1.54226\omega_i - 0.26992\omega_i^2$ (where ω_i is the acentric factor of the ith component). When ω_i is larger than 0.49, m_i is calculated as $m_i = 0.3796 + 1.485\omega_i - 0.1644\omega_i^2 + 0.01667\omega_i^3$ (Robinson and Peng, 1978).

Consideration of capillary pressure leads to that the pressures of the three phases are different. The following gives the fugacity of the *i*th component in oleic phase,

$$ln\frac{f_i}{x_i P_o} = ln\,\phi_i = \frac{B_i}{B}(Z-1) - ln(Z-B) + \frac{A}{2\sqrt{2}B}(\frac{B_i}{B} - \frac{2}{A}\sum_{i=1}^{N_c} x_i A_{ij})\, ln[\frac{Z+(1+\sqrt{2}B)}{Z-(1-\sqrt{2}B)}], i = 1, \dots, N_c \quad (3\text{-}20)$$

The following gives the fugacity of the *i*th component in vapor phase,

$$ln\frac{f_i}{y_i P_g} = ln\,\phi_i = \frac{B_i}{B}(Z-1) - ln(Z-B) + \frac{A}{2\sqrt{2}B}(\frac{B_i}{B} - \frac{2}{A}\sum_{i=1}^{N_c} y_i A_{ij})\, ln[\frac{Z+(1+\sqrt{2}B)}{Z-(1-\sqrt{2}B)}], i = 1, \dots, N_c \quad (3\text{-}21)$$

The following gives the fugacity of the *i*th component in aqueous phase,

$$ln\frac{f_i}{w_i P_w} = ln\,\phi_i = \frac{B_i}{B}(Z-1) - ln(Z-B) + \frac{A}{2\sqrt{2}B}(\frac{B_i}{B} - \frac{2}{A}\sum_{i=1}^{N_c} w_i A_{ij})\, ln[\frac{Z+(1+\sqrt{2}B)}{Z-(1-\sqrt{2}B)}], i = 1, \dots, N_c \quad (3\text{-}22)$$

It is noted that the three phase pressures in Eqs. (3-20)-(3-22) can be related to each other based on the two capillary pressures. In order to start the three-phase equilibria calculation procedure,

phase equilibrium ratios (k_i) must be first initialized. Wilson equation (Wilson 1969) is used to initialize the phase equilibrium ratios for the non-water component and is given in Eq. (3-23).

$$k_i = \frac{P_{ci}}{P} exp[\,5.37(1+\omega_i)(1-\frac{T_{ci}}{T})],\ i \neq w \tag{3-23}$$

where k_i is the phase equilibrium ratios of the non-water component between any two phases, P_{ci} is the critical pressure of the *i*th non-water component, P is the system pressure, ω_i is the acentric factor of the *i*th non-water component, T_{ci} is the critical temperature of the *i*th non-water component, and T is the system temperature. To initialize the phase equilibrium ratios for the water component, the equation proposed by Peng and Robinson (1976b) is used and is given in Eq. (3-24).

$$k_w = \frac{P_{cw}}{P}\frac{T}{T_{cw}},\ i = w \tag{3-24}$$

where k_w is the phase equilibrium ratios of the water component between any two phases, P_{cw} is the critical pressure of water component, P is the system pressure, T_{cw} is the critical temperature of water component, and T is the system temperature.

The fugacity coefficient is related to k_i according to,

$$\begin{cases} ln\, k_{iy} = ln\, \phi_{ix} - ln\, \phi_{iy} \\ ln\, k_{iw} = ln\, \phi_{ix} - ln\, \phi_{iw} \end{cases} \qquad i = 1, \dots, N_c \tag{25}$$

where $k_{iy} = \frac{y_i}{x_i}$ is the vapor to oleic phase equilibrium ratio, and $k_{iw} = \frac{w_i}{x_i}$ is the aqueous to oleic phase equilibrium ratio. Based on material balance, we can obtain the following Rachford-Rice equation for a three-phase equilibrium (Rachford and Rice, 1952),

$$\begin{cases} \sum_{i=1}^{N_c}(y_i - x_i) = \sum_{i=1}^{N_c}[\frac{z_i(1-k_{iy})}{1+\beta_y(k_{iy}-1)+\beta_w(k_{iw}-1)}] = 0 \\ \sum_{i=1}^{N_c}(w_i - x_i) = \sum_{i=1}^{N_c}[\frac{z_i(1-k_{iw})}{1+\beta_y(k_{iy}-1)+\beta_w(k_{iw}-1)}] = 0 \end{cases} \quad i = 1, \dots, N_c \qquad (3\text{-}26)$$

where β_y and β_w are mole fractions of vapor phase and aqueous phase, respectively, z_i is the mole fraction of the *i*th component in the feed. Newton's method is employed to solve for the phase mole fractions. Within the Newton method, at the end of each iteration, the obtained results need to be checked for convergence and the following stopping criteria is used (Whitson and Brulé, 2000)

$$Err < 10^{-10} \qquad (3\text{-}27)$$

where $Err = max(\{|\Delta \ln k_{iy}|\}, \{|\Delta \ln k_{iw}|\}, |\Delta\beta_y|, |\Delta\beta_w|)$, $\Delta \ln k_{iy}$ represents the difference in the natural logarithm value of the vapor to oleic phase equilibrium ratios between the current iteration and the previous iteration. $\Delta \ln k_{iw}$ represents the difference in the natural logarithm value of the vapor to oleic phase equilibrium ratios between the current iteration and the previous iteration. $\Delta\beta_y$ represents the difference in the vapor phase mole fractions between the current iteration and the previous iteration. $\Delta\beta_w$ represents the difference in the aqueous phase mole fractions between the current iteration and the previous iteration.

If the calculated phase mole fractions do not satisfy the stopping criteria, the phase equilibrium ratios are updated based on the following formula (Whitson and Brulé, 2000),

$$\begin{cases} k_{iy}^{n+1} = k_{iy}^{n} \frac{f_{iy}^{n}}{f_{ix}^{n}} \\ k_{iw}^{n+1} = k_{iw}^{n} \frac{f_{iw}^{n}}{f_{ix}^{n}} \end{cases} \qquad i = 1, \dots, N_c \tag{3-28}$$

where n represents the current iteration and n+1 represents the next iteration. After the updating of phase equilibrium ratios, the phase mole fractions are again solved based on the updated phase equilibrium ratios. The convergence is checked again with the above criteria. The above steps are repeated until the convergence is reached.

The standard procedure of conducting three-phase flash calculation coupled with capillary pressure is summarized below:

Step 1. Input the necessary parameter values used for computation, including system pressure, system temperature, feed compositions, BIP, critical temperature, critical pressure, and acentric factor for each component;

Step 2. Use Eq. (3-23) (Wilson, 1969) to initialize vapor and aqueous phase equilibrium ratios for the non-water components and Eq. (3-24) (Peng and Robinson, 1976b) to initialize vapor and aqueous phase equilibrium ratios for water component;

Step 3. Solve the Rachford-Rice equations (Rachford and Rice, 1952) to obtain phase mole fractions using the Newton method;

Step 4. Update phase compositions (x_i, y_i, w_i);

Step 5. Calculate z factor from PR EOS (Peng and Robinson, 1976a);

Step 6. Update the two capillary pressures using Eqs. (3-9)-(3-13); update the fugacity using Eqs. (3-16)-(3-22); update the phase equilibrium ratios using Eq. (3-28); and update the phase mole fractions using Eq. (3-26);

Step 7. Check convergence: if convergence is reached, then output the phase mole fractions and compositions; if convergence is not reached, repeat from Step 3 using the updated phase equilibrium ratios until convergence is reached.

A flowchart is provided in **Fig. 3-3** to describe the above three-phase flash calculation procedure coupled with capillary pressures.

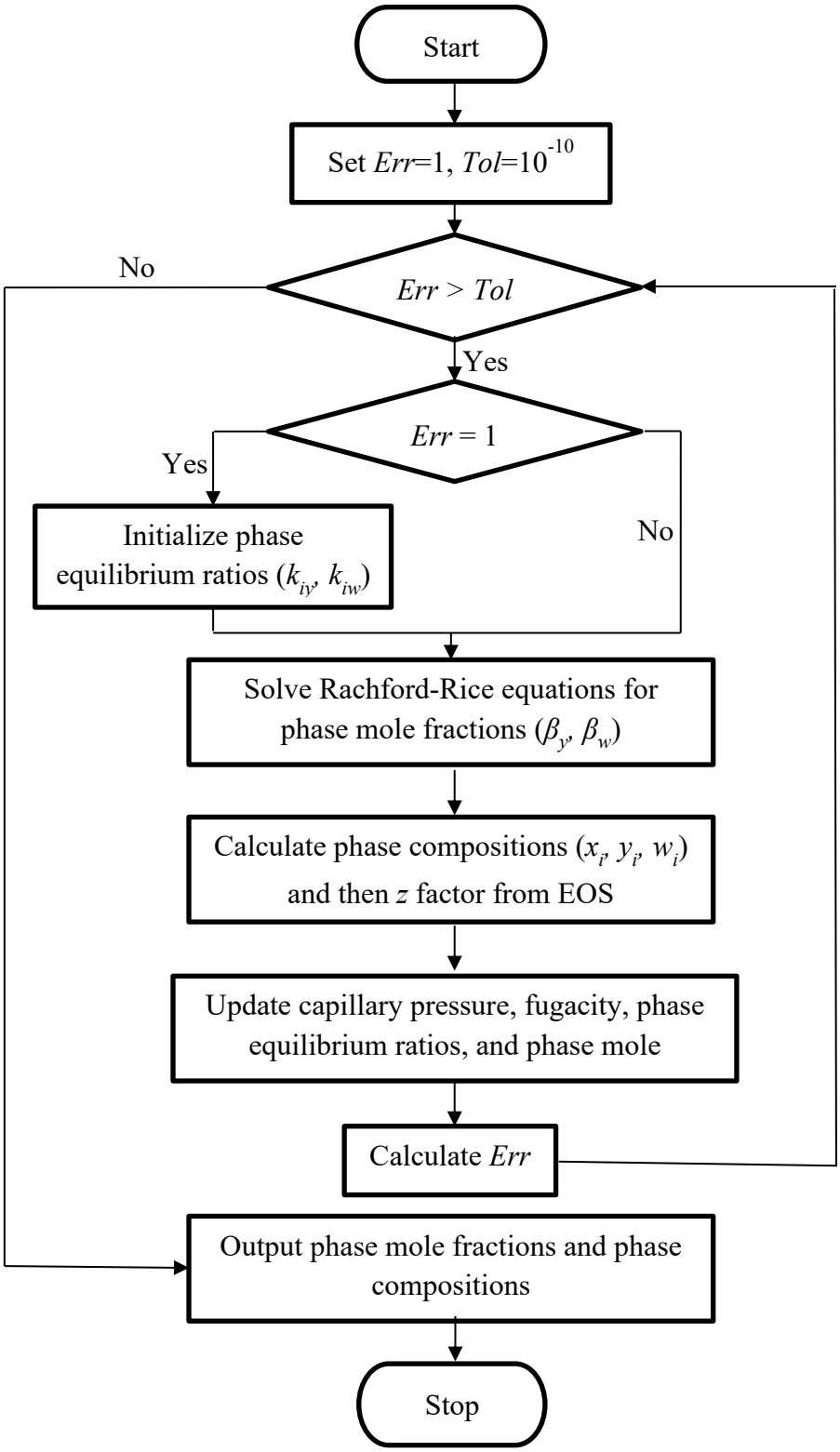

Fig. 3-3. Flowchart showing the procedure used for conducting three-phase flash calculation coupled with capillary pressure.

3.5. Summary of Examples

Three-phase flash calculations are conducted on four fluid mixtures to examine the performance and robustness of the new algorithm. What is used in the first example (Example #1) is a fluid mixture consisting of water and four hydrocarbon pseudo-components (PC_1-PC_4). Its feed composition is (50 mol% H_2O, 15 mol% PC_1, 10 mol% PC_2, 10 mol% PC_3, 15 mol% PC_4). **Table 3-1** lists the properties of the components used in Example #1, while **Table 3-2** lists the BIP used in the EOS model. Phase envelopes are calculated for this mixture. Sensitivity analysis is also conducted to investigate the effect of pore radius on capillary-pressure induced alteration of the mixture's phase behavior. The second example (Example #2) is a mixture containing H_2O, N_2, C_{10}, and C_{20} and has a feed composition of (55 mol% H_2O, 10 mol% N_2, 10 mol% C_{10}, 25 mol% C_{20}). **Table 3-3** lists the properties of the components used in Example #2, while **Table 3-4** lists the BIP used in the EOS model. Through this example, the effect of capillary pressure on three-phase equilibria is studied when the spreading coefficient switches from being positive to being negative under high pressure/temperature conditions.

Table 3-1. Component properties of fluid mixture used in Example #1 (Luo and Barrufet, 2005).

Component	T_c, K	P_c, bar	ω	MW, g/mol	P_{chi}
H_2O	647.3	220.89	0.344	18.015	52
PC_1	305.586	48.82	0.098	30	108
PC_2	638.889	19.65	0.535	156	415.87
PC_3	788.889	10.2	0.891	310	742.23
PC_4	838.889	7.72	1.085	400	847.9

*T_c is the critical temperature, P_c is the critical pressure, ω is the acentric factor, MW is the molecular weight, P_{chi} is the Parachor of each component and its value for each component is from Quayle (1953), and PC_1 – PC_4 stand for the pseudo-components #1-4.

Table 3-2. BIP used in the EOS model for fluid mixture used in Example #1 (Luo and Barrufet, 2005).

BIP	H_2O	PC_1	PC_2	PC_3	PC_4
H_2O	0	0.7192	0.4598	0.2673	0.2417
PC_1	0.7192	0	0	0	0
PC_2	0.4598	0	0	0	0
PC_3	0.2673	0	0	0	0
PC_4	0.2417	0	0	0	0

Table 3-3. Component properties of Example #2 mixture (Lapene *et al*., 2010).

Component	T_c, *K*	P_c, bar	ω	*MW,* g/mol	P_{chi}
H_2O	647.3	220.89	0.344	18.015	52
N_2	126.2	34	0.04	28	41
C_{10}	622	25.3	0.443	134	381.9168
C_{20}	782	14.6	0.816	275	710.475

Table 3-4. BIP used in the EOS model for Example #2 mixture (Lapene *et al*., 2010).

BIP	H_2O	N_2	C_{10}	C_{20}
H_2O	0	0.4778	0.4598	0.2673
N_2	0.4778	0	0	0
C_{10}	0.5000	0	0	0
C_{20}	0.5000	0	0	0

The third example (Example #3) is a ternary mixture containing H_2O, C_4, and C_{20}. It is observed in this example that the upper critical end point is shifted due to the presence of capillary pressure. The last example (Example #4) has the same components as Example #3, but with different feed compositions. The feed composition of the mixture used in Example #3 is (80 mol% H_2O, 16 mol% C_4, 4 mol% C_{20}), and the feed composition of the mixture used in Example #4 is (30 mol% H_2O, 30 mol% C_4, 40 mol% C_{20}). **Table 3-5** lists the properties of the components used in Examples #3 and #4, while **Table 3-6** lists the BIP used in the EOS model.

Table 3-5. Component properties of fluid mixture used in Examples #3 & #4 (Li and Li, 2017)

Component	T_c, K	P_c, bar	ω	MW, g/mol	P_{chi}
H_2O	647.3	220.89	0.344	18.015	52
C_4	425.2	38	0.1928	58.124	189.9
C_{20}	782	14.6	0.816	275	710.475

Table 3-6. BIP used in the EOS model for Example #3 and Example #4 mixtures (Li and Li, 2017).

BIP	H_2O	C_4	C_{20}
H_2O	0	0.5	0.5
C_4	0.5	0	0
C_{20}	0.5	0	0

3.6.Results and Discussion

Three-phase envelope with and without the effect of capillary pressure has been computed for each mixture listed above. Effect of capillary pressure on the phase mole fractions and effect of pore radius on the alteration of three-phase equilibria are also presented to analyze the effect of capillarity on phase equilibria.

3.6.1. Cross-Validation with PVTsim

To confirm the correctness and robustness of our own code, we first compare the three-phase envelopes (without considering the effect of capillary pressure) that are calculated with our three-phase flash code and with the commercial software PVTsim. **Fig. 3-4** shows the comparison results, which demonstrates that the three-phase envelopes calculated from our algorithm for all the four examples are in an excellent agreement with those calculated from PVTsim software. These results verify the reliability of our own code.

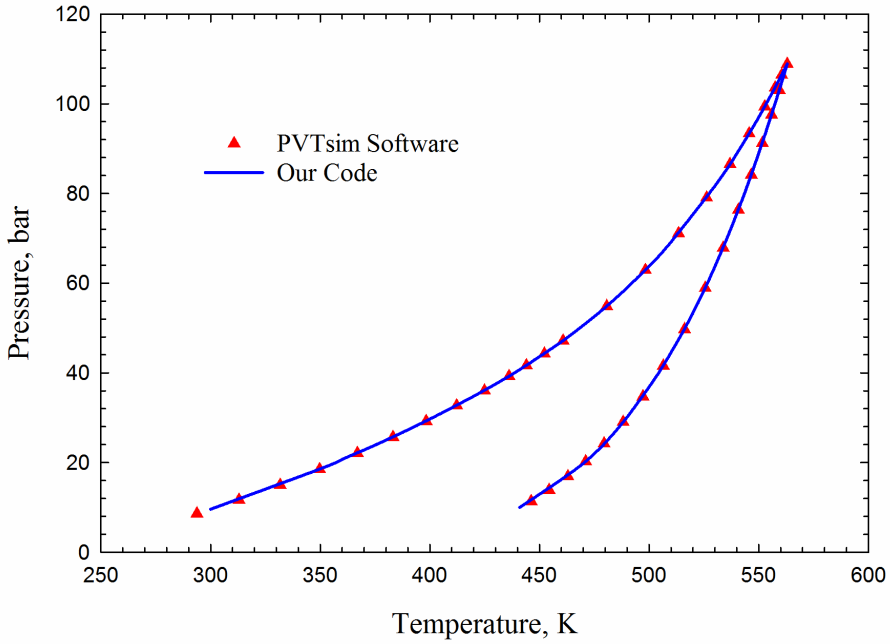
PVTsim Software
Our Code
Pressure, bar
Temperature, K
0
20
40
60
80
100
120
250
300
350
400
450
500
550
600

(a)

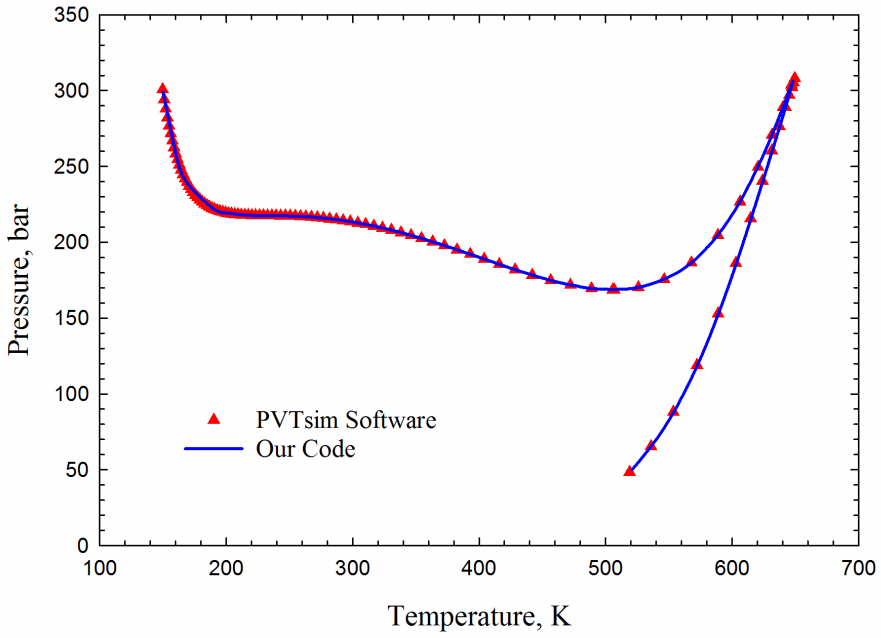
PVTsim Software
Our Code
Pressure, bar
Temperature, K
0
50
100
150
200
250
300
350
100
200
300
400
500
600
700

(b)

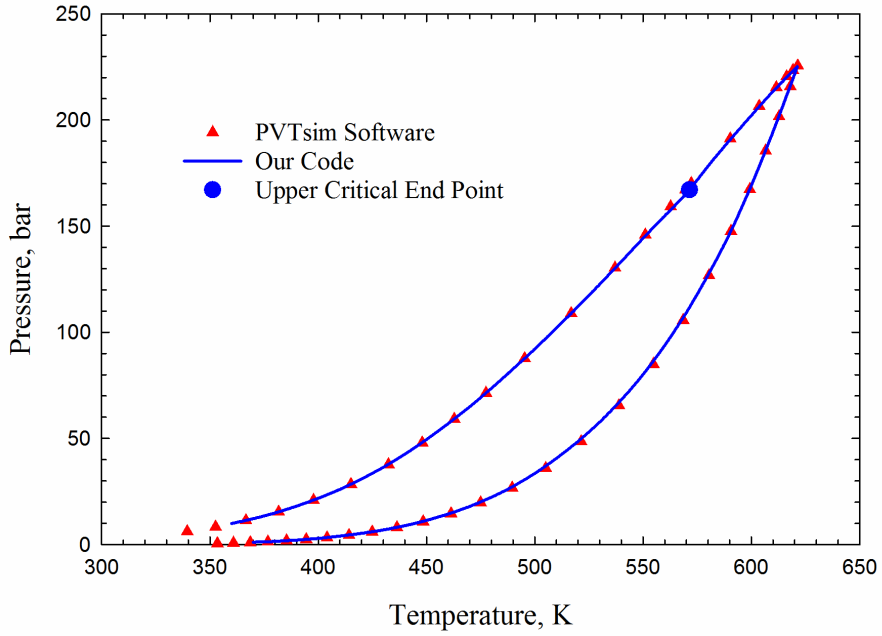

(c)

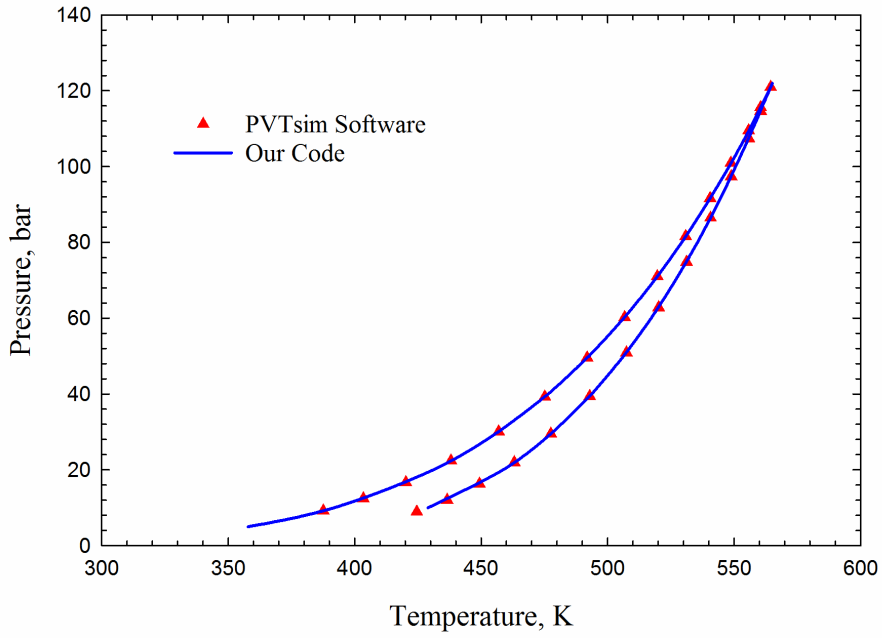

(d)

Fig. 3-4. Comparison of three-phase boundaries calculated from our code and PVTsim: (a) Example #1 (50 mol% H_2O, 15 mol% PC_1, 10 mol% PC_2, 10 mol% PC_3, 25 mol% PC_4); (b) Example #2 (55 mol% H_2O, 10 mol% N_2, 10 mol% C_{10}, 25 mol% C_{20}); (c) Example #3 (80 mol% H_2O, 16 mol% C_4, 4 mol% C_{20}); (d) Example #4 (30 mol% H_2O, 30 mol% C_4, 40 mol% C_{20}).

3.6.2. Example #1 – Mixture of H_2O-PC_1-PC_2-PC_3-PC_4

The mixture examined in the first example (Example #1) contains water and four hydrocarbon pseudo-components. **Fig. 3-5** shows the phase envelope calculated for this mixture, which includes both three-phase and two-phase boundaries. In this study, we focus on the shift of the three-phase boundaries and the upper critical end point caused by capillary pressure. In this example (Example #1), the shift of the three-phase boundaries is presented later. The upper critical end point, however, does not exist for this example (Example #1). Only an oleic-vapor critical point can be found on the two-phase boundary, but this critical point is not shifted by capillary pressure because the oleic-vapor capillary pressure vanishes at the critical point.

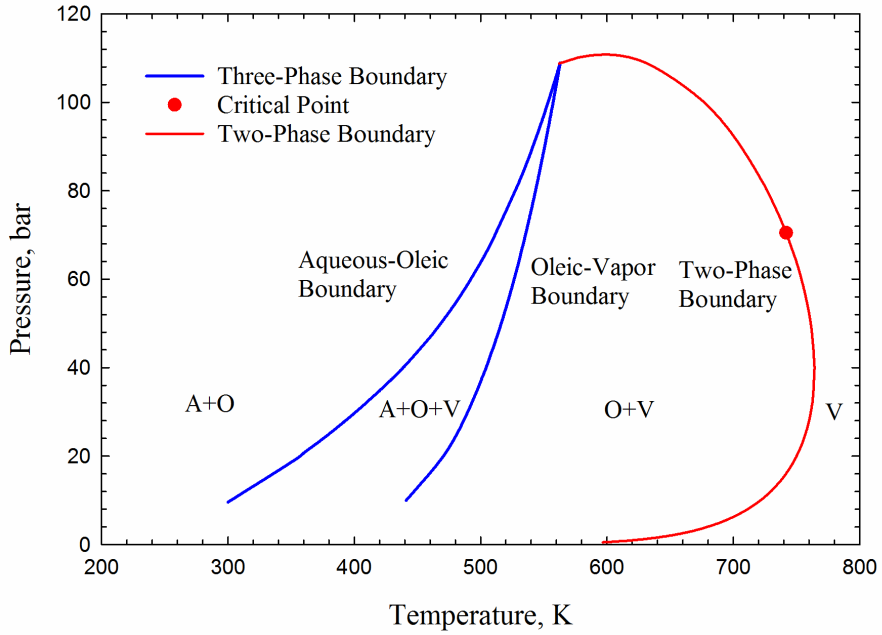

Fig. 3-5. Phase diagram calculated for Example #1 mixture showing both three-phase and two-phase boundaries.

Fig. 3-6 shows the three-phase envelopes in both water-wet and oil-wet formations considering the capillarity effect. The pore radius used in this practice is 10 nm. Zoomed views of tips of the three-phase envelopes are provided in **Fig. 3-7** for a clearer look in the high-pressure region.

Throughout the entire three-phase envelopes shown in **Fig. 3-6**, the spreading coefficient is constantly greater than zero. Thus, the aqueous phase and the vapor phase are always separated by the oleic phase. It is clear that the boundaries are affected to a larger extent in the low-pressure region. In the high-pressure region, the capillary pressure leads to less deviation from the conventional three-phase envelope. Also, in the oil-wet formation, the capillary effect alters the three-phase envelope more significantly than in the water-wet formation. Given that the porous medium that contains organic matters in shale reservoirs is mostly oil-wet, the alteration of the three-phase equilibria could occur extensively in tight/shale reservoirs. Nevertheless, the alteration follows the same trend regardless of the formation wetting condition: there is an apparent decrease in the three-phase boundary pressure at a fixed temperature. The maximum pressure and temperature of the three-phase envelope are both reduced due to capillarity. **Fig. 3-8** shows the changes in the phase mole fractions under isobaric and isothermal conditions. At a given temperature and pressure within the three-phase region, the capillary pressure leads to higher fractions of the aqueous and oleic phases but a lower fraction of the vapor phase. Such trend remains the same for both water-wet and oil-wet formations.

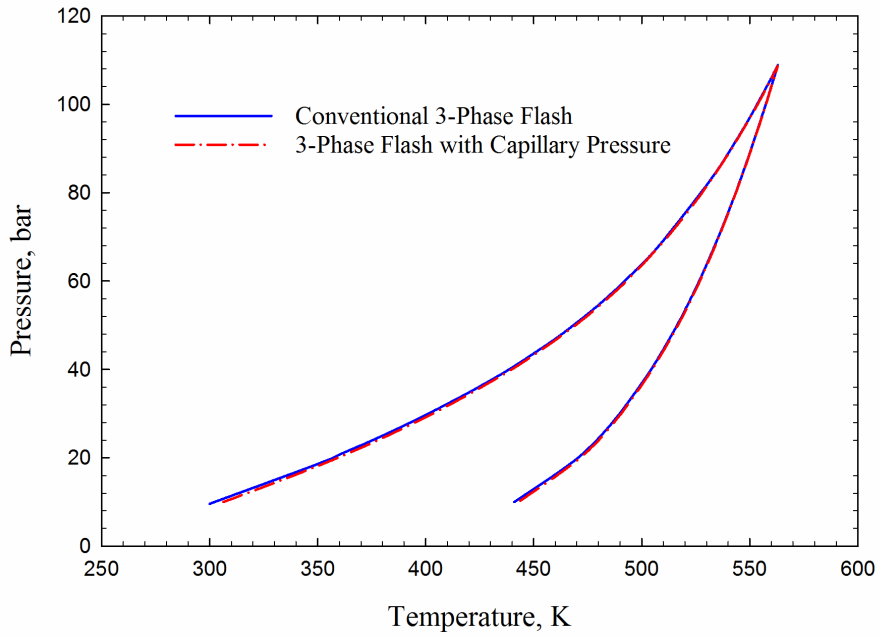

(a)

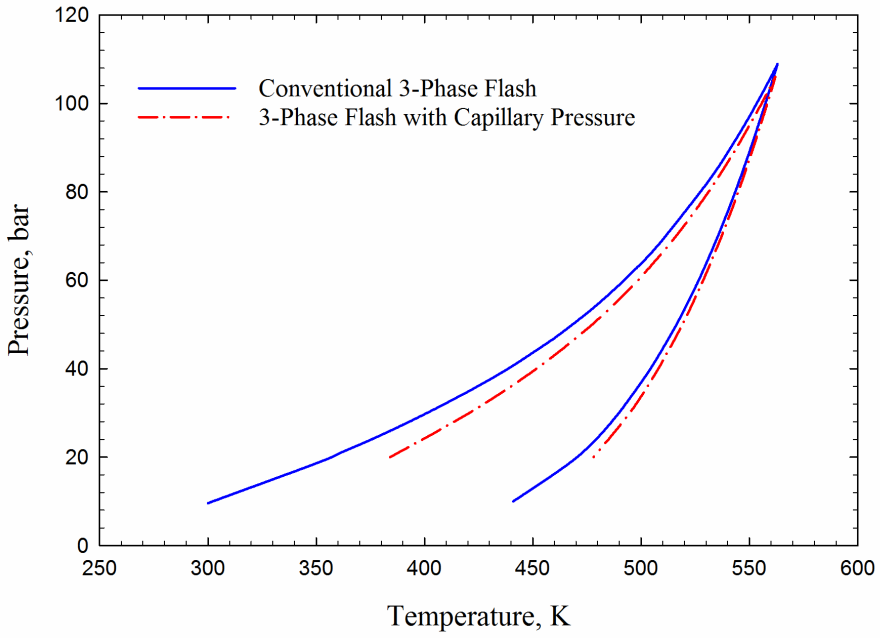

(b)

Fig. 3-6. Three-phase diagrams calculated for Example #1 mixture considering capillary pressure effect in (a) a water-wet formation and (b) an oil-wet formation with a pore radius of 10 nm.

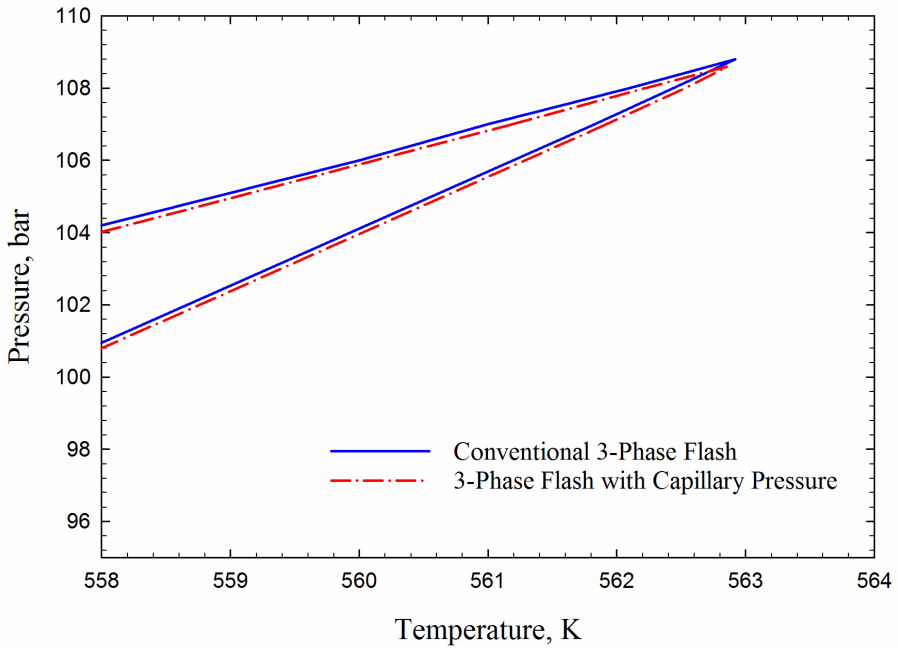

(a)

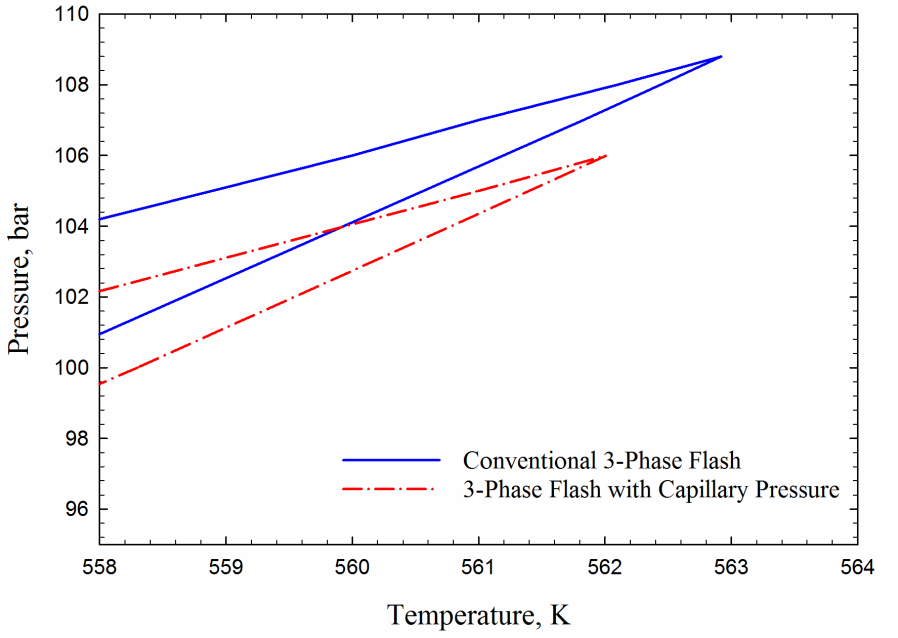

(b)

Fig. 3-7. Zoomed views of the three-phase diagrams calculated for Example #1 mixture considering capillary pressure effect in (a) a water-wet formation and (b) an oil-wet formation with a pore radius of 10 nm.

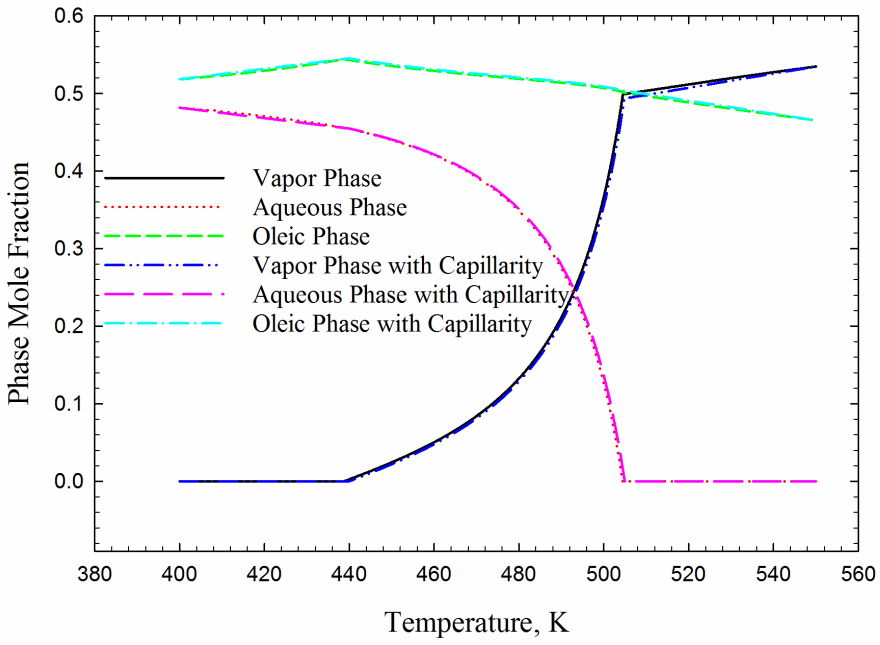
Phase Mole Fraction
Temperature, K
Vapor Phase
Aqueous Phase
Oleic Phase
Vapor Phase with Capillarity
Aqueous Phase with Capillarity
Oleic Phase with Capillarity
0.0
0.1
0.2
0.3
0.4
0.5
0.6
380
400
420
440
460
480
500
520
540
560

(a)

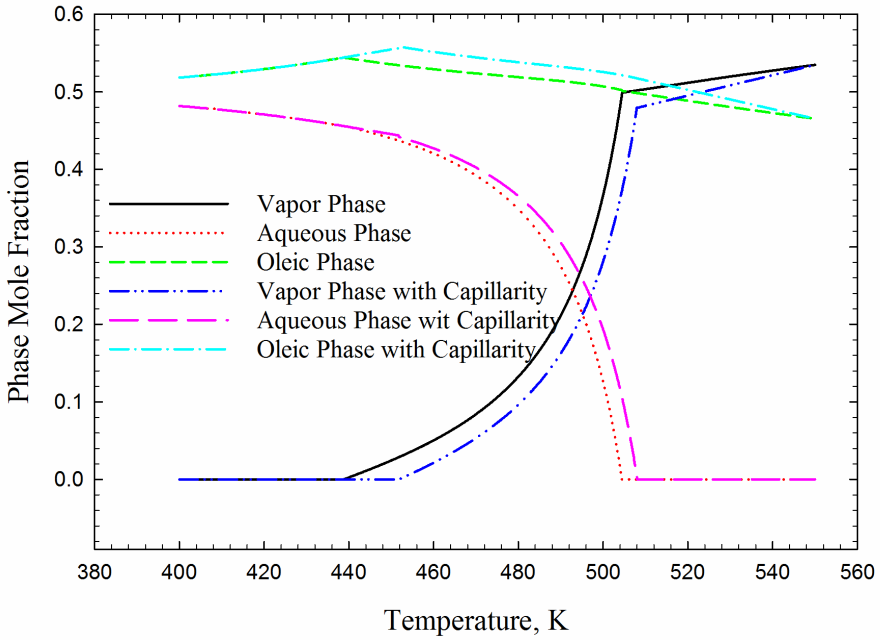
Phase Mole Fraction
Temperature, K
Vapor Phase
Aqueous Phase
Oleic Phase
Vapor Phase with Capillarity
Aqueous Phase wit Capillarity
Oleic Phase with Capillarity
0.0
0.1
0.2
0.3
0.4
0.5
0.6
380
400
420
440
460
480
500
520
540
560

(b)

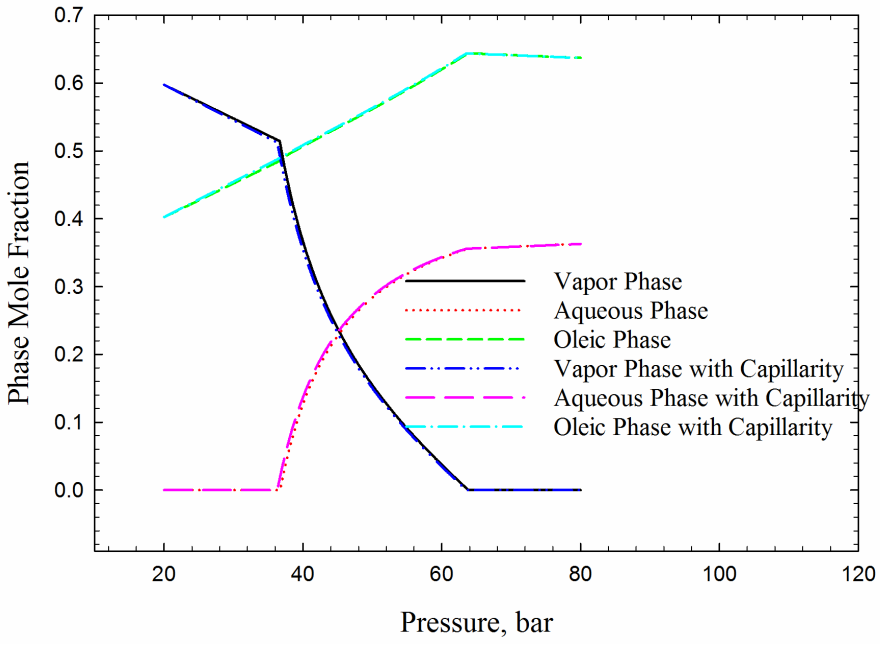

(c)

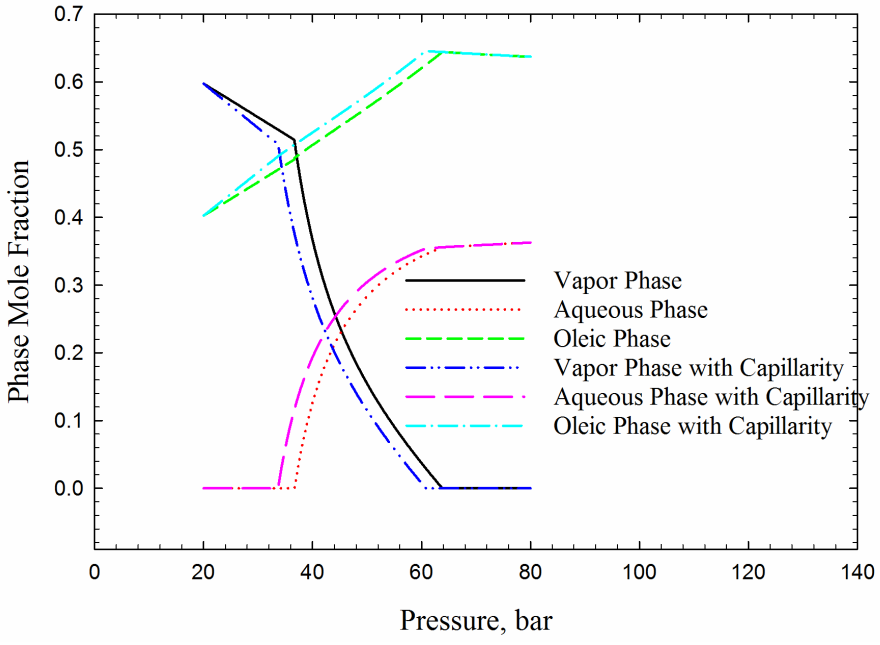

(d)

Fig. 3-8. Phase mole fractions curves calculated for Example #1 mixture considering capillary pressure under isobaric condition (P=40 bar) in (a) a water-wet formation and (b) an oil-wet formation and under isothermal condition (T=500 K) in (c) a water-wet formation and (d) an oil-wet formation.

Note that the aqueous-vapor IFT is always larger than the oleic-vapor IFT throughout the computations made for this mixture. Therefore, it is possible to have the vapor-phase trapping scenario in oil-wet formations. This phenomenon is most likely to occur when an aqueous-oleic two-phase equilibrium switches to a three-phase equilibrium, and a vapor phase suddenly appears. **Fig. 3-9 (a)** shows the shifted three-phase boundary in the case of vapor-phase trapping in oil-wet formations. It can be seen from **Fig. 3-9 (a)** that both the upper and lower three-phase boundaries are shifted away from the original ones to the lower right part of the diagram. A zoomed view (**Fig. 3-9 (b)**) reveals that the tip of the three-phase envelope also shifts to the lower right part of the diagram. **Fig. 3-10** shows the phase mole fractions curves calculated for Example #1 mixture under isobaric and isothermal conditions. As shown in **Fig. 3-10**, at a given pressure and temperature, the fraction of vapor phase is decreased, while the fractions of aqueous and oleic phases are increased due to the presence of capillary pressure. This trend is shown in **Fig. 3-8**. Furthermore, in an oil-wet formation, the three-phase envelope is altered by capillary pressure to a lesser extent when the vapor-phase trapping occurs in a pore space, compared to the case without vapor-phase trapping.

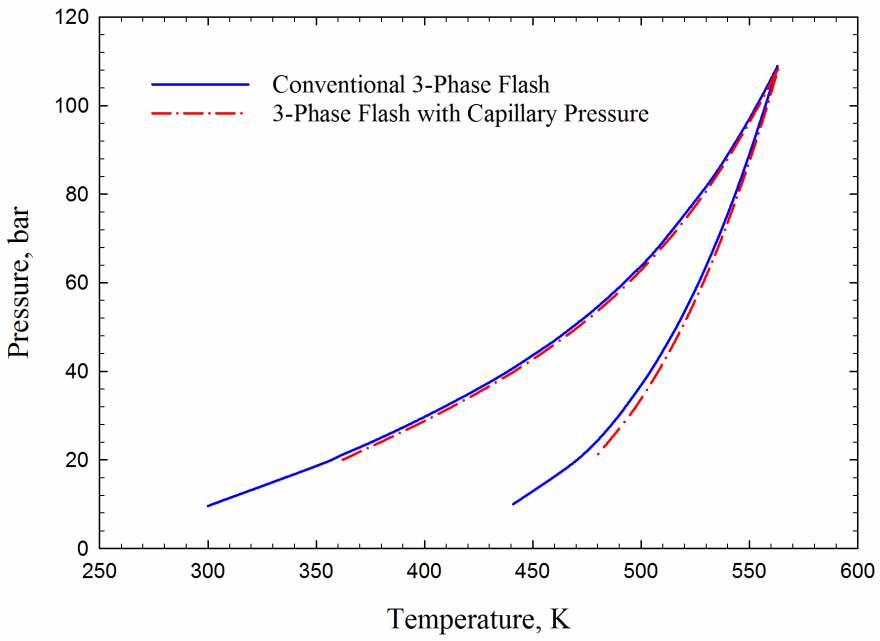

(a)

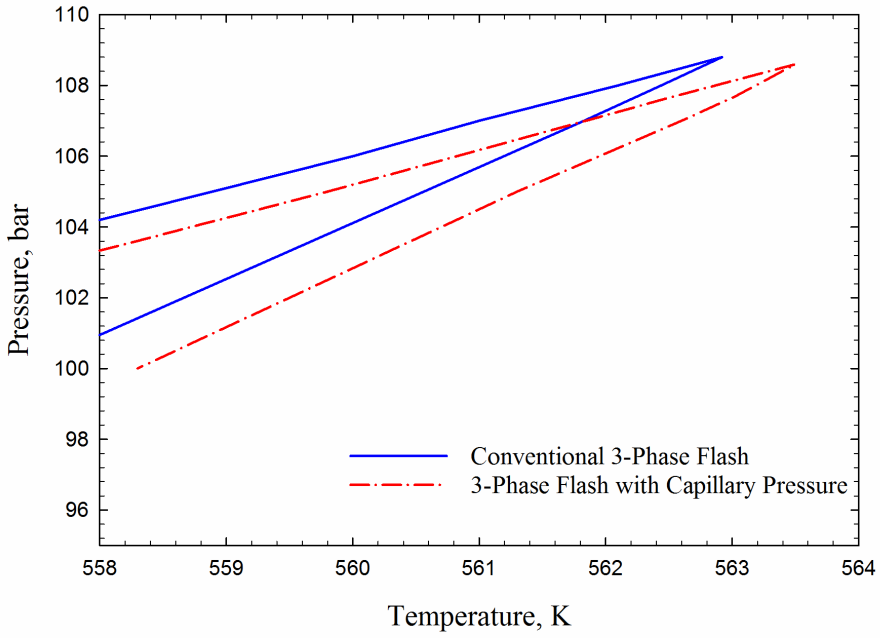

(b)

Fig. 3-9. (a) Overview and (b) zoomed view of the three-phase diagram calculated for Example #1 mixture in an oil-wet formation with a pore radius of 10 nm considering the vapor-phase trapping phenomenon.

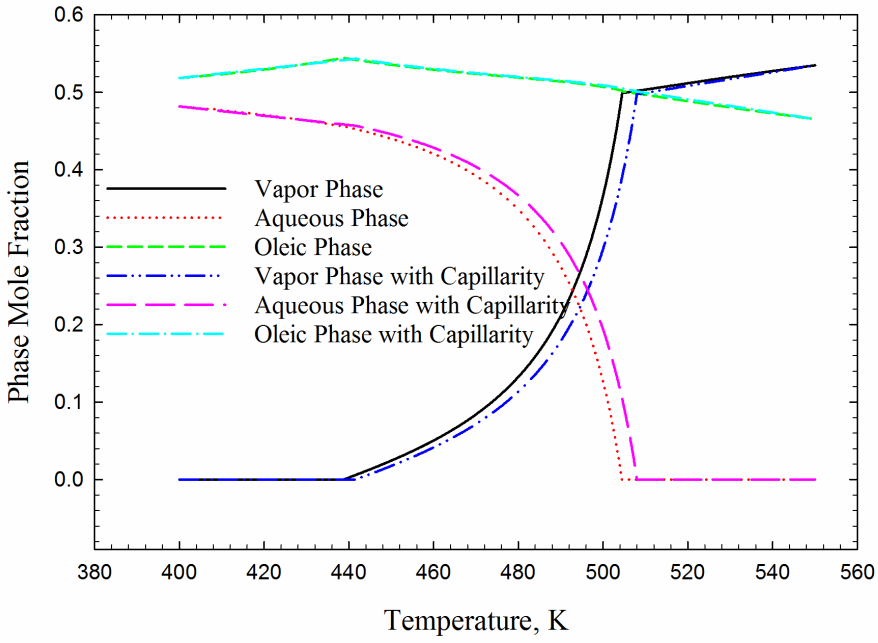

(a)

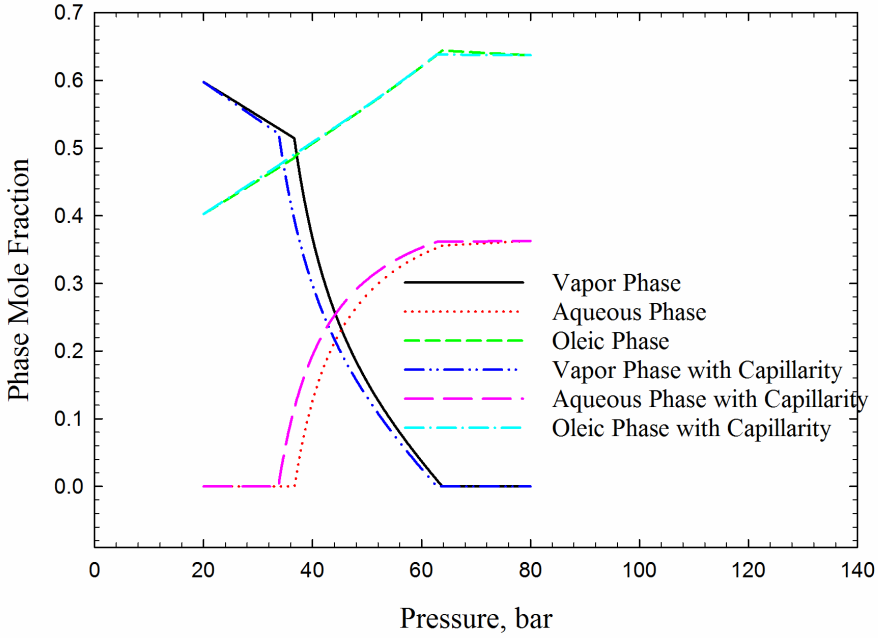

(b)

Fig. 3-10. Phase mole fractions curves calculated for Example #1 mixture under (a) isobaric condition (P=40 bar) and (b) isothermal condition (T=500 K) in an oil-wet formation with a pore radius of 10 nm considering vapor-phase trapping phenomenon.

Pore radius is an essential parameter involved in capillary pressure calculations. It can directly affect the extent of alteration in three-phase equilibria caused by capillary pressure. **Fig. 3-11** shows four three-phase envelopes computed for Example #1 mixture considering capillary pressure in an oil-wet formation with various pore radii: 5 nm, 10 nm, 50 nm, and 100 nm. **Fig. 3-12** shows zoomed views near the tips of the shifted three-phase envelopes.

From **Figs. 3-11 – 3-12**, it can be seen that a smaller pore radius results in a larger shift of the three-phase boundaries due to the capillarity effect. Also, in the cases where the pore radii are equal to 5 nm and 10 nm, the three-phase boundaries are shifted significantly in both the low-pressure region and high-pressure region. In contrast, in the case where the pore radius is equal to 100 nm, the shift of the three-phase boundaries is insignificant in both the low-pressure region and high-pressure region. Therefore, it is rational to conclude that the effect of capillary pressure on alteration of three-phase equilibria can be neglected when the pore radius is larger than 100 nm in our case studies.

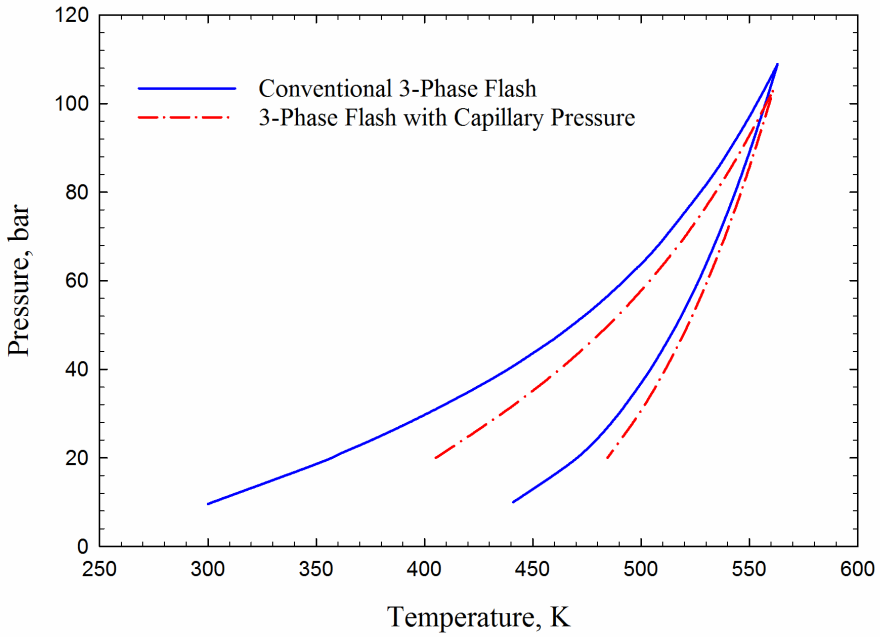
Conventional 3-Phase Flash
3-Phase Flash with Capillary Pressure
Pressure, bar
Temperature, K
0
20
40
60
80
100
120
250
300
350
400
450
500
550
600

(a)

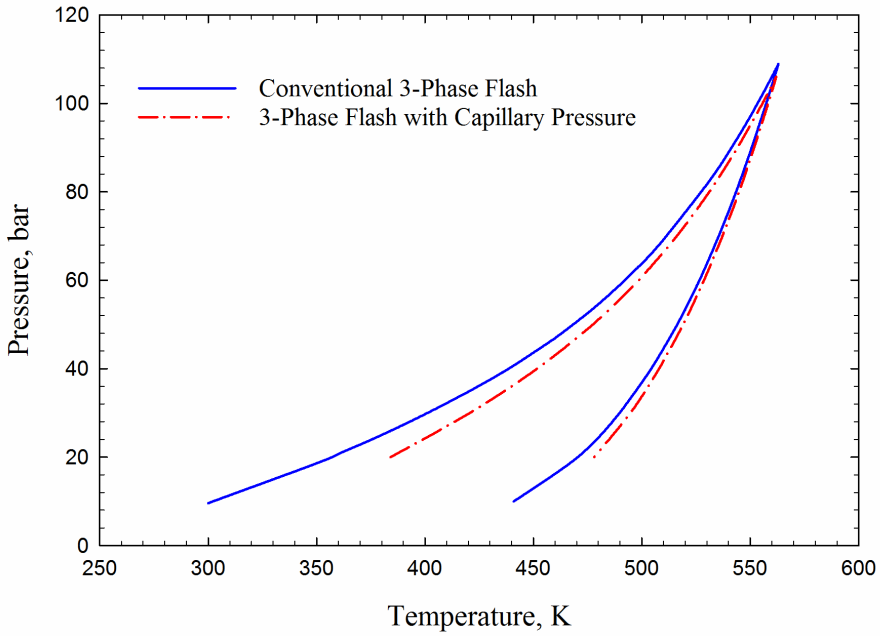
Conventional 3-Phase Flash
3-Phase Flash with Capillary Pressure
Pressure, bar
Temperature, K
0
20
40
60
80
100
120
250
300
350
400
450
500
550
600

(b)

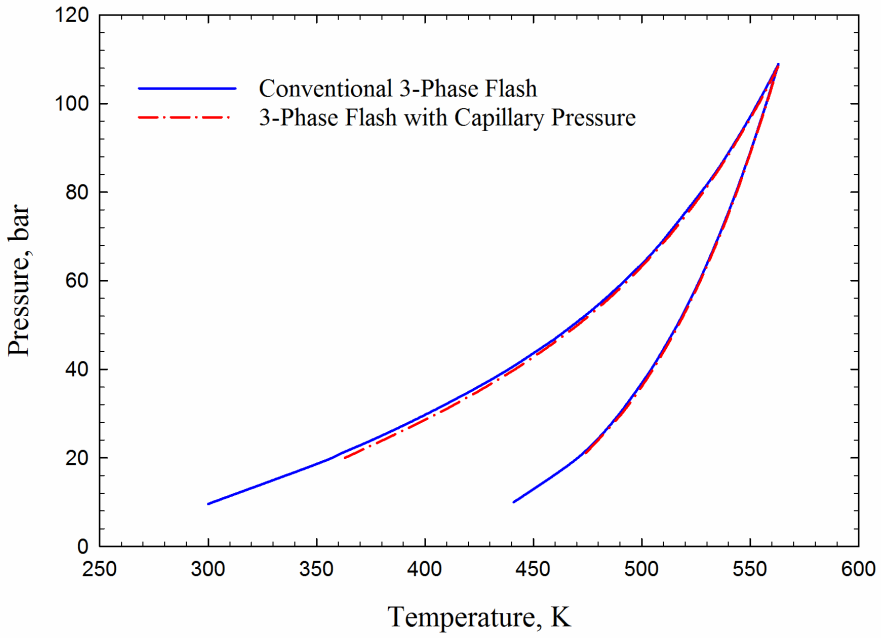

(c)

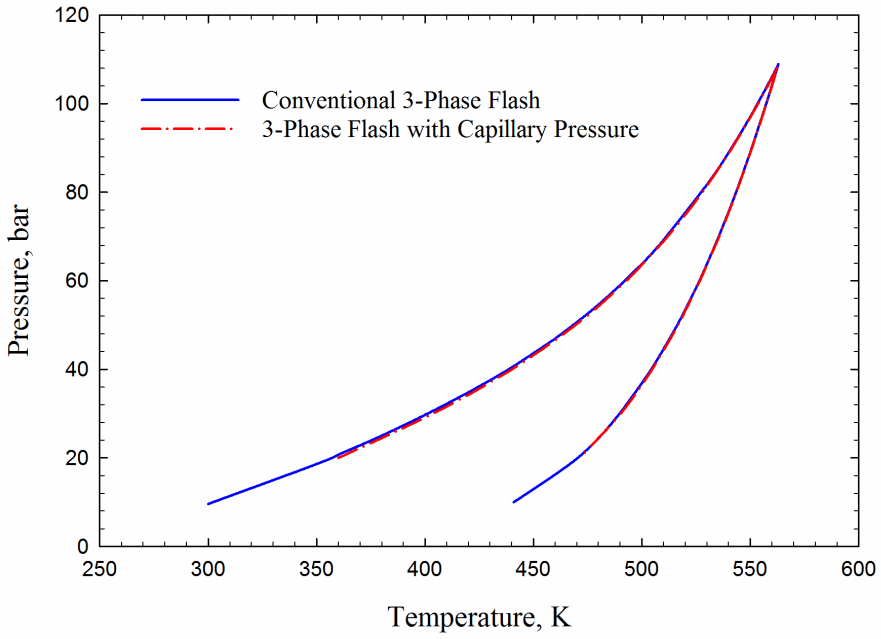

(d)

Fig. 3-11. Three-phase diagrams calculated for Example #1 mixture considering the effect of capillary pressure in an oil-wet formation with pore radii of (a) 5 nm, (b) 10 nm, (c) 50 nm, and (d) 100 nm.

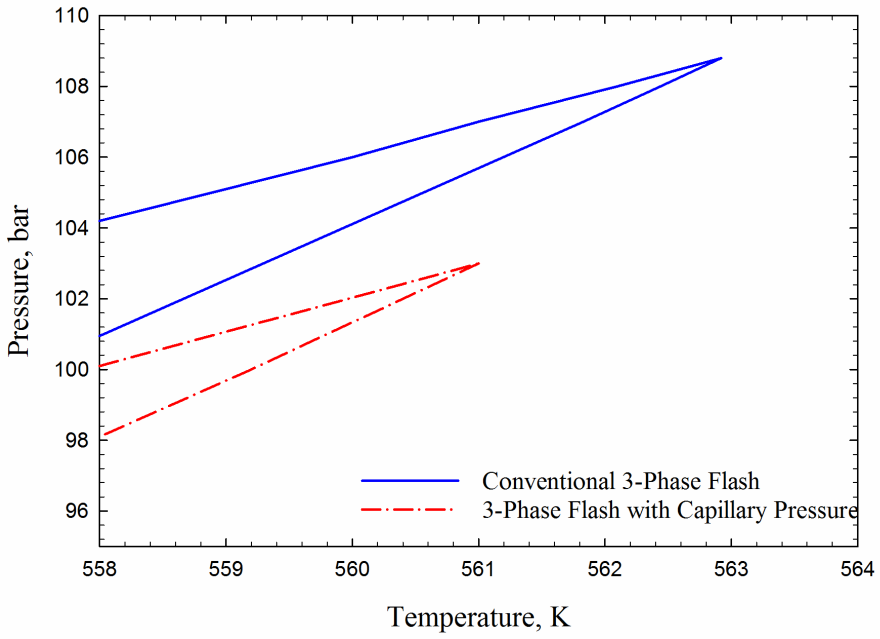
Pressure, bar
Temperature, K
Conventional 3-Phase Flash
3-Phase Flash with Capillary Pressure

(a)

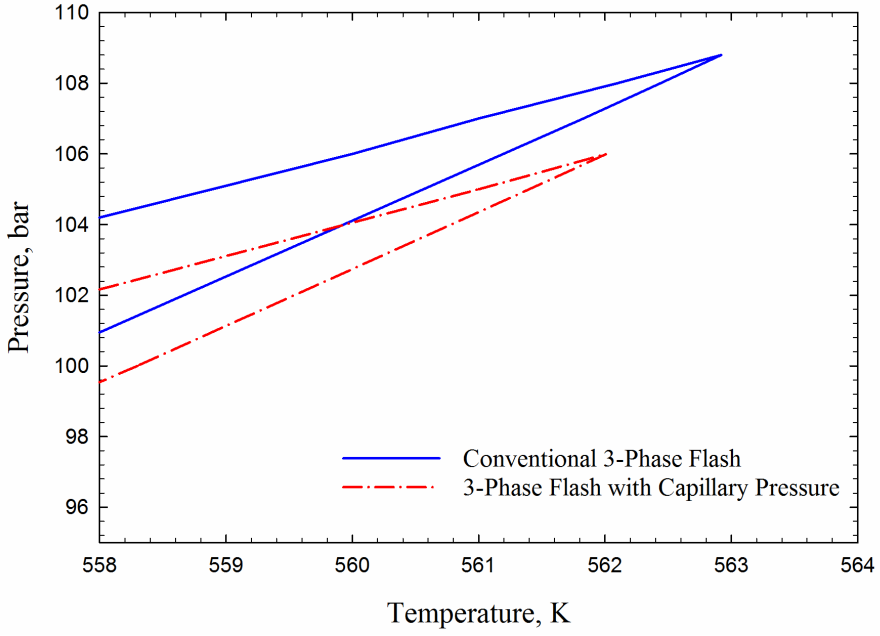
Pressure, bar
Temperature, K
Conventional 3-Phase Flash
3-Phase Flash with Capillary Pressure

(b)

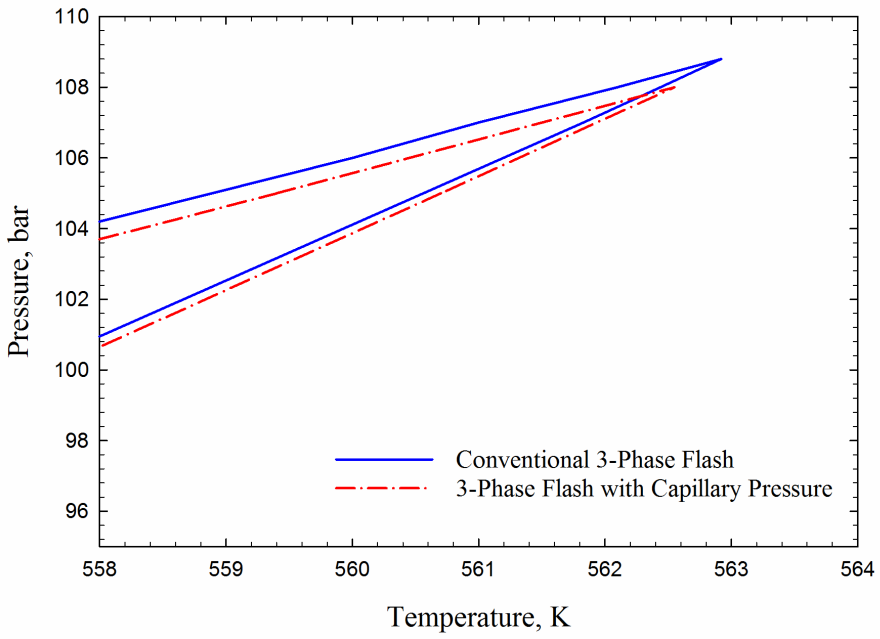

(c)

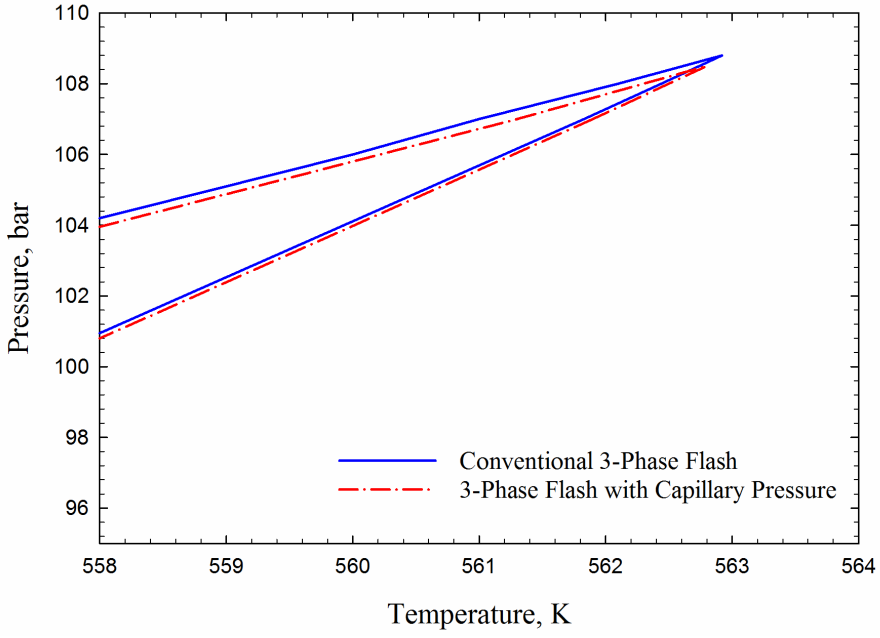

(d)

Fig. 3-12. Zoomed views of the three-phase diagrams calculated for Example #1 mixture considering the effect of capillary pressure in an oil-wet formation with pore radii of (a) 5 nm, (b) 10 nm, (c) 50 nm, and (d) 100 nm.

3.6.3. Example #2 – Mixture of H_2O-N_2-C_{10}-C_{20}

Example #2 is used to study the effect of capillary pressure on three-phase equilibria in a confined space when light components, such as N_2, are present in water-hydrocarbon mixtures. **Fig. 3-13** shows three-phase envelopes calculated for Example #2 mixture considering capillary pressure in both water-wet and oil-wet formations. **Fig. 3-14** shows the zoomed views of the shifted three-phase envelopes. The pore radius used during the computation is 10 nm. The spreading coefficient is positive throughout most of the envelope. However, when the bulk pressure is greater than 260 bar and when the bulk temperature is greater than 635 K, the spreading coefficient becomes negative. This indicates that under extreme conditions (P>260 bar, T>635 K), the fluid distribution inside a nanopore can change from the oil spreading case (i.e., the aqueous phase and the vapor phase are separated by the oleic phase) to the oil non-spreading case (i.e., the oleic phase and the vapor phase are separated by the aqueous phase).

Both **Fig. 3-13** and **Fig. 3-14** suggest that the three-phase boundaries are shifted from the original locations to lower locations due to the presence of capillary pressures. This trend is similar to the calculation results for Example #1 as shown in **Figs. 3-6 – 3-7**. From **Figs. 3-13 – 3-14**, we can also find that at a fixed bulk temperature, the presence of capillary pressures shifts the boundary pressures downward. At a fixed bulk pressure, however, the existence of capillary pressures increases the boundary temperature when the bulk temperature is larger than 520 K, while decreases the boundary temperature when the bulk temperature is lower than 520 K.

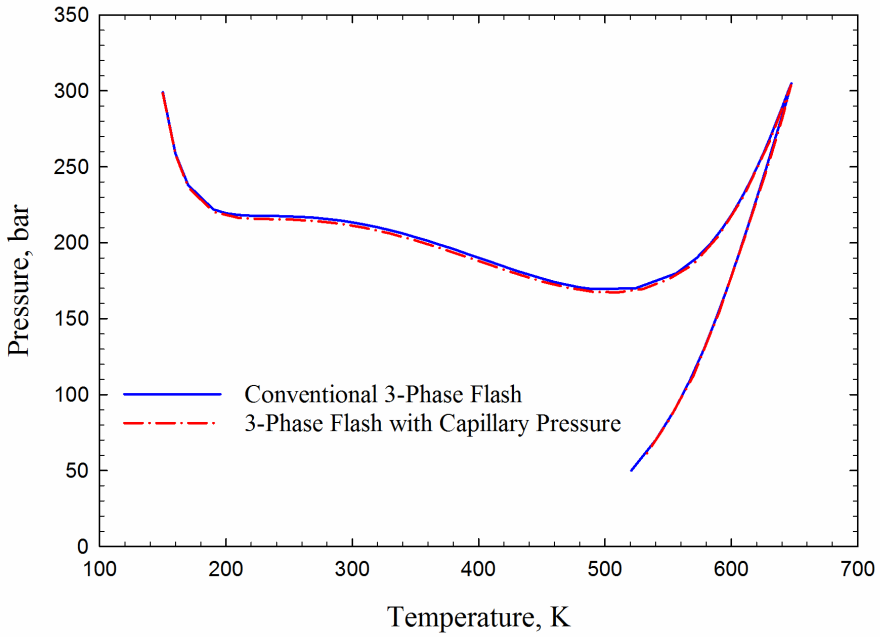

(a)

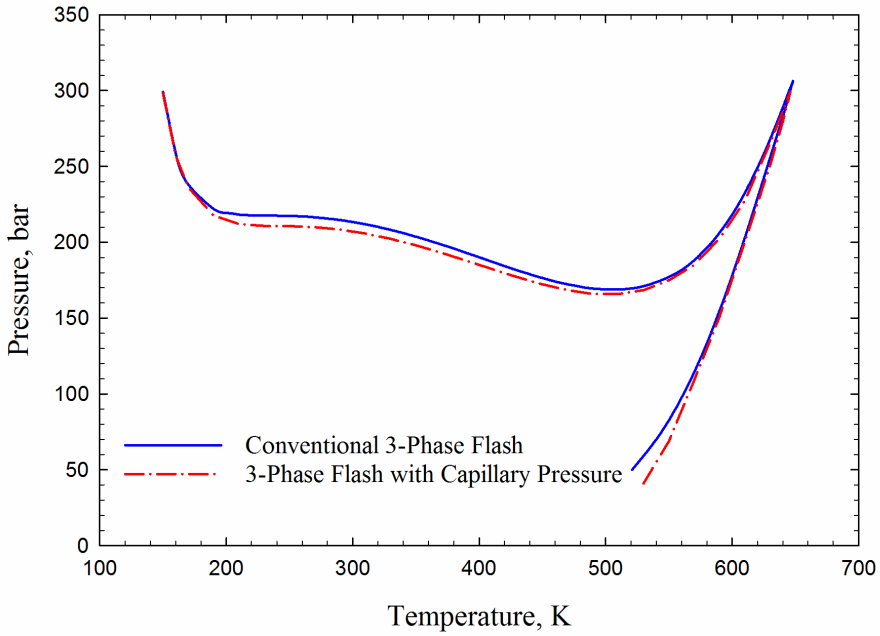

(b)

Fig. 3-13. Three-phase diagrams calculated for Example #2 mixture considering capillary pressure in (a) a water-wet formation and (b) an oil-wet formation with a pore radius of 10 nm.

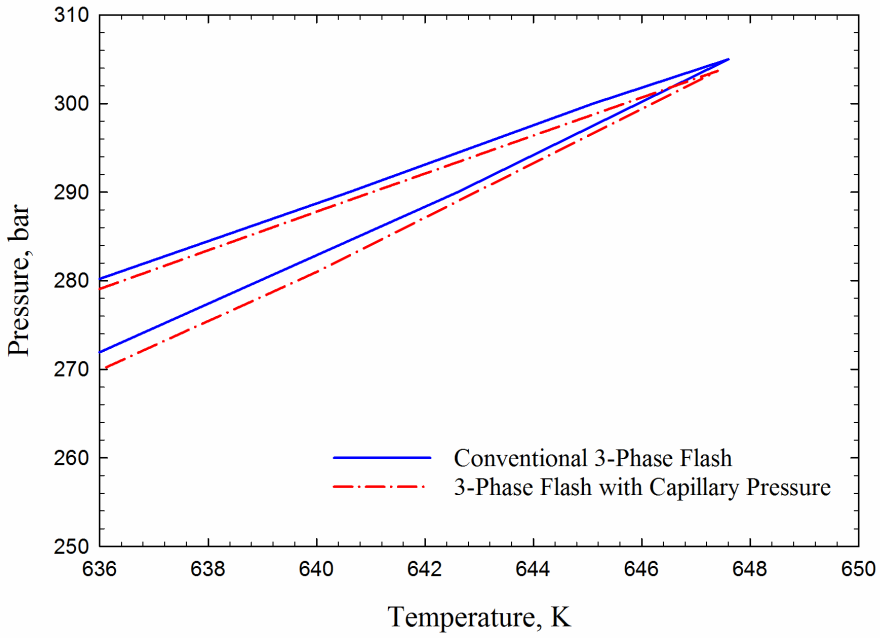

(a)

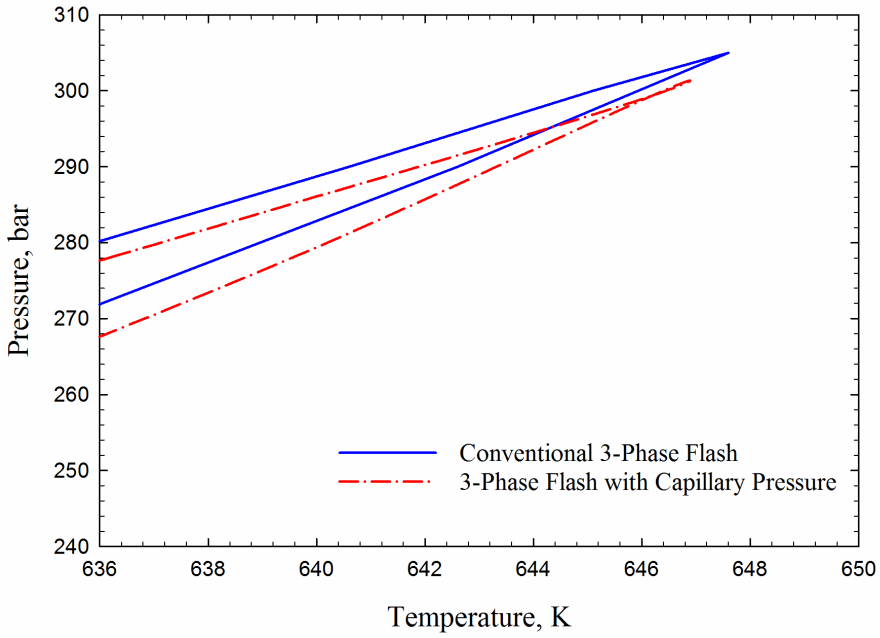

(b)

Fig. 3-14. Zoomed views of the three-phase diagrams calculated for Example #2 mixture in (a) a water-wet formation and (b) an oil-wet formation with a pore radius of 10 nm.

By tracking the IFTs between each two phases in this example (Example #2), we find that the aqueous-vapor IFT is larger than the oleic-vapor IFT throughout the envelope. This leads to possible vapor-phase trapping in an oil-wet formation. **Fig. 3-15** shows the overview and zoomed view of the three-phase envelope calculated for Example #2 mixture in an oil-wet formation when vapor-phase trapping is considered. **Fig. 3-15** shows that the presence of capillary pressures shifts the three-phase boundaries from the original locations to lower locations when vapor-phase trapping occurs in an oil-wet formation. Also, at a fixed bulk pressure, the capillary pressure increases the boundary temperature when the bulk temperature is larger than 520 K, while decreases the boundary temperature when the bulk temperature is lower than 520 K. Furthermore, by comparing **Fig. 3-13 (b)** and **Fig. 3-15 (a)**, we can observe that the three-phase envelope is altered by capillary pressure to a lesser extent when the vapor-phase trapping occurs in a pore space, compared to the case without vapor-phase trapping. This trend is similar to the one found for Example #1 mixture.

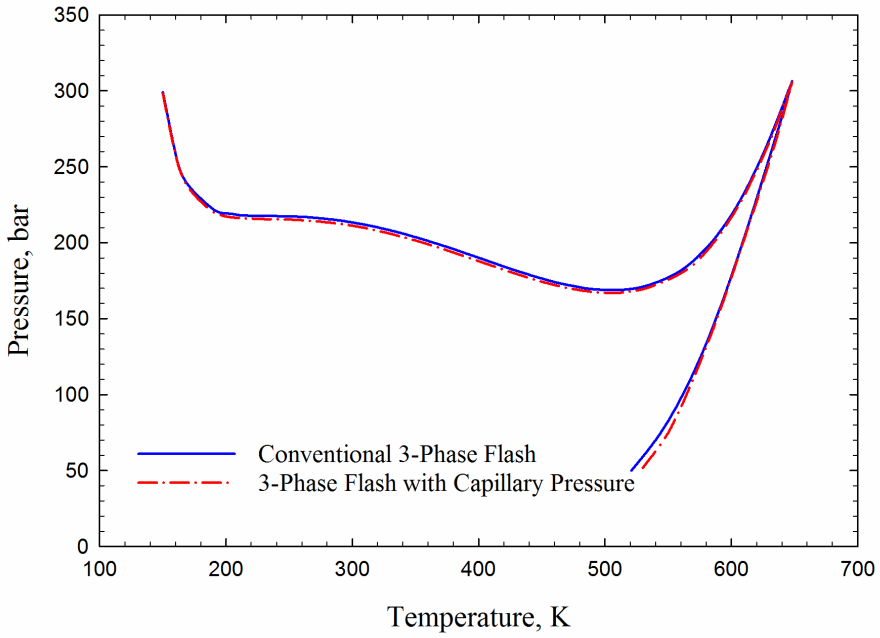

(a)

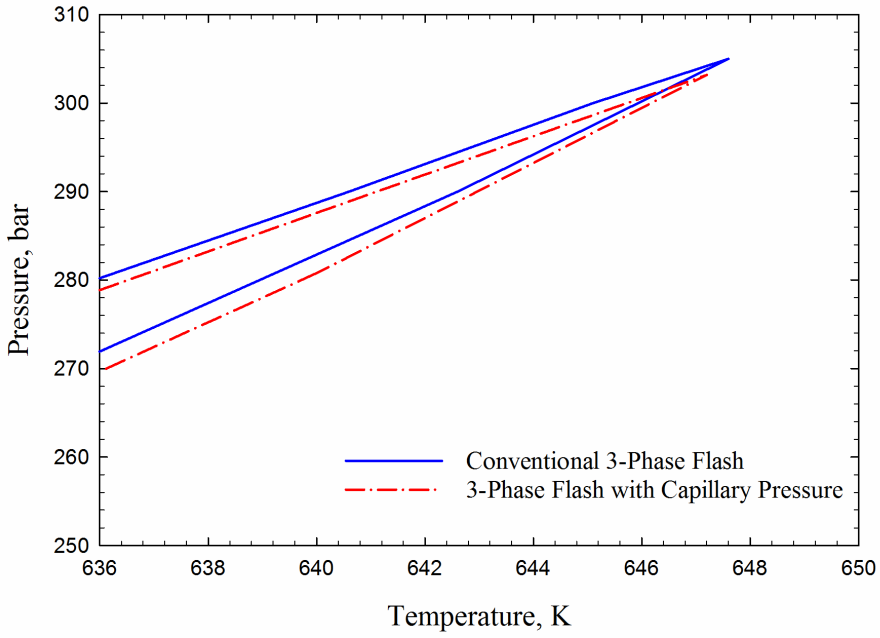

(b)

Fig. 3-15. (a) Overview and (b) zoomed view of the three-phase diagram calculated for Example #2 mixture in an oil-wet formation with a pore radius of 10 nm considering the vapor-phase trapping phenomenon.

3.6.4. Example #3 – Ternary Mixture of H_2O-C_4-C_{20}

This example is designed to study the effect of capillary pressure on the alteration of three-phase boundaries and upper critical end point. The upper critical end point is defined as the point at which the oleic phase and the vapor phase become one phase (Shaw and Zou, 2007). Therefore, the capillary pressure between the oleic phase and the vapor phase becomes zero at the upper critical end point. However, because the aqueous phase is present at the upper critical end point, the aqueous-oleic capillary pressure and the aqueous-vapor capillary pressure are not zero. Therefore, a shift of the upper critical end point due to capillary pressure is expected. **Fig. 3-16** shows three-phase envelopes calculated for Example #3 mixture considering capillary pressure in both water-wet and oil-wet formations with a pore radius of 10 nm. **Fig. 3-17** shows the zoomed views of the three-phase envelopes presented in **Fig. 3-16**. The upper critical end points are highlighted in the diagrams shown in **Figs. 3-16** and **3-17**.

During the calculation of the three-phase envelopes, the spreading coefficient is found to be always positive, which corresponds to an oil spreading case in a nanopore (i.e., the aqueous phase and the vapor phase are separated by the oleic phase). From **Fig. 3-16**, the following trends can be found: the three-phase boundaries are shifted from the original locations to lower locations due to the existence of the capillary pressures. Also, the three-phase boundaries are shifted to a larger extent in an oil-wet formation than in a water-wet formation.

In this case study, we also examine the shift of the upper critical end point caused by capillary pressure. From the zoomed views in **Fig. 3-17**, it is clearly seen that the upper critical end point shifts from the original location to the lower-left location because of the capillarity effect in both water-wet and oil-wet formations. This indicates that the mixture used in this example (Example

#3) will reach upper critical end point under the conditions with a lower pressure and a lower temperature in a confined space, as compared to the situation where the mixture is not in a confined space.

Vapor-phase trapping phenomenon is possible in an oil-wet formation for this example (Example #3) because the aqueous-vapor IFT is found to be larger than the oleic-vapor IFT throughout the envelope. **Fig. 3-18** shows an overview and zoomed view of the three-phase envelope calculated for Example #3 mixture in an oil-wet formation considering vapor-phase trapping phenomenon. In **Fig. 3-18**, the presence of the capillary pressures shifts the three-phase boundaries from the original locations to lower locations. As for the upper critical end point, it is shifted towards a lower-pressure/lower-temperature position due to capillary pressure. Also, by comparing **Fig. 3-17 (b)** and **Fig. 3-18 (b)**, we can find that the three-phase envelope is altered by capillary pressure to a lesser extent when the vapor-phase trapping occurs in a pore space, compared to the case without vapor-phase trapping.

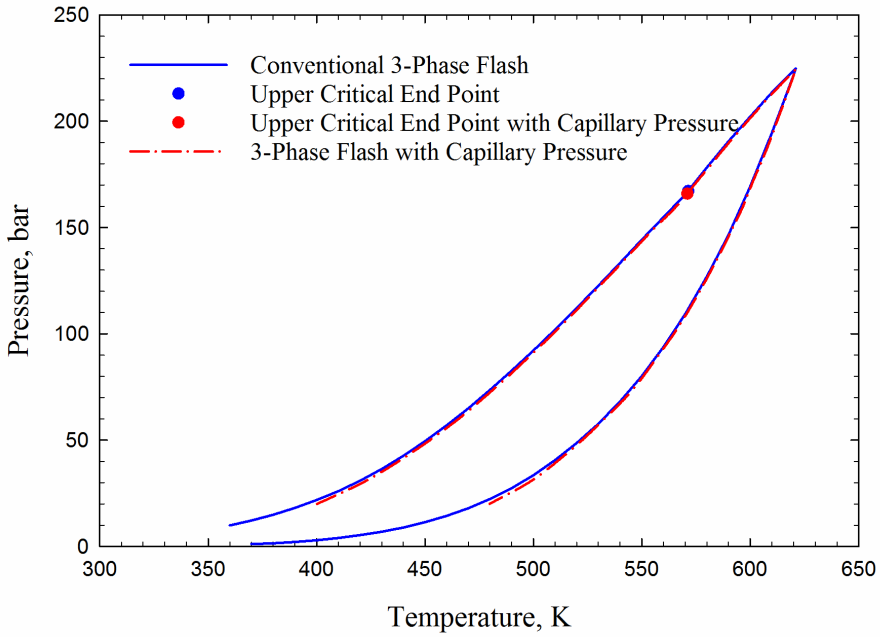

(a)

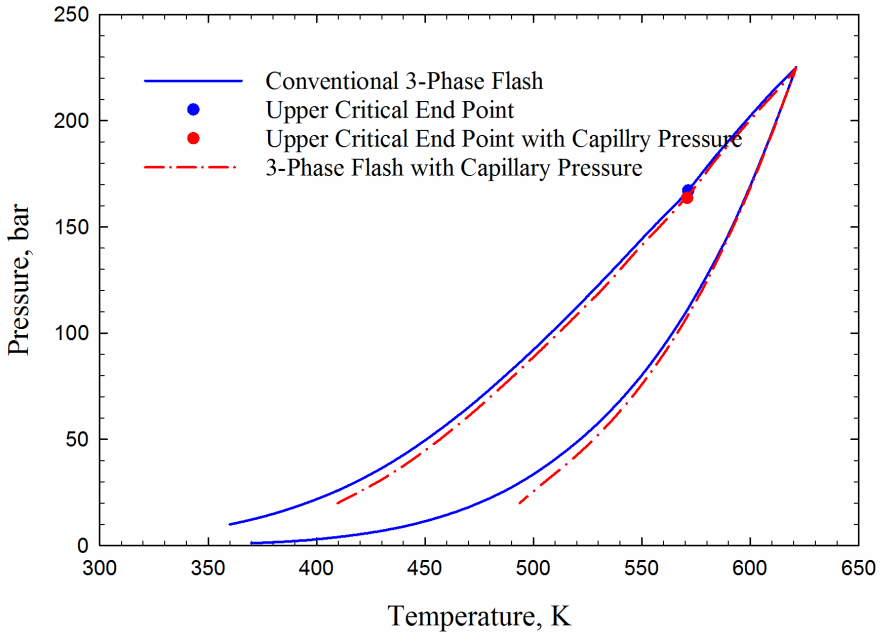

(b)

Fig. 3-16. Three-phase diagrams calculated for Example #3 mixture considering capillary pressure in (a) a water-wet formation and (b) an oil-wet formation with a pore radius of 10 nm.

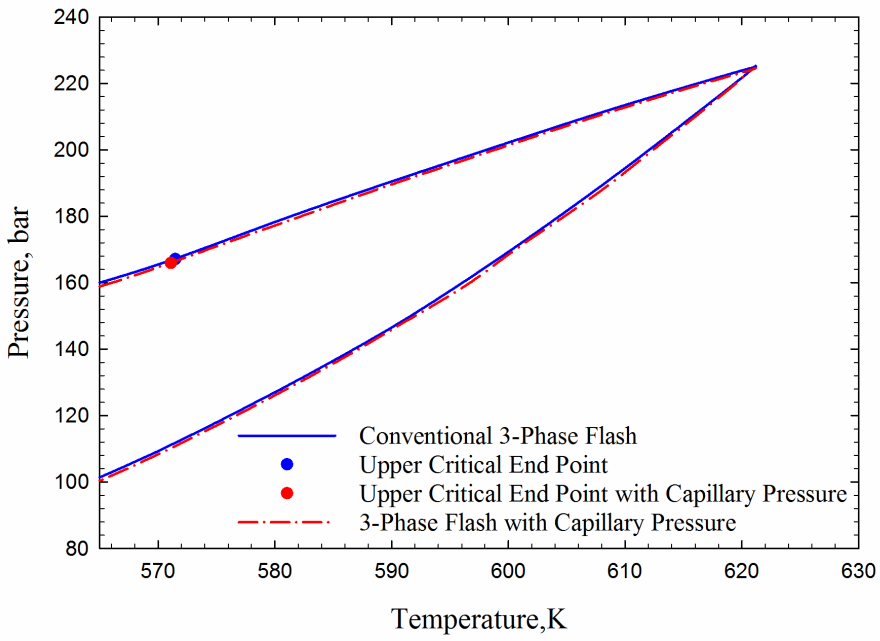

(a)

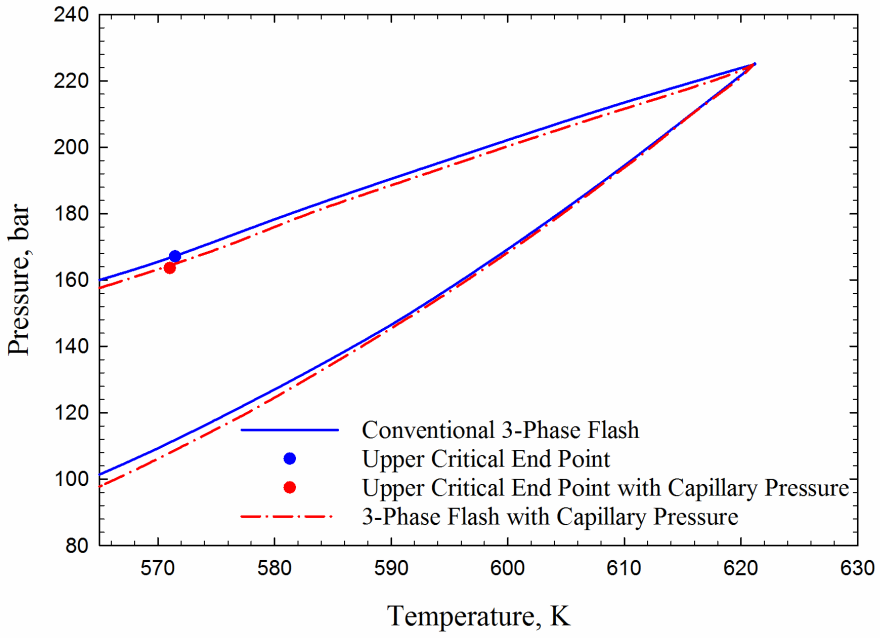

(b)

Fig. 3-17. Zoomed views of the three-phase diagrams calculated for Example #3 considering capillary pressure in (a) a water-wet formation and (b) an oil-wet formation with a pore radius of 10 nm.

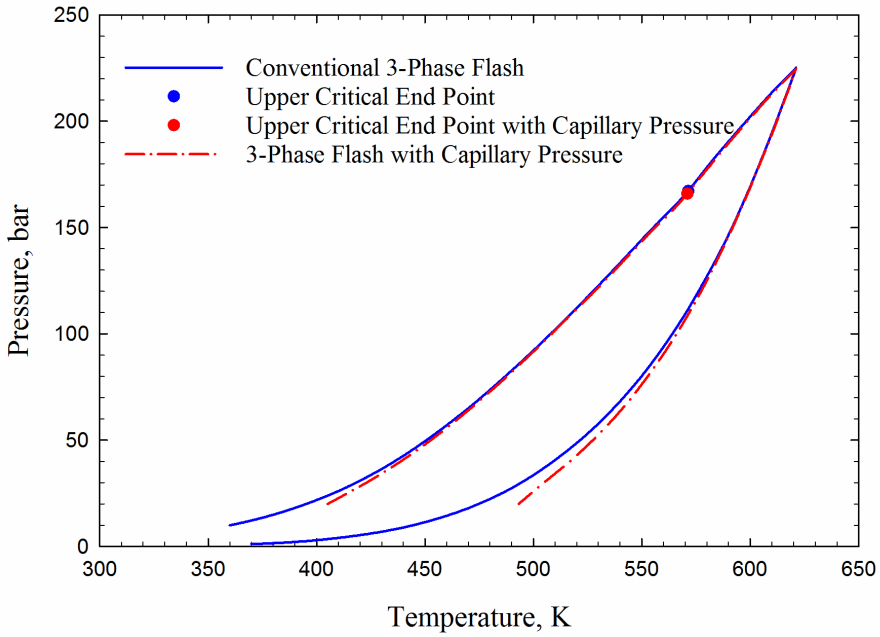

(a)

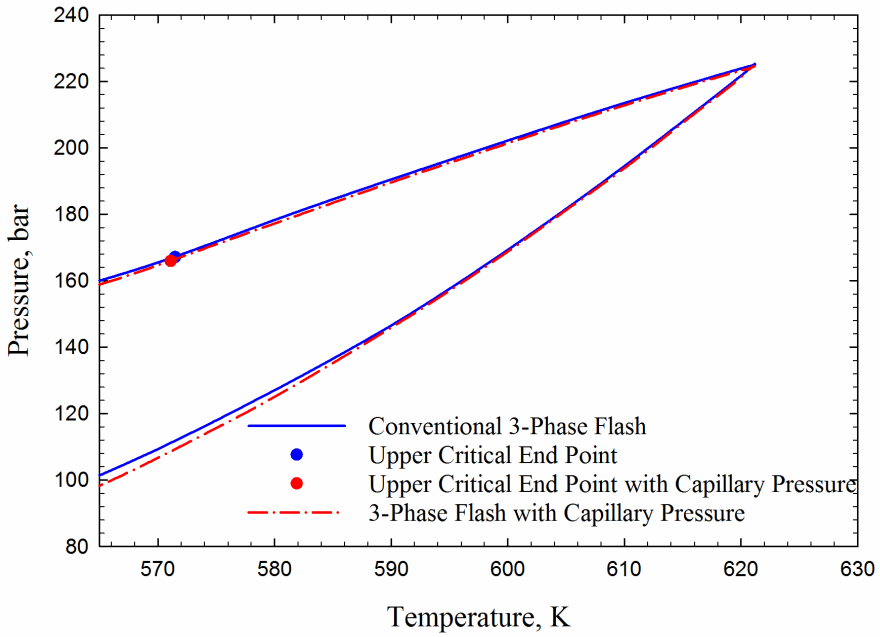

(b)

Fig. 3-18. (a) Overview and (b) zoomed view of the three-phase diagram calculated for Example #3 mixture in an oil-wet formation with a pore radius of 10 nm considering the vapor-phase trapping phenomenon.

3.6.5. Example #4 – Ternary Mixture of H_2O-C_4-C_{20} with Different Feed Compositions

Phase behavior calculations for this example (Example #4) are carried out to examine if the trend of the alteration in three-phase equilibria of a water-hydrocarbon mixture due to capillary pressure remains the same when the feed composition of the mixture is changed. **Fig. 3-19** shows three-phase envelopes calculated for Example #4 mixture considering capillary pressure in a water-wet formation and an oil-wet formation. **Fig. 3-20** shows the zoomed views of the three-phase envelopes presented in **Fig. 3-19**. Also, because the aqueous-vapor IFT is found to be larger than the oleic-vapor IFT throughout the diagrams, the vapor-phase trapping phenomenon can occur in oil-wet formations for this example (Example #4). **Fig. 3-21** shows the overview and the zoomed view of the three-phase envelope calculated for Example #4 mixture in an oil-wet formation considering vapor-phase trapping phenomenon. The pore radius used in the calculations for this example (Example #4) is 10 nm.

From **Figs. 3-16** and **3-19**, it is found that the trend of the alteration in three-phase equilibria of a water-hydrocarbon mixture due to capillary pressure is the same when the feed composition of the mixture is changed. The three-phase boundaries are shifted away from the original location to a lower part of the diagram due to the capillarity effect. In an oil-wet formation, the three-phase boundaries are severely altered by capillary pressure more compared to the case in a water-wet formation. Furthermore, by comparing **Fig. 3-19 (b)** and **Fig. 3-21 (a)**, one can find that when the vapor-phase trapping phenomenon occurs in an oil-wet formation, the three-phase boundaries are shifted to a lesser extent compared to the case without vapor-phase trapping. This is also consistent with what is found for the other mixtures.

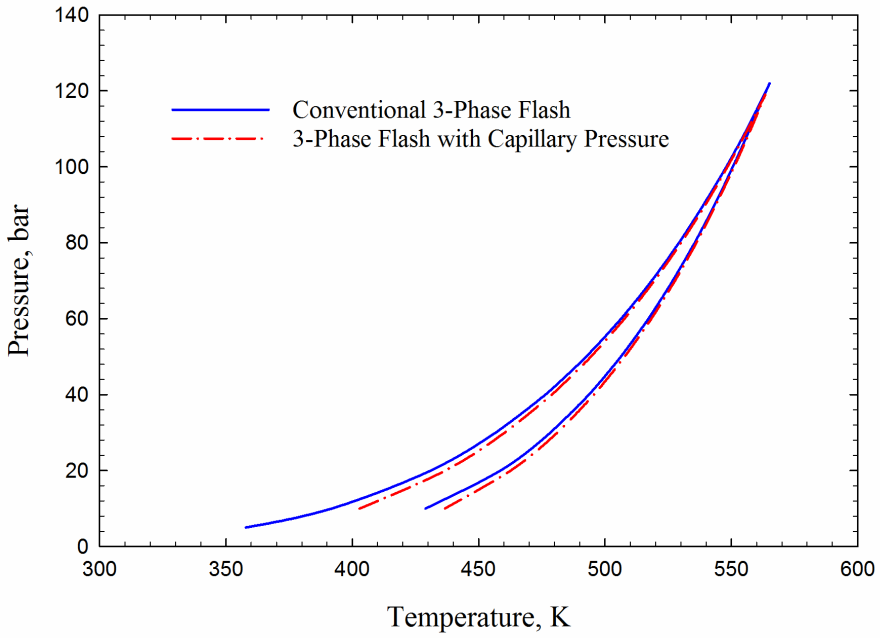

(a)

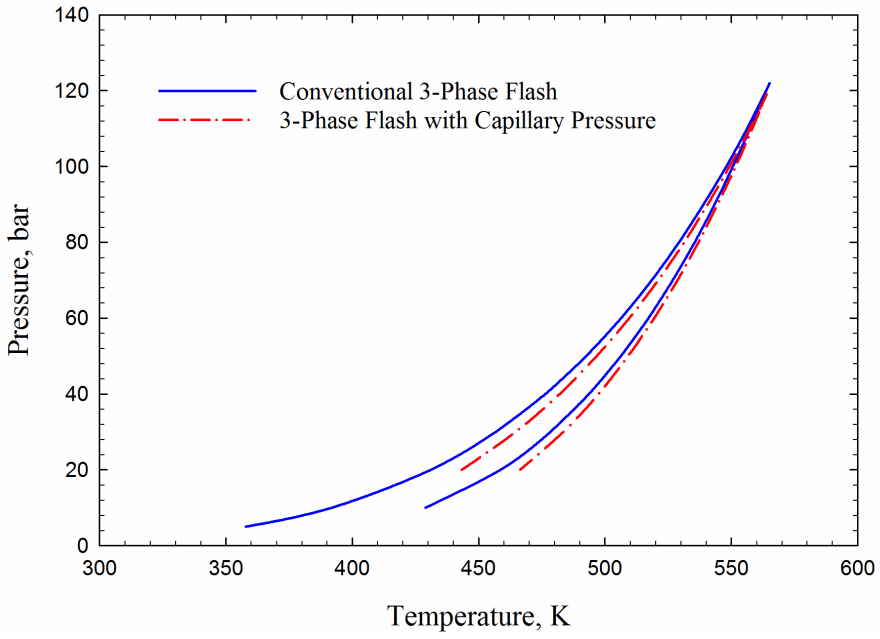

(b)

Fig. 3-19. Three-phase diagrams calculated for Example #4 mixture considering capillary pressure in (a) a water-wet formation and (b) an oil-wet formation with a pore radius of 10 nm.

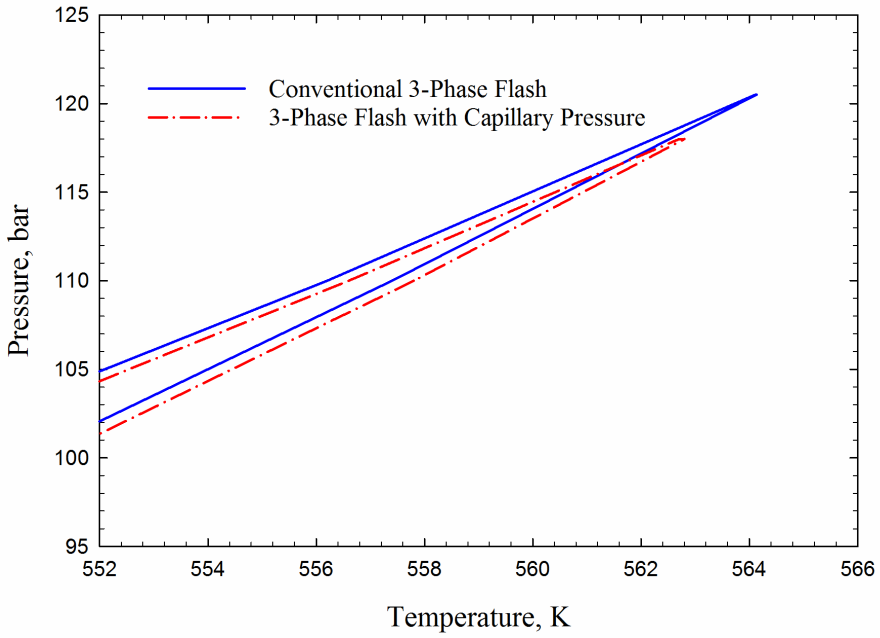

(a)

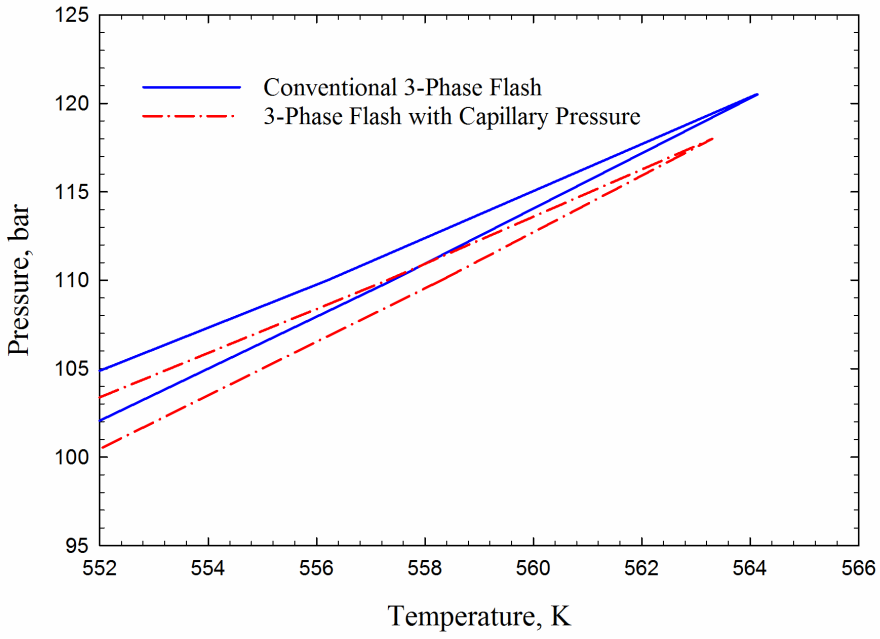

(b)

Fig. 3-20. Zoomed views of the three-phase diagrams calculated for Example #4 mixture considering capillary pressure in (a) a water-wet formation and (b) an oil-wet formation with a pore radius of 10 nm.

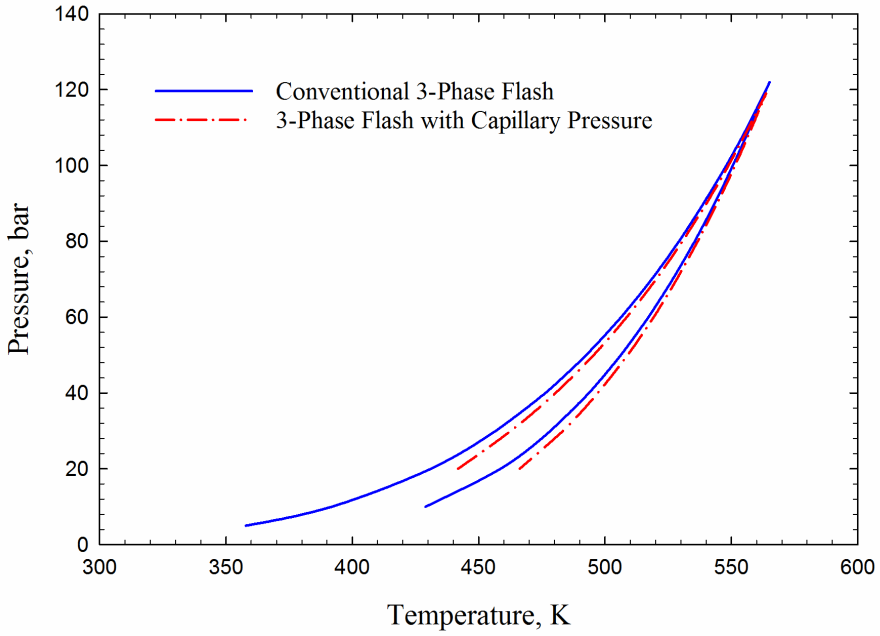

(a)

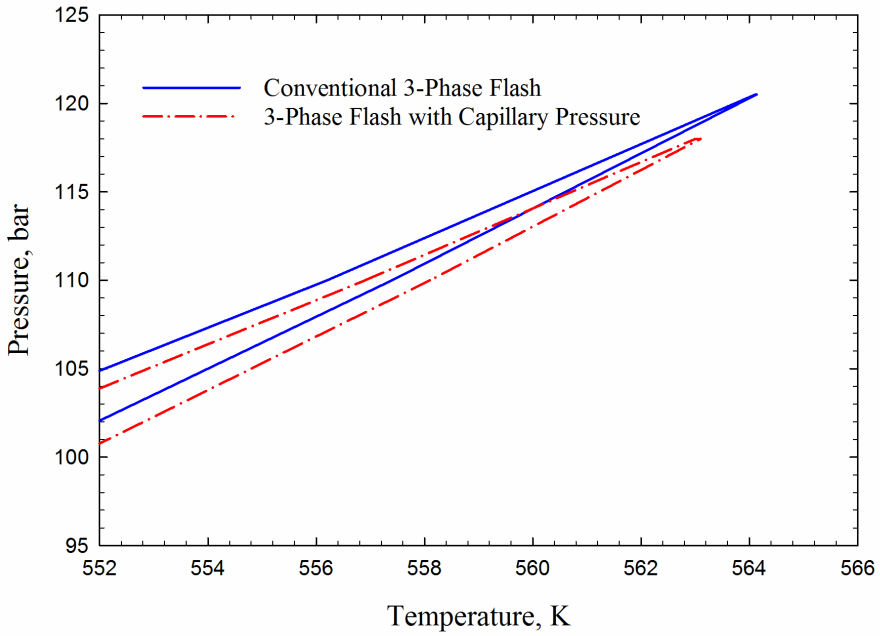

(b)

Fig. 3-21. (a) Overview and (b) zoomed view of the three-phase diagram calculated for Example #4 mixture in an oil-wet formation with a pore radius of 10 nm considering the vapor-phase trapping phenomenon.

3.7.Conclusions

In this work, we propose a new three-phase P-T flash algorithm that considers the effect of capillary pressure in a confined space. The unique features of our new algorithm include the following:

- We summarize six types of possible fluid distributions based on formation wettability and spreading coefficient. Vapor-phase trapping phenomenon is considered as a special case. Each fluid distribution leads to a unique capillary pressure system and is coupled into our algorithm.
- Phase capillary pressure is calculated using Young-Laplace equation (Young 1805) with the assumptions of equal principle curvature radii and zero contact angle. The liquid-vapor IFTs are calculated using Weinaug-Katz model (Weinaug and Katz 1943), while the water-hydrocarbon IFT is calculated using the model introduced by Danesh (2007).
- Rachford-Rice equations (Rachford and Rice, 1952) are solved to calculate phase mole fractions and phase compositions at a given pressure and a given temperature. In order to couple capillary pressures into the conventional three-phase flash algorithm, phase densities, IFT, and capillary pressure are updated when updating the fugacity of a given component in each phase.

We present four examples to examine the performance of our algorithm and to study the effect of capillary pressure on the three-phase equilibria alteration from various aspects. The following conclusions can be drawn:

- The existence of phase capillary pressures significantly alters the three-phase equilibria. Generally, the three-phase boundary pressure is decreased at a fixed temperature, while the three-phase boundary temperature is increased at a fixed pressure.
- The three-phase envelope is altered by capillary pressure to a lesser extent when the vapor-phase trapping occurs in a pore space, compared to the case without vapor-phase trapping.
- Pore radius is an essential factor in affecting how much alteration of the three-phase equilibria will take place due to capillary pressure. A smaller pore radius leads to a larger alteration of the three-phase envelope. The effect of capillary pressure on alteration of three-phase envelope can be neglected when the pore radius is larger than 100 nm in our calculations.
- It is observed that the upper critical end point is shifted towards a lower-pressure and lower-temperature position due to capillary pressure. This is because the aqueous-oleic capillary pressure and the aqueous-vapor capillary pressure will not vanish at the upper critical end point.

Acknowledgments

The authors greatly acknowledge a Discovery Grant from the Natural Sciences and Engineering Research Council of Canada (NSERC) to H. Li. The authors would also like to express gratitude to PVTsim for providing academic license to the University of Alberta.

References

Abu Al-Rub, F. and Datta, R. 1999. Theoretical Study of Vapor–Liquid Equilibrium Inside Capillary Porous Plates. Fluid Phase Equilibria, 162(1-2), pp.83-96. http://doi.org/10.1016/s0378-3812(99)00197-1.

Bhatia, S., Bonilla, M. and Nicholson, D. 2011. Molecular Transport in Nanopores: A Theoretical Perspective. Physical Chemistry Chemical Physics, 13(34), 15350. http://doi.org/10.1039/c1cp21166h.

Bonapace, J. 2015. Water Management for Tight and Shale Reservoir: A Review of What Has Been Learned and What Should Be Considered for Development in Argentina. In: SPE Latin American and Caribbeen Health, Safety, Environment and Sustainability Conference. Bogota: Society of Petroleum Engineers. https://doi.org/10.2118/174119-MS.

Brusilovsky, A. 1992. Mathematical Simulation of Phase Behavior of Natural Multicomponent Systems at High Pressures with an Equation of State. SPE Reservoir Engineering, 7(01), pp.117-122. http://doi.org/10.2118/20180-pa.

Danesh, A. 2007. PVT and Phase Behaviour of Petroleum Reservoir Fluids. Amsterdam: Elsevier.

Dong, J. 2014. A High Order Method for Three Phase Flow in Homogeneous Porous Media. SIAM Undergraduate Research Online, 7, pp.74-88. http://doi.org/10.1137/13s012637.

Firincioglu, T., Ozkan, E. and Ozgen, C. 2012. Thermodynamics of Multiphase Flow in Unconventional Liquids-Rich Reservoirs. In: SPE Annual Technical Conference and Exhibition. San Antonio: Society of Petroleum Engineers. https://doi.org/10.2118/159869-MS.

Firoozabadi, A. and Ramey, H. 1988. Surface Tension of Water-Hydrocarbon Systems at Reservoir Conditions. Journal of Canadian Petroleum Technology, 27(03), pp.41-48. http://doi.org/10.2118/88-03-03.

Green, D. W. and Willhite, G. P. 1998. Enhanced oil Recovery. Richardson, TX: Henry L. Doherty Memorial Fund of AIME, Society of Petroleum Engineers.

Hamada, Y., Koga, K. and Tanaka, H. 2007. Phase Equilibria and Interfacial Tension of Fluids Confined in Narrow Pores. The Journal of Chemical Physics, 127(8), 084908. http://doi.org/10.1063/1.2759926.

Hustad, O. and Browning, D. 2010. A Fully Coupled Three-Phase Model for Capillary Pressure and Relative Permeability for Implicit Compositional Reservoir Simulation. SPE Journal, 15(04), pp.1003-1019. http://doi.org/10.2118/125429-pa.

Iwere, F. O., Heim, R. N., and Cherian, B. V. 2012. Numerical Simulation of Enhanced Oil Recovery in the Middle Bakken and Upper Three Forks Tight Oil Reservoirs of the Williston Basin. In: The Americas Unconventional Resources Conference. Pittsburgh: Society of Petroleum Engineers. http://doi.org/10.2118/154937-MS.

Jin, Z. and Firoozabadi, A. 2016. Thermodynamic Modeling of Phase Behavior in Shale Media. SPE Journal, 21(01), pp.190-207. http://doi.org/10.2118/176015-pa.

Kantzas, A., Nikakhtar, B. and Pow, M. 1998. Principles of Three Phase Capillary Pressures. Journal of Canadian Petroleum Technology, 37(07), pp.48-54. http://doi.org/10.2118/98-07-05.

Lapene, A., Nichita, D., Debenest, G. and Quintard, M. 2010. Three-Phase Free-Water Flash Calculations Using a New Modified Rachford–Rice Equation. Fluid Phase Equilibria, 297(1), pp.121-128. http://doi.org/10.1016/j.fluid.2010.06.018.

Li, R. and Li, H. 2018. New Two-Phase and Three-Phase Rachford-Rice Algorithms Based on Free-Water Assumption. The Canadian Journal of Chemical Engineering, 96(1), pp.390-403. http://doi.org/10.1002/cjce.23018.

Li, X., Wei, H., Chen, B., Liu, X., Wang, W. and Zhao, X. 2008. Multi-Stage Fracturing Stimulations Improve Well Performance in Tight Oil Reservoirs of the Changqing Oilfield. In: The International Petroleum Technology Conference. Kuala Lumpur: International Petroleum Technology Conference. http://doi.org/10.2523/IPTC-12303-MS.

Li, Z., Qu, X., Liu, W., Lei, Q., Sun, H. and He, Y. 2015. Development Modes of Triassic Yanchang Formation Chang 7 Member tight oil in Ordos Basin, NW China. Petroleum Exploration and Development, 42(2), pp.241-246. http://doi.org/10.1016/s1876-3804(15)30011-2.

Loucks, R., Reed, R., Ruppel, S. and Jarvie, D. 2009. Morphology, Genesis, and Distribution of Nanometer-Scale Pores in Siliceous Mudstones of the Mississippian Barnett Shale. Journal of Sedimentary Research, 79(12), pp.848-861. http://doi.org/10.2110/jsr.2009.092.

Luo, S. and Barrufet, M. 2005. Reservoir Simulation Study of Water-in-Oil Solubility Effect on Oil Recovery in Steam Injection Process. SPE Reservoir Evaluation & Engineering, 8(06), pp.528-533. http://doi.org/10.2118/89407-pa.

Macleod, D. 1923. On a Relation Between Surface Tension and Density. Transactions of the Faraday Society, 19, pp.38-41. http://doi.org/10.1039/tf9231900038.

Moortgat, J. and Firoozabadi, A. 2013. Three-Phase Compositional Modeling with Capillarity in Heterogeneous and Fractured Media. SPE Journal, 18(06), pp.1150-1168. https://doi.org/10.2118/159777-PA.

Neshat, S.S., Okuno, R. and Pope, G.A. 2018. A Rigorous Solution to the Problem of Phase Behavior in Unconventional Formations with High Capillary Pressure. SPE Journal, 23(4), pp.1438-1451. http://doi:10.2118/187260-PA.

Nojabaei, B., Johns, R. and Chu, L. 2013. Effect of Capillary Pressure on Phase Behavior in Tight Rocks and Shales. SPE Reservoir Evaluation & Engineering, 16(03), pp.281-289. http://doi.org/10.2118/159258-pa.

Øren, P. and Pinczewski, W. 1991. The Effect of Film-Flow on the Mobilization of Waterflood Residual Oil by Gas Flooding. 6th European Symposium on Improved Oil Recovery, Stavanger, 705. http://doi.org/10.3997/2214-4609.201411204.

Øren, P., Billiotte, J. and Pinczewski, W. 1992. Mobilization of Waterflood Residual Oil by Gas Injection for Water-Wet Conditions. SPE Formation Evaluation, 7(01), pp.70-78. http://doi.org/10.2118/20185-pa.

Øren, P. and Pinczewski, W. 1994. The Effect of Wettability and Spreading Coefficients on the Recovery of Waterflood Residual Oil by Miscible Gasflooding. SPE Formation Evaluation, 9(02), pp.149-156. http://doi.org/10.2118/24881-pa.

Pang, J., Zuo, J., Zhang, D. and Du, L. 2012. Impact of Porous Media on Saturation Pressures of Gas and Oil in Tight Reservoirs. In: SPE Canadian Unconventional Resources Conference. Calgary: Society of Petroleum Engineers. https://doi.org/10.2118/161143-MS.

Pang, W. and Li, H. 2017. An Augmented Free-Water Three-Phase Rachford-Rice Algorithm for CO_2/hydrocarbons/water mixtures. Fluid Phase Equilibria, 450, pp.86-98. http://doi.org/10.1016/j.fluid.2017.07.010.

Passey, Q., Bohacs, K., Esch, W., Klimentidis, R. and Sinha, S. 2010. From Oil-Prone Source Rock to Gas-Producing Shale Reservoir-Geologic and Petrophysical Characterization of Unconventional Shale-Gas Reservoirs. In: CPS/SPE International Oil & Gas Conference and Exhibition. Beijing: Society of Petroleum Engineers. https://doi.org/10.2118/131350-MS.

Peng, D. and Robinson, D. 1976a. A New Two-Constant Equation of State. Industrial & Engineering Chemistry Fundamentals, 15(1), pp.59-64. http://doi.org/10.1021/i160057a011.

Peng, D. and Robinson, D. 1976b. Two and three phase equilibrium calculations for systems containing water. The Canadian Journal of Chemical Engineering, 54(6), pp.595-599. http://doi.org.10.1002/cjce.5450540620.

Ping, G., Liangtian, S., Li, S. and Sun, L., 1996. A Theoretical Study of the Effect of Porous Media on the Dew Point Pressure of a Gas Condensate. In: SPE Gas Technology Symposium. Calgary: Society of Petroleum Engineers. http://dx.doi.org/10.2118/35644-MS.

Qi, Z., Liang, B., Deng, R., Du, Z., Wang, S. and Zhao, W. 2007. Phase Behavior Study in the Deep Gas-Condensate Reservoir with Low Permeability. In: SPE Europec/EAGE Annual Conference and Exhibition. London: Society of Petroleum Engineers. https://doi.org/10.2118/107315-MS.

Quayle, O. R. 1953. The Parachors of Organic Compounds. An Interpretation and Catalogue. Chemical Reviews, 53 (3), pp.439-589. https://doi.org/10.1021/cr60166a003.

Rachford, H. and Rice, J. 1952. Procedure for Use of Electronic Digital Computers in Calculating Flash Vaporization Hydrocarbon Equilibrium. Journal of Petroleum Technology, 4(10), pp.19-3. http://doi.org/10.2118/952327-g.

Redlich, O. and Kwong, J.N. 1949. On the Thermodynamics of Solutions. V. An Equation of State. Fugacities of Gaseous Solutions. Chemical Reviews, 44, pp.233-244. http://doi.org/ 10.1021/cr60137a013.

Rezaveisi, M., Sepehrnoori, K., Pope, G. and Johns, R. 2015. Compositional Simulation Including Effect of Capillary Pressure on Phase Behavior. In: SPE Annual Technical Conference and Exhibition. Houston: Society of Petroleum Engineers. https://doi.org/10.2118/175135-MS.

Robinson, D. and Peng, D. 1978. The Characterization of the Heptanes and Heavier Fractions for the GPA Peng-Robinson programs. Tulsa, Okla.: Gas Processors Association.

Sandoval, D., Yan, W., Michelsen, M. and Stenby, E. 2015. Phase Envelope Calculations for Reservoir Fluids in the Presence of Capillary Pressure. In: SPE Annual Technical Conference and Exhibition. Houston: Society of Petroleum Engineers. https://doi.org/10.2118/175110-MS.

Shaw, J.M. and Zou, X. 2007. Phase Behavior of Heavy Oils. In: Mullins O.C., Sheu E.Y., Hammami A., Marshall A.G. (eds) Asphaltenes, Heavy Oils, and Petroleomics. Springer, New York, NY. https://doi.org/10.1007/0-387-68903-6_19.

Sherafati, M. and Jessen, K. 2017. Stability Analysis for Multicomponent Mixtures Including Capillary Pressure. Fluid Phase Equilibria, 433, pp.56-66. http://doi.org/10.1016/j.fluid.2016.11.013.

Siripatrachai, N., Ertekin, T. and Johns, R. 2017. Compositional Simulation of Hydraulically Fractured Tight Formation Considering the Effect of Capillary Pressure on Phase Behavior. SPE Journal, 22(04), pp.1046-1063. https://doi.org/10.2118/179660-PA.

van Dijke, M., McDougall, S. and Sorbie, K. 2001. Three-Phase Capillary Pressure and Relative Permeability Relationships in Mixed-Wet System. Transport in Porous Media, 44(1), pp.1-32. http://doi.org/10.1023/A:1010773606657.

Wang, F. and Reed, R. 2009. Pore Networks and Fluid Flow in Gas Shales. In: SPE Annual Technical Conference and Exhibition. New Orleans: Society of Petroleum Engineers. https://doi.org/10.2118/124253-MS.

Wang, Y., Yan, B. and Killough, J. 2013. Compositional Modeling of Tight Oil Using Dynamic Nanopore Properties. In: SPE Annual Technical Conference and Exhibition. New Orleans: Society of Petroleum Engineers. https://doi.org/10.2118/166267-MS.

Weinaug, C. and Katz, D. 1943. Surface Tensions of Methane-Propane Mixtures. Industrial & Engineering Chemistry, 35(2), pp.239-246. http://doi.org/10.1021/ie50398a028.

Whitson, C. and Brulé, M. 2000. Phase behavior. Richardson, Texas: Henry L. Doherty Memorial Fund of AIME, Society of Petroleum Engineers.

Wilson, G. M., 1969. A Modified Redlich-Kwong Equation of State, Application to General Physical Data Calculations. In: 65th National AIChE Meeting. Cleveland.

Wong, S. W., O'Dell, P. M., de Pater, C. J. and Shaoul, J. 2000. Fresh Water Injection Stimulation in a Deep Tight Oil Reservoir. In: the 2000 SPE/AAPG Western Regional Meeting. Long Beach: Society of Petroleum Engineers. http://doi.org/10.2118/62618-MS.

Wu, K., Chen, Z., Li, X. and Dong, X. 2016. Methane Storage in Nanoporous Material at Supercritical Temperature Over a Wide Range of Pressures. Scientific Reports, 6(1), 33461. http://doi.org/10.1038/srep33461.

Wu, K., Chen, Z., Li, J., Li, X., Xu, J. and Dong, X. 2017. Wettability Effect on Nanoconfined Water Flow. Proceedings of the National Academy of Sciences, 114(13), pp.3358-3363. http://doi.org/10.1073/pnas.1612608114.

Wu, K., Chen, Z., Li, J., Xu, J., Wang, K., Wang, S., Dong, X., Zhu, Z., Peng, Y., Jia, X. and Li, X. 2018. Manipulating the Flow of Nanoconfined Water by Temperature Stimulation. Angewandte Chemie International Edition, 57(28), pp.8432-8437. http://doi.org/10.1002/anie.201712915.

Young, T. 1805. An Essay on the Cohesion of Fluids. Philosophical Transactions of the Royal Society of London, 95, pp.65-87. http://doi.org/10.1098/rstl.1805.0005.

Zhang, Y., Lashgari, H., Di, Y. and Sepehrnoori, K. 2016. Capillary Pressure Effect on Hydrocarbon Phase Behavior in Unconventional Reservoir. In: SPE Low Perm Symposium. Denver: Society of Petroleum Engineers. https://doi.org/10.2118/180235-MS.

Nomenclature

A = equation of state constant

B = equation of state constant

EOS = equation of state

f_{ix} = fugacity of component I in oleic phase, bar

f_{iy} = fugacity of component I in vapor phase, bar

f_{iw} = fugacity of component I in aqueous phase, bar

IFT = interfacial tension, mN/m

k_{iy} = vapor-oleic phase equilibrium ratio of component i

k_{iw} = aqueous-oleic phase equilibrium ratio of component i

M_l = molecular weight of liquid phase, g/mol

M_g = molecular weight of vapor phase, g/mol

N_c = number of components

P = bulk pressure, bar

P_{chi} = Parachor of component i

P_g = vapor phase pressure, bar

P_w = aqueous phase pressure, bar

P_o = oleic phase pressure, bar

P_{cwo} = aqueous-oleic capillary pressure, bar

P_{cog} = oleic-vapor capillary pressure, bar

P_{cwg} = aqueous-vapor capillary pressure, bar

r = pore radius, nm

R = universal gas constant, 0.08314459848 $L \cdot bar \cdot K^{-1} \cdot mol^{-1}$

S = spreading coefficient

T = bulk temperature, K

T_{ch} = critical temperature of hydrocarbon, K

x_i = mole fraction of component I in liquid phase

y_i = mole fraction of component I in vapor phase

Z = compressibility factor

z_i = feed composition

β_y = vapor phase mole fraction

β_w = aqueous phase mole fraction

σ_{og} = oleic-vapor interfacial tension, mN/m

σ_{wg} = aqueous-vapor interfacial tension, mN/m

σ_{wo} = aqueous-oleic interfacial tension, mN/m

ρ_h = oleic phase density, g/cm^3

ρ_g = vapor phase density, g/cm^3

ρ_l = liquid phase density, g/cm^3

ρ_w = aqueous phase density, g/cm^3

ϕ_{ix} = fugacity coefficient of component *I* in oleic phase

ϕ_{iy} = fugacity coefficient of component *I* in vapor phase

ϕ_{iw} = fugacity coefficient of component *I* in aqueous phase

μ_{ix} = chemical potential of component *I* in oleic phase

μ_{iy} = chemical potential of component *I* in vapor phase

μ_{iw} = chemical potential of component I in aqueous phase

CHAPTER 4 MINIMUM MISCIBILITY PRESSURE DETERMINATION IN CONFINED NANOPORES CONSIDERING PORE SIZE DISTRIBUTION OF TIGHT/SHALE FORMATIONS

A version of this chapter has been published in *Fuel*.

Abstract

This work develops a modified minimum miscibility pressure (MMP) calculation algorithm that couples the effects of pore size distribution, capillarity, and confinement. Also, a volume translated Peng-Robinson equation of state (PR-EOS) is employed in the proposed algorithm to provide a more accurate prediction on phase densities. To calibrate the proposed algorithm, this study uses a real crude oil sample (Zhang and Gu, 2015) to perform all calculations. The binary interactive parameters (BIPs) of the components in this oil sample are tuned to match the measured oil-CO_2 MMP in tight cores by Zhang and Gu (2015). Using the proposed algorithm, the effects of temperature and pore radius on the confined oil-CO_2 MMPs are studied in detail. It is found that the oil-CO_2 MMP in nanopores decreases with decreasing pore radii. However, the confined MMP becomes almost constant when the pore radius is larger than 10 nm. With an increasing temperature, the confined oil-CO_2 MMP first increases to a certain temperature, and then decreases for all the tested pore radii. Hence, there exists a maximum confined MMP for every pore radius, and the maximum confined MMP decreases with a decreasing pore radius. Moreover, when predicting the confined MMP for a real tight reservoir, the pore size distribution is crucial, and the average pore radius is no longer applicable in the calculations because the confined MMP does not change linearly with pore radius. Results show that the confined MMP calculated using the proposed strategy is noticeably lower than the MMP calculated using the average pore radius.

Keywords: Minimum miscibility pressure, Phase behavior, Unconventional reservoir, Two-phase flash, Capillary pressure, Confinement effect, Pore size distribution, Volume translation

4.1. Introduction

The method of miscible carbon dioxide (CO_2) injection is proved to be an effective way of improving oil recovery in unconventional light to medium oil reservoirs, such as tight or shale reservoirs (Yu *et al*., 2015; Lashgari *et al*., 2019). The oil-CO_2 minimum miscibility pressure (MMP) is a crucial parameter in designing and executing CO_2 injections. Therefore, a precise description of the oil-CO_2 MMP in unconventional reservoirs is much desired for the industry. Conventionally, the oil-CO_2 MMP is determined by experimental studies (Rathmell *et al*., 1971; Yellig, 1982; Christiansen and Haines, 1987; Rao, 1997; Nguyen *et al*., 2015), empirical correlations (Holm and Josendal, 1974; Lee, 1979; Mungan, 1981; Orr and Jensen, 1984; Shokir, 2007; ZareNezhad, 2016; Li *et al*., 2012; Ahmadi *et al*., 2017), and computational simulations (Johns and Orr, 1996; Wang and Orr, 1997; Ahmadi and Johns, 2011). However, most of these MMP prediction methods are developed to determine the oil-CO_2 MMPs in the bulk conditions and are not valid in predicting the MMPs in nanopores which can be found extensively in tight/shale reservoirs. Over the years, several modifications have been made to the conventional MMP determination methods in order to predict the oil-CO_2 MMPs in confined nanopores.

Experiments are the most accurate way of determining the oil-CO_2 MMP. The most widely applied experimental methods to measure the MMP in conventional reservoirs are the coreflood test (Rathmell *et al*., 1971) and the slim-tube test (Yellig, 1982). Attempts have been made to utilize the coreflood test to study the oil-CO_2 MMP in tight/shale reservoirs by using tight/shale core samples in the experiments (Gamadi, *et al*., 2013; Zhang and Gu, 2015; Li *et al*., 2017; Li *et al*., 2018). They successfully measured the oil-CO_2 MMP in tight/shale core samples and concluded that oil recovery increases significantly with increasing injection pressures up to the oil-CO_2 MMP. When the injection pressure is above the MMP, only a slight improvement in oil recovery is

obtained. The slim-tube test is accepted as a fine alternative to the coreflood test. To measure the oil-CO_2 MMP in a confined space, some works replaced the coiled tubing with a silica capillary column without permeable material inside (Mungan, 1991; Adyani and Kechut, 2007). However, the inner diameter of the capillary column used in the slim-tube apparatus is with a scale of millimeters instead of nanometers. Therefore, the conventional slim-tube test using the capillary tubes cannot properly reflect the oil-CO_2 MMP in tight/shale reservoirs. More recently, a microfluidic model was developed and has been successfully applied in measuring the oil-CO_2 MMP (Nguyen *et al*., 2015). The model is constructed with fully visible microchannels that can withstand high temperatures and high pressure. The width and the depth of the channels are also with the scale of micrometers. Given that the nanopores in tight/shale reservoirs generally have diameters ranging from 5 to 1000 nm (Wang and Reed, 2009), the MMP measurements from the microfluidic models may lose accuracy in describing the oil-CO_2 MMP in tight/shale reservoirs.

Provided that the experimental works of the oil-CO_2 MMP measurements are very demanding on time and material, some empirical correlations are developed to provide a simple and quick estimation of the oil-CO_2 MMP under reservoir conditions. The developed MMP empirical correlations range from simple temperature-dependent forms (Lee, 1979; Yellig and Metcalfe, 1980; Orr and Jensen, 1984) to more complex temperature, oil composition, and gas composition-dependent models (Shokir, 2007; Li *et al*., 2012; Ahmadi *et al*., 2017). These correlations are all targeted at predicting the oil-CO_2 MMP in bulk conditions. In order to reflect the effect of a confined space on the MMP calculations, Zhang *et al*. (2018a) integrated the pore radius into an existing empirical MMP correlation (Li *et al*., 2012) and developed a new correlation to calculation the MMP in a confined space. The new MMP correlation developed by Zhang *et al*. (2018a) is

shown to be more accurate in predicting the oil-CO_2 MMP in confined nanopores compared to other existing correlations.

Since all the existing MMP empirical correlations are developed with limited experimental data and no correlation is universally valid, the application of these empirical correlations becomes troublesome in certain circumstances. Hence, computational simulation methods have been developed to predict the oil-CO_2 MMP through the cubic equation of state (CEOS). Because of the decent accuracy and robustness of these computational methods, many researchers have made certain modifications to study the MMP in a confined space using these computational methods. These modifications mainly focus on improving the phase behavior predictability of the CEOS in a confined space because a strong capillary pressure can significantly affect the phase behavior of reservoir fluids (Sun and Li, 2019; Sun and Li, 2020). One of the first attempts in modeling the confined oil-CO2 MMP was initiated by Teklu *et al*. (2014a). The authors coupled capillary pressure and a critical point shift model (Zarragoicoechea and Kuz, 2004) in the PR-EOS model (Peng and Robinson, 1976) and calculated vapor-liquid IFT using the Parachor model (Weinaug and Katz, 1943). They found that the oil-CO_2 MMP is reduced due to the effect of nanopores compared to the MMP calculated in the bulk conditions. The theory of the vanishing interfacial tension (IFT) was originally proposed to be used as a criterion to measure the oil-gas MMPs in experiments (Rao, 1997). It was then adopted in the computational methods to predict the oil-gas MMP in a confined space by calculating vapor-liquid IFT using modified CEOS (Wang *et al*., 2016a). Wang *et al*. (2016a) applied Perturbed-Chain Statistical Associating Fluid Theory (PC-SAFT) (Gross and Sadowski, 2011) to calculate vapor-liquid IFT in the vanishing IFT method. In addition, the authors also considered IFT reduction due to the confinement effect. They observed

a significant MMP reduction in confined nanopores from their calculation results. This conclusion corroborates with several later research works (Zhang *et al*., 2017a; Zhang *et al*, 2017b).

The method of characteristics (MOC) was proposed by Johns and Orr (1996) to calculate the MMP for a multicomponent system with more than four components. Zhang *et al*. (2018b) modified the MOC algorithm by coupling a large capillary pressure in an EOS model. They found that the MMP is only affected by capillary pressure when the fluid system has more than three components. On the other hand, the MOC method is very complex and suffers from convergence issues (Yuan and Johns, 2005). Another well-developed computation method to calculate the MMP is the multiple mixing cell (MMC) method proposed and refined by Ahmadi and Johns (2011). Teklu *et al*. (2014b) coupled capillary pressure and critical point shift (Zarragoicoechea and Kuz, 2004) in PR-EOS (Peng and Robinson, 1976) and conducted the MMC calculations. They obtained a dramatic reduction of the oil-CO_2 MMP due to the confinement effect at a pore radius of 4 nm. However, with a pore radius of 20 nm, MMP reduction in the confined space is negligible. In their work (Teklu *et al*., 2014b), volume translation is not applied in the PR-EOS model (Peng and Robinson, 1976) which leads to an incorrect prediction of phase densities and thereby an inaccurate calculation of vapor-liquid IFT.

The aforementioned methods used to study the oil-CO_2 MMP in a confined space suffer from poor accuracy. Experimental works are complicated and not entirely reliable. The correlations developed to calculate the confined MMPs are heavily limited by the low availability of comprehensive experimental data. The modified MOC method (Zhang *et al*. 2018b) is complex and has serious convergence issues. The modified MMC method developed by Teklu *et al*. (2014b) is the most promising method to study the confined oil-CO_2 MMP. However, their algorithm did not employ a volume translation model. This may cause incorrect phase density prediction in the

confined space. Also, actual tight/shale formations all have highly heterogeneous pore spaces. Therefore, the effect of pore size distribution on the oil-CO_2 MMP should be properly addressed in an MMP prediction method. However, the pore size distribution is not considered in the existing confined oil-CO_2 MMP calculation methods (Teklu *et al*., 2014b).

This work is devoted to developing a comprehensive thermodynamic model that can more reasonably describe the oil-CO_2 MMP profiles in tight/shale reservoirs with the consideration of pore size distribution. In this study, a new MMP calculation algorithm is developed based on the MMC algorithm (Ahmadi and Johns, 2011). The effects of pore size distribution, capillarity, and confinement are coupled in the proposed algorithm. Also, a decent volume translated PR-EOS model (Peng and Robinson, 1976; Abudour *et al*., 2013) is employed for a better prediction of vapor-liquid IFT. The proposed MMP calculation algorithm is first calibrated with a CO_2 coreflood test conducted using tight core samples (Zhang and Gu, 2015). It is then applied to perform a series of calculations to examine the robustness of the algorithm and to study the effect of temperature and pore radius on the oil-CO_2 MMPs in confined nanopores.

4.2. Methodology

This section presents the mathematical formulations of the PR-EOS model (Peng and Robinson, 1976) coupled with capillary pressure, confinement effect, and the volume translation method proposed by Abudour *et al.* (2013).

4.2.1. Confined Thermodynamic Model

In this study, the volume translated PR-EOS (Peng and Robinson, 1976; Abudour *et al*., 2013) is employed for the two-phase equilibrium calculations. In order to reflect the effect of confined

nanopores on the two-phase equilibrium calculations, capillary pressure and a critical point shift model are coupled with the EOS model during the calculations.

At given pressure, temperature, and mixture compositions, the two-phase equilibrium can be determined by satisfying the chemical potential equality condition given in Eq. (4-1) (Whitson and Brulé, 2000).

$$\mu_{ix}(P_l, T, z_i) = \mu_{iy}(P_v, T, z_i) \qquad i = 1, \dots, N_c \tag{4-1}$$

where μ_{ix} and μ_{iy} are the chemical potential of component *I* in the liquid phase and the vapor phase, respectively, P_l is the liquid-phase pressure, P_v is the vapor-phase pressure. T is the system temperature, and z_i is the mixture feed compositions. The chemical potential equality condition can be alternatively expressed in terms of fugacity which can be calculated by PR-EOS (Peng and Robinson, 1976). The fugacity equality condition is given in Eq. (4-2) (Whitson and Brulé, 2000).

$$f_{ix}(P_l, T, z_i) = f_{iy}(P_v, T, z_i) \qquad i = 1, \dots, N_c \tag{4-2}$$

where f_{ix} and f_{iy} are the fugacities of component *I* in the liquid phase and the vapor phase, respectively. Note that in the bulk conditions, the liquid pressure and the vapor pressure are equal to each other. In confined nanopores, however, the liquid pressure and the vapor pressure are different due to the existence of capillary pressure. Capillary pressure can be expressed by Eq. (4-3).

$$P_c = P_v - P_l \tag{4-3}$$

where P_c is the capillary pressure of the adjacent liquid and vapor phases. The Young-Laplace equation (Young, 1805) is employed here to calculate capillary pressure with the assumptions of

zero contact angle and equal principle pore radii. The Young-Laplace equation is given in Eq. (4-4) (Young, 1805).

$$P_c = \frac{2\sigma}{r_p} \tag{4-4}$$

where r_p is the pore radius, σ represents the IFT between the liquid phase and the vapor phase and can be calculated using the Parachor model (Weinaug and Katz, 1943) given in Eq. (4-5).

$$\sigma = \left[\sum_{i=1}^{N_c} P_{chi}\left(x_i\rho_l - y_i\rho_g\right)\right]^4 \qquad i = 1, \dots, N_c \tag{4-5}$$

where P_{chi} is the Parachor constant of component I, ρ_l and ρ_g are the liquid-phase molar density and the vapor-phase molar density, respectively. In the proposed MMP calculation algorithm, the liquid-phase molar density is corrected by volume translation and is calculated by Eq. (4-6).

$$\rho_l = \frac{1}{V_{corr,l}} \tag{4-6}$$

where $V_{corr,l}$ is the corrected liquid-phase molar volume. This volume translation model will be discussed in detail in section 2.2.

Apart from a large capillary pressure introduced by nanopores, the critical properties (i.e., critical pressure and critical temperature) of mixtures inside a confined space are shifted as well due to the strong molecule-wall interactions (Qiu *et al*., 2019; Tan *et al*., 2019). An analytical model recently proposed by Tan *et al*. (2019) is coupled in the PR-EOS model (Peng and Robinson, 1976) to mathematically calculate the critical properties shift of the oil-constituting components generated by confined nanopores. This model is based on the one proposed by Zarragoicoechea and Kuz

(2004) but is modified and validated with recent experiments. The analytical model (Tan *et al*., 2019) used to calculate the critical properties shift is given in Eq. (4-7).

$$\begin{cases} \frac{T_{cb}-T_{cp}}{T_{cb}} = 0.0519\left(\frac{\sigma_{LJ}}{r_p}\right)^2 - 25.7585\left(\frac{\sigma_{LJ}}{r_p}\right)^4 \\ \frac{P_{cb}-P_{cp}}{P_{cb}} = 0.7689\frac{\sigma_{LJ}}{r_p} - 28.7529\left(\frac{\sigma_{LJ}}{r_p}\right)^3 \\ \sigma_{LJ} = 0.244\sqrt[3]{\frac{T_{cb}}{P_{cb}}} \end{cases} \tag{4-7}$$

where T_{cb} and T_{cp} are the critical temperatures in the bulk conditions and nanopores, respectively, P_{cb} and P_{cp} are the critical pressure in the bulk conditions and nanopores, respectively, and σ_{LJ} is the collision diameter, also known as the Lennard-Jones size parameter. **Fig. 4-1** illustrates the calculated critical properties reductions for hydrocarbon components of a real crude oil sample due to the confinement effect (Zhang and Gu, 2015). It is seen from **Fig. 4-1** that the critical temperatures and critical pressures of hydrocarbon components are all reduced in the confined space. The reduction effect becomes more significant with a smaller pore radius.

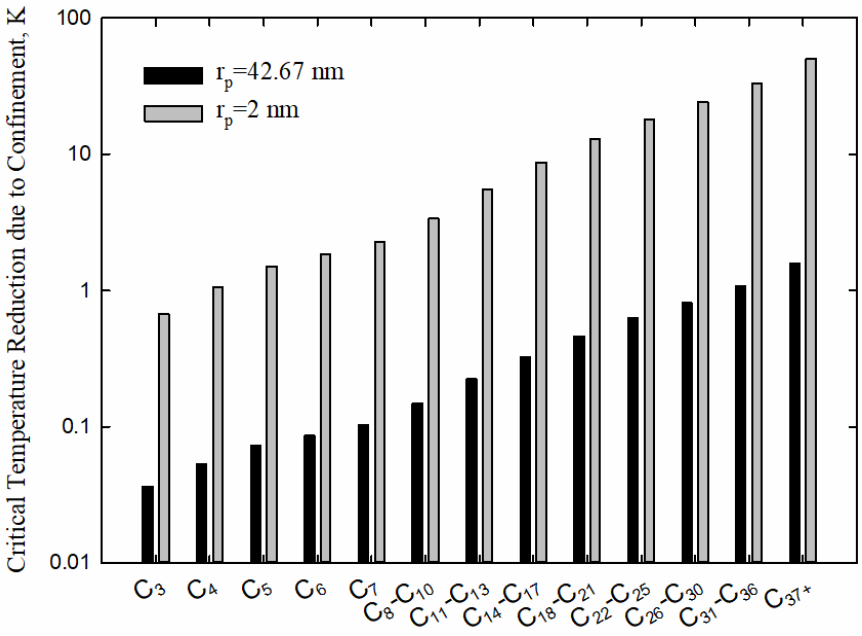

(a)

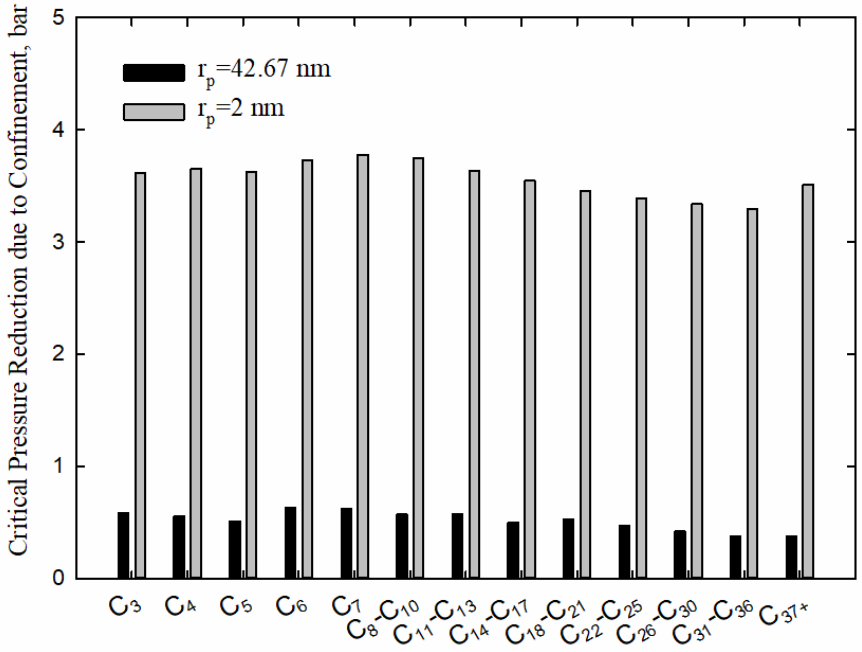

(b)

Fig. 4-1: Reductions of (a) critical temperature and (b) critical pressure due to the confinement effect of constituting components of a crude oil sample studied by Zhang and Gu (2015).

4.2.2. Volume Translation Model

The volume translation model developed by Abudour *et al*. (2013) is a temperature-dependent model that can be applied to multicomponent systems. The equation is given in Eq. (4-8) (Abudour *et al*. 2013).

$$V_{corr} = V_{PR} + C_m - \delta_m \left(\frac{0.35}{0.35+d_m}\right) \tag{4-8}$$

where V_{corr} is the corrected molar volume, V_{PR} is the original molar volume calculated by PR-EOS (Peng and Robinson, 1976), C_m is the volume translation term for mixtures, δ_{cm} is the volume correction for mixtures at the critical point, and d_m is the dimensionless distance function.

The volume translation term for mixtures C_m is calculated using Eq. (4-9) (Abudour *et al*., 2013).

$$C_m = \frac{RT_{cm}}{P_{cm}}[C_{1m} - (0.004 - C_{1m})exp(-2d_m)] \tag{4-9}$$

where T_{cm} is the critical temperature for mixture, P_{cm} is the critical pressure for mixture, and C_{1m} is a fluid-dependent parameter for multicomponent systems.

The critical pressure of the mixture P_{cm} is calculated by Eq. (4-10) (Aalto *et al*., 1996).

$$P_{cm} = \frac{(0.2905-0.085\omega_m)RT_{cm}}{V_{cm}} \tag{4-10}$$

where R is the universal gas constant and ω_m is the acentric factor for the mixture. Ω_m can be calculated using a simple linear mixing rule given in Eq. (4-11) (Aalto *et al*., 1996).

$$\omega_m = \sum_{i=1}^{N_c} x_i\omega_i \qquad i = 1, \dots, N_c \tag{4-11}$$

where ω_i is the acentric factor for component *i*. The same linear mixing rule is also applied to calculate C_{1m} given in Eq. (4-12) (Peneloux *et al*. 1982).

$$C_{1m} = \sum_{i=1}^{N_c} x_i C_{1i} \qquad i = 1, \dots, N_c \tag{4-12}$$

where C_{1i} is a fluid-dependent parameter for component *I* and can be calculated using Eq. (4-13) (Peneloux *et al*. 1982).

$$C_{1i} = 0.4266 Z_{exp,i} - 0.1101 \tag{4-13}$$

where $Z_{exp,\,i}$ is the experimental critical compressibility factor for component *i*.

The dimensionless distance function is applied to improve the accuracy of volume correction in the near-critical region. The dimensionless function d_m is calculated by Eq. (4-14) (Chou and Prausnitz, 1989).

$$d_m = \frac{1}{RT_{cm}} \left(\frac{\partial P_{PR}}{\partial \rho_m} \right)_T \tag{4-14}$$

P_{PR} is the system pressure, and ρ_m is the molar density of the mixture.

In Eq. (4-8), the volume correction for mixtures at the critical point δ_{cm} is a composition-dependent function and the equation is given by Eq. (4-15) (Abudour *et al*., 2013).

$$\delta_{cm} = V_{cm,PR}(x) - V_{cm}(x) \tag{4-15}$$

where $V_{cm,\,PR(x)}$ is the predicted mixture critical volume that calculated from PR-EOS (Peng and Robinson, 1976), and $V_{cm(x)}$ is the true critical volume of mixtures. $V_{cm,\,PR}(x)$ is calculated by Eq. (4-16) (Abudour *et al*., 2013).

$$V_{cm,PR}(x) = \frac{RT_{cm}}{P_{cm}}\left(Z_{c,EOS}\right) \tag{4-16}$$

where $Z_{c,\ EOS}$ is the calculated critical compressibility factor calculated from PR-EOS (Peng and Robinson, 1976) that has a constant value of 0.3074. $V_{cm}(x)$ is estimated based on the component surface fraction (θ) and V_{ci} according to (Chueh and Prausnitz, 1967):

$$V_{cm}(x) = \sum_{i=1}^{N_c} \theta_i V_{ci} \qquad i = 1, \dots, N_c \tag{4-17}$$

4.3. MMP Algorithm Considering Pore Size Distribution

The algorithm of the proposed MMP calculation is based on the standard MMC calculation procedure (Ahmadi and Johns, 2005). The two-phase equilibrium calculation within the standard MMC calculation is modified to reflect the effects of capillarity and confinement in nanopores. A detailed procedure for conducting the proposed MMP calculation is presented as follows.

1) The algorithm is initiated with a specification on the reservoir temperature. The critical properties shift of each component is calculated to include the confinement effect.
2) The first contact is made by mixing the first two cells that are filled with injection gas and reservoir oil. The feed composition of the mixture can be calculated by the material balance equation given in Eq. (4-18).

$$z_i = x_i^O + 0.5\left(y_i^G - x_i^O\right) \tag{4-18}$$

where z_i is the mole fraction of component *I* in the gas-oil mixture, x_i^O and y_i^G represent the mole fraction of component *I* in the liquid phase and the vapor phase, respectively.

3) After the overall feed compositions of a gas-oil mixture are obtained, the two-phase equilibrium calculation coupled with capillary pressure and the critical point shift model is conducted with the overall feed compositions. Then, the mole fraction and the

compositions of the equilibrium vapor phase and the equilibrium liquid phase can be acquired from the flash calculations. In addition, the tie-line length of this contact is recorded and can be calculated by Eq. (4-19) (Ahmadi and Johns, 2011):

$$TL = \sqrt{\sum_{i=1}^{Nc}(x_i - y_i)^2} \tag{4-19}$$

where TL is the tie-line length, N_c is the number of components, x_i and y_i represent the mole fractions of component I in the equilibrium liquid phase and the equilibrium vapor phase, respectively.

4) Then the algorithm moves on to the second contact where two contacts occur: the contact between the injection gas and the equilibrium liquid phase; the contact between the equilibrium vapor phase and the reservoir oil. Two-phase equilibrium calculation coupled with capillary pressure and volume translation is conducted for both contacts and the tie-line length of each contact is recorded.
5) The additional contacts between the neighboring cells proceed until the key tie-lines are developed. Note that the key tie lines are fully developed when the same values of the tie-line lengths are obtained for three successive cells (Ahmadi and Johns, 2005). The minimum tie-line length for all contacts is recorded.
6) The proposed MMP calculation is performed at different pressures. The minimum key-tie line is reduced with a higher pressure. The MMP is determined at the pressure where the minimum key tie-line length reaches zero and can be estimated by extrapolating the minimum key tie-line lengths at the last several pressures. The power-law extrapolation used to estimate the MMP is given in Eq. (4-20) (Ahmadi and Johns, 2005):

$$TL^n = aP + b \tag{4-20}$$

where n is the exponential parameter, a is the slope, and b is the intercept of the y-axis. It is suggested that the parameters n, a, and b can be finalized when the square of the correlation coefficient exceeds 0.999 (Ahmadi and Johns, 2005).

7) The proposed MMP calculation algorithm possesses the capability of predicting the confined MMP when the pore size distribution is available. Ideally, the capillary pressure should be calculated using a function of oil and gas saturations in a reservoir simulator to consider the pore size distribution. Such an equation is given below (Rezaveisi *et al*., 2018).

$$P_c = C_{pc}\sigma\sqrt{\frac{\overline{\emptyset}}{k}}\left(\frac{\overline{S_g}}{\overline{S_g}+\overline{S_o}}\right)^{E_{pc}} \tag{4-21}$$

where $\overline{S_g}$ and $\overline{S_o}$ are the normalized saturation of oil and gas, respectively, σ represents the IFT between the liquid phase and the vapor phase, $\emptyset$ is porosity, k is permeability, and C_{pc} and E_{pc} are constants. To apply this equation, the normalized saturation of oil and gas should be obtained for each contact. Then the capillary pressure considering pore size distribution can be calculated. However, in a standalone confined MMP calculation practice as developed in this work, a mixing rule is used as an alternative to include the effect of pore size distribution on the confined MMP calculation. When the representative pore size distribution of a given tight/shale formation is available, the following mixing rule is proposed to calculate the average confined MMP.

$$MMP_{avg} = \sum_{i=1}^{N_r} D_{r_i} \times MMP_{r_i} \tag{4-22}$$

where MMP_{avg} is the average confined MMP, N_r is the total number of representative pore sizes obtained from the pore-size-distribution charts, D_{ri} is the distribution of pore radius r_i, and MMP_{ri} is the MMP at pore radius r_i. In general, the confined MMP corresponding to each pore radius is first calculated. Then, the mixing rule expressed by Eq. (4-22) is used to calculate the average confined MMP in tight/shale reservoirs.

This proposed MMP calculation algorithm provides an estimation of the oil-CO_2 MMP in confined nanopores with the consideration of the pore size distribution. The MMP calculation algorithm proposed by this work is similar to the one developed by Teklu *et al*. (2014b). However, our algorithm adopts a volume translation method (Abudour *et al*., 2013) to improve the accuracy of vapor-liquid IFT prediction which results in a better description of the two-phase equilibrium in confined nanopores. Also, the algorithm proposed by this work employs a state-of-art critical point shift model which has been validated by experiments (Tan *et al*., 2019). Furthermore, the pore size distribution is considered in the algorithm and a new MMP calculation strategy is proposed; to our knowledge, this is not featured in any previous research. An overview of the proposed confined MMP calculation workflow is given in **Fig. 4-2**.

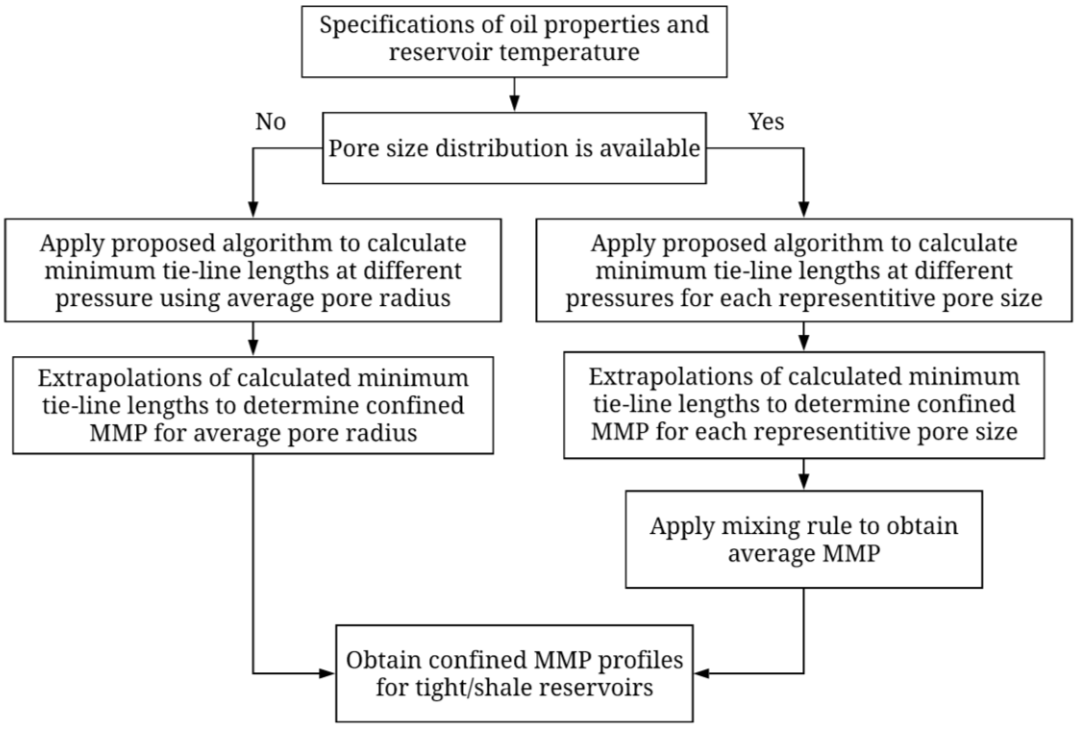

Fig. 4-2: Overview of the MMP calculation workflow using the proposed algorithm with the consideration of pore size distribution.

4.4. Results and Discussions

During the two-phase equilibrium calculations in the proposed MMC algorithm, the volume translated PR-EOS (Peng and Robinson, 1976; Abudour *et al*., 2013) is employed to provide a more accurate prediction on phase densities and thereby improve the accuracy of IFT calculations. The performance of coupling volume translation in the confined two-phase equilibrium calculations is examined by comparing the calculated IFT with the experimental data (Weinaug and Katz, 1943; Seneviratne *et al*., 2017) for a binary hydrocarbon system. Then, the compositions and properties of a real oil sample are extracted from the study by Zhang and Gu (2015). The binary interactive parameters (BIPs) of this oil sample are calibrated using the MMP data measured in tight cores by Zhang and Gu (2015). This oil sample is used in the subsequent calculations to study the effects of temperature, pore radius, and pore size distribution on the confined MMP calculations.

4.4.1. Validation of IFT Calculation

The experimental IFT data are collected from the literature (Weinaug and Katz, 1943; Seneviratne *et al*., 2017) for a binary hydrocarbon mixture methane-propane (C_1-C_3). The experimental IFTs are measured at different temperatures and compositions. Vapor-liquid IFTs of the mixture C_1-C_3 are calculated at the experimental conditions to examine whether using a more accurate volume translation method in PR-EOS (Peng and Robinson, 1976) improves the interfacial tension reproduction. **Fig. 4-3**. Shows a parity plot that compares the calculated IFTs against the measured IFTs.

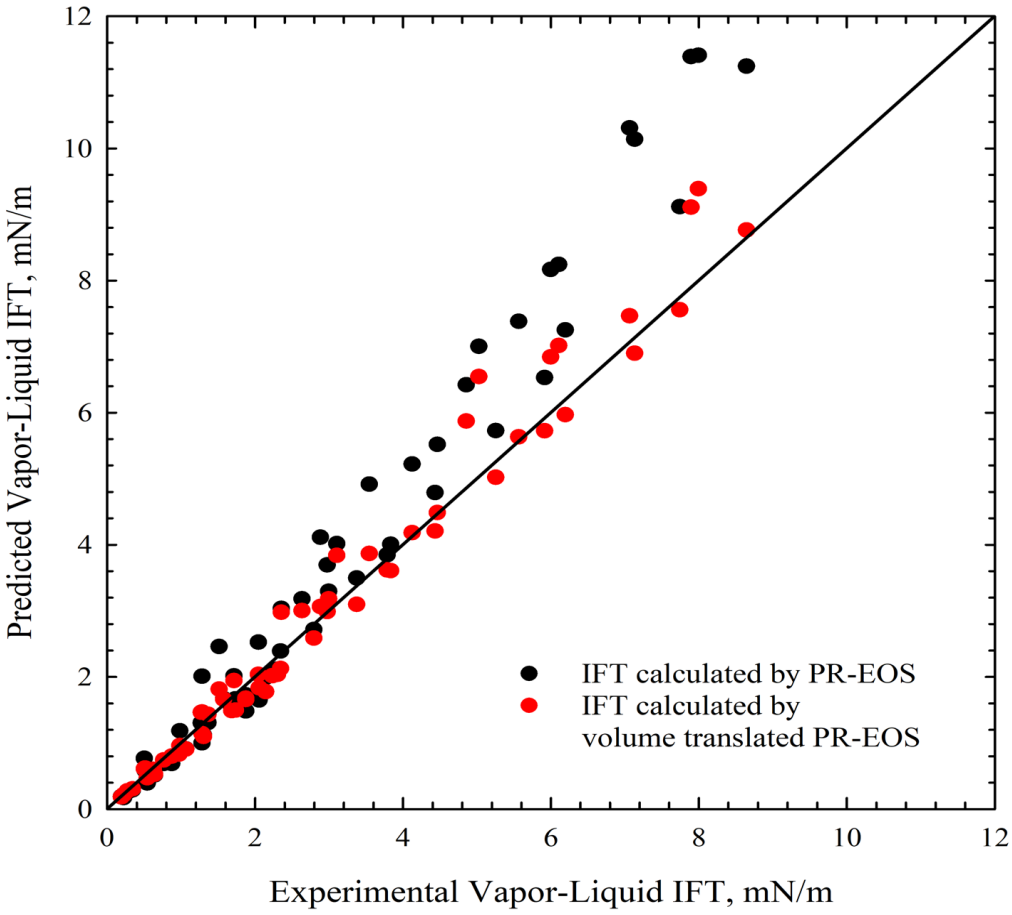

Fig. 4-3: Comparison between calculated vapor-liquid IFTs and experimental data (Weinaug and Katz, 1943; Seneviratne et al., 2017) for hydrocarbon mixture C_1-C_3.

The average absolute deviation of IFTs calculated by PR-EOS (Peng and Robinson, 1976) from the experimental data (Weinaug and Katz, 1943; Seneviratne *et al*., 2017) for the C_1-C_3 mixture is 21%. After the volume translation method (Abudour, *et al*., 2013) is applied, the average absolute deviation of calculated IFTs from the measured ones (Weinaug and Katz, 1943; Seneviratne *et al*., 2017) is reduced to 9%. The volume translated PR-EOS (Peng and Robinson, 1976; Abudour *et al*., 2013) significantly increases the accuracy of IFT prediction for the hydrocarbon mixture C_1-C_3. As such, the implementation of volume translation in the PR-EOS model (Peng and Robinson,

1976; Abudour *et al*., 2013) can effectively improve the accuracy of the two-phase equilibrium calculations in confined nanopores.

4.4.2. Calibration of the MMC Code with Measured MMP

The proposed MMP calculation algorithm is validated using the measured confined MMP data (Zhang and Gu, 2015). Using six cores, Zhang and Gu (2015) conducted CO_2 flooding experiments to study the efficiency of CO_2 flooding for tight oil recovery. Oil recovery factors of five tight core samples being displaced by pure CO_2 were measured in the experiments. The experiments were carried out with a reservoir temperature of 326.15 K. They conducted the coreflood tests with five tight core samples at different injection pressures and they performed quadratic extrapolation to obtain the oil recovery factor curve. The oil-CO_2 MMP in tight core samples was determined to be 123 bar at an oil recovery of 87% (Zhang and Gu, 2015).

The measured MMP is used to calibrate the BIPs between the constituting components in the crude oil and CO_2. Then the calibrated MMC code is employed to perform all the subsequent calculations. The C_{7+} fraction of this oil sample is lumped into seven pseudo components. The critical properties of these pseudo components are calculated using the mixing rules proposed by Lee and Kesler (1975). The BIPs between each constituting component and CO_2 are tuned by matching the calculated MMP and the confined MMP measured by Zhang and Gu (2015). Because the pore size distribution chart is not available for the tested core samples, the average pore radii of the five tested tight core samples are estimated in order to properly calculate the confined MMP. The average pore radii can be estimated using the Winland equation (Kolodzie Jr. 1980) given in Eq. (4-23).

$$logr_{35} = 0.732 + 0.588logk - 0.864log\emptyset \tag{4-23}$$

where r_{35} is the pore radius at 35% mercury saturation, k is the core permeability in *mD*, and $\emptyset$ is the core porosity in percentage. The average pore radius of five tested core samples is calculated to be 42.67 nm. Then, the BIPs can be determined by matching the calculated confined MMP with the experimental data. The compositions, physical properties, and tuned BIPs of the constituting components for the tested oil sample are listed in **Table 4-1**.

Table 4-1: Compositions and physical properties of the oil sample used in the experimental study by Zhang and Gu (2015).

	Compositions	Critical pressure (P_c), bar	Critical temperature (T_c), K	Acentric factor (ω)	*Parachor* (P_{ch})	*BIPs* with CO_2
C_3	0.002	42.46	369.80	0.152	150.30	0.070
C_4	0.012	38.00	425.20	0.193	189.90	0.070
C_5	0.037	33.74	469.60	0.251	231.50	0.070
C_6	0.050	32.89	507.50	0.275	250.11	0.073
C_7	0.107	31.38	543.20	0.308	278.40	0.073
C_8-C_{10}	0.218	27.34	597.49	0.395	345.66	0.073
C_{11}-C_{13}	0.154	22.10	662.26	0.517	448.65	0.074
C_{14}-C_{17}	0.138	18.09	724.30	0.662	573.30	0.074
C_{18}-C_{21}	0.091	15.01	775.23	0.799	695.05	0.074
C_{22}-C_{25}	0.052	12.73	818.78	0.926	793.57	0.074
C_{26}-C_{30}	0.047	11.01	855.30	1.034	879.70	0.074
C_{31}-C_{36}	0.031	9.41	895.40	1.147	967.66	0.074
C_{37+}	0.062	8.51	1014.58	1.685	1078.87	0.074

The oil-CO_2 MMP of this oil sample under the experiment conditions (T=326.15 K) (Zhang and Gu, 2015) is calculated to demonstrate how the confined MMP is determined using the concept of key tie-line lengths (Ahmadi and Johns, 2011). The MMP of this oil sample in the bulk condition is also calculated for comparison. The calculated minimum tie-line length curves with different pressure and their extrapolations are shown in **Fig. 4-4**.

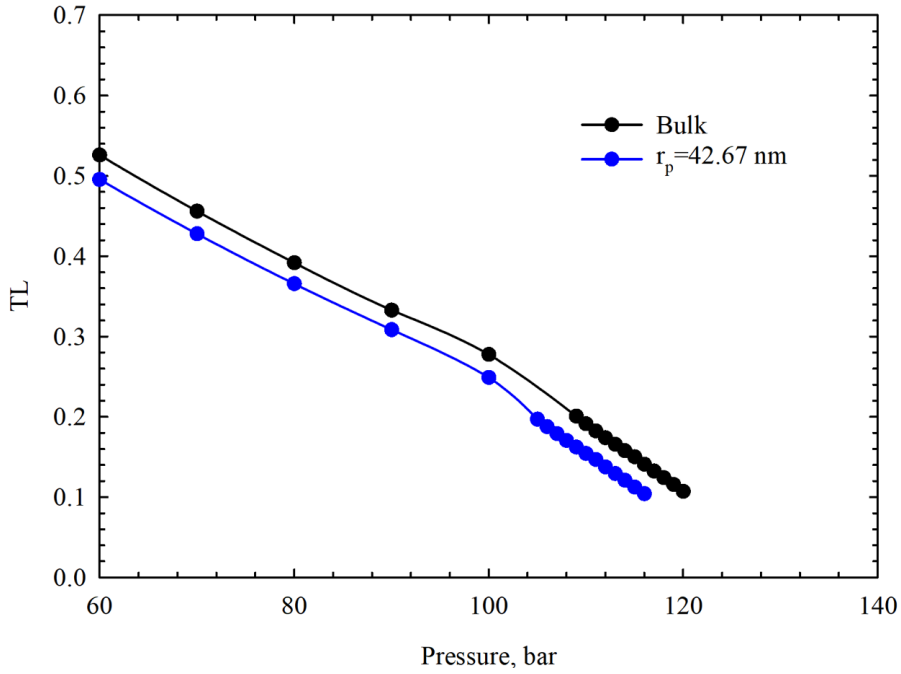

(a)

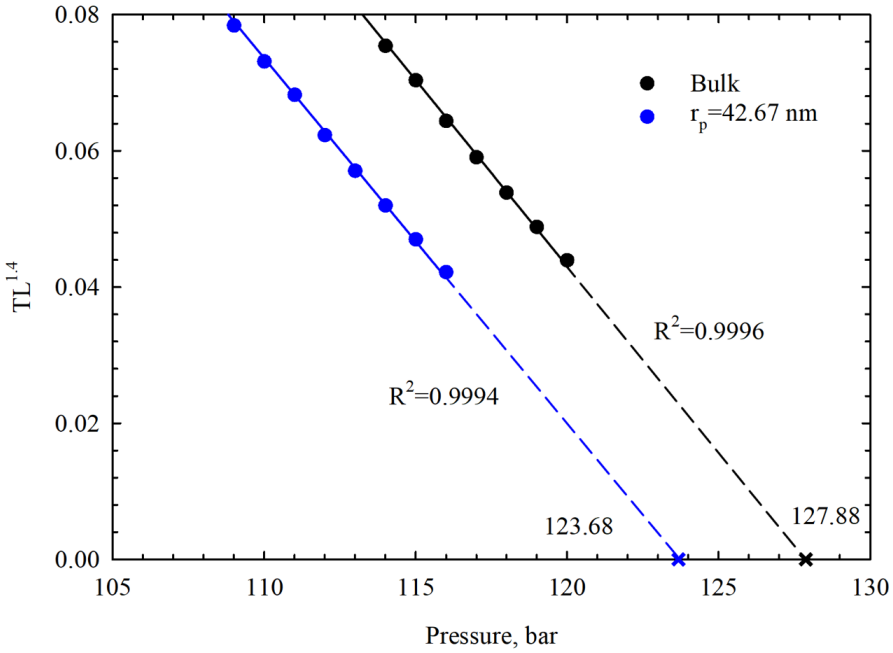

(b)

Fig. 4-4: (a) Minimum tie-line length curves at different pressures and (b) their extrapolation for the oil sample being displaced by CO_2 under the bulk conditions and experimental conditions (Zhang and Gu, 2015).

It is seen from **Fig. 4-4** that there is a clear reduction of the MMP in a confined space compared to the bulk MMP. This is due to the combined effects of capillary pressure and critical point shift. This result proves that the proposed algorithm is able to reflect the effect of the confined space on the MMP calculations. To examine the robustness of the proposed algorithm in finding the key tie-line lengths, four profiles of tie-line length for the oil sample being displaced by pure CO_2 in the bulk conditions and a confined space at a reservoir temperature of 326.15 K and an injection pressure of 115 bar are calculated as functions of the contact numbers. **Fig. 4-5**. Shows the calculation results.

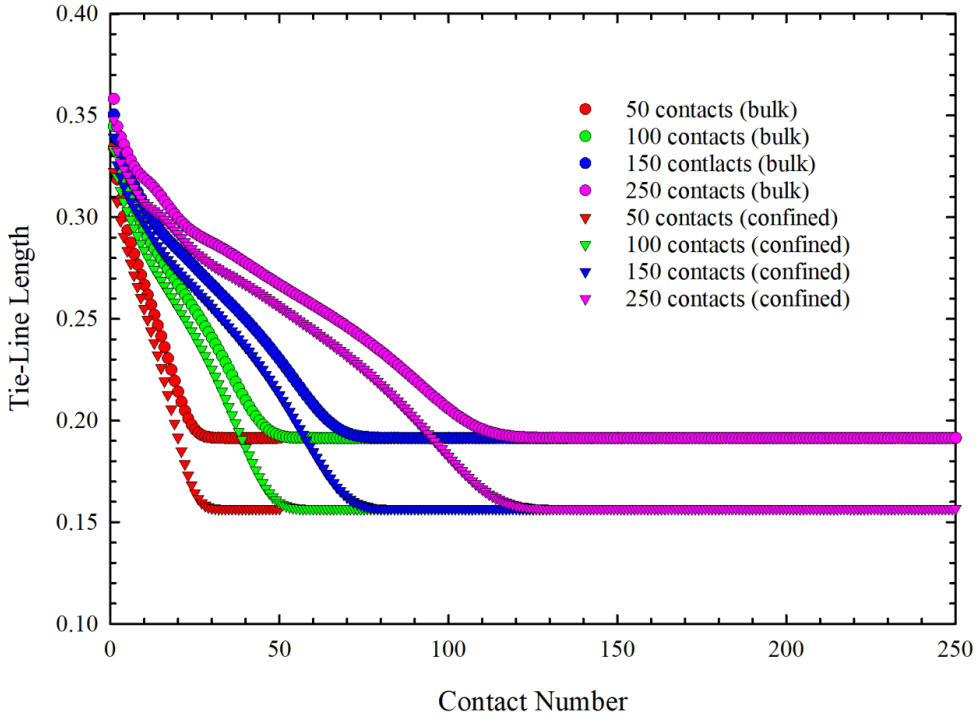

Fig. 4-5: Key tie-line development for the oil sample being displaced by pure CO_2 at 326.15 K and 110 bar in the bulk conditions and a confined space with a pore radius of 42.67 nm.

Fig. 4-5 shows the development of key tie-line lengths of the oil sample being displaced by pure CO_2 with four different total contact numbers. It is previously mentioned that the key tie-line is

considered to be fully developed when three successive cells yield the same tie-line length (i.e., the slope among the three neighboring contacts becomes zero). It is seen from **Fig. 4-5** that the shortest key tie-line is the oil tie-line, indicating a miscibility generated by a vaporizing drive between the oil sample and CO_2. As **Fig. 4-5** suggests, the shortest key tie-line length (oil tie-line) is fully developed after 50 contacts, demonstrating that the proposed algorithm offers reliable performance in developing the key tie-line lengths. To ensure decent robustness, the proposed algorithm sets the total contact number as 250 for the confined MMP calculations.

4.4.3. Effects of Pore Radius and Temperature on the Confined MMPs Calculations

It is well established that the pore radius and temperature pose strong effects on the oil-CO_2 MMP (Yuan *et al*., 2005; Wang *et al*., 2016a; Zhang *et al*., 2019a). By applying the proposed algorithm on the tight oil sample used by Zhang and Gu (2015), this work presents more comprehensive studies and discussions on the effects of pore radius and temperature on the confined MMP calculations. The confined MMPs of the tested oil sample being displaced by pure CO_2 at a wide range of temperatures with different pore radii are calculated and illustrated in a three-dimensional rendering shown in **Fig. 4-6**.

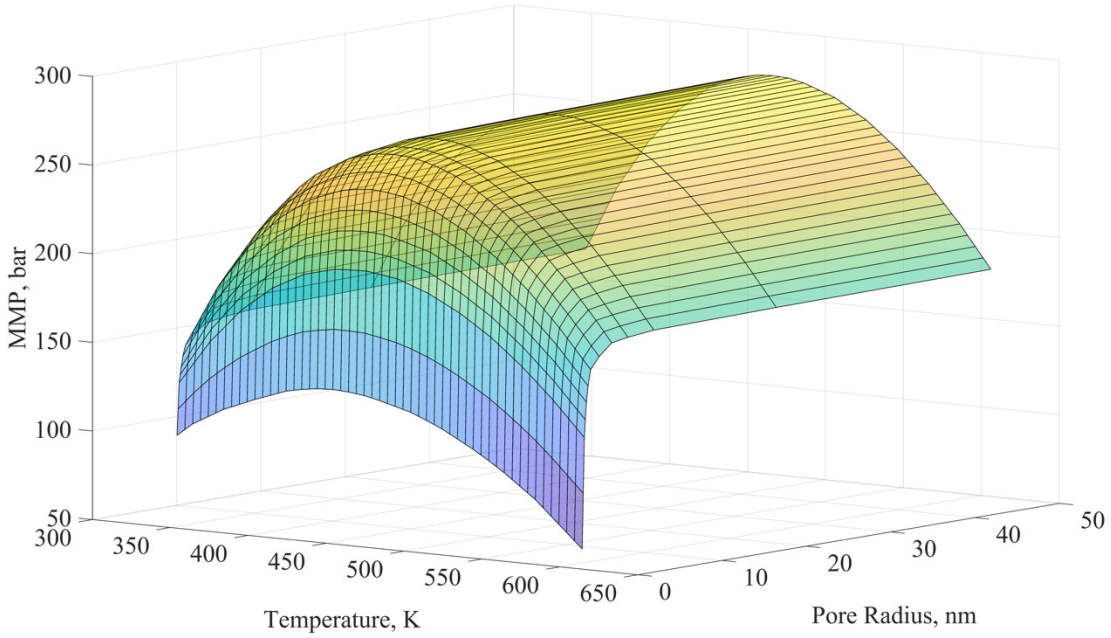

(a)

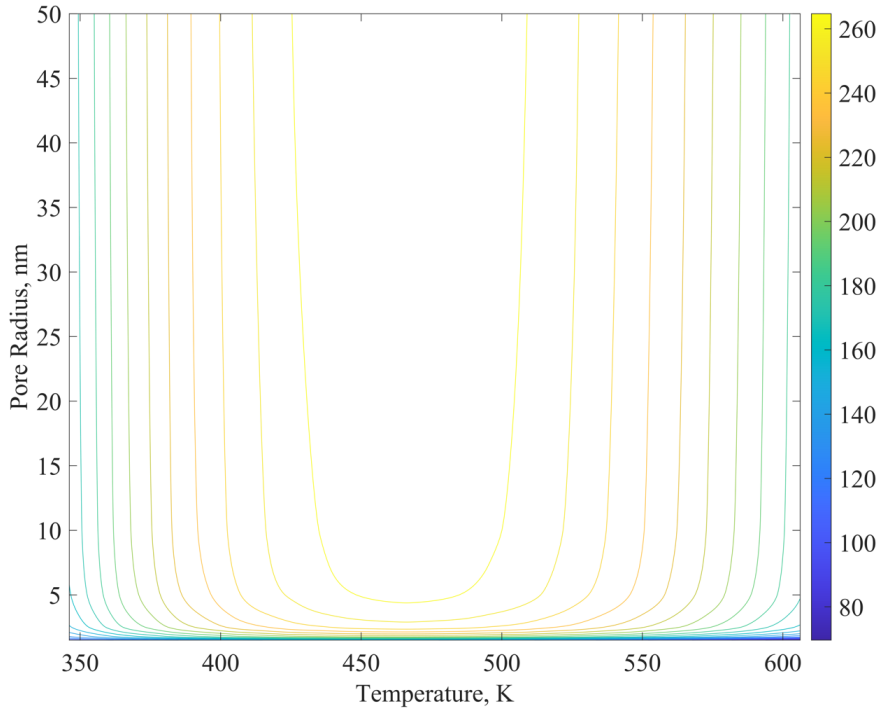

(b)

Fig. 4-6: (a) Three-dimensional illustration and (b) contour plot of the calculated confined MMPs for the oil sample being displaced by pure CO_2 at different temperatures and pore radii.

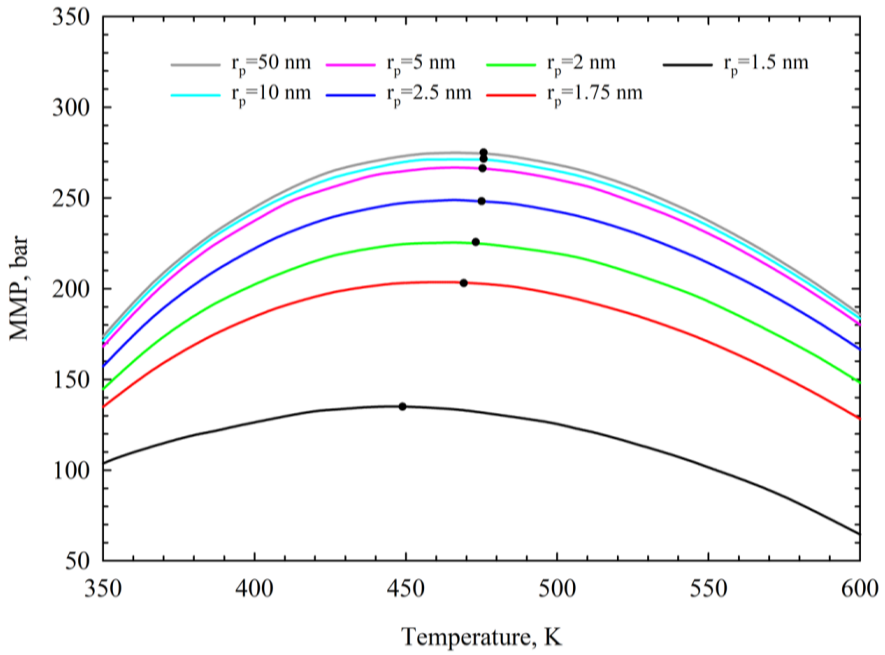

Fig. 4-7: The effect of temperature on the confined oil-CO2 MMP calculations with different pore radii.

Fig. 4-7 shows the effect of temperature on the confined MMPs calculated with different pore radii. The solid lines in **Fig. 4-7** show the calculated oil-CO_2 MMPs in confined nanopores at different temperatures. **Fig. 4-7** suggests that the oil-CO_2 MMP in a confined space first increases and then decreases with an increasing temperature. Hence, there exists a maximum MMP in the confined space, and this maximum MMP differs at different pore radii. The maximum MMP for every pore radius is labeled in **Fig. 4-7** as black marks. This trend was also observed for the bulk MMP calculations in a previous study (Yuan *et al*., 2005). This is attributed to the changes in the phase behavior of CO_2 and crude oil mixtures in response to the temperature changes. At an elevated temperature, the crude oil tends to be more vapor-phase like, and the oil-CO_2 MMP becomes the miscibility pressure between one vapor phase and one vapor-phase-like liquid phase or between two vapor phases. This explains why, above a certain temperature, the calculated oil-CO_2 MMP in

a confined space starts to decrease with an increasing temperature. Furthermore, the maximum confined MMP is a unique value for every pore radius. **Fig. 4-8** depicts the relation between the maximum confined MMP and the pore radius on the basis of the results shown in **Fig. 4-7**.

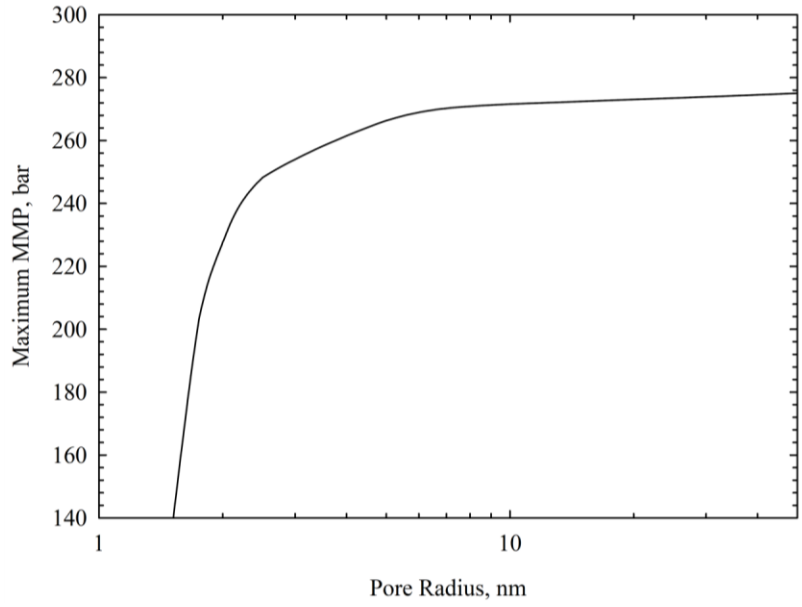

(a)

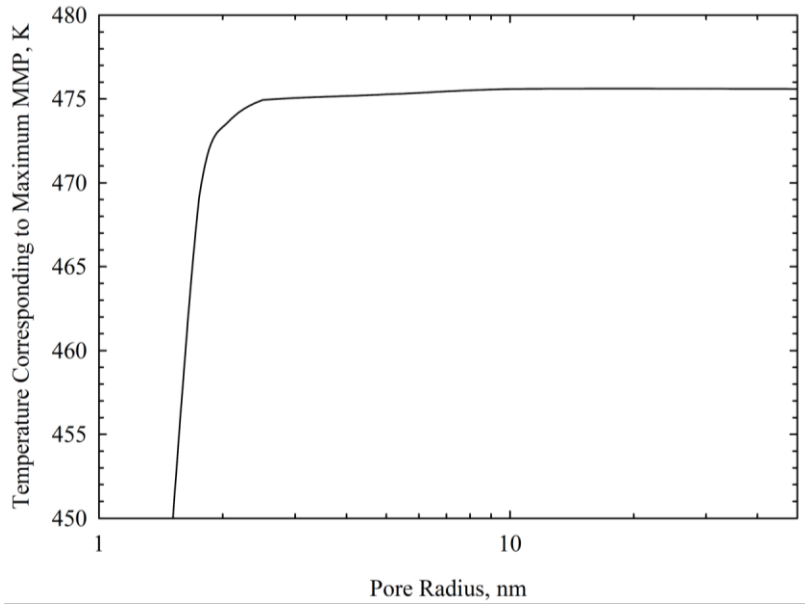

(b)

Fig. 4-8: (a) The maximum confined oil-CO_2 MMPs and (b) temperatures corresponding to the maximum confined MMPs with respect to pore radius.

The maximum confined MMP decreases with decreasing pore radii. This reduction of the maximum confined MMP is negligible when the pore radius is larger than 10 nm. Thus, the maximum confined MMP is considered to be independent of the pore radius when the pore radius is larger than 10 nm. In addition, a temperature corresponds to the maximum confined MMP for every pore radius. It is seen in **Fig. 4-8(b)** that the temperatures corresponding to the maximum confined MMPs decrease with a decreasing pore radius. Also, temperatures corresponding to the maximum confined MMP become constant when the pore radius is larger than 2.5 nm. Further calculations are conducted to investigate the effect of pore radius on the confined MMP calculations. The effects of capillary pressure and critical point shift on the confined MMP calculations are studied in **Fig. 4-9**.

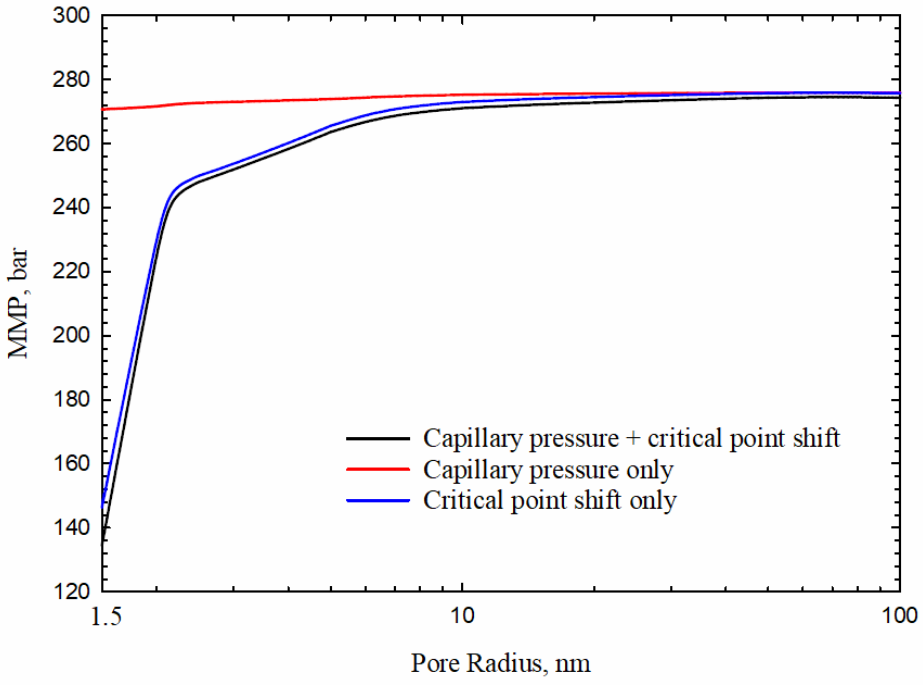

Fig. 4-9: Effect of pore radius on confined oil-CO_2 MMPs when only capillary pressure or critical point shift is considered. The combined effect of capillary pressure and critical point shift on the confined MMP calculations is also illustrated.

It is seen from **Fig. 4-9** that both the capillary pressure and critical point shift tend to decrease the calculated MMP in confined nanopores. **Fig. 4-9** further shows that the MMP reduction in confined nanopores is caused primarily by the critical point shift due to the confinement effect.

Fig. 4-10 shows the variations of the confined oil-CO_2 MMP as a function of pore radius under three reservoir temperatures. In **Fig. 4-10**, three solid lines with different colors are the calculated oil-CO_2 MMPs with various pore radii at three different reservoir temperatures. It is seen from **Fig. 4-10** that the oil-CO_2 MMP is significantly reduced in confined nanopores. Such MMP reduction due to the confined space is most significant when the pore radius is less than 2.5 nm. But it must be also noted that the MMP calculations in such small nanopores may become less reliable as molecule-level phenomena start to play a more important role in affecting the phase behavior of CO_2 and crude oil within the nanopores (such as adsorption and non-homogeneous density distributions in the nanopore). When the pore radius is larger than 10 nm, the confined MMP becomes almost constant which is close to the oil-CO_2 MMP in the bulk conditions. A similar MMP variation trend as a function of pore radius has been also reported in the MMP study by Wang *et al*. (2016). Their algorithm employs the PC-SAFT and the vanishing IFT method to calculate the confined MMP, while our algorithm applies the PR-EOS model (Peng and Robinson, 1976) and a modified MMC method to calculate the confined MMP. Also, it is seen from the enlarged views in **Fig. 4-10** that the confined MMP increases with an increasing temperature when the pore radius is relatively large. This trend is in line with the temperature effect on the bulk MMPs. When the pore radius becomes extremely small, the confined MMP starts to decrease with an increasing temperature.

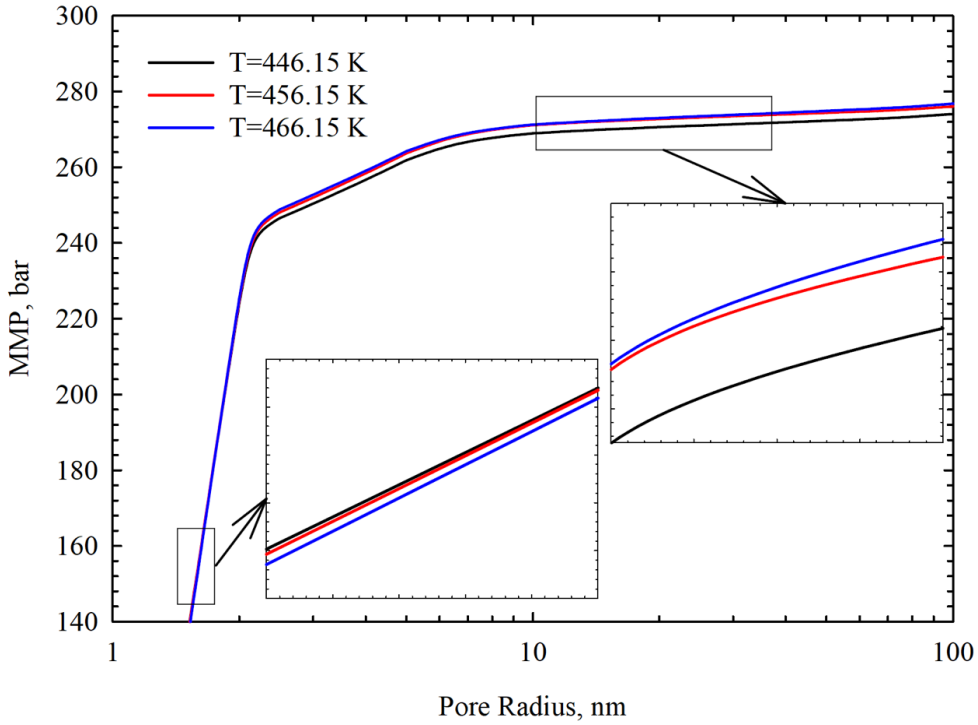

Fig. 4-10: The effect of pore radius on the confined oil-CO_2 MMP calculations under three different reservoir temperatures. The enlarged views illustrate the MMP variations at relatively smaller pore radii and relatively larger pore radii.

4.4.4. Confined MMP with the Consideration of Pore Size Distribution

In tight and shale reservoirs, the pore size heterogeneity is proved to have a great impact on the phase behavior calculation in confined nanopores (Tolbert and Wu, 2015; Wang *et al*., 2016b; Li and Mezzatesta, 2017; Zhang *et al*., 2019b). Zhang *et al*. (2020) considered the pore size distribution in simulating CO_2 injection for oil recovery. They found that the oil recovery factors calculated by considering the capillary pressure in the flash calculations are higher than those obtained using a single pore size. However, when the capillary pressure is included in both flash calculations and flow simulations, the oil recovery factors obtained with the consideration of the pore size distribution are lower than those obtained using a single pore size. Conventionally, when the pore size distribution is involved in the phase behavior calculation, one tends to apply the

average pore radius for further calculations. However, as for the confined MMP calculations, adopting the average pore radius becomes invalid. The aforementioned results on the relationship between MMP and pore size indicate that the confined MMP does not change linearly with the pore radius (See **Fig. 4-10**). Hence, given that the information of pore size distribution is provided, we propose to use a simple mixing rule to calculate the confined oil-CO_2 MMP in order to reflect the effect of pore size distribution on the confined MMPs. For comparison purposes, the average MMPs are calculated by using both Eq. (4-22) and the average pore radius for two shale core samples (Li and Sheng, 2017; Li and Mezzatesta, 2017). The pore size distribution charts for the two shale core samples are found in **Fig. 4-11**. The figure also shows the calculated confined MMP for each representative pore size. It is seen in **Fig. 4-11** that the majority of nanopores in both core samples have a pore radius of less than 10 nm. The reservoir temperature for core sample 1 is 397 K, while the reservoir temperature for core sample 2 is 339 K.

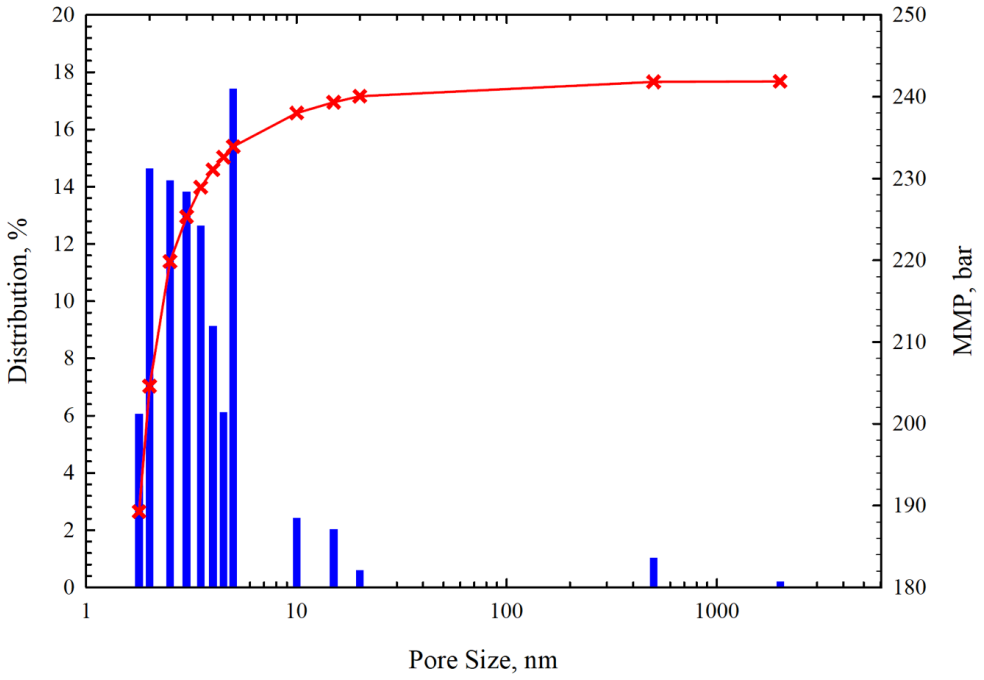

(a)

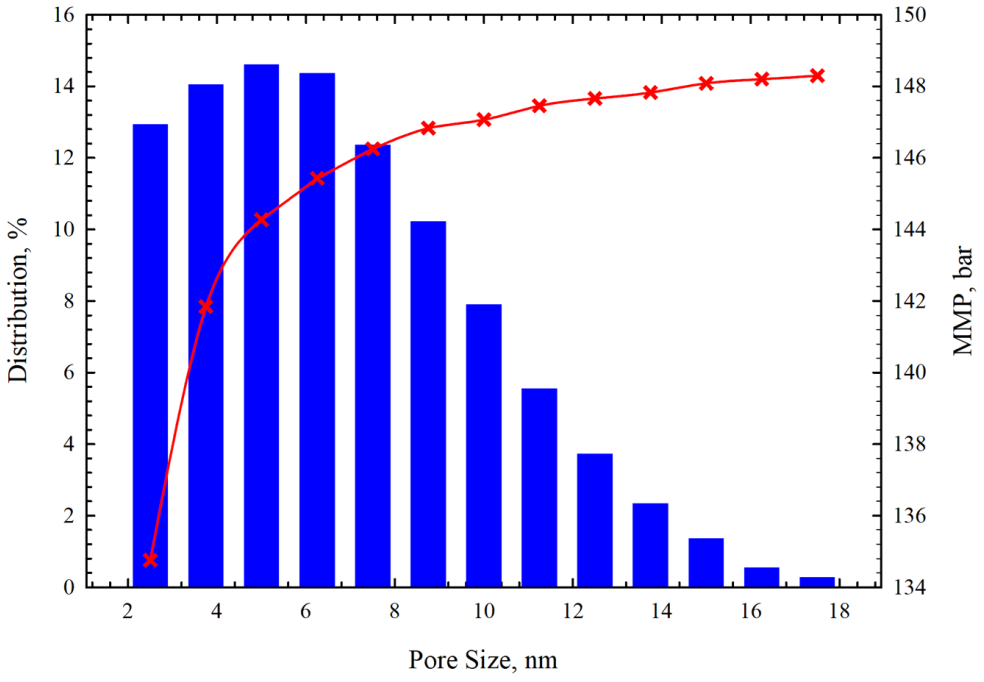

(b)

Fig. 4-11: Pore size distribution charts and the calculated confined MMPs at different pore sizes for (a) core sample 1 (Li and Sheng, 2017) and (b) core sample 2 (Li and Mezzatesta, 2017).

Table 4-2 summarizes the confined MMP calculation results for both core samples using the proposed mixing rule and the average pore radius. The results suggest that the confined MMP calculated using the proposed mixing rule is lower than the confined MMP calculated using the average pore radius. This statement is valid for both core samples. The difference between the confined MMPs calculated using two methods for core sample 1 is considerably larger than that of core sample 2. The difference is dependent on pore size distribution. Also, because the reservoir temperatures are different for both cores, the temperature may have an impact on the difference between the confined MMPs calculated from both methods. To validate this conclusion, the average confined MMPs for core sample 1 are calculated using both methods at three reservoir temperatures. **Table 4-3** presents the calculation results. With an increasing temperature, the difference between the average MMPs calculated by the two methods becomes much more significant, i.e., the average MMP calculated by using the proposed mixing rule becomes more reduced at a higher temperature than the one calculated by using the average pore size. It is more rational to calculate the average confined MMP using the proposed mixing rule than using the average pore radius since the confined MMP does not change with pore radius linearly. Note that a lower MMP as predicted by the proposed methodology can help design MMP injection projects at a lower cost. This is because: 1) once the injection pressure is above the theoretical oil-CO_2 MMP, the oil recovery is only improved modestly (Gamadi, *et al*.,2013; Li *et al*., 2017; Li *et al*., 2018); 2) a lower MMP suggests the use of a lower compressor pressure for injecting CO_2 into the reservoir.

Table 4-2: Overall MMPs calculated using the proposed mixing rule and the average pore radius for two core samples (Li and Sheng, 2017; Li and Mezzatesta, 2017).

	Temperature, K	Confined MMP calculated using the proposed mixing rule, bar	Confined MMP calculated using the average pore radius, bar
Core sample 1	397	223.14	238.93
Core sample 2	339	144.06	145.82

Table 4-3: Average confined MMPs calculated using the proposed mixing rule and the average pore radius for core sample 1 (Li and Sheng, 2017) at three different temperatures.

Temperature, K	Confined MMP using proposed mixing rule, bar	Confined MMP using average pore radius, bar
347	153.2	165.5
397	223.1	238.9
447	248.4	267.7

4.5. Conclusions

In this work, the conventional MMC method proposed by Ahmadi and Johns (2011) is modified to develop an improved MMP calculation algorithm that can reliably predict the oil-CO_2 MMP in confined nanopores with the consideration of pore size distribution. The new MMP calculation algorithm employs a volume translated PR-EOS (Peng and Robinson, 1976; Abudour, *et al*., 2013), and the effects of pore size distribution, capillarity, and confinement are integrated into the algorithm. Using the proposed MMP calculation algorithm, the effects of pore radius and temperature on the MMP calculation in confined nanopores are studied in detail. The following findings are highlighted from this work.

- We demonstrate how to apply the proposed algorithm by calibrating it using the measured MMP for tight core samples (Zhang and Gu, 2015). By tuning the BIPs between hydrocarbons in the crude oil sample and CO_2, the measured MMP can be perfectly matched by the developed algorithm.

- Example calculations made on the crude oil sample used by Zhang and Gu (2015) show that the confined oil-CO_2 MMP decreases with a decreasing pore radius. Such reduction is more obvious in smaller pores than in larger pores. When the pore radius is larger than 10 nm, the confined MMP becomes less sensitive to the change in the pore radius.
- When the pore radius is extremely small (pore radius is less than 2.5 nm), the confined MMP decreases with an increasing temperature. When the pore radius is relatively large, the confined MMP increases with an increasing temperature.
- For every pore radius, the confined oil-CO_2 MMP first increases and then decreases with an increasing temperature, indicating the existence of a maximum MMP at a given temperature.
- There also exists a maximum confined MMP for every pore radius. This maximum confined MMP decreases with a decreasing pore radius. The temperature corresponding to the maximum confined MMP also decreases with a decreasing pore radius.
- When the pore size distribution is considered, the confined MMP calculated using the proposed mixing rule is noticeably lower than the confined MMP calculated using the average pore radius. The difference between the confined MMP calculated using both methods depends on pore size distribution and temperature.

Acknowledgments

The authors acknowledge a Discovery Grant from the Natural Sciences and Engineering Research Council of Canada (NSERC) to H. Li.

Nomenclature

C_{Ii} = fluid-dependent parameter for the component *i*

C_{1m} = fluid-dependent parameter for multicomponent systems

CEOS = cubic equation of state

C_m = volume translation term for mixtures

d_m = dimensionless distance function

EOS = equation of state

f_{ix} = fugacity of component *i* in liquid phase, bar

f_{iy} = fugacity of component *i* in vapor phase, bar

IFT = interfacial tension, mN/m

N_c = total number of components

P = bulk pressure, bar

P_c = vapor-liquid capillary pressure, bar

P_{cb} = bulk critical pressure, bar

P_{chi} = Parachor of component *i*

P_{cm} = critical pressure for mixture

P_{cp} = confined critical pressure, bar

P_g = vapor phase pressure, bar

P_l = liquid phase pressure, bar

R = universal gas constant, 83.14459848 $cm^3 \cdot bar \cdot K^{-1} \cdot mol^{-1}$

r_p = pore radius, nm

T = bulk temperature, K

T_{cb} = bulk critical temperature, K

T_{ci} = critical temperature for the component i

T_{cm} = critical temperature for mixture

T_{cp} = confined critical temperature, K

TL = tie-line length

V_{ci} = critical molar volume of component i

$V_{corr,l}$ = corrected liquid-phase molar volume

V_{PR} = original molar volume calculated by the PR-EOS

x_i = mole fraction of component i in liquid phase

y_i = mole fraction of component i in vapor phase

Z = compressibility factor

$Z_{c,\ EOS}$ = calculated critical compressibility factor calculated from the PR-EOS

$Z_{exp,\ i}$ = experimental critical compressibility factor for component i

z_i = feed composition

δ_{cm} = volume correction for mixtures at the critical point

θ_i = surface fraction of the component *i*

μ_{ix} = chemical potential of component *i* in liquid phase

μ_{iy} = chemical potential of component *i* in vapor phase

ρ_g = vapor molar phase density, mole/cm^3

ρ_l = liquid molar phase density, mole/cm^3

ρ_m = molar density of the mixture

σ = vapor-liquid interfacial tension, mN/m

σ_{LJ} = Lennard-Jones size parameter

ω_i = acentric factor for the component *i*

ω_m = acentric factor for the mixture

References

Aalto, M., Keskinen, K.I., Aittamaa, J. and Liukkonen, S. 1996. An Improved Correlation for Compressed Liquid Densities of Hydrocarbons. Part 2. Mixtures. Fluid Phase Equilibria, 114, 21-35. https://doi.org/10.1016/0378-3812(95)02824-2.

Abudour, A., Mohammad, S., Robinson, R. and Gasem, K. 2013. Volume-Translated Peng-Robinson Equation of State for Liquid Densities of Diverse Binary Mixtures. Fluid Phase Equilibria, 349, 37-55. http://doi.org/10.1016/j.fluid.2013.04.002.

Adyani, W.N. and Kechut, N.I., 2007. Advanced Technology for Rapid Minimum Miscibility Pressure Determination (Part 1). In: Asia Pacific Oil and Gas Conference and Exhibition. Society of Petroleum Engineers. https://doi.org/10.2118/110265-MS.

Ahmadi, K. and Johns, R. 2011. Multiple-Mixing-Cell Method for MMP Calculations. SPE Journal, 16(04), 733-742. http://doi.org/10.2118/116823-pa.

Ahmadi, M., Zendehboudi, S. and James, L. 2017. A Reliable Strategy to Calculate Minimum Miscibility Pressure of CO_2-Oil System in Miscible Gas Flooding Processes. Fuel, 208, 117-126. http://doi.org/10.1016/j.fuel.2017.06.135.

Chou, G.F. and Prausnitz, J.M. 1989. A Phenomenological Correction to an Equation of State for the Critical Region. AIChE Journal, 35, 1487-1496. https://doi.org/10.1002/aic.690350909.

Christiansen, R.L. and Haines, H.K. 1987. Rapid Measurement of Minimum Miscibility Pressure with the Rising-Bubble Apparatus. SPE Reservoir Engineering, 2(4), 443–449. https://doi.org/10.2118/13114-PA

Chueh, P.L. and Prausnitz, J.M. 1967. Vapor-Liquid Equilibria at High Pressures: Calculation of Critical Temperatures, Volumes, and Pressures of Nonpolar Mixtures. AIChE Journal, 13, 1107-1113. https://doi.org/10.1002/aic.690130613.

Gamadi, T.D., Sheng, J.J. and Soliman, M.Y. 2013. An Experimental Study of Cyclic Gas Injection to Improve Shale Oil Recovery. In: SPE Annual Technical Conference and Exhibition. New Orleans: Society of Petroleum Engineers. https://doi.org/10.2118/166334-MS.

Holm, L. and Josendal, V. 1974. Mechanisms of Oil Displacement by Carbon Dioxide. Journal of Petroleum Technology, 26(12), 1427-1438. http://doi.org/10.2118/4736-pa.

Johns, R. and Orr, F. 1996. Miscible Gas Displacement of Multicomponent Oils. SPE Journal, 1(01), 39-50. http://doi.org/10.2118/30798-pa.

Kolodzie Jr., S. 1980. Analysis of Pore Throat Size and Use of the Waxman-Smits Equation to Determine OOIP in Spindle Field, Colorado. In: 55th Annual Fall Technical Conference and Exhibition of the Society of Petroleum Engineers of AIME. Dallas: Society of Petroleum Engineers. https://doi.org/10.2118/9382-MS.

Lashgari, H., Sun, A., Zhang, T., Pope, G. and Lake, L. 2019. Evaluation of Carbon Dioxide Storage and Miscible Gas EOR in Shale Oil Reservoirs. Fuel, 241, 1223-1235. http://doi.org/10.1016/j.fuel.2018.11.076.

Lee, B. and Kesler, M. 1975. A Generalized Thermodynamic Correlation Based on Three-Parameter Corresponding States. AIChE Journal, 21(3), 510-527. http://doi.org/10.1002/aic.690210313.

Lee, J.I. 1979. Effectiveness of Carbon Dioxide Displacement under Miscible and Immiscible Conditions. Report RR-40. Petroleum Recovery Institute, Calgary.

Li, B. and Mezzatesta, A. 2017. Evaluation of Pore Size Distribution Effects on Phase Behavior of Hydrocarbons Produced in Shale Gas Condensate Reservoirs. In SPE Middle East Oil & Gas Show and Conference. Manama: Society of Petroleum Engineers. https://doi.org/10.2118/183833-MS.

Li, H., Qin, J. and Yang, D. 2012. An Improved CO_2–Oil Minimum Miscibility Pressure Correlation for Live and Dead Crude Oils. Industrial & Engineering Chemistry Research, 51(8), 3516-3523. http://doi.org/10.1021/ie202339g.

Li, L. and Sheng, J. 2017. Nanopore Confinement Effects on Phase Behavior and Capillary Pressure in a Wolfcamp Shale Reservoir. Journal of the Taiwan Institute of Chemical Engineers, 78, 317-328. http://doi.org/10.1016/j.jtice.2017.06.024.

Li, L., Sheng, J., Su, Y. and Zhan, S. 2018. Further Investigation of Effects of Injection Pressure and Imbibition Water on CO_2 Huff-n-Puff Performance in Liquid-Rich Shale Reservoirs. Energy & Fuels, 32(5), 5789-5798. http://doi.org/10.1021/acs.energyfuels.8b00536.

Li, L., Zhang, Y. and Sheng, J. 2017. Effect of the Injection Pressure on Enhancing Oil Recovery in Shale Cores during the CO_2 Huff-n-Puff Process When It Is above and below the Minimum Miscibility Pressure. Energy & Fuels, 31(4), 3856-3867. http://doi.org/10.1021/acs.energyfuels.7b00031.

Mungan, N. 1981. Carbon Dioxide Flooding-Fundamentals. Journal of Canadian Petroleum Technology, 20(01), 87-92. http://doi.org/10.2118/81-01-03.

Mungan, N. 1991. An Evaluation of Carbon Dioxide Flooding. In: SPE Western Regional Meeting. Long Beach: Society of Petroleum Engineers. https://doi.org/10.2118/21762-MS.

Nguyen, P., Mohaddes, D., Riordon, J., Fadaei, H., Lele, P. and Sinton, D. 2015. Fast Fluorescence-Based Microfluidic Method for Measuring Minimum Miscibility Pressure of CO_2 in Crude Oils. Analytical Chemistry, 87(6), 3160-3164. http://doi.org/10.1021/ac5047856.

Orr, F. and Jensen, C. 1984. Interpretation of Pressure-Composition Phase Diagrams for CO2/Crude-Oil Systems. SPE Journal, 24(05), 485-497. http://doi.org/10.2118/11125-pa.

Péneloux, A., Rauzy, E. and Fréze, R. 1982. A Consistent Correction for Redlich-Kwong-Soave Volumes. Fluid Phase Equilibria, 8(1), 7-23. http://doi.org/10.1016/0378-3812(82)80002-2.

Peng, D. and Robinson, D. 1976. A New Two-Constant Equation of State. Industrial & Engineering Chemistry Fundamentals, 15(1), 59-64. http://doi.org/10.1021/i160057a011.

Qiu, X., Tan, S., Dejam, M. and Adidharma, H. 2019. Experimental Study on the Criticality of a Methane/Ethane Mixture Confined in Nanoporous Media. Langmuir, 35(36), 11635-11642. http://doi.org/10.1021/acs.langmuir.9b01399.

Quayle, O.R. 1953. The Parachors of Organic Compounds. An Interpretation and Catalogue. Chemical Reviews, 53 (3), 439-589. https://doi.org/10.1021/cr60166a003

Randall, T. and Bennion, D. 1988. Recent Developments in Slim Tube Testing for Hydrocarbon-Miscible Flood (HCMF) Solvent Design. Journal of Canadian Petroleum Technology, 27(06), 33-44. http://doi.org/10.2118/88-06-02.

Rao, D. 1997. A New Technique of Vanishing Interfacial Tension for Miscibility Determination. Fluid Phase Equilibria, 139(1-2), 311-324. http://doi.org/10.1016/s0378-3812(97)00180-5.

Rathmell, J.J., Stalkup, F.I. and Hassinger, R.C. 1971. A Laboratory Investigation of Miscible Displacement by Carbon Dioxide. In: The Fall Meeting of the Society of Petroleum Engineers of AIME. New Orleans: Society of Petroleum Engineers. http://doi.org/10.2118/3483-MS

Rezaveisi, M., Sepehrnoori, K., Pope, G.A. and Johns, R.T. 2018. Thermodynamic Analysis of Phase Behavior at High Capillary Pressure. SPE Journal, 23(06), 1977-1990. https://doi.org/10.2118/175135-PA.

Rolo, L., Caço, A., Queimada, A., Marrucho, I. and Coutinho, J. 2002. Surface Tension of Heptane, Decane, Hexadecane, Eicosane, and Some of Their Binary Mixtures. Journal of Chemical & Engineering Data, 47(6), 1442-1445. http://doi.org/10.1021/je025536+.

Seneviratne, K., Hughes, T., Johns, M., Marsh, K. and May, E. 2017. Surface Tension and Critical Point Measurements of Methane + Propane Mixtures. The Journal of Chemical Thermodynamics, 111, 173-184. http://doi.org/10.1016/j.jct.2017.03.002.

Shokir, E. 2007. CO_2-Oil Minimum Miscibility Pressure Model for Impure and Pure CO_2 Streams. Journal of Petroleum Science and Engineering, 58(1-2), 173-185. http://doi.org/10.1016/j.petrol.2006.12.001.

Sun, H. and Li, H. 2019. A New Three-Phase Flash Algorithm Considering Capillary Pressure in a Confined Space. Chemical Engineering Science, 193, 346-363. https://doi.org/10.1016/j.ces.2018.09.013.

Sun, H. and Li, H. 2020. Phase Behavior Modeling of Hydrocarbon Fluids in Nanopores Using PR-EOS Coupled with a Modified Young-Laplace Equation. ACS Omega, 5, 15177-15191. https://doi.org/10.1021/acsomega.0c00963.

Tan, S., Qiu, X., Dejam, M. and Adidharma, H. 2019. Critical Point of Fluid Confined in Nanopores: Experimental Detection and Measurement. The Journal of Physical Chemistry C, 123(15), 9824-9830. http://doi.org/10.1021/acs.jpcc.9b00299.

Teklu, T.W., Alharthy, N., Kazemi, H., Yin, X. and Graves, R.M. 2014a. Vanishing Interfacial Tension Algorithm for MMP Determination in Unconventional Reservoirs. In: SPE Western North American and Rocky Mountain Joint Regional Meeting. Denver: Society of Petroleum Engineers. http://doi.org/10.2118/169517-MS.

Teklu, T., Alharthy, N., Kazemi, H., Yin, X., Graves, R. and AlSumaiti, A. 2014b. Phase Behavior and Minimum Miscibility Pressure in Nanopores. SPE Reservoir Evaluation & Engineering, 17(03), 396-403. http://doi.org/10.2118/168865-pa.

Tolbert, B.T. and Wu, X. 2015. Quantifying Pore Size Distribution Effect on Gas in Place and Recovery Using SLD-PR EOS for Multiple-Components Shale Gas Reservoir. In: SPE Asia Pacific Unconventional Resources Conference and Exhibition. Brisbane: Society of Petroleum Engineers. https://doi.org/10.2118/176992-MS.

Wang, F. and Reed, R. 2009. Pore Networks and Fluid Flow in Gas Shales. In: SPE Annual Technical Conference and Exhibition. New Orleans: Society of Petroleum Engineers. https://doi.org/10.2118/124253-MS.

Wang, S., Ma, M. and Chen, S. 2016a. Application of PC-SAFT Equation of State for CO2 Minimum Miscibility Pressure Prediction in Nanopores. In: SPE Improved Oil Recovery Conference. Tulsa: Society of Petroleum Engineers. https://doi.org/10.2118/179535-MS.

Wang, L., Yin, X., Neeves, K. and Ozkan, E. 2016b. Effect of Pore-Size Distribution on Phase Transition of Hydrocarbon Mixtures in Nanoporous Media. SPE Journal, 21(06), 1981-1995. http://doi.org/10.2118/170894-pa.

Wang, Y. and Orr, F. 1997. Analytical Calculation of Minimum Miscibility Pressure. Fluid Phase Equilibria, 139(1-2), 101-124. http://doi.org/10.1016/s0378-3812(97)00179-9.

Weinaug, C. and Katz, D. 1943. Surface Tensions of Methane-Propane Mixtures. Industrial & Engineering Chemistry, 35(2), 239-246. http://doi.org/10.1021/ie50398a028.

Whitson, C. and Brulé, M. 2000. Phase behavior. Richardson, Texas: Henry L. Doherty Memorial Fund of AIME, Society of Petroleum Engineers.

Yellig, W. 1982. Carbon Dioxide Displacement of a West Texas Reservoir Oil. SPE Journal, 22(06), 805-815. http://doi.org/10.2118/9785-pa.

Yellig, W. and Metcalfe, R. 1980. Determination and Prediction of CO_2 Minimum Miscibility Pressures (includes associated paper 8876). Journal of Petroleum Technology, 32(01), 160-168. http://doi.org/10.2118/7477-pa.

Young, T. 1805. An Essay on the Cohesion of Fluids. Philosophical Transactions of the Royal Society of London, 95(0), 65-87. http://doi.org/10.1098/rstl.1805.0005.

Yu, W., Lashgari, H., Wu, K. and Sepehrnoori, K. 2015. CO_2 Injection for Enhanced Oil Recovery in Bakken Tight Oil Reservoirs. Fuel, 159, 354-363. http://doi.org/10.1016/j.fuel.2015.06.092.

Yuan, H. and Johns, R. 2005. Simplified Method for Calculation of Minimum Miscibility Pressure or Enrichment. SPE Journal, 10(04), 416-425. http://doi.org/10.2118/77381-pa.

Yuan, H., Johns, R., Egwuenu, A. and Dindoruk, B. 2005. Improved MMP Correlation for CO2 Floods Using Analytical Theory. SPE Reservoir Evaluation & Engineering, 8(05), 418-425. http://doi.org/10.2118/89359-pa.

ZareNezhad, B. 2016. A New Correlation for Predicting the Minimum Miscibility Pressure Regarding the Enhanced Oil Recovery Processes in the Petroleum Industry. Petroleum Science and Technology, 34(1), 56-62. http://doi.org/10.1080/10916466.2015.1117493.

Zarragoicoechea, G. and Kuz, V. 2004. Critical Shift of a Confined Fluid in a Nanopore. Fluid Phase Equilibria, 220(1), 7-9. https://doi.org/10.1016/j.fluid.2004.02.014.

Zhang, K. and Gu, Y. 2015. Two Different Technical Criteria for Determining the Minimum Miscibility Pressures (MMPs) from the Slim-Tube and Coreflood Tests. Fuel, 161, 146-156. http://doi.org/10.1016/j.fuel.2015.08.039.

Zhang, K., Jia, N., Zeng, F. and Luo, P. 2017a. A New Diminishing Interface Method for Determining the Minimum Miscibility Pressures of Light Oil–CO_2 Systems in Bulk Phase and Nanopores. Energy & Fuels, 31(11), 12021-12034. http://doi.org/10.1021/acs.energyfuels.7b02439.

Zhang, K., Jia, N. and Li, S. 2017b. Exploring the Effects of Four Important Factors on Oil–CO_2 Interfacial Properties and Miscibility in Nanopores. RSC Advances, 7(85), 54164-54177. http://doi.org/10.1039/c7ra10671h.

Zhang, K., Jia, N., Li, S. and Liu, L. 2018a. Nanoscale-Extended Correlation to Calculate Gas Solvent Minimum Miscibility Pressures in Tight Oil Reservoirs. Journal of Petroleum Science and Engineering, 171, 1455-1465. http://doi.org/10.1016/j.petrol.2018.08.057.

Zhang, K., Nojabaei, B., Ahmadi, K. and Johns, R.T. 2018b. Minimum Miscibility Pressure Calculation for Oil Shale and Tight Reservoirs with Large Gas-Oil Capillary Pressure. In:

Unconventional Resources Technology Conference. Houston: Society of Petroleum Engineers. https://doi.org/10.15530/URTEC-2018-2901892.

Zhang, K., Nojabaei, B., Ahmadi, K. and Johns, R.T. 2020. Effect of Gas/Oil Capillary Pressure on Minimum Miscibility Pressure for Tight Reservoirs. SPE Journal, 25(2), 820-831. https://doi.org/10.2118/199354-PA

Zhang, Y., Di, Y., Yu, W. and Sepehrnoori, K. 2019a. A Comprehensive Model for Investigation of Carbon Dioxide Enhanced Oil Recovery with Nanopore Confinement in the Bakken Tight Oil Reservoir. SPE Reservoir Evaluation & Engineering, 22(01), 122-136. http://doi.org/10.2118/187211-pa.

Zhang, K., Du, F. and Nojabaei, B. 2019b. Effect of Pore Size Heterogeneity on Hydrocarbon Fluid Distribution and Transport in Nanometer-Sized Porous Media. In: SPE Eastern Regional Meeting. Charleston: Society of Petroleum Engineers. https://doi.org/10.2118/196586-MS.

CHAPTER 5 A MODIFIED CELL-TO-CELL SIMULATION MODEL TO DETERMINE THE MINIMUM MISCIBILITY PRESSURE IN TIGHT/SHALE FORMATIONS

A version of this chapter was submitted to *Oil & Gas Science and Technology* for possible publication on March 14, 2021.

Abstract

A new oil-gas minimum miscibility pressure (MMP) calculation algorithm is developed in this work based on the classic cell-to-cell simulation model proposed by Metcalfe *et al.* (1973). The proposed algorithm couples the effects of capillary pressure and confinement in the original cell-to-cell simulation model to predict the oil-gas MMPs in a confined space. Given that the original cell-to-cell algorithm relies on the volume predictions of the reservoir fluids in each cell, a volume-translated Peng-Robinson equation of state (PR-EOS) (Peng and Robinson, 1976; Abudour *et al.*, 2013) is applied in this work for improved accuracy on volume calculations of the reservoir fluids. The robustness of the proposed algorithm is examined by performing the confined MMP calculations for four oil-gas systems. The tie-line length method proposed by Ahmadi and Johns (2011) is used to determine the oil-gas MMP in confined space. The oil recovery factor calculated by the proposed MMP calculation algorithm is then used to validate the results. First, to achieve stable modeling results for all four examples, a total cell number of 500 is determined by examining the variations in the oil recovery as a function of cell number. Then, by calculating the oil recovery factor near the MMP region, it is found that the MMP determined by the tie-line length method is slightly lower than the inflection point of the oil recovery curve. Through the case studies, the effects of temperature, pore radius, and injection gas impurity on the confined oil-gas MMP calculations are studied in detail. It is found that the oil-gas MMP is reduced in confined space and the degree of this reduction depends on the pore radius. For all the tested pore radii, the confined MMP first increases and then decreases with an increasing temperature. Furthermore, compared to pure carbon dioxide (CO_2) injection, the addition of methane (CH_4) in the injection gas increases the oil-gas in confined nanopores. Therefore, it is recommended to control the content of CH_4 in the injection gas in order to achieve a more efficient gas injection design.

Keywords: Minimum miscibility pressure, Phase behavior, Unconventional reservoir, Cell-to-cell simulation, Two-phase flash, Capillary pressure, Confinement effect, Volume translation

5.1. Introduction

The gas injection process has long been applied in the petroleum industry as an effective means of enhancing oil recovery (Belhaj, *et al.*, 2013). It offers the advantage of a theoretical 100% local oil recovery efficiency over other enhanced oil recovery methods (Elsharkawy, *et al.*, 1996). More recently, it has also been widely applied in unconventional light to medium oil reservoirs and has led to major oil recovery increases (Yu *et al*., 2015; Lashgari *et al*., 2019). The oil-gas minimum miscibility pressure (MMP), being the most crucial parameter in a gas injection project, needs to be accurately predicted to maximize the efficiency of a gas injection process. The conventional methods of determining the oil-gas MMP are empirical correlations (Holm and Josendal, 1974; Lee, 1979; Mungan, 1981; Orr and Jensen, 1984; Shokir, 2007; ZareNezhad, 2016; Li *et al*., 2012; Ahmadi *et al*., 2017), experimental methods (Rathmell *et al*., 1971; Yellig, 1982; Christiansen and Haines, 1986; Randall and Bennion, 1988; Rao, 1997; Nguyen *et al*., 2015), and numerical simulations (Metcalfe, *et al.*, 1973; Johns and Orr, 1996; Wang and Orr, 1997; Ahmadi and Johns, 2011). The empirical correlations are simple and fast to use, but they are developed with limited experimental data and they could become invalid under certain circumstances. The experimental methods provide reliable and accurate predictions on the oil-gas MMPs under reservoir conditions, but they are very expensive and time-consuming. Provided that all the empirical correlations and the experimental methods come with inherent drawbacks, numerical simulations have become the most popular methods to offer oil-gas MMP estimations in both conventional and unconventional reservoirs with decent accuracy.

The numerical simulation models currently applied in studying the oil-gas MMP in conventional reservoirs include the one cell simulation algorithm (Neau *et al.*, 1996), the vanishing interfacial tension (IFT) calculation method (Weinaug and Katz, 1943; Rao, 1997), the original cell-to-cell

simulation method (Metcalfe *et al.*, 1973), and the multiple-mixing-cell (MMC) method (Ahmadi and Johns, 2011). One cell simulation model is the simplest model to estimate the oil-gas MMP (Neau *et al.*, 1996). In this model, only a single cell is considered, and only forward or backward contacts are performed to determine the oil-gas MMP corresponding to a vaporizing or condensing drive miscibility. This method is useful when the miscibility is controlled by the gas tie-line or the oil tie-line (Neau *et al.*, 1996). It becomes invalid when the miscibility is controlled by a crossover tie-line because the one cell simulation tends to overestimate the oil-gas MMP when the miscibility is induced by a vaporizing/condensing drive mechanism (Jaubert *et al.*, 1998b). The vanishing IFT method was originally proposed as a criterion in measuring the oil-gas MMP in experiments (Rao, 1997). The essence of this method is that the oil-gas MMP is determined when the vapor-liquid IFT reaches zero. Later, researchers modified this method and used the Parachor model (Weinaug and Katz, 1943) combined with a cubic equation of states to calculate the vapor-liquid IFT to determine the theoretical oil-gas MMP (Teklu *et al.*, 2014b; Wang *et al.*, 2016; Zhang *et al.*, 2017a; Zhang *et al.*, 2017b). The original cell-to-cell simulation method was first proposed by Metcalfe *et al.* (1973). This method mimics the physical 1-D gas displacement process and provides the results of final oil recovery, as well as the oil-gas MMP. This model is slower than the previous two methods (i.e., the one cell simulation and the vanishing IFT model) but offers more reliable results. The MMP determination criteria for this method include tracking the tie-line path in a ternary diagram (Metcalfe *et al.*, 1973), tracking the final oil recovery at different pressures until the oil recovery reaches 97% (Jaubert *et al.*, 1998a), and tracking the minimum key tie-line length at different pressures until it reaches zero (Zhao *et al*., 2006; Yang *et al.*, 2020). The MMC model proposed by Ahmadi and Johns (2011) is a simplified and accelerated model of the original cell-to-cell model (Metcalfe *et al.*, 1973). The minimum key tie-line length is recorded at each pressure

and the last few minimum key tie-line lengths are extrapolated to zero, at which the oil-gas MMP is determined (Ahmadi and Johns, 2011). However, in this method, the volumes of each cell and mixing fluids are not calculated. As a result, oil recovery calculations are not made available in this model. More recently, machine learning has been applied to estimate MMP in conventional oil reservoirs. The MMP prediction methods based on machine learning algorithm include neural network analysis method, genetic function approximation method, multiple linear regression method, and partial least squares method (Li, *et al*., 2019; Khan, *et al*., 2019). However, no attempt has been made to apply these methods to predict MMP in unconventional reservoirs.

The aforementioned MMP determination methods are all proposed to predict the oil-gas MMP in conventional oil reservoirs. They tend to lose accuracy in calculating the oil-gas MMP in unconventional reservoirs due to the strong capillarity and confinement effects introduced by the nanopores prevalent in unconventional formations. One of the first attempts to reflect the effect of nanopores on the oil-gas MMP prediction is performed by Teklu *et al*. (2014a). They coupled the capillary pressure and critical point shift model (Zarragoicoechea and Kuz, 2004) in the MMC method to calculate the oil-gas MMP for three oil-gas systems. They found that the oil-gas MMPs are greatly reduced in nanopores compared to the bulk MMPs. It was also concluded that most of the MMP reductions in nanopores are caused by the effect of critical point shift (Teklu *et al.*, 2014a). Other efforts have tried to modify the vanishing IFT calculation model by coupling the effect of nanopores. Teklu *et al*. (2014b) coupled the capillary pressure and critical point shift (Zarragoicoechea and Kuz, 2004) in vapor-liquid equilibrium calculations and calculated vapor-liquid IFT using Parachor model (Weinaug and Katz, 1943). They found that using the proposed model, the oil-gas MMP decreases with a decreasing pore radius. Similar results have also been observed in the study of Wang *et al.* (2016). They employed the Perturbed-Chain Statistical

Associating Fluid Theory (PC-SAFT) (Gross and Sadowski, 2011) to calculate the vapor-liquid IFT with increasing pressure. They also considered IFT reduction due to the confinement effect. A significant MMP reduction in confined nanopores is observed in their research. Zhang *et al*. (2017a) coupled the effect of nanopores in Peng-Robinson equation of state (PR-EOS) (Peng and Robinson, 1976) and calculated the confined oil-gas MMP using the vanishing IFT model. In addition, the interface thickness is considered in their model by taking account of the two-way mass transfer effects. The proposed model is tested with two crude oil samples and it was found that the oil-gas MMP is reduced in nanopores for both oil samples (Zhang *et al.*, 2017a). Zhang *et al*. (2017b) applied a similar methodology and observed a linear increase of the confined oil-gas MMP with an increasing temperature.

The MMC method (Ahmadi and Johns, 2011) modified for tight/shale formations is incapable of calculating the oil recovery factors during the gas displacement process. In addition, volume translation is absent in all PR-EOS-based confined MMP calculation models. This work aims to develop a comprehensive confined MMP calculation algorithm to predict the oil-gas MMP in confined nanopores. The proposed MMP calculation algorithm is based on the original cell-to-cell simulation model proposed by Metcalfe *et al*. (1973) and the minimum tie-line length criterion is applied to determine the confined oil-gas MMP. The cell-to-cell model is selected as the very foundation of this study is because this model offers the results of the final oil recovery and the calculated recovery factors can be used to determine the required total cell number in a robust manner to avoid numerical dispersion issues. Also, the fluid-moving mechanism of the cell-to-cell model is more realistic than that of the MMC method. The vapor-liquid equilibrium calculations in confined nanopores are conducted using a volume translated PR-EOS (Peng and Robinson, 1976; Abudour *et al.*, 2013) coupled with capillary pressure and a state-of-art critical point shift model

(Tan *et al*., 2019). The robustness of the proposed algorithm is examined using four examples. The effects of temperature, pore radius, and injection gas impurity on the confined oil-gas MMP calculations are investigated in detail.

5.2. Methodology

The mathematical formulations of the thermodynamic model used in this work is presented in this section. A volume translated PR-EOS (Peng and Robinson, 1976; Abudour *et al.*, 2013) is employed in the two-phase equilibrium calculations. The capillary pressure and a critical point shift model are coupled with PR-EOS to reflect the effects of capillarity and confinement yielded by nanopores.

The two-phase equilibrium is reached when the fugacity-equality condition is satisfied at given pressure, temperature, and mixture compositions. The fugacity-equality condition in confined nanopores is given in Eq. (5-1) (Whitson and Brulé, 2000).

$$f_{ix}(P_l, T, z_i) = f_{iy}(P_v, T, z_i) \qquad i = 1, \dots, n_c \tag{5-1}$$

where f_{ix} and f_{iy} represent the fugacities of component i in the liquid phase and the vapor phase, respectively. P_l is the liquid-phase pressure, P_v is the vapor-phase pressure. T is the reservoir temperature, z_i is the feed compositions of the mixture, and n_c is the number of components. Because of the existence of large capillary pressure, the vapor-phase pressure and the liquid-phase pressure cannot be assumed equal and can be related using Eq. (5-2).

$$P_c = P_v - P_l \tag{5-2}$$

where P_c is the capillary pressure of the adjacent liquid and vapor phases. The vapor-liquid capillary pressure can be calculated using the Young-Laplace equation (Young, 1805) with assumptions of zero contact angle and equal principal radii. The Young-Laplace equation is expressed in Eq. (5-3) (Young, 1805).

$$P_c = \frac{2\sigma}{r_p} \tag{5-3}$$

where r_p is the pore radius, σ represents the IFT between the liquid phase and the vapor phase. The Parachor model (Weinaug and Katz, 1943) is employed to calculate the vapor-liquid IFT given in Eq. (5-4).

$$\sigma = \left[\sum_{i=1}^{n_c} P_{chi}\left(x_i\rho_l - y_i\rho_g\right)\right]^4 \qquad i = 1, \ldots, n_c \tag{5-4}$$

where P_{chi} is the Parachor constant of component i, ρ_l and ρ_g are the molar density of the liquid-phase and the vapor-phase, respectively, and can be calculated by the volume translated PR-EOS (Peng and Robinson, 1976; Abudour *et al.*, 2013).

In addition to capillary pressure, the strong wall-molecule interactions present in nanopores also alter the critical point of the constituting components in reservoir fluids (Qiu *et al*., 2019). An analytical solution to express the critical point shift due to the confinement effect was originally proposed by Zarragoicoechea and Kuz (2004). More recently, Tan *et al*. (2019) developed a new critical point shift model based on the one developed by Zarragoicoechea and Kuz (2004). The model proposed by Tan *et al*. (2019) is validated by experiments, making it more representative in describing the critical point shift in confined nanopores. The critical point shift model is given in Eq. (5-5).

$$\begin{cases} \frac{T_{cb}-T_{cp}}{T_{cb}} = 0.0519\left(\frac{\sigma_{LJ}}{r_p}\right)^2 - 25.7585\left(\frac{\sigma_{LJ}}{r_p}\right)^4 \\ \frac{P_{cb}-P_{cp}}{P_{cb}} = 0.7689\frac{\sigma_{LJ}}{r_p} - 28.7529\left(\frac{\sigma_{LJ}}{r_p}\right)^3 \\ \sigma_{LJ} = 0.244\sqrt[3]{\frac{T_{cb}}{P_{cb}}} \end{cases} \quad (5\text{-}5)$$

where T_{cb} and T_{cp} are the critical temperatures in the bulk conditions and nanopores, respectively, P_{cb} and P_{cp} are the critical pressure in the bulk conditions and nanopores, respectively, and σ_{LJ} is the Lennard-Jones size parameter. It is worth noting that although the capillary pressure and a critical shift model (Tan *et al.*, 2019) are coupled in the proposed algorithm, this work does not reflect the effect of interactions at the molecular level, such as adsorption, on the confined MMP calculations.

5.3. Proposed MMP Calculation Algorithm

The proposed MMP calculation algorithm is based on the original cell-to-cell simulation model developed by Metcalfe *et al.* (1973). A detailed step-by-step procedure of performing the confined MMP calculations using the proposed algorithm is shown as follows.

1) The reservoir temperature, compositions of injection gas and reservoir oil, cell volume (v_c), gas/oil ratio (GOR), and total cell number (N_c) are specified to initiate the algorithm. Then the shifted critical properties of each constituting component are calculated using the critical point shift model (Tan *et al.*, 2019).
2) The total volume of injection is set to be 1.2 pore volume (PV) as suggested by Metcalfe *et al.* (1973). Then the total batch number (N_b) can be calculated using Eq. (5-6).

$$N_b = \frac{1.2\times N_c}{GOR} \quad (5\text{-}6)$$

where N_b is the total batch number, N_c is the total cell number, and GOR is the gas/oil ratio.

3) The volume of the first batch of injection gas is calculated as GOR×v_c. then the first contact is made by mixing the first batch of injection gas with reservoir oil. It is assumed that all the cells are initially filled with reservoir oil and perfect mixing is reached with each contact. Therefore, the feed compositions can be calculated using the volume of the injection gas and the reservoir oil. Then the compositions and the phase volumes of the resulting mixture can be calculated using the two-phase equilibrium calculation algorithm coupled with capillary pressure and the critical point shift model (Tan *et al.*, 2019). The phase volumes are predicted using the volume translated PR-EOS (Peng and Robinson, 1976; Abudour *et al.*, 2013) for better accuracy. In addition, the tie-line length of this contact is calculated using Eq. (5-7) and recorded (Ahmadi and Johns, 2011).

$$TL = \sqrt{\sum_{i=1}^{n_c}(x_i - y_i)^2} \tag{5-7}$$

where TL is the tie-line length, x_i and y_i represent the mole fractions of component i in the equilibrium liquid phase and the equilibrium vapor phase, respectively.

4) The moving strategy used in the proposed algorithm is to move the excess fluid. If the resulting mixture after the two-phase equilibrium calculation is single-phase, then the excess gas or oil is moved to the next cell. If the resulting mixture is a two-phase system, then the excess gas is moved to the next cell first. If after all the gas is moved to the next cell and the volume of the remaining oil is still larger than the cell volume, then the excess oil is also moved to the next cell (Metcalfe *et al.*, 1973).

5) The overall feed compositions of the fluids in cell 2 are calculated and the two-phase equilibrium calculation is conducted using the calculated overall feed compositions. The tie-line length is also recorded for this contact. The excess fluid is then moved to cell 3. This step is repeated until the last cell.

6) After one batch of gas injection is completed, another batch of gas is injected into cell 1 until all the 1.2 PV of gas is injected. The fluid moved from the last cell is treated as the final oil production. The final oil recovery factor is calculated using Eq. (5-8) (Zhao *et al.*, 2006).

$$RF_{1.2} = \frac{V_r}{V_o} \tag{5-8}$$

where $RF_{1.2}$ is the oil recovery factor after 1.2 PV gas injection, V_r is the volume of the oil recovered from the last cell at 1 atm and 298 K, V_o is the volume of the original oil in place at 1 atm and 298 K K. The minimum tie-line length among the tie-line lengths of all contacts is recorded.

7) The above steps are repeated at different pressures and the minimum tie-line length is recorded for each pressure. The minimum tie-line length is reduced at a higher pressure and the MMP can be theoretically found at the pressure where the minimum tie-line length reaches zero. However, it is difficult to calculate the tie-line length when the pressure approaches the MMP (Teklu *et al.*, 2014a). This issue can be effectively addressed by extrapolating the minimum tie-line length at the last few pressures (Ahmadi and Johns, 2011). A power-law extrapolation as shown in Eq. (5-9) is applied (Ahmadi and Johns, 2011).

$$TL^n = aP + b \tag{5-9}$$

where n is the exponential parameter, a is the slope, and b is the intercept of the y-axis. It is recommended that the square of the correlation coefficient should exceed 0.999 when finalizing the parameters n, a, and b (Ahmadi and Johns, 2011).

8) The confined oil-gas MMP determined by the tie-line length method is then validated by the oil recovery factors calculated by the proposed algorithm. At a constant temperature, the oil recovery factor at 1.2 PV gas injection is calculated at different pressures. The MMP determined by the tie-line length method is considered reasonable if it is near the inflection point of the oil recovery curve.

Compared to the original cell-to-cell simulation model (Metcalfe *et al.*, 1973) which can only estimate the oil-gas MMP under bulk conditions, the proposed algorithm is capable of predicting the oil-gas MMP in a confined space. Also, the proposed algorithm employs a volume translated PR-EOS (Peng and Robinson, 1976; Abudour *et al.*, 2013) to improve the accuracy of phase volume predictions. Compared to the MMC method proposed by Ahmadi and Johns (2011), the cell-to-cell simulation model (Metcalfe *et al.*, 1973) on which this work is based has the advantage of calculating the final oil recovery at each pressure which can be used to determine the required total cell number in order to achieve stable MMP results. The calculated oil recovery factor can also be used to validate the MMP results determined by the tie-line length method. Therefore, the calculated final oil recovery profile is used as a secondary validation of the proposed algorithm. This can effectively improve the reliability of the confined MMP calculations and is not featured in the previous confined MMP calculation algorithms. A schematic of the cell-to-cell simulation model and an overall procedure of conducting the confined MMP calculations using the proposed algorithm can be visualized in the flowchart shown in **Fig. 5-1**.

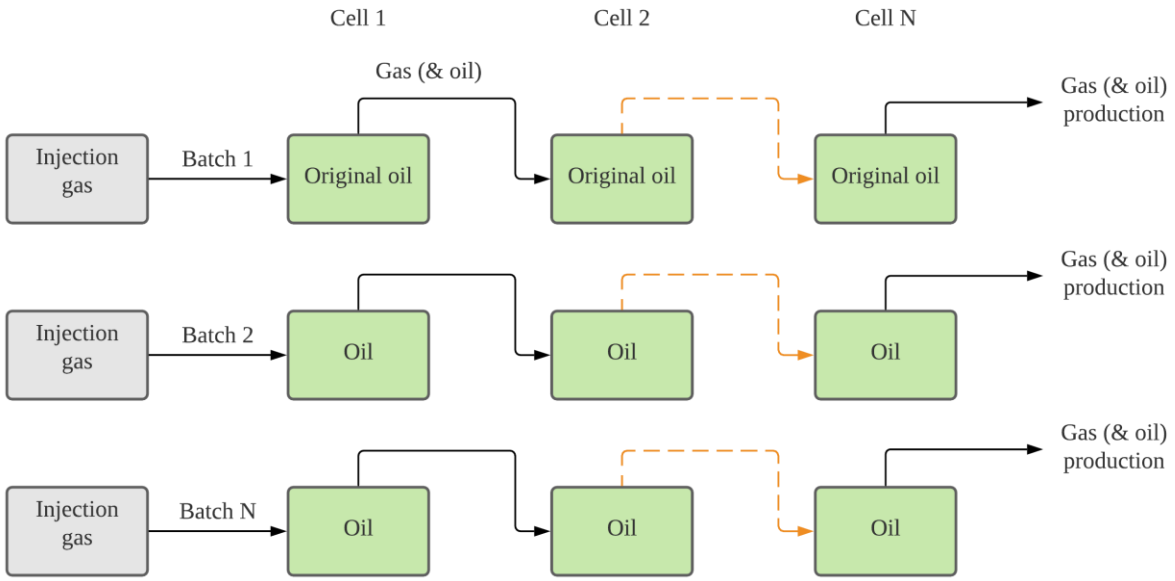
Cell 1
Cell 2
Cell N
Gas (& oil)
Injection gas
Batch 1
Original oil
Original oil
Original oil
Gas (& oil) production
Injection gas
Batch 2
Oil
Oil
Oil
Gas (& oil) production
Injection gas
Batch N
Oil
Oil
Oil
Gas (& oil) production

(a)

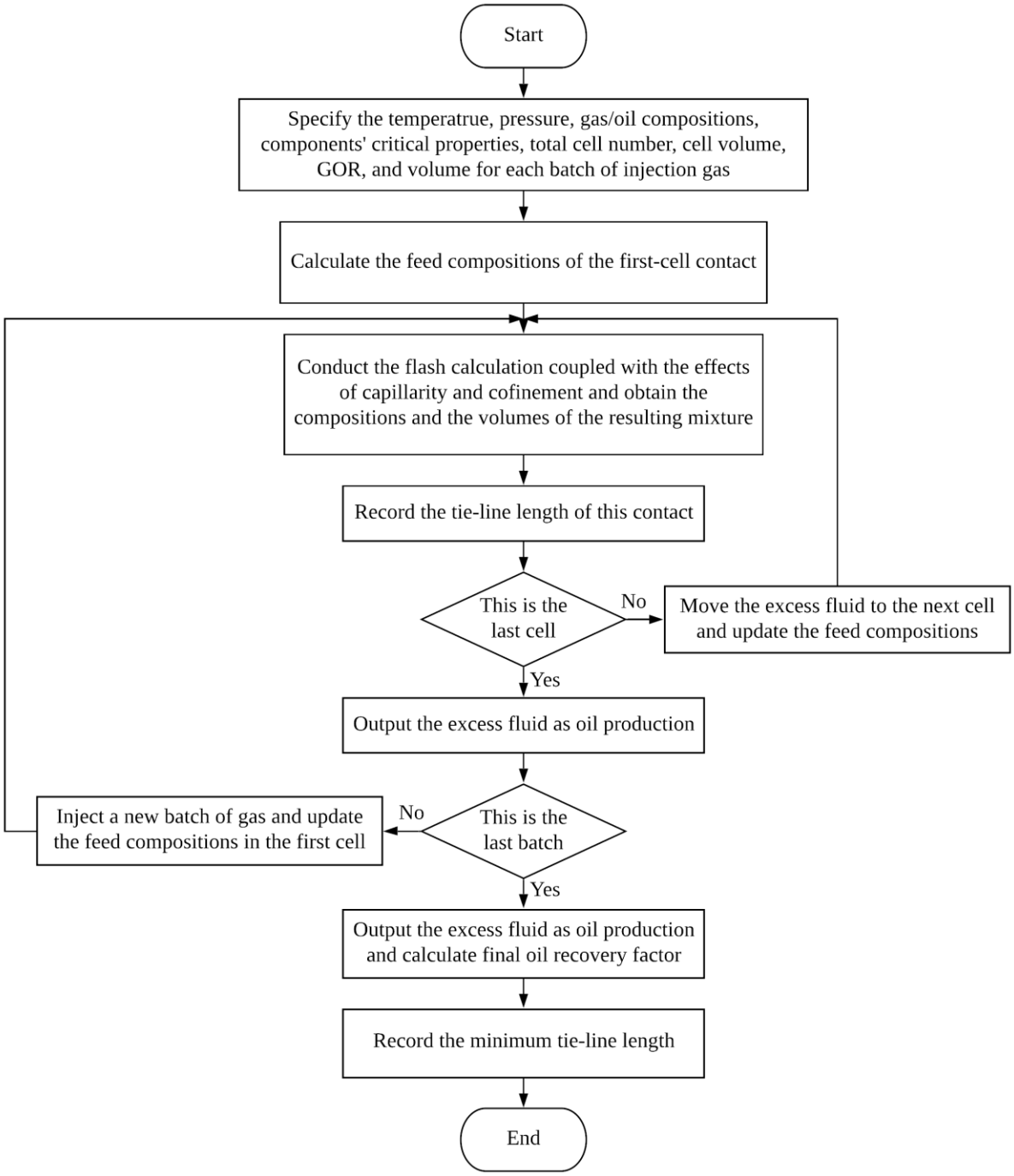

(b)

Fig. 5-1: (a) A schematic of the cell-to-cell simulation model and (b) a workflow of conducting the confined oil-gas MMP calculations using the proposed algorithm.

5.4. Results and Discussions

This section presents the confined oil-gas MMP calculations for four oil-gas systems using the proposed algorithm. The effects of temperature, pore radius, and injection gas impurity on the confined MMP calculations are also studied.

5.4.1. Summary of the Tested Oil-Gas Systems

A total of four oil-gas systems are tested in this work. The first three fluid systems are simple synthetic oil samples being displaced by CO_2, CH_4, and their mixture. The detailed compositions of the injection gas and the oil for the first three fluid systems are summarized in **Table 5-1**.

Table 5-1: The compositions of the injection gas and the oil in the first three oil-gas systems (Zhao *et al*., 2006; Yang *et al*., 2020).

	Oil-Gas System 1		**Oil-Gas System 2**		**Oil-Gas System 3**	
	Gas	Oil	Gas	Oil	Gas	Oil
CO_2	1	0	0.8	0	0	0
C_1	0	0.25	0.2	0.25	1	0
C_4	0	0.30	0	0.30	0	0.5
C_{10}	0	0.45	0	0.45	0	0.5

The physical properties of the constituting components in the first three oil-gas systems and their binary interactive parameters (BIPs) with CO_2 used in the PR-EOS model are given in **Table 5-2**.

Table 5-2: The physical properties (Quayle, 1953) of the constituting components in the first three oil-gas systems (Zhao *et al*., 2006; Yang *et al*., 2020).

	Critical pressure (P_c), bar	Critical temperature (T_c), K	Acentric factor (ω)	Parachor (P_{ch})	BIPs with CO_2
CO_2	73.84	304.21	0.2250	78.0	0
C_1	46.04	190.59	0.0104	77.0	0.1000
C_4	37.97	425.18	0.2010	189.9	0.1257
C_{10}	21.08	617.65	0.4900	433.5	0.0942

The last fluid system is a real dead crude oil sample being displaced by pure CO_2 (Zhang and Gu, 2015). The BIPs of the hydrocarbon components in this oil sample are tuned by matching the calculated confined MMP with the experimental data and the detailed procedure can be found in the work of Sun and Li (2020). The physical properties of the constituting components and their BIPs with CO_2 for the fourth oil-gas system are given in **Table 5-3.**

Table 5-3: Physical properties (Quayle, 1953) of the constituting components in the oil sample of the fourth fluid system and their BIPs with CO_2 (Zhang and Gu, 2015).

	Compositions	Critical pressure (P_c), bar	Critical temperature (T_c), K	Acentric factor (ω)	Parachor (P_{ch})	BIPs with CO_2
C_3	0.002	42.46	369.80	0.152	150.30	0.070
C_4	0.012	38.00	425.20	0.193	189.90	0.070
C_5	0.037	33.74	469.60	0.251	231.50	0.070
C_6	0.050	32.89	507.50	0.275	250.11	0.073
C_7	0.107	31.38	543.20	0.308	278.40	0.073
C_8-C_{10}	0.218	27.34	597.49	0.395	345.66	0.073
C_{11}-C_{13}	0.154	22.10	662.26	0.517	448.65	0.074
C_{14}-C_{17}	0.138	18.09	724.30	0.662	573.30	0.074
C_{18}-C_{21}	0.091	15.01	775.23	0.799	695.05	0.074
C_{22}-C_{25}	0.052	12.73	818.78	0.926	793.57	0.074
C_{26}-C_{30}	0.047	11.01	855.30	1.034	879.70	0.074
C_{31}-C_{36}	0.031	9.41	895.40	1.147	967.66	0.074
C_{37+}	0.062	8.51	1014.58	1.685	1078.87	0.074

The confined oil-gas MMPs of the above four fluid systems at different temperatures and pore radii are calculated using the proposed algorithm. The obtained confined MMPs are then analyzed to study the effects of temperature, pore radius, and injection gas impurity on the confined MMP calculations.

5.4.2. Determining the Total Cell Number

The total cell number and GOR are the two factors that might cause severe numerical dispersion issues. The GOR in this work is set to be 0.3 as suggested by Metcalfe *et al*. (1973). The total cell

number, however, has not received a widely accepted criterion that can eliminate the numerical dispersion. In this work, the final oil recovery is calculated with different total cell numbers until the final oil recovery flattens out with an increasing total cell number. The appropriate total cell number can be selected to be the one at which the stable oil recovery is maintained in both bulk conditions and in confined nanopores. The final oil recoveries as a function of the total cell number for all four oil-gas systems are shown in **Fig. 5-2**.

It can be seen from **Fig. 5-2** that the calculated final oil recovery increases with an increasing total cell number in both bulk and confined spaces. The final oil recovery for the first three fluids systems becomes stable at a total cell number of 150. The fourth fluid system, however, requires 450 to reach a stable final oil recovery. This can be attributed to the presence of the heavy components in the crude oil sample of the fourth fluid system. The injected CO_2 needs to be enriched with additional contacts before it is able to reach miscibility with the crude oil. In order to guarantee reliable and accurate results, this work applies a total cell number of 500 in all the confined oil-gas MMP calculations. **Fig. 5-3** shows the change of the resulting gas and oil compositions after each contact at different cell numbers for fluid system 3 as an example to visualize the gas enrichment process through multiple contacts in bulk conditions and in a confined space. The solid lines and the dashed line in **Fig. 5-3** represent the compositions of the liquid phase and the gas phase, respectively. Along the displacing path, the injection gas is enriched with C_4 and C_{10}. It is seen that the gas enrichment path in bulk conditions is different from that in a confined space. In general, the gas is enriched with more hydrocarbon components in a confined space than in bulk conditions at a fixed pressure. For the gas enrichment process in a confined space, the calculated MMP at 306.15 K with a pore radius of 10 nm is 251.02 bar. From **Fig. 5-3**, it is found that with an increasing pressure, the injection gas is enriched with more hydrocarbon components.

Also, when the pressure approaches the MMP, the oil and gas compositions become almost identical. This also proves the correctness of the proposed algorithm.

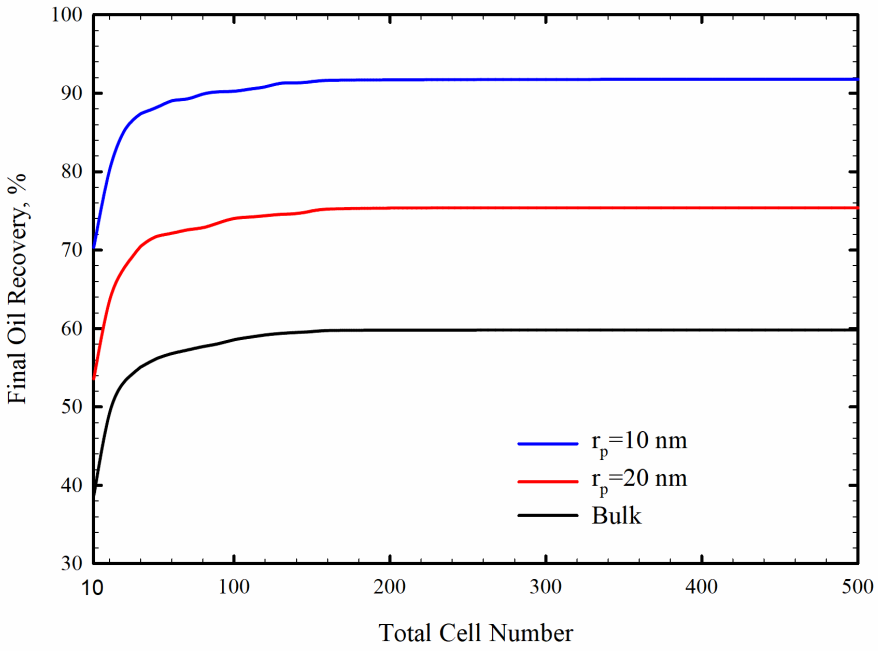

(a)

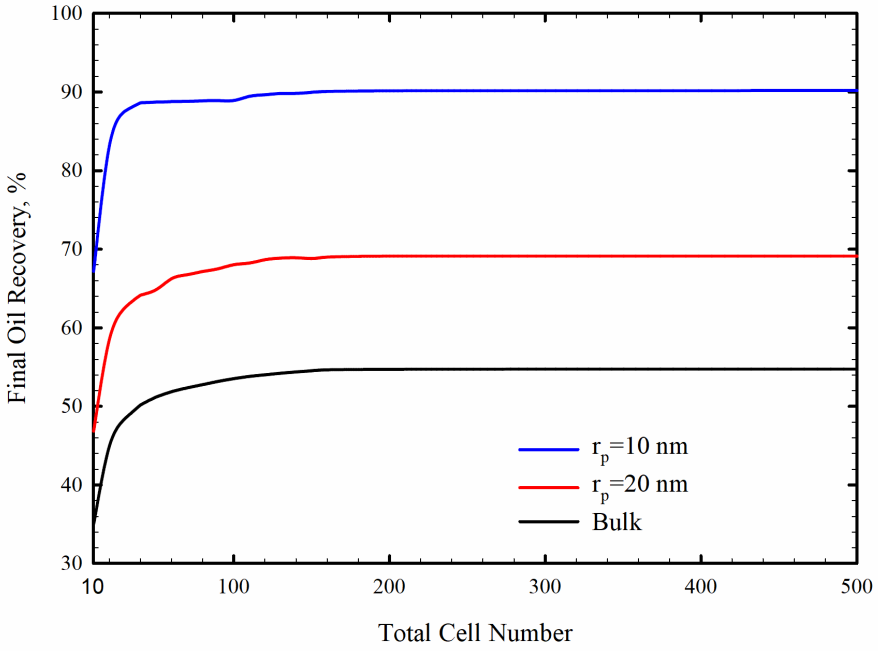

(b)

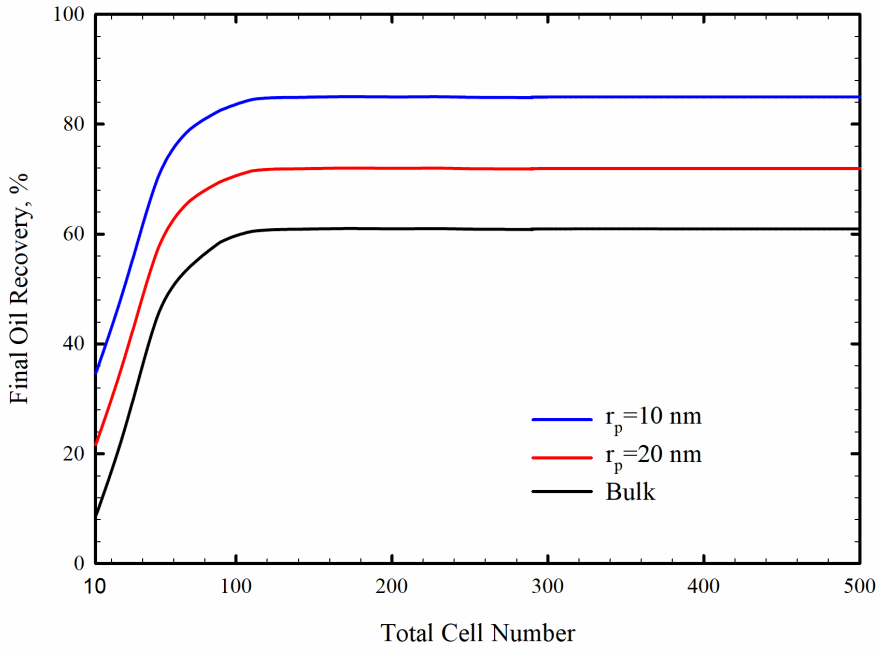

(c)

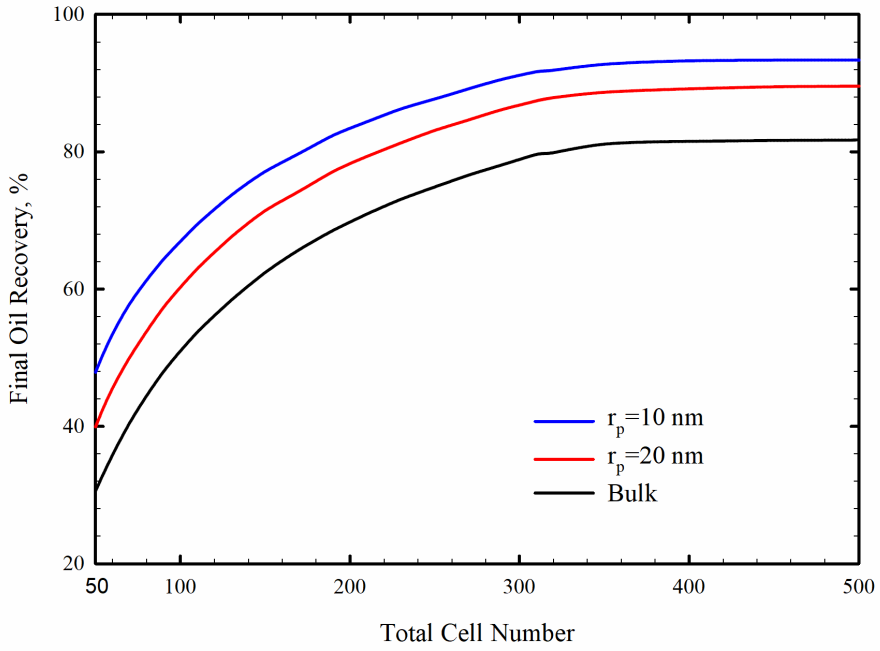

(d)

Fig. 5-2: The effect of the total cell number on the final oil recovery under bulk conditions and in confined nanopores for the (a) oil-gas system 1, (b) oil-gas system 2, (c) oil-gas system 3, and (d) oil-gas system 4.

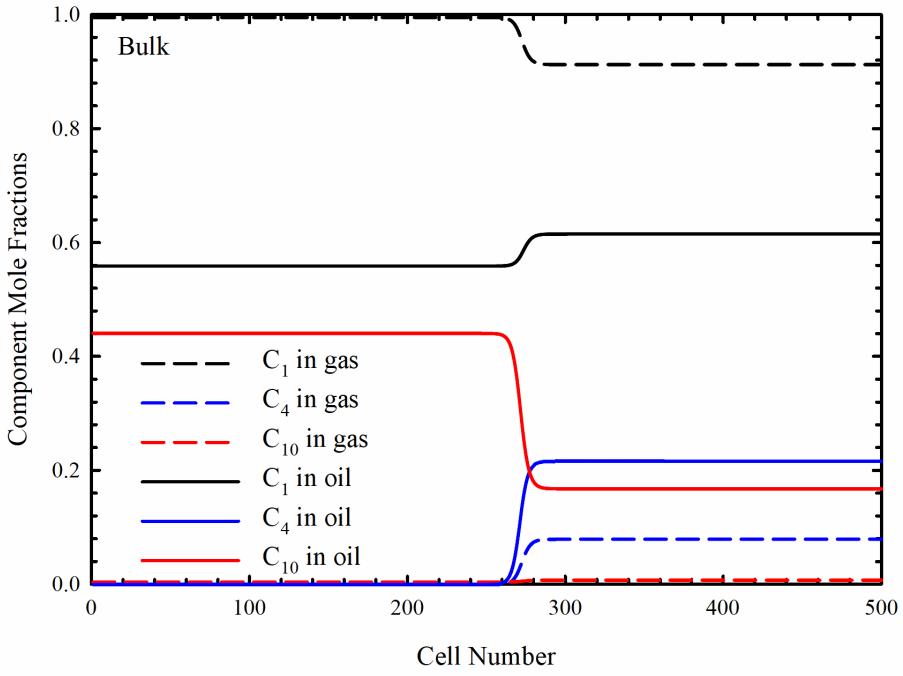
Bulk
Component Mole Fractions
Cell Number
C1 in gas
C4 in gas
C10 in gas
C1 in oil
C4 in oil
C10 in oil
0.0
0.2
0.4
0.6
0.8
1.0
0
100
200
300
400
500

(a)

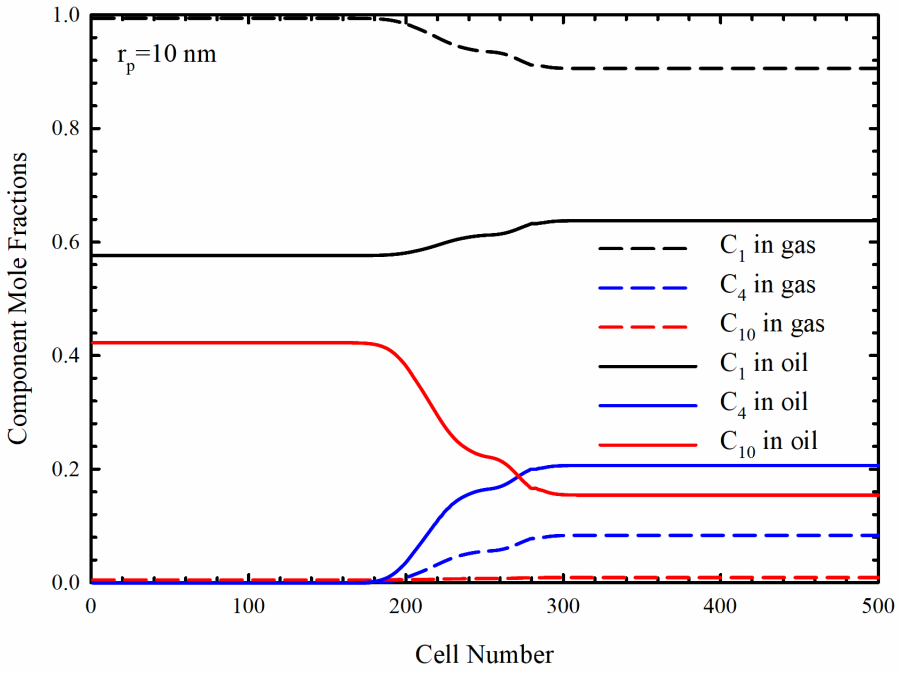
rp=10 nm
Component Mole Fractions
Cell Number
C1 in gas
C4 in gas
C10 in gas
C1 in oil
C4 in oil
C10 in oil
0.0
0.2
0.4
0.6
0.8
1.0
0
100
200
300
400
500

(b)

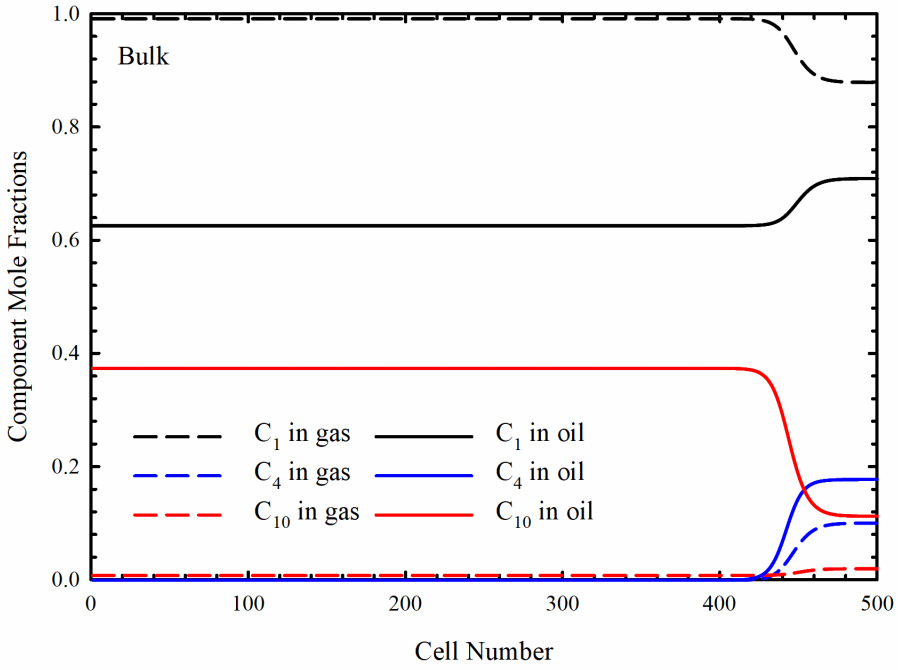

(c)

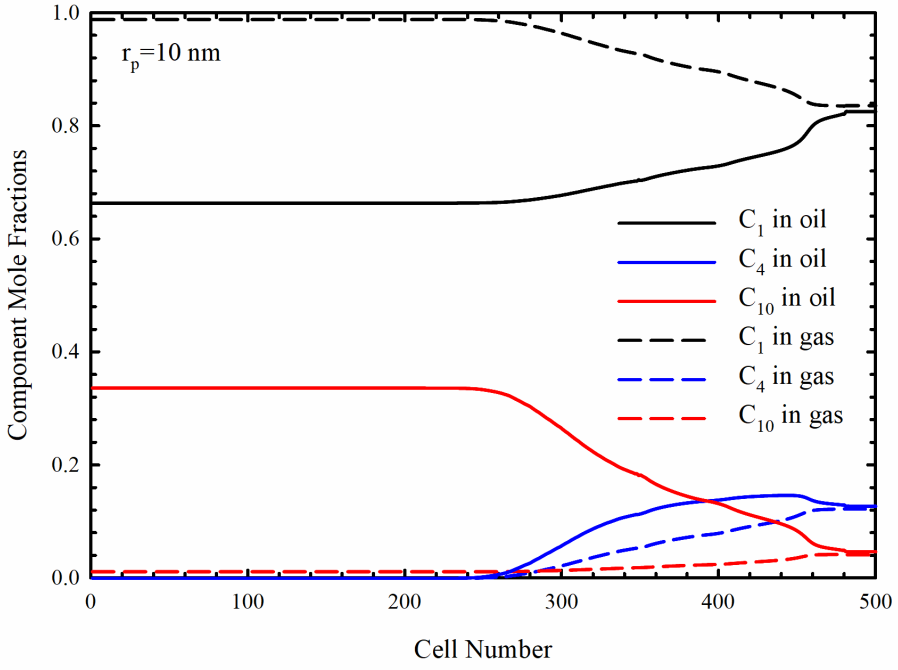

(d)

Fig. 5-3: The mole fractions of the constituting components in oil phase and gas phase for the oil-gas system 3 at a temperature of 306.15 K and a pressure of (a) 220 bar in bulk conditions, (b) 220 bar in a confined space, (c) 250 bar in bulk conditions, and (d) 250 in a confined space.

5.4.3. Further Validation of MMP Using the Calculated Oil Recovery Factors

As described before, the calculated oil recovery from the proposed MMP calculation algorithm is used to validate the confined oil-gas MMP determined by the tie-line length method. As per the slim-tube test protocols, the MMP can be determined as the inflection point of the oil recovery curve (Yellig, 1982). This criterion is also used in this work to validate the MMP results obtained from the tie-line length method. It is worth noting that under most circumstances, the Wilson equation (Wilson, 1969) is applied to provide a reliable initialization of the phase equilibrium ratios (k_i) given in Eq. (5-10).

$$k_i = \frac{P_{ci}}{P} exp\left[5.37(1+\omega_i)\left(1-\frac{T_{ci}}{T}\right)\right], i = 1, \dots, N_c \quad (5\text{-}10)$$

where k_i is the phase equilibrium ratios of the *i*th component, P_{ci} is the critical pressure of the *i*th component, P is the system pressure, ω_i is the acentric factor of the *i*th component, T_{ci} is the critical temperature of the *i*th component, and T is the system temperature. In the near-MMP region or the region above MMP, other k_i initialization strategies are required including $k_i/3$ and $\sqrt[3]{k_i}$ (Whitson and Brulé, 2000). **Fig. 5-4** shows the oil recovery curves calculated for all four fluid systems at different temperatures with a pore radius of 2 nm. In **Fig. 5-4**, the confined MMPs determined using the tie-line length method are also highlighted using vertical lines.

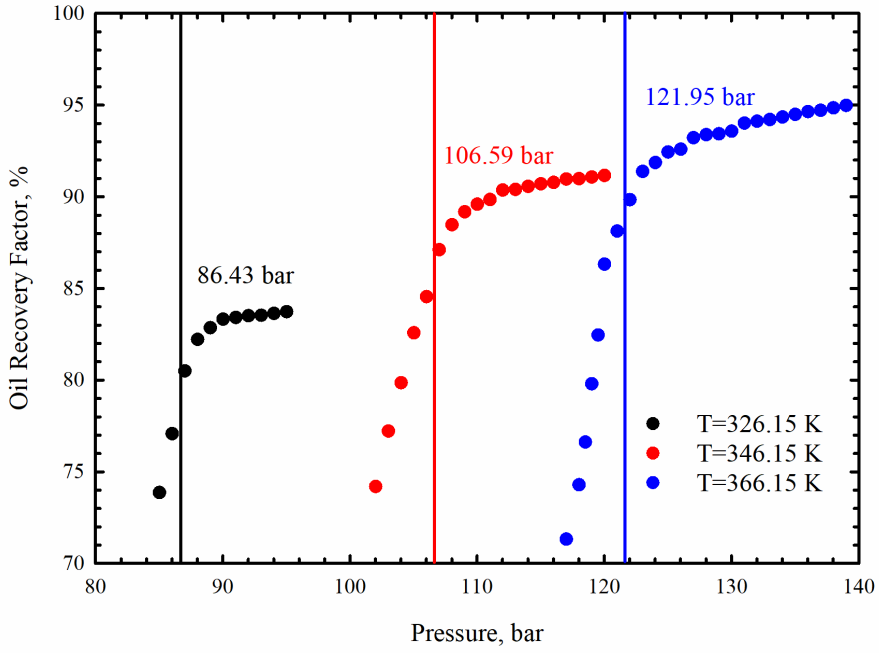
Oil Recovery Factor, %
Pressure, bar
86.43 bar
106.59 bar
121.95 bar
T=326.15 K
T=346.15 K
T=366.15 K

(a)

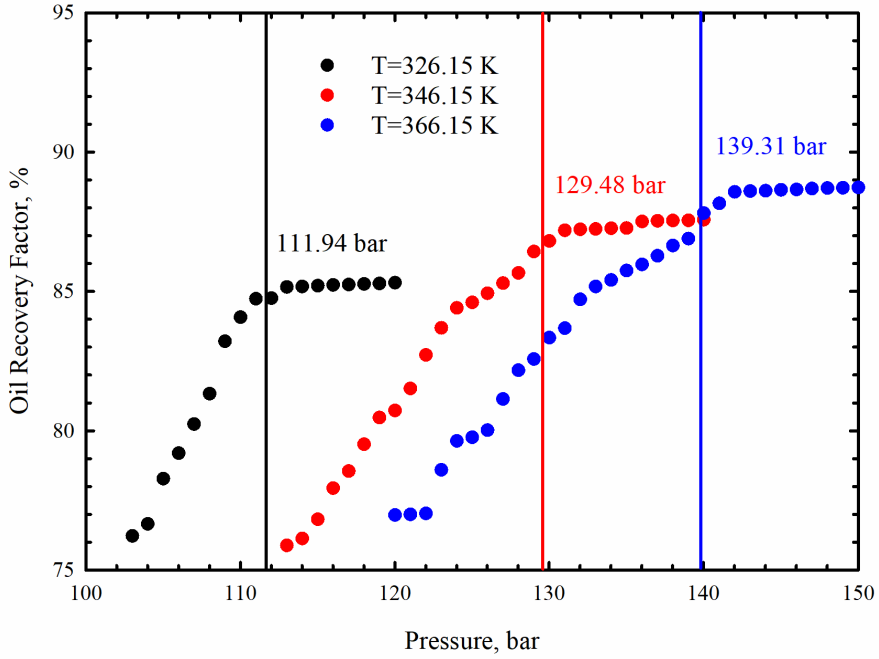
Oil Recovery Factor, %
Pressure, bar
111.94 bar
129.48 bar
139.31 bar
T=326.15 K
T=346.15 K
T=366.15 K

(b)

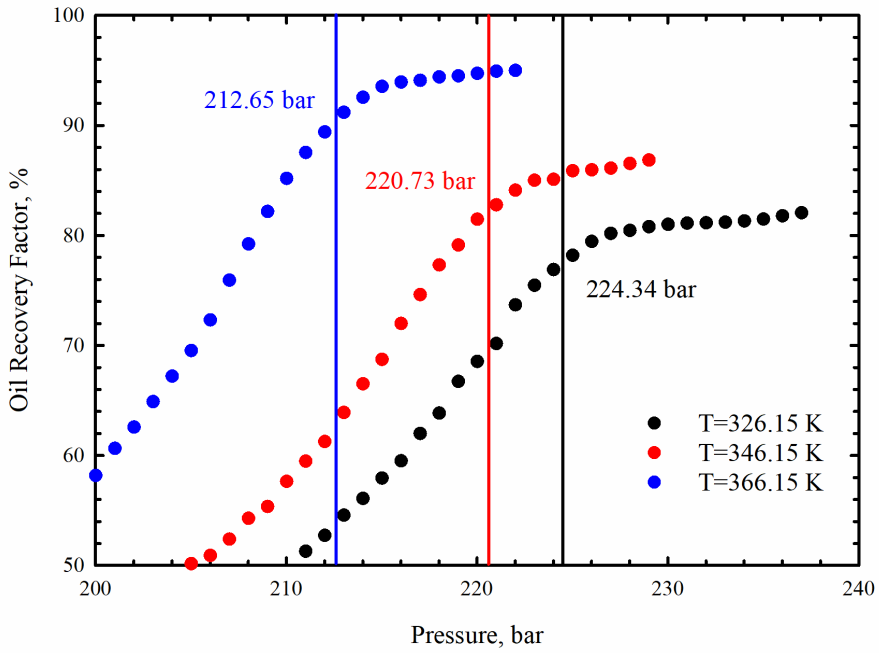

(c)

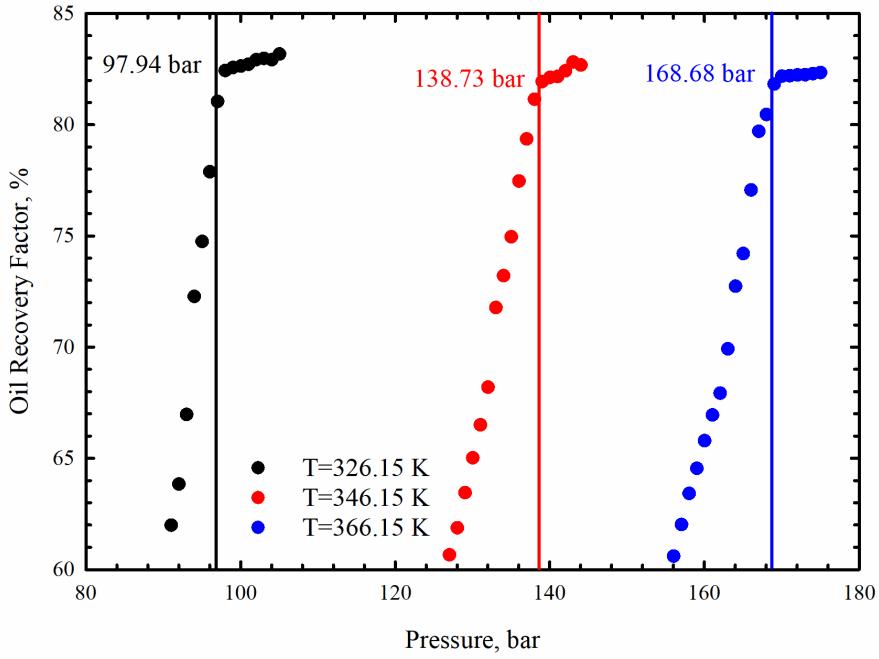

(d)

Fig. 5-4: Calculated oil recovery as a function of pressure for the (a) fluid system 1, (b) fluid system 2, (c) fluid system 3, and (d) fluid system 4 at different temperatures with a pore radius of 2 nm.

It can be seen from **Fig. 5-4** that the oil recovery factor increases with an increasing pressure. Above a certain pressure, the increase rate of oil recovery is reduced dramatically. The inflection point can be determined as the oil-gas MMP (Yellig, 1982). It is found from **Fig. 5-4** that for all the four fluid systems, the confined MMPs determined by the tie-line length method are slightly lower than the inflection points of the oil recovery curve for all tested temperatures. Nevertheless, the MMPs determined by the tie-line length method are very close to the inflection point of the oil recovery curve. We also compare the confined MMPs calculated using the proposed algorithm with the ones calculated using the confined MMC method (Sun and Li, 2021). **Fig. 5-5** shows the comparison results in a parity chart. It can be seen from **Fig. 5-5** that the confined MMPs calculated by the proposed algorithm and the MMC method (Sun and Li, 2021) are in excellent agreement. This is expected because both methods employ the tie-line length extrapolation method to determine the confined MMPs. Furthermore, for this oil sample, the experimentally measured CO_2-oil MMP in the tested tight cores is 123 bar at 326.15 K (Zhang and Gu, 2015). The confined MMP calculated using the proposed algorithm is 122.38 bar under experimental conditions. This demonstrates that the proposed algorithm is able to reproduce the experimental results using the properly tuned BIPs. The advantage of the proposed algorithm over the previous one is that the proposed algorithm offers the opportunity to validate the determined MMPs using the oil recovery factors. This feature of the secondary validation is crucial because it allows this simulation study to mimic the realistic gas displacement process in a slim-tube experiment and hence significantly improves the reliability of the obtained simulation results.

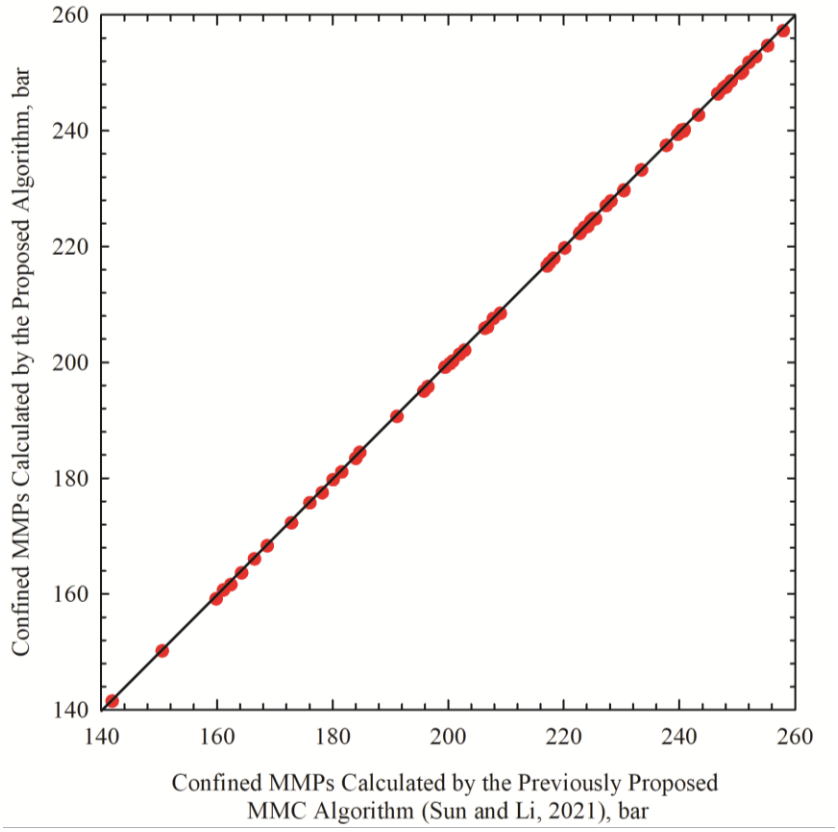

Fig. 5-5: Confined MMPs calculated by the proposed algorithm and the previously proposed MMC algorithm (Sun and Li, 2021).

5.4.4. Effects of Temperature and Pore Radius on the Confined MMP Calculations

It is observed in many studies that the oil-gas MMP is heavily dependent on the reservoir temperature and pore size (Teklu *et al*., 2014a; Teklu *et al*., 2014b; Sun and Li, 2021). This work calculates the oil-gas MMP in confined nanopores with different pore sizes at a wide range of temperatures to investigate the effects of temperature and pore radius on confined MMP calculations. The results are incredibly similar to our previous study (Sun and Li, 2021). The calculated oil-gas MMP in confined nanopores first increases and then decreases with an increasing temperature. It is intriguing to notice that this trend has also been introduced for bulk oil-gas MMP (Yuan *et al.*, 2005). The reason for the MMP decreases after a certain temperature is that at an elevated temperature, the liquid phase in the reservoir becomes more vapor-phase like.

Hence, the oil-gas MMP becomes the miscibility pressure between one vapor phase and one vapor-phase-like liquid phase. Moreover, a smaller pore radius clearly results in a decreasing oil-gas MMP. The MMP decreases in the confined nanopores from the bulk MMP significantly when the pore radius is less than 5 nm, while it becomes almost constant when the pore radius is larger than 20 nm. The above findings are in high consistency with the ones obtained in Sun and Li (2021) which applied a modified MMC method in calculating the confined MMPs.

5.4.5. Injection Gas Impurity Effect on the Confined MMP Calculations

Another advantage of the proposed MMC algorithm is that it can be used to conveniently investigate the effect of injection gas compositions on the gas-oil MMP. As an example, here we employ the proposed algorithm to examine the effect of CH_4 contamination in CO_2 on the gas-oil MMP. Due to the difficulty of acquiring pure CO_2 for the injection, it is a common practice in the field to reinject the produced CH4 together with CO_2 back into the reservoir for EOR purposes (Zick, 1986; Zhang *et al.*, 2017b). The previous calculation results for the first and the second fluid systems clearly show that the confined MMP is generally increased when injecting a CH_4-CO_2 mixture as compared to pure CO_2 injection. Herein, we calculate the confined MMP of the first and the second fluids systems being displaced by CO_2-CH_4 mixture with various CH_4 content. **Fig. 5-6** shows the calculation results.

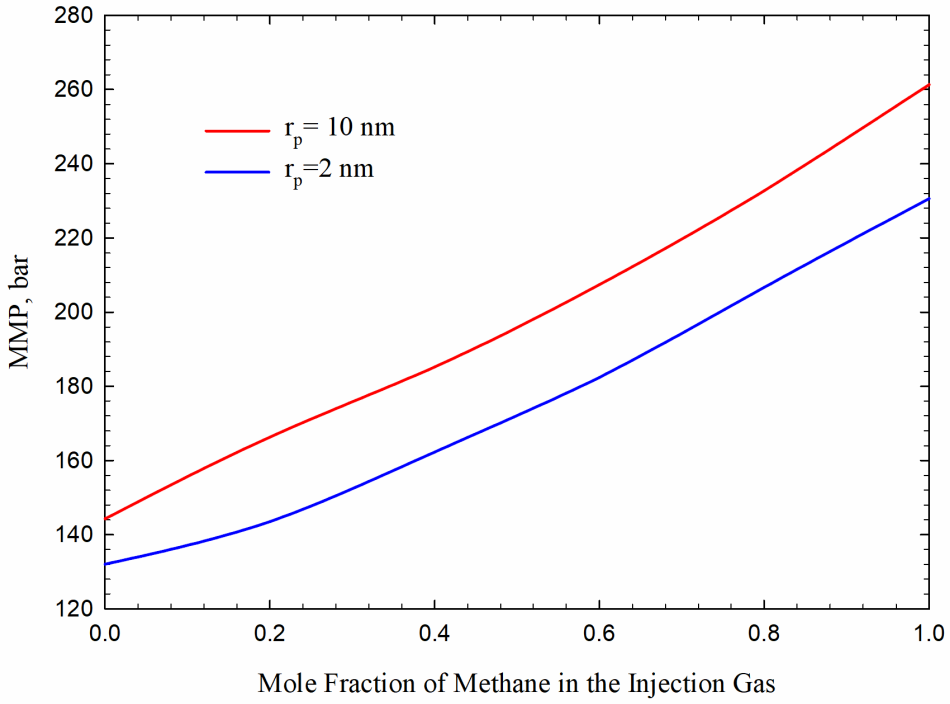

Fig. 5-6: Calculated confined oil-gas MMP as a function of the CH_4 mole fraction in the injection gas.

The calculation results in **Fig. 5-6** suggest that the calculated oil-gas MMP in confined nanopores increases with an increasing CH_4 content. The MMP increasing trend appears to be almost linear, which is similar to the MMP predictions in bulk conditions (Jin *et al.*, 2017). Such observation seems to be true for all the tested pore radii. Therefore, in a real gas injection practice in tight/shale reservoirs, the content of CH_4 in the injection gas should be limited in order to achieve a lower oil-gas MMP. Through this example, it is demonstrated that the proposed algorithm can be readily used to study the effect of injection gas impurity on the confined MMP calculations.

5.5.Conclusions

We develop a new oil-gas MMP calculation algorithm based on the original cell-to-cell simulation model (Metcalfe *et al.*, 1973) to predict the oil-gas MMP in confined nanopores with decent

reliability and accuracy. The results of the final oil recovery are utilized to determine the required total cell number to avoid numerical dispersion and to validate the confined MMPs determined by the tie-line length method. The capillary pressure and a critical point shift model (Tan *et al*., 2019) are coupled with the conventional two-phase equilibrium calculation algorithm to reflect the capillarity and confinement effect in nanopores. A volume translated PR-EOS (Peng and Robinson, 1976; Abudour *et al.*, 2013) is employed to provide accurate phase densities calculations. By conducting confined oil-gas MMP calculations for four oil-gas systems at different temperatures and pore radii, we can reach the following conclusions:

- A total cell number of 500 is determined as the cell number that can give stable simulation results. Compared to a light to medium oil sample, the oil sample containing more heavy components requires a larger total cell number to reach a stable oil-recovery-factor calculation result. This is because the injection gas requires more contacts to be enriched when displacing a heavier oil as compared to the displacement of a lighter oil.
- The confined MMP determined by the tie-line length method can be further validated by the calculated oil recovery curves. It is found that the confined MMPs determined by the tie-line length method are slightly lower than the inflection point of the oil recovery curve. The calculated confined MMP corresponds to the pressure at which the increase of the oil recovery factor starts to slow down.
- The effects of the temperature and pore radius on the confined gas-oil MMP calculations discussed in this work are in excellent agreement with our previous study (Sun and Li, 2021) where a modified MMC method was applied. The confined oil-gas MMP first increases and then decreases with an increasing temperature. This is due to the phase behavior limit where the oil phase becomes a vapor-like phase or vapor phase at an elevated

temperature. Also, the oil-gas MMP in confined nanopores is reduced. The reduction of the confined MMP becomes significant when the pore radius is less than 10 nm. When the pore radius is larger than 20 nm, the oil-gas MMP becomes almost constant and is close to the bulk MMP.

- The injection gas impurity has a strong effect on the confined oil-gas MMP. The simulation results using the proposed MMC algorithm suggest that the confined MMP increases with an increasing CH_4 content in the injection gas.

Acknowledgments

The authors acknowledge a Discovery Grant from the Natural Sciences and Engineering Research Council of Canada (NSERC) to H. Li (Grant No.: NSERC RGPIN-2020-04571).

References

Abudour, A., Mohammad, S., Robinson, R. and Gasem, K. 2013. Volume-Translated Peng-Robinson Equation of State for Liquid Densities of Diverse Binary Mixtures. Fluid Phase Equilibria, 349, 37-55. http://doi.org/10.1016/j.fluid.2013.04.002.

Ahmadi, K. and Johns, R. 2011. Multiple-Mixing-Cell Method for MMP Calculations. SPE Journal, 16(04), 733-742. http://doi.org/10.2118/116823-pa.

Ahmadi, M., Zendehboudi, S. and James, L. 2017. A Reliable Strategy to Calculate Minimum Miscibility Pressure of CO_2-Oil System in Miscible Gas Flooding Processes. Fuel, 208, 117-126. http://doi.org/10.1016/j.fuel.2017.06.135.

Belhaj, H., Abukhalifeh, H. and Javid, K. 2013. Miscible Oil Recovery Utilizing N_2 and/or HC Gases in CO_2 Injection. Journal of Petroleum Science and Engineering, 111, 144-152. https://doi.org/10.1016/j.petrol.2013.08.030.

Christiansen, R.L. and Haines, H.K. 1987. Rapid Measurement of Minimum Miscibility Pressure with the Rising-Bubble Apparatus. SPE Reservoir Engineering, 2(4), 443–449. https://doi.org/10.2118/13114-PA

Elsharkawy, A.M., Poettmann, F.H. and Christiansen, R.L. 1996. Measuring CO2 Minimum Miscibility Pressures: Slim-Tune or Rising-Bubble Method? Energy & Fuels, 10, 443-449. https://doi.org/10.1021/ef940212f.

Gross J. and Sadowski G. 2002. Application of the perturbed-chain SAFT equation of state to associating systems. Industrial & Engineering Chemistry Research. 41(22), 5510-5515. https://doi.org/10.1021/ie010954d.

Holm, L. and Josendal, V. 1974. Mechanisms of Oil Displacement by Carbon Dioxide. Journal of Petroleum Technology, 26(12), 1427-1438. http://doi.org/10.2118/4736-pa.

Jaubert, J.N., Arras, L., Neau, E. and Avaullée, L. 1998. Properly Defining the Classical Vaporizing the Condensing Mechanisms when a Gas is Injected into a Crude Oil. Industrial & Engineering Chemistry Research, 37, 4860-4869. https://doi.org/10.1021/ie9803016.

Jaubert, J.N., Wolff, L., Neau, E. and Avaullée, L. 1998. A Very Simple Multiple Mixing Cell Calculation to Compute the Minimum Miscibility Pressure Whatever the Displacement Mechanism. Industrial & Engineering Chemistry Research, 37, 4854-4859. https://doi.org/10.1021/ie980348r.

Jin, L., Pekot, L.J., Hawthorne, S.B., Gobran, B., Greeves, A., Bosshart, N.W., Jiang, T., Hamling, J.A. and Gorecki, C.D. 2016. Impact of CO_2 Impurity on MMP and Oil Recovery Performance of the Bell Creek Oil Field. Energy Procedia, 114, 6997-7008. https://doi.org/10.1016/j.egypro.2017.03.1841.

Johns, R. and Orr, F. 1996. Miscible Gas Displacement of Multicomponent Oils. SPE Journal, 1(01), 39-50. http://doi.org/10.2118/30798-pa.

Lashgari, H., Sun, A., Zhang, T., Pope, G. and Lake, L. 2019. Evaluation of Carbon Dioxide Storage and Miscible Gas EOR in Shale Oil Reservoirs. Fuel, 241, 1223-1235. http://doi.org/10.1016/j.fuel.2018.11.076.

Lee, J.I. 1979. Effectiveness of Carbon Dioxide Displacement under Miscible and Immiscible Conditions. Report RR-40. Petroleum Recovery Institute, Calgary.

Li, D., Li, X., Zhang, Y., Sun, L. and Yuan, S. 2019. Four Methods to Estimate Minimum Miscibility Pressure of CO_2-Oil Based on Machine Learning. Chinese Journal of Chemistry, 37, 1271-1278. http://doi.org/10.1002/cjoc.201900337.

Li, H., Qin, J. and Yang, D. 2012. An Improved CO_2–Oil Minimum Miscibility Pressure Correlation for Live and Dead Crude Oils. Industrial & Engineering Chemistry Research, 51(8), 3516-3523. http://doi.org/10.1021/ie202339g.

Metcalfe, R.S., Fussell, D.D. and Shelton, J.L. 1973. A Multicell Equilibrium Separation Model for the Study of Multiple Contact Miscibility in Rich-Gas Drives. SPE Journal, 13(3), 147-155. https://doi.org/10.2118/3995-PA.

Mungan, N. 1981. Carbon Dioxide Flooding-Fundamentals. Journal of Canadian Petroleum Technology, 20(01), 87-92. http://doi.org/10.2118/81-01-03.

Neau, E., Avaullée, L., and Jaubert, J.N. 1996. A New Algorithm for Enhanced Oil Recovery Calculations. Fluid Phase Equilibria, 117, 265-272. https://doi.org/10.1016/0378-3812(95)02962-1.

Nguyen, P., Mohaddes, D., Riordon, J., Fadaei, H., Lele, P. and Sinton, D. 2015. Fast Fluorescence-Based Microfluidic Method for Measuring Minimum Miscibility Pressure of CO_2 in Crude Oils. Analytical Chemistry, 87(6), 3160-3164. http://doi.org/10.1021/ac5047856.

Orr, F. and Jensen, C. 1984. Interpretation of Pressure-Composition Phase Diagrams for CO2/Crude-Oil Systems. SPE Journal, 24(05), 485-497. http://doi.org/10.2118/11125-pa.

Peng, D. and Robinson, D. 1976. A New Two-Constant Equation of State. Industrial & Engineering Chemistry Fundamentals, 15(1), 59-64. http://doi.org/10.1021/i160057a011.

Qiu, X., Tan, S., Dejam, M. and Adidharma, H. 2019. Experimental Study on the Criticality of a Methane/Ethane Mixture Confined in Nanoporous Media. Langmuir, 35(36), 11635-11642. http://doi.org/10.1021/acs.langmuir.9b01399.

Quayle, O.R. 1953. The Parachors of Organic Compounds. An Interpretation and Catalogue. Chemical Reviews, 53 (3), 439-589. https://doi.org/10.1021/cr60166a003.

Randall, T. and Bennion, D. 1988. Recent Developments in Slim Tube Testing for Hydrocarbon-Miscible Flood (HCMF) Solvent Design. Journal of Canadian Petroleum Technology, 27(06), 33-44. http://doi.org/10.2118/88-06-02.

Rao, D. 1997. A New Technique of Vanishing Interfacial Tension for Miscibility Determination. Fluid Phase Equilibria, 139(1-2), 311-324. http://doi.org/10.1016/s0378-3812(97)00180-5.

Rathmell, J.J., Stalkup, F.I. and Hassinger, R.C. 1971. A Laboratory Investigation of Miscible Displacement by Carbon Dioxide. In: The Fall Meeting of the Society of Petroleum Engineers of AIME. Society of Petroleum Engineers. http://doi.org/10.2118/3483-MS

Shokir, E. 2007. CO_2-Oil Minimum Miscibility Pressure Model for Impure and Pure CO_2 Streams. Journal of Petroleum Science and Engineering, 58(1-2), 173-185. http://doi.org/10.1016/j.petrol.2006.12.001.

Sun, H. and Li, H. 2021. Minimum Miscibility Pressure Determination in Confined Nanopores Considering Pore Size Distribution of Tight/Shale Formations. Fuel, 286, 119450. https://doi.org/10.1016/j.fuel.2020.119450.

Tan, S., Qiu, X., Dejam, M. and Adidharma, H. 2019. Critical Point of Fluid Confined in Nanopores: Experimental Detection and Measurement. The Journal of Physical Chemistry C, 123(15), 9824-9830. http://doi.org/10.1021/acs.jpcc.9b00299.

Teklu, T.W., Alharthy, N., Kazemi, H., Yin, X. and Graves, R.M. 2014a. Vanishing Interfacial Tension Algorithm for MMP Determination in Unconventional Reservoirs. In: SPE Western North American and Rocky Mountain Joint Regional Meeting. Society of Petroleum Engineers. http://doi.org/10.2118/169517-MS.

Teklu, T., Alharthy, N., Kazemi, H., Yin, X., Graves, R. and AlSumaiti, A. 2014b. Phase Behavior and Minimum Miscibility Pressure in Nanopores. SPE Reservoir Evaluation & Engineering, 17(03), 396-403. http://doi.org/10.2118/168865-pa.

Wang, S., Ma, M. and Chen, S. 2016. Application of PC-SAFT Equation of State for CO2 Minimum Miscibility Pressure Prediction in Nanopores. In: SPE Improved Oil Recovery Conference. Society of Petroleum Engineers. https://doi.org/10.2118/179535-MS.

Wang, Y. and Orr, F. 1997. Analytical Calculation of Minimum Miscibility Pressure. Fluid Phase Equilibria, 139(1-2), 101-124. http://doi.org/10.1016/s0378-3812(97)00179-9.

Weinaug, C. and Katz, D. 1943. Surface Tensions of Methane-Propane Mixtures. Industrial & Engineering Chemistry, 35(2), 239-246. http://doi.org/10.1021/ie50398a028.

Whitson, C. and Brulé, M. 2000. Phase behavior. Richardson, Texas: Henry L. Doherty Memorial Fund of AIME, Society of Petroleum Engineers.

Wilson, G. M. 1969. A Modified Redlich-Kwong Equation of State, Application to General Physical Data Calculations. In: 65th National AIChE Meeting. Cleveland.

Yang, F., Yu, P. and Zhang, X. 2020. Multiple-Mixing-Cell Model for Calculation of Minimum Miscibility Pressure Controlled by Tie-Line Length. Geofluids, 1-8. https://doi.org/10.1155/2020/9587254.

Yellig, W. 1982. Carbon Dioxide Displacement of a West Texas Reservoir Oil. SPE Journal, 22(06), 805-815. http://doi.org/10.2118/9785-pa.

Young, T. 1805. An Essay on the Cohesion of Fluids. Philosophical Transactions of the Royal Society of London, 95(0), 65-87. http://doi.org/10.1098/rstl.1805.0005.

Yu, W., Lashgari, H., Wu, K. and Sepehrnoori, K. 2015. CO_2 Injection for Enhanced Oil Recovery in Bakken Tight Oil Reservoirs. Fuel, 159, 354-363. http://doi.org/10.1016/j.fuel.2015.06.092.

Yuan, H. and Johns, R. 2005. Simplified Method for Calculation of Minimum Miscibility Pressure or Enrichment. SPE Journal, 10(04), 416-425. http://doi.org/10.2118/77381-pa.

ZareNezhad, B. 2016. A New Correlation for Predicting the Minimum Miscibility Pressure Regarding the Enhanced Oil Recovery Processes in the Petroleum Industry. Petroleum Science and Technology, 34(1), 56-62. http://doi.org/10.1080/10916466.2015.1117493.

Zarragoicoechea, G. and Kuz, V. 2004. Critical Shift of a Confined Fluid in a Nanopore. Fluid Phase Equilibria, 220(1), 7-9. https://doi.org/10.1016/j.fluid.2004.02.014.

Zhang, K. and Gu, Y. 2015. Two Different Technical Criteria for Determining the Minimum Miscibility Pressures (MMPs) from the Slim-Tube and Coreflood Tests. Fuel, 161, 146-156. http://doi.org/10.1016/j.fuel.2015.08.039.

Zhang, K., Du, F. and Nojabaei, B. 2019. Effect of Pore Size Heterogeneity on Hydrocarbon Fluid Distribution and Transport in Nanometer-Sized Porous Media. In: SPE Eastern Regional Meeting. Society of Petroleum Engineers. https://doi.org/10.2118/196586-MS.

Zhang, K., Jia, N., Zeng, F. and Luo, P. 2017a. A New Diminishing Interface Method for Determining the Minimum Miscibility Pressures of Light Oil–CO2 Systems in Bulk Phase and Nanopores. Energy & Fuels, 31(11), 12021-12034. http://doi.org/10.1021/acs.energyfuels.7b02439.

Zhang, K., Jia, N. and Li, S. 2017b. Exploring the Effects of Four Important Factors on Oil–CO2 Interfacial Properties and Miscibility in Nanopores. RSC Advances, 7(85), 54164-54177. http://doi.org/10.1039/c7ra10671h.

Zhao, G., Adidharma, H., Towler, B., and Radosz, M. 2006. Using a Multiple-Mixing-Cell Model to Study Minimum Miscibility Pressure Controlled by Thermodynamic Equilibrium Tie Lines. Industrial & Engineering Chemistry Research, 45(23), 7913-7923. https://doi.org/10.1021/ie0606237.

Zick, A.A. 1986. A Combined Condensing/Vaporizing Mechanism in the Displacement of Oil by Enriched Gases. In: SPE Annual Technical Conference and Exhibition. Society of Petroleum Engineers.

CHAPTER 6 CONCLUSIONS, CONTRIBUTIONS, AND RECOMMENDATIONS

6.1. Conclusions and Scientific Contributions to the Literature

Robust and efficient two-phase and three-phase equilibrium calculation algorithms coupled with capillarity and confinement effects are developed in this dissertation. Furthermore, the developed two-phase equilibrium calculation algorithm is applied to study the oil-gas MMP in confined nanopores. The major conclusions are summarized as follows.

Chapter 2:

The accuracy of the vapor-liquid equilibrium calculation of hydrocarbons in confined nanopores is improved in this work by coupling a modified Young-Laplace equation (Tan and Piri, 2015) in the PR-EOS (Peng and Robinson, 1976) model. In order to apply the modified Young-Laplace equation in the two-phase flash calculation at different temperatures and pore radii, we developed correlations of the tuning parameter λ for six pure hydrocarbon substances and two binary hydrocarbon mixtures based on the experimental data collected from the literature. The correlations of the tuning parameter λ for both pure substance and mixture can be expressed as a quadratic polynomial function with temperature, and the tuning parameter λ increases with an increasing pore radius and carbon number. Also, the value of the tuning parameter λ is always less than one. But it can become negative which adjusts the calculated capillary pressure to a lower value. Moreover, because that the temperature interval of hydrocarbon mixtures' two-phase region is often above the critical temperatures of the constituting components, we also demonstrate that the tuning parameter λ under supercritical conditions can be back-calculated using a simple mixing rule and the correlation can also be expressed as polynomial functions with temperature. With the

correlations of the tuning parameter λ for hydrocarbon substances and mixtures developed, we applied the modified Young-Laplace (Tan and Piri, 2015) in PR-EOS and found that the accuracy of the vapor-liquid equilibrium calculations in confined nanopores is significantly improved. Nevertheless, it is worth noting that the development of λ correlations heavily relies on the availability of phase transition experiments in nanopores. However, there is no comprehensive experimental data available from one single research group due to the technical challenges associated with such nano-scale experiments. Being validated by more experimental data made available in the future, the thermodynamic model developed in this work should provide more reliable and systematic results on two-phase equilibrium predictions in nanopores.

Chapter 3:

We developed a new three-phase flash algorithm that considers the effect of the capillary pressure in confined nanopores. Phase capillary pressures are coupled in the proposed algorithm and the phase IFTs are calculated using two computational models: the Weinaug-Katz model (Weinaug and Katz, 1943) for the liquid-vapor IFT calculations and the Danesh model (Danesh, 2007) for the water-hydrocarbon IFT calculations. The proposed algorithm considers six types of possible fluid distributions based on formation wettability and spreading coefficient, which leads to six different capillary pressure systems. The performance of the proposed algorithm is examined by calculating the three-phase equilibrium in confined nanopores for four examples. It is found that the large capillary pressures greatly shift the three-phase equilibrium boundaries from the bulk ones. Specifically, the three-phase boundary temperature is increased at a fixed pressure and the three-phase boundary pressure is decreased at a fixed temperature. Also, when the vapor-phase trapping phenomenon is found in pore space, the three-phase envelope is altered to a lesser extent by phase capillary pressures compared to the system without the vapor-phase trapping

phenomenon. Furthermore, with a decreasing pore radius, the alteration of the three-phase envelope from the bulk one becomes more significant. When the pore radius is larger than 100 nm, the effect of capillary pressure on the three-phase equilibrium calculation can be neglected. Finally, because the aqueous-vapor and the aqueous-oleic capillary pressures do not vanish at the upper critical end point, the upper critical end point is shifted towards a lower-pressure and lower-temperature position in a confined space.

Chapter 4:

In this work, we developed a modified MMC method to calculate the oil-CO_2 MMP in confined nanopores. The modified MMC method is based on the conventional MMC method (Ahmadi and Johns, 2011), but coupled with the effects of capillarity, confinement, and pore size distribution. A volume-translated PR-EOS (Peng and Robinson, 1976; Abudour, *et al*., 2013) is employed in the proposed algorithm to provide accurate phase density predictions. The proposed algorithm is then applied to calculate the oil-CO_2 MMPs for a real crude oil sample in confined nanopores. The BIPs of the crude oil sample are carefully calibrated using the measured MMP for tight core samples (Zhang and Gu, 2015). It is shown that the measured MMP can be perfectly matched by using the developed algorithm and the tuned BIPs of the oil sample. Then, the effects of temperature and pore radius on the confined oil-CO_2 MMP are investigated in detail. The calculation results suggest that the confined oil-CO_2 MMP is reduced with a smaller pore radius and the reduction becomes more obvious in smaller pores than in larger pores. It is also found that the confined MMP decreases with an increasing temperature at an extremely small pore radius (less than 2.5 nm) and increases with an increasing temperature when the pore radius is relatively large. Furthermore, for each pore radius, the confined MMP first increases and then decreases with an increasing temperature, which indicates that there exists a maximum MMP at a given

temperature. This maximum MMP and the temperature corresponding to the maximum confined MMP both decrease with a decreasing pore radius. Finally, when the pore size distribution is applied in the proposed algorithm, the confined MMP is calculated using a mixing rule and the MMP calculated using this proposed mixing rule is noticeably lower than the confined MMP calculated using the average pore radius. The difference between the MMP calculated using these two methods depends on the temperature and pore size distribution.

Chapter 5:

In this chapter, we modified the original cell-to-cell simulation model (Metcalfe *et al.*, 1973) and developed a new MMP calculation algorithm that predicts the oil-gas MMP in confined nanopores. The capillary pressure model and a state-of-art critical point shift model (Tan *et al*., 2019) are coupled in a volume-translated PR-EOS (Peng and Robinson, 1976; Abudour *et al.*, 2013). The proposed algorithm first examines the effect of the number of cells on the calculated oil recovery factor at a given pressure. A cell number of 500 is found to be effective in providing reliable simulation results. Also, the confined MMPs determined by the tie-line length method are validated using the oil recovery curves produced by the proposed algorithm. It is found that the confined MMPs calculated from the tie-line length method are very close to but slightly lower than the inflection points of the oil recovery curves. The confined oil-gas MMP are calculated for four oil-gas systems at different temperatures and pore radii. It is found that the obtained results are in excellent agreement with our previous study (Sun and Li, 2021). The oil-gas MMP is reduced in nanopores and when the pore radius is larger than 20 nm, the oil-gas MMP becomes almost constant and approaches the bulk MMP. The effect of temperature on the confined MMP calculation is studied by calculating the confined MMP at a wide range of temperatures with different pore radii. For all tested pore radii, the confined MMP first increases and then decreases

with an increasing temperature. This is because, at an elevated temperature, the oil phase becomes a vapor phase and the miscibility between two vapor phases requires a lower pressure than the miscibility between one liquid phase and one vapor phase. The effect of injection gas impurity on the confined oil-gas MMP is also studied in this work. With an increasing CH_4 content in the injection gas, the confined MMP increases because CH_4 has a lower solubility in oil than CO_2.

6.2. Suggested Future Work

- The multiphase equilibrium calculations algorithms and the confined MMP calculation algorithms developed in this thesis should be implemented in a compositional reservoir simulator for simulating the multiphase flow in unconventional reservoirs. The proposed algorithms provide more accurate computational results on the reservoir fluids phase behavior and the gas-oil MMP in a confined space compared to the conventional multiphase equilibrium and MMP calculation models. This can potentially improve the predictive accuracy of the compositional simulations in unconventional reservoirs and thereby could be used to optimize the field design of EOR projects in these reservoirs.
- It is pointed out in **Chapter 2** that the correlations of the tuning parameter λ are developed with limited experimental data. It is recommended that the phase transition experiments for pure hydrocarbon substances in nanomaterials (e.g., MCM-41 and SBA-15) should be conducted systematically by a single research group. Then the λ correlations for different hydrocarbons can be developed using the comprehensive experimental dataset. The λ correlations developed using the systematic experimental results should be more consistent and more reliable compared to the λ correlations developed in **Chapter** 2. Eventually, these λ correlations can be applied to reliably predict the λ values of fluid mixtures using the simple linear mixing rule.

- The confined three-phase equilibrium results presented in **Chapter 3** are not validated by experimental data. Such experimental results (three-phase equilibrium measurement in a confined space) are not available due to many technical difficulties (such as manufacturing a high-pressure nanoscale PVT apparatus). It is recommended that the phase transition measurements in a confined space for a three-phase system (aqueous-oleic-vapor) should be conducted in the future to validate the results obtained in **Chapter 3**.
- The critical point shift model (Tan *et al*., 2019) applied in this thesis is developed using the experimental data of capillary condensation for light hydrocarbon components. Therefore, this model does not necessarily work well for heavier hydrocarbons. More experiments should be conducted to measure the confined critical points of heavier hydrocarbons to develop a more reliable critical point shift model. Furthermore, the shift of the upper critical end point as predicted for a three-phase system (aqueous-oleic-vapor) in a confined space should be also experimentally verified in future work.
- The confined gas-oil MMP measurements should be carried out using a nanomaterial with uniform pore size. Conventionally, the confined MMP is measured with tight/shale formation cores which contain pores of different sizes. The pore size heterogeneity could largely affect the accuracy of the measured confined MMP. Recently, a microfluidic device has been developed to measure the CO_2-oil MMP. Such a device can be modified to measure the CO_2-oil MMP in nanopores (Bao *et al*., 2020). Systematic MMP measurements could be conducted using such uniform-size nanofluidic devices. Then, the experimental data can be used to further validate the accuracy and reliability of the proposed MMC algorithms.

References

Abudour, A., Mohammad, S., Robinson, R., and Gasem, K. 2013. Volume-Translated Peng-Robinson Equation of State for Liquid Densities of Diverse Binary Mixtures. *Fluid Phase Equilibria*, 349, 37-55.

Ahmadi, K. and Johns, R. 2011. Multiple-Mixing-Cell Method for MMP Calculations. *SPE Journal*, 16(04), 733-742.

Bao B., Feng, J., Qiu, J., and Zhao, S. 2020. Direct Measurement of Minimum Miscibility Pressure of Decane and CO_2 in Nanoconfined Channels. *ACS Omega*, 6, 943-953.

Danesh, A. 2007. PVT and Phase Behaviour of Petroleum Reservoir Fluids. Amsterdam: Elsevier.

Metcalfe, R.S., Fussell, D.D., and Shelton, J.L. 1973. A Multicell Equilibrium Separation Model for the Study of Multiple Contact Miscibility in Rich-Gas Drives. *SPE Journal*, 13(3), 147-155.

Peng, D. and Robinson, D. 1976. A New Two-Constant Equation of State. *Industrial & Engineering Chemistry Fundamentals*, 15(1), 59-64.

Rezaveisi, M., Sepehrnoori, K., Pope, G.A., and Johns, R.T. 2018. Thermodynamic Analysis of Phase Behavior at High Capillary Pressure. *SPE Journal*, 23(06), 1977-1990.

Tan, S. and Piri, M. 2015. Equation-of-State Modeling of Confined-Fluid Phase Equilibria in Nanopores. *Fluid Phase Equilibria*, 393, 48-63.

Tan, S., Qiu, X., Dejam, M., and Adidharma, H. 2019. Critical Point of Fluid Confined in Nanopores: Experimental Detection and Measurement. *The Journal of Physical Chemistry C*, 123(15), 9824-9830.

Weinaug, C. and Katz, D. 1943. Surface Tensions of Methane-Propane Mixtures. *Industrial & Engineering Chemistry*, 35(2), 239-246.

Zhang, K. and Gu, Y. 2015. Two Different Technical Criteria for Determining the Minimum Miscibility Pressures (MMPs) from the Slim-Tube and Coreflood Tests. *Fuel*, 161, 146-156.

BIBLIOGRAPHY

Aalto, M., Keskinen, K.I., Aittamaa, J., and Liukkonen, S. 1996. An Improved Correlation for Compressed Liquid Densities of Hydrocarbons. Part 2. Mixtures. *Fluid Phase Equilibria*, 114, 21-35.

Abu Al-Rub, F. and Datta, R. 1999. Theoretical Study of Vapor–Liquid Equilibrium inside Capillary Porous Plates. *Fluid Phase Equilibria*, 162, 83-96.

Abudour, A.M., Mohammad, S.A., Robinson Jr., R.L., and Gasem, K.A.M. 2012. Volume-Translated Peng-Robinson Equation of State for Saturated and Single-Phase Liquid Densities. *Fluid Phase Equilibria*, 335, 74-87.

Abudour, A.M., Mohammad, S.A., Robinson Jr., R.L., and Gasem, K.A.M. 2013. Volume-Translated Peng-Robinson Equation of State for Liquid Densities of Diverse Binary Mixtures. *Fluid Phase Equilibria*, 349, 37-55.

Adidharma, H., Dejam, M., and Qiu, X. 2020. Methods and Systems for Isochoric Measurements Using Differential Scanning Calorimetry. *U.S. Patent Application* 16/548, 898.

Adyani, W.N. and Kechut, N.I. 2007. Advanced Technology for Rapid Minimum Miscibility Pressure Determination (Part 1). In: Asia Pacific Oil and Gas Conference and Exhibition. Society of Petroleum Engineers.

Ahmadi, K. and Johns, R. 2011. Multiple-Mixing-Cell Method for MMP Calculations. *SPE Journal*, 16(04), 733-742.

Ahmadi, M., Zendehboudi, S., and James, L. 2017. A Reliable Strategy to Calculate Minimum Miscibility Pressure of CO_2-Oil System in Miscible Gas Flooding Processes. *Fuel*, 208, 117-126.

Alfi, M., Nasrabadi, H., and Banerjee, D. 2017. Effect of Confinement on Bubble Point Temperature Shift of Hydrocarbon Mixtures: Experimental Investigation Using Nanofluidic Devices. In: SPE Annual Technical Conference and Exhibition. Society of Petroleum Engineers.

Baidakov, V.G., Kaverin, A.M., and Khotienkova, M.N. 2013. Surface Tension of Ethane-Methane Solutions: 1. Experiment and Thermodynamic Analysis of the Results. *Fluid Phase Equilibria*, 356, 90-95.

Bao B., Feng, J., Qiu, J., and Zhao, S. 2020. Direct Measurement of Minimum Miscibility Pressure of Decane and CO_2 in Nanoconfined Channels. *ACS Omega*, 6, 943-953.

Barsotti, E., Tan, S., Piri, M., and Chen, J. 2018. Phenomenological Study of Confined Criticality: Insights from the Capillary Condensation of Propane, *n*-Butane, and *n*-Pentane in Nanopores. *Langmuir*, 34, 4473-4483.

Belhaj, H., Abukhalifeh, H., and Javid, K. 2013. Miscible Oil Recovery Utilizing N_2 and/or HC Gases in CO_2 Injection. *Journal of Petroleum Science and Engineering*, 111, 144-152.

Bhatia, S., Bonilla, M., and Nicholson, D. 2011. Molecular Transport in Nanopores: A Theoretical Perspective. *Physical Chemistry Chemical Physics*, 13(34), 15350.

Bonapace, J. 2015. Water Management for Tight and Shale Reservoir: A Review of What Has Been Learned and What Should Be Considered for Development in Argentina. In: SPE Latin

American and Caribbean Health, Safety, Environment, and Sustainability Conference. Society of Petroleum Engineers.

Brusilovsky, A. 1992. Mathematical Simulation of Phase Behavior of Natural Multicomponent Systems at High Pressures with an Equation of State. *SPE Reservoir Engineering*, 7(01), 117-122.

Chou, G.F. and Prausnitz, J.M. 1989. A Phenomenological Correction to an Equation of State for the Critical Region. *AIChE Journal*, 35, 1487-1496.

Christiansen, R.L. and Haines, H.K. 1987. Rapid Measurement of Minimum Miscibility Pressure with the Rising-Bubble Apparatus. *SPE Reservoir Engineering*, 2(4), 443-449.

Chueh, P.L. and Prausnitz, J.M. 1967. Vapor-Liquid Equilibria at High Pressures: Calculation of Critical Temperatures, Volumes, and Pressures of Nonpolar Mixtures. *AIChE Journal*, 13, 1107-1113.

Cui, X., Yang, E., Song, K., Huang, J., Killough, J., and Dong, C. 2018. Phase Equilibrium of Hydrocarbons Confined in Nanopores from a Modified Peng-Robinson Equation of State. In: SPE Annual Technical Conference and Exhibition. Society of Petroleum Engineers.

Danesh, A. 2007. PVT and Phase Behaviour of Petroleum Reservoir Fluids. Amsterdam: Elsevier.

Dong, J. 2014. A High Order Method for Three Phase Flow in Homogeneous Porous Media. *SIAM Undergraduate Research Online*, 7, 74-88.

Dong, X., Liu, H., Hou, J., Wu, K., and Chen, Z. 2016. Phase Equilibria of Confined Fluids in Nanopores of Tight and Shale Rocks Considering the Effect of Capillary Pressure and Adsorption Film. *Industrial & Engineering Chemistry Research*, 55, 798-811.

Elsharkawy, A.M., Poettmann, F.H., and Christiansen, R.L. 1996. Measuring CO_2 Minimum Miscibility Pressures: Slim-Tune or Rising-Bubble Method? *Energy & Fuels*, 10, 443-449.

Firincioglu, T., Ozkan, E., and Ozgen, C. 2012. Thermodynamics of Multiphase Flow in Unconventional Liquids-Rich Reservoirs. In: SPE Annual Technical Conference and Exhibition. Society of Petroleum Engineers.

Firoozabadi, A., Katz, D., Soroosh, H., and Sajjadian, V. 1988. Surface Tension of Reservoir Crude Oil/Gas Systems Recognizing the Asphalt in the Heavy Fraction. *SPE Reservoir Engineering*, 3, 265-272.

Firoozabadi, A. and Ramey, H. 1988. Surface Tension of Water-Hydrocarbon Systems at Reservoir Conditions. *Journal of Canadian Petroleum Technology*, 27(03), 41-48.

Gamadi, T.D., Sheng, J.J., and Soliman, M.Y. 2013. An Experimental Study of Cyclic Gas Injection to Improve Shale Oil Recovery. In: SPE Annual Technical Conference and Exhibition. Society of Petroleum Engineers.

Green, D.W. and Willhite, G.P. 1998. Enhanced Oil Recovery. Richardson, TX: Henry L. Doherty Memorial Fund of AIME, Society of Petroleum Engineers.

Gross, J. and Sadowski, G. 2001. Perturbed-Chain SAFT: An Equation of State Based on a Perturbation Theory for Chain Molecules. *Industrial & Engineering Chemistry Research*, 40, 1244-1260.

Gross, J. and Sadowski, G. 2002. Application of the Perturbed-Chain SAFT Equation of State to Associating Systems. *Industrial & Engineering Chemistry Research*, 41(22), 5510-5515.

Hamada, Y., Koga, K., and Tanaka, H. 2007. Phase Equilibria and Interfacial Tension of Fluids Confined in Narrow Pores. *The Journal of Chemical Physics*, 127(8), 084908.

Holm, L. and Josendal, V. 1974. Mechanisms of Oil Displacement by Carbon Dioxide. *Journal of Petroleum Technology*, 26(12), 1427-1438.

Hugill, J.A. and van Welsenes, A.J. 1986. Surface Tension: A Simple Correlation for Natural Gas + Condensate System. *Fluid Phase Equilibria*, 29, 383-390.

Hustad, O. and Browning, D. 2010. A Fully Coupled Three-Phase Model for Capillary Pressure and Relative Permeability for Implicit Compositional Reservoir Simulation. *SPE Journal*, 15(04), 1003-1019.

Iwere, F.O., Heim, R.N., and Cherian, B.V. 2012. Numerical Simulation of Enhanced Oil Recovery in the Middle Bakken and Upper Three Forks Tight Oil Reservoirs of the Williston Basin. In: The Americas Unconventional Resources Conference. Society of Petroleum Engineers.

Jaubert, J.N., Arras, L., Neau, E., and Avaullée, L. 1998a. Properly Defining the Classical Vaporizing the Condensing Mechanisms when a Gas is Injected into a Crude Oil. *Industrial & Engineering Chemistry Research*, 37, 4860-4869.

Jaubert, J.N., Wolff, L., Neau, E., and Avaullée, L. 1998b. A Very Simple Multiple Mixing Cell Calculation to Compute the Minimum Miscibility Pressure Whatever the Displacement Mechanism. *Industrial & Engineering Chemistry Research*, 37, 4854-4859.

Jin, L., Pekot, L.J., Hawthorne, S.B., Gobran, B., Greeves, A., Bosshart, N.W., Jiang, T., Hamling, J.A., and Gorecki, C.D. 2016. Impact of CO_2 Impurity on MMP and Oil Recovery Performance of the Bell Creek Oil Field. *Energy Procedia*, 114, 6997-7008.

Jin, Z. and Firoozabadi, A. 2016. Thermodynamic Modeling of Phase Behavior in Shale Media. *SPE Journal*, 21(01), 190-207.

Johns, R. and Orr, F. 1996. Miscible Gas Displacement of Multicomponent Oils. *SPE Journal*, 1(01), 39-50.

Kantzas, A., Nikakhtar, B., and Pow, M. 1998. Principles of Three Phase Capillary Pressures. *Journal of Canadian Petroleum Technology*, 37(07), 48-54.

Khan, M.R., Kalam, S., Khan, R.A., Tariq, Z., and Abdulraheem, A. 2019. Comparative Analysis of Intelligent Algorithms to Predict the Minimum Miscibility Pressure for Hydrocarbon Gas Flooding. In: Abu Dhabi International Petroleum Exhibition & Conference. Society of Petroleum Engineers.

Kolodzie Jr., S. 1980. Analysis of Pore Throat Size and Use of the Waxman-Smits Equation to Determine OOIP in Spindle Field, Colorado. In: 55th Annual Fall Technical Conference and Exhibition of the Society of Petroleum Engineers of AIME. Society of Petroleum Engineers.

Lapene, A., Nichita, D., Debenest, G., and Quintard, M. 2010. Three-Phase Free-Water Flash Calculations Using a New Modified Rachford–Rice Equation. *Fluid Phase Equilibria*, 297(1), 121-128.

Lashgari, H., Sun, A., Zhang, T., Pope, G., and Lake, L. 2019. Evaluation of Carbon Dioxide Storage and Miscible Gas EOR in Shale Oil Reservoirs. *Fuel*, 241, 1223-1235.

Lee, B. and Kesler, M. 1975. A Generalized Thermodynamic Correlation Based on Three-Parameter Corresponding States. *AIChE Journal*, 21(3), 510-527.

Lee, J.I. 1979. Effectiveness of Carbon Dioxide Displacement under Miscible and Immiscible Conditions. Report RR-40. Petroleum Recovery Institute, Calgary.

Li, B. and Mezzatesta, A. 2017. Evaluation of Pore Size Distribution Effects on Phase Behavior of Hydrocarbons Produced in Shale Gas Condensate Reservoirs. In: SPE Middle East Oil & Gas Show and Conference. Society of Petroleum Engineers.

Li, D., Li, X., Zhang, Y., Sun, L., and Yuan, S. 2019. Four Methods to Estimate Minimum Miscibility Pressure of CO_2-Oil Based on Machine Learning. *Chinese Journal of Chemistry*, 37, 1271-1278.

Li, H., Qin, J., and Yang, D. 2012. An Improved CO_2–Oil Minimum Miscibility Pressure Correlation for Live and Dead Crude Oils. *Industrial & Engineering Chemistry Research*, 51(8), 3516-3523.

Li, L. and Sheng, J. 2017. Nanopore Confinement Effects on Phase Behavior and Capillary Pressure in a Wolfcamp Shale Reservoir. *Journal of the Taiwan Institute of Chemical Engineers*, 78, 317-328.

Li, L., Sheng, J., Su, Y., and Zhan, S. 2018. Further Investigation of Effects of Injection Pressure and Imbibition Water on CO_2 Huff-n-Puff Performance in Liquid-Rich Shale Reservoirs. *Energy & Fuels*, 32(5), 5789-5798.

Li, L., Zhang, Y., and Sheng, J. 2017. Effect of the Injection Pressure on Enhancing Oil Recovery in Shale Cores during the CO_2 Huff-n-Puff Process When It Is above and below the Minimum Miscibility Pressure. *Energy & Fuels*, 31(4), 3856-3867.

Li, R. and Li, H. 2018. New Two-Phase and Three-Phase Rachford-Rice Algorithms Based on Free-Water Assumption. *The Canadian Journal of Chemical Engineering*, 96(1), 390-403.

Li, X., Wei, H., Chen, B., Liu, X., Wang, W., and Zhao, X. 2008. Multi-Stage Fracturing Stimulations Improve Well Performance in Tight Oil Reservoirs of the Changqing Oilfield. In: The International Petroleum Technology Conference. International Petroleum Technology Conference.

Li, Z., Qu, X., Liu, W., Lei, Q., Sun, H., and He, Y. 2015. Development Modes of Triassic Yanchang Formation Chang 7 Member tight oil in Ordos Basin, NW China. *Petroleum Exploration and Development*, 42(2), 241-246.

Loucks, R., Reed, R., Ruppel, S., and Jarvie, D. 2009. Morphology, Genesis, and Distribution of Nanometer-Scale Pores in Siliceous Mudstones of the Mississippian Barnett Shale. *Journal of Sedimentary Research*, 79(12), 848-861.

Luo, S. and Barrufet, M. 2005. Reservoir Simulation Study of Water-in-Oil Solubility Effect on Oil Recovery in Steam Injection Process. *SPE Reservoir Evaluation & Engineering*, 8(06), 528-533.

Macleod, D. 1923. On a Relation Between Surface Tension and Density. *Transactions of the Faraday Society*, 19, 38-41.

Metcalfe, R.S., Fussell, D.D., and Shelton, J.L. 1973. A Multicell Equilibrium Separation Model for the Study of Multiple Contact Miscibility in Rich-Gas Drives. *SPE Journal*, 13(3), 147-155.

Mohsen-Nia, M., Rasa, H., and Naghibi, S.F. 2009. Experimental and Theoretical Study of Surface Tension of *n*-Pentane, *n*-Heptane, and Some of Their Mixtures at Different Temperatures. *Journal of Chemical Thermodynamics*, 42, 110-113.

Moortgat, J. and Firoozabadi, A. 2013. Three-Phase Compositional Modeling with Capillarity in Heterogeneous and Fractured Media. *SPE Journal*, 18(06), 1150-1168.

Mungan, N. 1981. Carbon Dioxide Flooding-Fundamentals. *Journal of Canadian Petroleum Technology*, 20(01), 87-92.

Mungan, N. 1991. An Evaluation of Carbon Dioxide Flooding. In: SPE Western Regional Meeting. Society of Petroleum Engineers.

Neau, E., Avaullée, L., and Jaubert, J.N. 1996. A New Algorithm for Enhanced Oil Recovery Calculations. *Fluid Phase Equilibria*, 117, 265-272.

Neshat, S.S., Okuno, R., and Pope, G.A. 2018. A Rigorous Solution to the Problem of Phase Behavior in Unconventional Formations with High Capillary Pressure. *SPE Journal*, 23(04), 1438-1451.

Nguyen, P., Mohaddes, D., Riordon, J., Fadaei, H., Lele, P., and Sinton, D. 2015. Fast Fluorescence-Based Microfluidic Method for Measuring Minimum Miscibility Pressure of CO_2 in Crude Oils. *Analytical Chemistry*, 87(6), 3160-3164.

Nikpoor, M., Dejam, M., Chen, Z., and Clarke, M. 2016. Chemical–Gravity–Thermal Diffusion Equilibrium in Two-Phase Non-isothermal Petroleum Reservoirs. *Energy & Fuels*, 30, 2021-2034.

Nojabaei, B., Johns, R., and Chu, L. 2013. Effect of Capillary Pressure on Phase Behavior in Tight Rocks and Shales. *SPE Reservoir Evaluation & Engineering*, 16(03), 281-289.

Oellrich, L., Plocker, U., Prausnitz, J., and Knapp, H. 1981. Equation-of-State Methods for Computing Phase Equilibria and Enthalpies. *International Chemical Engineering*, 21, 1-15.

Øren, P. and Pinczewski, W. 1991. The Effect of Film-Flow on the Mobilization of Waterflood Residual Oil by Gas Flooding. In: 6th European Symposium on Improved Oil Recovery. European Association of Geoscientists & Engineers.

Øren, P. and Pinczewski, W. 1994. The Effect of Wettability and Spreading Coefficients on the Recovery of Waterflood Residual Oil by Miscible Gasflooding. *SPE Formation Evaluation*, 9(02), 149-156.

Øren, P., Billiotte, J., and Pinczewski, W. 1992. Mobilization of Waterflood Residual Oil by Gas Injection for Water-Wet Conditions. *SPE Formation Evaluation*, 7(01), 70-78.

Orr, F. and Jensen, C. 1984. Interpretation of Pressure-Composition Phase Diagrams for CO2/Crude-Oil Systems. *SPE Journal*, 24(05), 485-497.

Pang, J., Zuo, J., Zhang, D., and Du, L. 2012. Impact of Porous Media on Saturation Pressures of Gas and Oil in Tight Reservoirs. In: SPE Canadian Unconventional Resources Conference. Society of Petroleum Engineers.

Pang, W. and Li, H. 2017. An Augmented Free-Water Three-Phase Rachford-Rice Algorithm for CO_2 /hydrocarbons/water mixtures. *Fluid Phase Equilibria*, 450, 86-98.

Passey, Q., Bohacs, K., Esch, W., Klimentidis, R., and Sinha, S. 2010. From Oil-Prone Source Rock to Gas-Producing Shale Reservoir-Geologic and Petrophysical Characterization of Unconventional Shale-Gas Reservoirs. In: CPS/SPE International Oil & Gas Conference and Exhibition. Society of Petroleum Engineers.

Péneloux, A., Rauzy, E., and Fréze, R. 1982. A Consistent Correction for Redlich-Kwong-Soave Volumes. *Fluid Phase Equilibria*, 8(1), 7-23.

Peng, D. and Robinson, D. 1976a. A New Two-Constant Equation of State. *Industrial & Engineering Chemistry Fundamentals*, 15(1), 59-64.

Peng, D. and Robinson, D. 1976b. Two and three phase equilibrium calculations for systems containing water. *The Canadian Journal of Chemical Engineering*, 54(6), 595-599.

Ping, G., Liangtian, S., Li, S., and Sun, L., 1996. A Theoretical Study of the Effect of Porous Media on the Dew Point Pressure of a Gas Condensate. In: SPE Gas Technology Symposium. Society of Petroleum Engineers.

Qi, Z., Liang, B., Deng, R., Du, Z., Wang, S., and Zhao, W. 2007. Phase Behavior Study in the Deep Gas-Condensate Reservoir with Low Permeability. In: SPE Europec/EAGE Annual Conference and Exhibition. Society of Petroleum Engineers.

Qiao, S., Bhatia, S., and Nicholson, D. 2004. Study of Hexane Adsorption in Nanoporous MCM-41 Silica. *Langmuir*, 20, 389-395.

Qiu, X., Tan, S., Dejam, M., and Adidharma, H. 2019. Experimental Study on the Criticality of a Methane/Ethane Mixture Confined in Nanoporous Media. *Langmuir*, 35(36), 11635-11642.

Qiu, X., Tan, S., Dejam, M., and Adidharma, H. 2020. Isochoric Measurement of the Evaporation Point of Pure Fluids in Bulk and Nanoporous Media Using Differential Scanning Calorimetry. *Physical Chemistry Chemical Physics*, 22, 7048-7057.

Qiu, X., Tan, S., Dejam, M., and Adidharma, H. 2018. Simple and Accurate Isochoric Differential Scanning Calorimetry Measurements: Phase Transitions for Pure Fluids and Mixtures in Nanopores. *Physical Chemistry Chemical Physics*, 21, 224-231.

Quayle, O.R. 1953. The Parachors of Organic Compounds. An Interpretation and Catalogue. *Chemical Reviews*, 53 (3), 439-589.

Rachford, H. and Rice, J. 1952. Procedure for Use of Electronic Digital Computers in Calculating Flash Vaporization Hydrocarbon Equilibrium. *Journal of Petroleum Technology*, 4(10), 19-3.

Randall, T. and Bennion, D. 1988. Recent Developments in Slim Tube Testing for Hydrocarbon-Miscible Flood (HCMF) Solvent Design. *Journal of Canadian Petroleum Technology*, 27(06), 33-44.

Rao, D. 1997. A New Technique of Vanishing Interfacial Tension for Miscibility Determination. *Fluid Phase Equilibria*, 139(1-2), 311-324.

Rathmell, J.J., Stalkup, F.I., and Hassinger, R.C. 1971. A Laboratory Investigation of Miscible Displacement by Carbon Dioxide. In: Fall Meeting of the Society of Petroleum Engineers of AIME. Society of Petroleum Engineers.

Redlich, O. and Kwong, J.N. 1949. On the Thermodynamics of Solutions. V. An Equation of State. Fugacities of Gaseous Solutions. *Chemical Reviews*, 44, 233-244.

Rezaveisi, M., Sepehrnoori, K., Pope, G., and Johns, R. 2015. Compositional Simulation Including Effect of Capillary Pressure on Phase Behavior. In: SPE Annual Technical Conference and Exhibition. Society of Petroleum Engineers.

Rezaveisi, M., Sepehrnoori, K., Pope, G.A., and Johns, R.T. 2018. Thermodynamic Analysis of Phase Behavior at High Capillary Pressure. *SPE Journal*, 23(06), 1977-1990.

Robinson, D. and Peng, D. 1978. The Characterization of the Heptanes and Heavier Fractions for the GPA Peng-Robinson programs. Tulsa, Oklahoma: Gas Processors Association.

Rolo, L., Caço, A., Queimada, A., Marrucho, I., and Coutinho, J. 2002. Surface Tension of Heptane, Decane, Hexadecane, Eicosane, and Some of Their Binary Mixtures. *Journal of Chemical & Engineering Data*, 47(6), 1442-1445.

Russo, P., Ribeiro Carrott, M., and Carrott, P. 2012. Trends in the Condensation/Evaporation and Adsorption Enthalpies of Volatile Organic Compounds on Mesoporous Silica Materials. *Microporous and Mesoporous Materials*, 151, 223-230.

Sandoval, D., Yan, W., Michelsen, M., and Stenby, E. 2015. Phase Envelope Calculations for Reservoir Fluids in the Presence of Capillary Pressure. In: SPE Annual Technical Conference and Exhibition. Society of Petroleum Engineers.

Seneviratne, K., Hughes, T., Johns, M., Marsh, K., and May, E. 2017. Surface Tension and Critical Point Measurements of Methane + Propane Mixtures. *The Journal of Chemical Thermodynamics*, 111, 173-184.

Shaw, J.M. and Zou, X. 2007. Phase Behavior of Heavy Oils. In: Mullins O.C., Sheu E.Y., Hammami A., Marshall A.G. (eds) Asphaltenes, Heavy Oils, and Petroleomics. Springer, New York, NY.

Sheng, L., Lutkenhaus, J. L., and Nasrabadi, H. 2015. Experimental Study of Confinement Effect on Hydrocarbon Phase Behavior in Nano-Scale Porous media Using Differential Scanning Calorimetry. In: SPE Annual Technical Conference and Exhibition. Society of Petroleum Engineers.

Sherafati, M. and Jessen, K. 2017. Stability Analysis for Multicomponent Mixtures Including Capillary Pressure. *Fluid Phase Equilibria*, 433, 56-66.

Shokir, E. 2007. CO_2-Oil Minimum Miscibility Pressure Model for Impure and Pure CO_2 Streams. *Journal of Petroleum Science and Engineering*, 58(1-2), 173-185.

Siripatrachai, N., Ertekin, T., and Johns, R. 2017. Compositional Simulation of Hydraulically Fractured Tight Formation Considering the Effect of Capillary Pressure on Phase Behavior. *SPE Journal*, 22(04), 1046-1063.

Sun, H. and Li, H. 2019. A New Three-Phase Flash Algorithm Considering Capillary Pressure in a Confined Space. *Chemical Engineering Science*, 193, 346-363.

Sun, H. and Li, H. 2020. Phase Behavior Modeling of Hydrocarbon Fluids in Nanopores Using PR-EOS Coupled with a Modified Young-Laplace Equation. *ACS Omega*, 5, 15177-15191.

Sun, H. and Li, H. 2021. Minimum Miscibility Pressure Determination in Confined Nanopores Considering Pore Size Distribution of Tight/Shale Formations. *Fuel*, 286, 119450.

Tan, S., Qiu, X., Dejam, M., and Adidharma, H. 2019. Critical Point of Fluid Confined in Nanopores: Experimental Detection and Measurement. *The Journal of Physical Chemistry C*, 123(15), 9824-9830.

Tan, S. and Piri, M. 2015. Equation-of-State Modeling of Associating-Fluids Phase Equilibria in Nanopores. *Fluid Phase Equilibria*, 405, 157-166.

Tan, S. and Piri, M. 2017. Retrograde Behavior Revisited: Implications for Confined Fluid Phase Equilibria in Nanopores. *Physical Chemistry Chemical Physics*, 19, 18890-18901.

Tan, S. and Piri, M. 2019. Application of Material Balance for the Phase Transition of Fluid Mixtures Confined in Nanopores. *Fluid Phase Equilibria*, 496, 31-41.

Teklu, T.W., Alharthy, N., Kazemi, H., Yin, X., and Graves, R.M. 2014a. Vanishing Interfacial Tension Algorithm for MMP Determination in Unconventional Reservoirs. In: SPE Western North American and Rocky Mountain Joint Regional Meeting. Society of Petroleum Engineers.

Teklu, T., Alharthy, N., Kazemi, H., Yin, X., Graves, R., and AlSumaiti, A. 2014b. Phase Behavior and Minimum Miscibility Pressure in Nanopores. *SPE Reservoir Evaluation & Engineering*, 17(03), 396-403.

Tolbert, B.T. and Wu, X. 2015. Quantifying Pore Size Distribution Effect on Gas in Place and Recovery Using SLD-PR EOS for Multiple-Components Shale Gas Reservoir. In: SPE Asia Pacific Unconventional Resources Conference and Exhibition. Society of Petroleum Engineers.

Travalloni, L., Castier, M., Tavares, F., and Sandler, S. 2010. Thermodynamic Modeling of Confined Fluids Using an Extension of the Generalized van der Waals Theory. *Chemical Engineering Science*, 65, 3088-3099.

van Dijke, M., McDougall, S., and Sorbie, K. 2001. Three-Phase Capillary Pressure and Relative Permeability Relationships in Mixed-Wet System. *Transport in Porous Media*, 44(1), 1-32.

Vinh-Thang, H., Huang, Q., Eić, M., Trong-On, D., and Kaliaguine, S. 2005. Adsorption of C7Hydrocarbons on Biporous SBA-15 Mesoporous Silica. *Langmuir*, 21, 5094-5101.

Wang, F. and Reed, R. 2009. Pore Networks and Fluid Flow in Gas Shales. In: SPE Annual Technical Conference and Exhibition. Society of Petroleum Engineers.

Wang, L., Yin, X., Neeves, K., and Ozkan, E. 2016a. Effect of Pore-Size Distribution on Phase Transition of Hydrocarbon Mixtures in Nanoporous Media. *SPE Journal*, 21(06), 1981-1995.

Wang, S., Ma, M., and Chen, S. 2016b. Application of PC-SAFT Equation of State for CO2 Minimum Miscibility Pressure Prediction in Nanopores. In: SPE Improved Oil Recovery Conference. Society of Petroleum Engineers.

Wang, Y. and Orr, F. 1997. Analytical Calculation of Minimum Miscibility Pressure. *Fluid Phase Equilibria*, 139(1-2), 101-124.

Wang, Y., Yan, B., and Killough, J. 2013. Compositional Modeling of Tight Oil Using Dynamic Nanopore Properties. In: SPE Annual Technical Conference and Exhibition. Society of Petroleum Engineers.

Weinaug, C. and Katz, D. 1943. Surface Tensions of Methane-Propane Mixtures. *Industrial & Engineering Chemistry*, 35(2), 239-246.

Whitson, C. and Brulé, M. 2000. Phase behavior. Richardson, Texas: Henry L. Doherty Memorial Fund of AIME, Society of Petroleum Engineers.

Wilson, G.M., 1969. A Modified Redlich-Kwong Equation of State, Application to General Physical Data Calculations. In: 65th National AIChE Meeting.

Wong, S.W., O'Dell, P.M., de Pater, C.J., and Shaoul, J. 2000. Fresh Water Injection Stimulation in a Deep Tight Oil Reservoir. In: the 2000 SPE/AAPG Western Regional Meeting. Society of Petroleum Engineers.

Wu, K., Chen, Z., Li, J., Li, X., Xu, J., and Dong, X. 2017. Wettability Effect on Nanoconfined Water Flow. *Proceedings of the National Academy of Sciences*, 114(13), 3358-3363.

Wu, K., Chen, Z., Li, J., Xu, J., Wang, K., Wang, S., Dong, X., Zhu, Z., Peng, Y., Jia, X., and Li, X. 2018. Manipulating the Flow of Nanoconfined Water by Temperature Stimulation. *Angewandte Chemie International Edition*, 57(28), 8432-8437.

Wu, K., Chen, Z., Li, X., and Dong, X. 2016. Methane Storage in Nanoporous Material at Supercritical Temperature over a Wide Range of Pressures. *Scientific Reports*, 6(1), 33461.

Xu, Y., Riordon, J., Cheng, X., Bao, B., and Sinton, D. 2017. The Full Pressure-Temperature Phase Envelope of a Mixture in 1000 Microfluidic Chambers. *Angewandte Chemie International Edition*, 129, 13963-13967.

Yang, F., Yu, P., and Zhang, X. 2020. Multiple-Mixing-Cell Model for Calculation of Minimum Miscibility Pressure Controlled by Tie-Line Length. *Geofluids*, 1-8.

Yellig, W. 1982. Carbon Dioxide Displacement of a West Texas Reservoir Oil. *SPE Journal*, 22(06), 805-815.

Yellig, W. and Metcalfe, R. 1980. Determination and Prediction of CO_2 Minimum Miscibility Pressures (includes associated paper 8876). *Journal of Petroleum Technology*, 32(01), 160-168.

Young, T. 1805. An Essay on the Cohesion of Fluids. *Philosophical Transactions of the Royal Society of London*, 95(0), 65-87.

Yu, W., Lashgari, H., Wu, K., and Sepehrnoori, K. 2015. CO_2 Injection for Enhanced Oil Recovery in Bakken Tight Oil Reservoirs. *Fuel*, 159, 354-363.

Yuan, H. and Johns, R. 2005. Simplified Method for Calculation of Minimum Miscibility Pressure or Enrichment. *SPE Journal*, 10(04), 416-425.

Yuan, H., Johns, R., Egwuenu, A., and Dindoruk, B. 2005. Improved MMP Correlation for CO_2 Floods Using Analytical Theory. *SPE Reservoir Evaluation & Engineering*, 8(05), 418-425.

ZareNezhad, B. 2016. A New Correlation for Predicting the Minimum Miscibility Pressure Regarding the Enhanced Oil Recovery Processes in the Petroleum Industry. *Petroleum Science and Technology*, 34(1), 56-62.

Zarragoicoechea, G. and Kuz, V. 2004. Critical Shift of a Confined Fluid in a Nanopore. *Fluid Phase Equilibria*, 220(1), 7-9.

Zhang, K. and Gu, Y. 2015. Two Different Technical Criteria for Determining the Minimum Miscibility Pressures (MMPs) from the Slim-Tube and Coreflood Tests. *Fuel*, 161, 146-156.

Zhang, K., Du, F., and Nojabaei, B. 2019a. Effect of Pore Size Heterogeneity on Hydrocarbon Fluid Distribution and Transport in Nanometer-Sized Porous Media. In: SPE Eastern Regional Meeting. Society of Petroleum Engineers.

Zhang, K., Jia, N., and Li, S. 2017a. Exploring the Effects of Four Important Factors on Oil–CO_2 Interfacial Properties and Miscibility in Nanopores. *RSC Advances*, 7(85), 54164-54177.

Zhang, K., Jia, N., Li, S., and Liu, L. 2018a. Nanoscale-Extended Correlation to Calculate Gas Solvent Minimum Miscibility Pressures in Tight Oil Reservoirs. *Journal of Petroleum Science and Engineering*, 171, 1455-1465.

Zhang, K., Jia, N., Zeng, F., and Luo, P. 2017b. A New Diminishing Interface Method for Determining the Minimum Miscibility Pressures of Light Oil–CO_2 Systems in Bulk Phase and Nanopores. *Energy & Fuels*, 31(11), 12021-12034.

Zhang, K., Nojabaei, B., Ahmadi, K., and Johns, R.T. 2018b. Minimum Miscibility Pressure Calculation for Oil Shale and Tight Reservoirs with Large Gas-Oil Capillary Pressure. In: Unconventional Resources Technology Conference. Society of Petroleum Engineers.

Zhang, K., Nojabaei, B., Ahmadi, K., and Johns, R.T. 2020. Effect of Gas/Oil Capillary Pressure on Minimum Miscibility Pressure for Tight Reservoirs. *SPE Journal*, 25(2), 820-831.

Zhang, Y., Di, Y., Yu, W., and Sepehrnoori, K. 2019b. A Comprehensive Model for Investigation of Carbon Dioxide Enhanced Oil Recovery with Nanopore Confinement in the Bakken Tight Oil Reservoir. *SPE Reservoir Evaluation & Engineering*, 22(01), 122-136.

Zhang, Y., Lashgari, H., Di, Y., and Sepehrnoori, K. 2016. Capillary Pressure Effect on Hydrocarbon Phase Behavior in Unconventional Reservoir. In: SPE Low Perm Symposium. Society of Petroleum Engineers.

Zhao, G., Adidharma, H., Towler, B., and Radosz, M. 2006. Using a Multiple-Mixing-Cell Model to Study Minimum Miscibility Pressure Controlled by Thermodynamic Equilibrium Tie Lines. *Industrial & Engineering Chemistry Research*, 45(23), 7913-7923.

Zhong, J., Zhao, Y., Lu, C., Xu, Y., Jin, Z., Mostowfi, F., and Sinton, D. 2018. Nanoscale Phase Measurement for the Shale Challenge: Multicomponent Fluids in Multiscale Volumes. *Langmuir*, 34, 9927-9935.

Zick, A.A. 1986. A Combined Condensing/Vaporizing Mechanism in the Displacement of Oil by Enriched Gases. In: SPE Annual Technical Conference and Exhibition. Society of Petroleum Engineers.

Zuo, J., Guo, X., Liu, Y., Pan, S., Canas, J., and Mullins, O. 2018. Impact of Capillary Pressure and Nanopore Confinement on Phase Behaviors of Shale Gas and Oil. *Energy & Fuels*, 32, 4705-4714.